UNIVERSITAT POLITÈCNICA DE VALÈNCIA

DESIGN OF HIGH MN FE-MN-AL-C LOW DENSITY STEELS FOR ADDITIVE MANUFACTURING

By

MANUEL SÁNCHEZ-PONCELA

DOCTOR OF PHILOSOPHY

In ENGINEERING AND INDUSTRIAL PRODUCTION (Technology of Materials)

UNIVERSITAT POLITÈCNICA DE VALÈNCIA

APRIL 2024

PhD Thesis Director: *PhD. Rosalía Rementeria*

PhD Thesis Tutor: *PhD. Vicente Amigó Borrás*

This PhD thesis has been approved in fulfillment of the requirements for the Degree of DOCTOR OF PHILOSOPHY in ENGINEERING AND INDUSTRIAL PRODUCTION (Technology of Materials) with MENTION in INDUSTRIAL PhD (ArcelorMittal Innovación, Investigación e Inversión S.L.).

Tecnología de Materiales / Materials Technology

Dedication

To my family all the ones I love. Especially: my parents, sister, brother, Lolo, and Inés.

Contents

List of Figures

List of Tables

Acknowledgments

As I contemplate the journey that has led to the culmination of this PhD thesis, I am overwhelmed with gratitude for the several persons who have provided guidance, support, and inspiration during this process.

First, I am deeply grateful to my director Rosalía Rementeria. Her expert guidance, insightful suggestions, commitment and dedication have been the fundamental basis of my research, providing a solid foundation upon which this thesis was built. Additionally, I would like to express my gratitude to my tutor Vicente Amigó Borrás, whose significant contribution in securing sufficient measurement time has greatly improved the scientific content of this PhD thesis. I am also grateful for his perspective recommendations. The cooperative environment they cultivated has been essential in improving the quality of my work.

This journey would have taken a very different course had it not been for the pivotal role played by Laura del Río, my boss at ArcelorMittal Global R&D Spain. Her proposal to start this PhD, marked a turning point in my academic career. Her multifaceted support, spanning the scientific, managerial and personal aspects, has been an essential encouragement in making this thesis a reality.

The unwavering support of all my family (parents, siblings, grandparents, uncles, aunts, cousins...) has been my backbone throughout this journey. Above all, my parents' constant love and help have been a source of strength in difficult times, and my

grandfather Lolo's early teachings in mathematics and spelling laid the foundation for my academic pursuits. Their collective support has been one of the pillars of this success.

I am especially grateful to my girlfriend Inés, the best partner I could ever have, whose patience, understanding and support have been essential. Her presence and encouragement have been vital in balancing the demanding workload of this PhD with personal life, making her an integral part of this achievement.

Finally, my sincere thanks to my friends, colleagues and co-workers. Their support has enriched my personal and professional growth.

In sum, the culmination of this PhD thesis has been made possible by the support, guidance and inspiration of those around me. To each of you, my deepest gratitude for your invaluable contribution to my academic and personal development.

List of Abbreviations

AHSS	Advanced High Strength Steel
AM	Additive Manufacturing
APT	Atom Probe Tomography
BCC	Body-Centered Cubic
BTR	Brittle Temperature Range
CALPHAD	Calculation of Phase Diagrams
CNC	Computer Numerical Control
CP	Complex Phase
CSC	Crack Susceptibility Criterion
CTB	Carbide Free Bainitic
DD	Double Diamond
DED	Directed Energy Deposition
DG	Double Gyroid
DoE	Design of Experiment
DP	Dual Phase
DSBR	Dynamic Slip Band Refinement
EBSD	Electron Backscatter Diffraction
EDXS	Energy-Dispersive X-ray Spectrometry
EHLA	Extreme High-speed LAser material deposition

FCC	Face-Centered Cubic
FEG-SEM	Field Emission Gun - Scanning Electron Microscopy
FIB	Focused Ion Beam
G	Temperature gradient in the liquid phase
HAADF	High-angle annular dark field
HAZ	Heat Affected Zone
HC	Hot Cracking
HCC	Hot Cracking Criterion
HCS	Hot Cracking Susceptibility
ICME	Integrated Computational Materials Engineering
IHT	Intrinsic Heat Treatment
IPF	Inverse Pole Figure
LC	Liquation Cracking
LED	Linear Energy Density
LEDS	Low Energy Dislocation Structure
LOF	Lack of Fusion
LOM	Light Optical Microscopy
L-PBF	Laser-Powder Bed Fusion
LRO	Long Range Order
MART	Martensitic
MBIP	Micro Band Induced Plasticity

NNS	Near-Net Shape
PBF	Powder Bed Fusion
PF	Pole Figure
Q&P	Quenching and Partitioning
R	Growth Rate
SC	Solidification Cracking
SDAS	Secondary Dendrite Arm Spacing
SDD	Silicon Drift Detector
SE	Secondary Electron
SEM	Scanning Electron Microscopy
STEM	Scanning Transmission Electron Microscopy
SFE	Stacking Fault Energy
S/L	Solid-Liquid
SRIP	Slip band Refinement-Induced Plasticity
SRO	Short Range Order
TE	Total Elongation
TOF	Time-of-flight
TRIP	Transformation Induced Plasticity
TWIP	Twinning Induced Plasticity
UTS	Ultimate Tensile Strength
VED	Volumetric Energy Density

XRD	X-Ray Diffraction
YS	Yield Strength
3D	Three-Dimension
ΔT	Solidification Interval

Abstract

Additive manufacturing (AM) is a process that builds three-dimensional solid objects by layering materials based on a computer-aided design model. AM is set to become the next industrial revolution, transforming the landscape of development and production. AM provides numerous benefits, including complex and flexible design possibilities, the elimination of intermediate processes like machining, production cost independence from batch size, reduced material waste, lightweight structures, customized machine repairs, and the ability to develop new materials, among other advantages. In additive manufacturing technologies that employ a laser beam as an energy source, the initial raw material (in the form of powder or wire) is melted by the laser heat source in a controlled manner, layer by layer, until a component with final or nearly final dimensions is created. These technologies involve subjecting the printed material to a unique thermal process, where the material is melted in a very specific area and then rapidly cooled at extremely high rates of up to 10^6 K/s. Hence, the microstructures that arise from the manufacturing processes in AM differ significantly from those achieved in traditional processes. Moreover, the materials predominantly employed in AM have not been explicitly designed for these technologies. The specific characteristics of AM processes can be utilized to achieve distinct microstructures and properties in steels that have been tailored to take advantage of the rapid cooling rates and thermal history of the process, among other factors.

For the moment, the number of commercial steel grades available in the AM market is limited. Various industries are demanding new steel grades with lower density to decrease weight without compromising mechanical properties. High manganese steels are regarded as highly promising materials for structural applications due to their exceptional combination of strength and ductility, with low density. Nevertheless, despite the exceptional properties of high manganese steels, they encounter various limitations or challenges during conventional processing techniques. Fortunately, rapid solidification may solve these issues. In this sense, laser-based AM technologies provide rapid cooling rates, as well as flexibility in terms of geometric design. The new challenges of these technologies will involve micro-segregation and hot cracking occurring during solidification.

This thesis is dedicated to exploiting the CALPHAD method to perform thermodynamic calculations in order to design various high manganese steels that can effectively prevent fast solidification issues in AM. The steel compositions designed were produced in the form of powder for AM using gas atomization. Powders were analyzed to determine their microstructure in relation to the chemistry and cooling rate. By adjusting properly, the printing parameters, these high manganese steel powders were successfully printed in AM, resulting in relative densities exceeding 99.9%. The microstructure of these fully dense samples was analyzed and compared to their respective powders, in order to identify any difference resulting from variations in cooling rate and thermal cycling. Lastly, after defining the best set of printing conditions for

each powder composition, various samples were produced to evaluate the mechanical properties, to determine the correlation between the composition, microstructure, and properties of these steels. In addition, lattice structures that are close to final part geometries were constructed to quantify the energy absorbed during compression by one of these high manganese steels. The results were then compared to those of 316L, revealing that the high manganese steel absorbs roughly twice as much the specific energy in compression. This finding demonstrates the potential of these novel AM steels for use in industrial applications.

Resumen

La fabricación aditiva, de sus siglas en inglés AM (*Additive Manufacturing*) es un proceso que construye objetos sólidos tridimensionales mediante la superposición de materiales basados en un modelo de diseño asistido por ordenador. La AM está llamada a convertirse en la próxima revolución industrial, transformando el panorama del desarrollo y la producción. La AM ofrece numerosas ventajas, como posibilidades de diseño complejas y flexibles, la eliminación de procesos intermedios como el mecanizado, la independencia de los costes de producción del tamaño de los lotes, la reducción de los residuos de material, las estructuras ligeras, las reparaciones personalizadas de las máquinas y la capacidad de desarrollar nuevos materiales, entre otras ventajas. En las tecnologías de fabricación aditiva que emplean un rayo láser como fuente de energía, la materia prima inicial (en forma de polvo o cable) es fundida por la fuente de calor láser de forma controlada, capa a capa, hasta crear un componente con dimensiones finales o casi finales. Estas tecnologías implican someter el material impreso a un proceso térmico único, en el que el material se funde en un área muy específica y luego se enfría rápidamente a velocidades extremadamente altas de hasta 10^6 K/s. Por lo tanto, las microestructuras que surgen de los procesos de fabricación en AM difieren significativamente de las que se consiguen en los procesos tradicionales. Además, los materiales que se emplean principalmente en la AM no se han diseñado explícitamente para estas tecnologías. Las características específicas

de los procesos de AM pueden utilizarse para lograr microestructuras y propiedades distintas en aceros que han sido adaptados para aprovechar las rápidas velocidades de enfriamiento y la historia térmica del proceso, entre otros factores.

Por el momento, el número de calidades de acero comerciales disponibles en el mercado de la AM es limitado. Diversas industrias demandan nuevos grados de acero con menor densidad para disminuir el peso sin comprometer las propiedades mecánicas. Los aceros con alto contenido en manganeso se consideran materiales muy prometedores para aplicaciones estructurales debido a su excepcional combinación de resistencia y ductilidad, con una baja densidad. Sin embargo, a pesar de sus excepcionales propiedades, los aceros con alto contenido en manganeso se enfrentan a diversas limitaciones o retos durante las técnicas de procesado convencionales. Afortunadamente, la solidificación rápida puede resolver estos problemas. En este sentido, las tecnologías de AM basadas en láser proporcionan velocidades de enfriamiento rápidas, así como flexibilidad en términos de diseño geométrico. Los nuevos retos de estas tecnologías implicarán la microsegregación y el agrietamiento en caliente o *hot cracking* en inglés, que se producen durante la solidificación.

Esta tesis está dedicada a explotar el método CALPHAD para realizar cálculos termodinámicos con el fin de diseñar varios aceros con alto contenido en manganeso que puedan prevenir eficazmente los problemas de solidificación rápida en AM. Las composiciones de acero diseñadas se produjeron en forma de polvo para AM mediante atomización con gas. Se analizaron los polvos para determinar su microestructura en

relación con la química y la velocidad de enfriamiento. Ajustando adecuadamente los parámetros de impresión, estos polvos de acero con alto contenido en manganeso se imprimieron con éxito en AM, dando lugar a densidades relativas superiores al 99.9%. Se analizó la microestructura de estas muestras totalmente densas y se comparó con sus respectivos polvos, con el fin de identificar cualquier diferencia resultante de las variaciones en la velocidad de enfriamiento y los ciclos térmicos. Por último, tras definir el mejor conjunto de condiciones de impresión para cada composición de polvo, se produjeron varias muestras para evaluar las propiedades mecánicas, con el fin de determinar la correlación entre la composición, la microestructura y las propiedades de estos aceros. Además, se construyeron estructuras reticulares próximas a las geometrías finales de las piezas para cuantificar la energía absorbida durante la compresión por uno de estos aceros con alto contenido en manganeso. Los resultados se compararon con los del 316L, revelando que el acero con alto contenido en manganeso absorbe aproximadamente el doble de energía específica en compresión. Este hallazgo demuestra el potencial de estos nuevos aceros AM para su uso en aplicaciones industriales.

Resum

La fabricació additiva, de les seues sigles en anglés AM *(Additive Manufacturing)* és un procés que construïx objectes sòlids tridimensionals mitjançant la superposició de materials basats en un model de disseny assistit per ordinador. L'AM està cridada a convertir-se en la pròxima revolució industrial, transformant el panorama del desenvolupament i la producció. L'AM oferix nombrosos avantatges, com a possibilitats de disseny complexes i flexibles, l'eliminació de processos intermedis com el mecanitzat, la independència dels costos de producció de la grandària dels lots, la reducció dels residus de material, les estructures lleugeres, les reparacions personalitzades de les màquines i la capacitat de desenvolupar nous materials, entre altres avantatges. En les tecnologies de fabricació additiva que empren un raig làser com a font d'energia, la matèria primera inicial (en forma de pols o filferro) és fosa per la font de calor làser de manera controlada, capa a capa, fins a crear un component amb dimensions finals o quasi finals. Estes tecnologies impliquen sotmetre el material imprés a un procés tèrmic únic, en el qual el material es funde en una àrea molt específica i després es refreda ràpidament a velocitats extremadament altes de fins a 10^6 K/s. Per tant, les microestructures que sorgixen dels processos de fabricació en AM diferixen significativament de les que s'aconseguixen en els processos tradicionals. A més, els materials que s'empren principalment en l'AM no s'han dissenyat explícitament per a estes tecnologies. Les característiques específiques dels processos d'AM poden utilitzar-se per

a aconseguir microestructures i propietats diferents en acers que han sigut adaptats per a aprofitar les ràpides velocitats de refredament i la història tèrmica del procés, entre altres factors.

De moment, el nombre de qualitats d'acer comercials disponibles en el mercat de l'AM és limitat. Diverses indústries demanden nous graus d'acer amb menor densitat per a disminuir el pes sense comprometre les propietats mecàniques. Els acers amb alt contingut en manganés es consideren materials molt prometedors per a aplicacions estructurals a causa de la seua excepcional combinació de resistència i ductilitat, amb una baixa densitat. No obstant això, malgrat les seues excepcionals propietats, els acers amb alt contingut en manganés s'enfronten a diverses limitacions o reptes durant les tècniques de processament convencionals. Afortunadament, la solidificació ràpida pot resoldre estos problemes. En este sentit, les tecnologies d'AM basades en làser proporcionen velocitats de refredament ràpides, així com flexibilitat en termes de disseny geomètric. Els nous reptes d'estes tecnologies implicaran la microsegregació i l'esquerdament en calent, o *hot cracking* en anglés, que es produïxen durant la solidificació.

Esta tesi està dedicada a explotar el mètode CALPHAD per a realitzar càlculs termodinàmics amb la finalitat de dissenyar diversos acers amb alt contingut en manganés que puguen previndre eficaçment els problemes de solidificació ràpida en AM. Les composicions d'acer dissenyades es van produir en forma de pols per a AM mitjançant atomització amb gas. Es van analitzar les pólvores per a determinar la seua

microestructura en relació amb la química i la velocitat de refredament. Ajustant adequadament els paràmetres d'impressió, estes pólvores d'acer amb alt contingut en manganés es van imprimir amb èxit en AM, donant lloc a densitats relatives superiors al 99.9%. Es va analitzar la microestructura d'estes mostres totalment denses i es va comparar amb les seues respectives pólvores, amb la finalitat d'identificar qualsevol diferència resultant de les variacions en la velocitat de refredament i els cicles tèrmics. Finalment, després de definir el millor conjunt de condicions d'impressió per a cada composició de pols, es van produir diverses mostres per a avaluar les propietats mecàniques, amb la finalitat de determinar la correlació entre la composició, la microestructura i les propietats d'estos acers. A més, es van construir estructures reticulars pròximes a les geometries finals de les peces per a quantificar l'energia absorbida durant la compressió per un d'estos acers amb alt contingut en manganés. Els resultats es van comparar amb els del 316L, revelant que l'acer amb alt contingut en manganés absorbix aproximadament el doble d'energia específica en compressió. Esta troballa demostra el potencial d'estos nous acers AM per al seu ús en aplicacions industrials.

Chapter 1

Introduction and Literature Review

The integration of additive manufacturing (AM) for near-net shape manufacturing (NNS) had garnered significant interest and demand across various industries owing to its numerous potential advantages, such as decreased lead time, streamlined process steps, and increased design flexibility. Therefore, it is imperative to enhance the scientific comprehension of the capabilities and constraints of the process.

This chapter delves into the material-process-properties relationship in AM. A description of the two main powder-processing AM technologies: laser-powder bed fusion (L-PBF) and directed energy deposition (DED) is provided, and following this, an overview of the steels currently available for these two AM technologies is presented, where their microstructure and mechanical properties are compared to the conventionally manufactured counterparts. Finally, the state-of-the-art of the of the

steel system targeted is reviewed, both in conventional processing route and AM.

1.1 Additive Manufacturing Industry

The standard definition for AM is: "a process of joining materials, to make objects from three-dimensional (3D) model data, usually layer by layer, as opposed to substractive manufacturing methodologies" [1]. The experimental arrangement comprises a computer that governs all operations, robotic arms, computer numerical control, nozzles, protective environments, scanning and recording systems, and specialized additive manufacturing software. Since the 1980s, a range of technologies have grown up to facilitate the deposition of materials, thereby enhancing dimensional precision and minimizing the need for subsequent machining or finishing processes in the production of fabricated parts [2].

A generic process for AM would require the following steps:

1. **The utilization of computer aided design (CAD):** involving a wide range of CAD modelling software, with 3D solid data format.
2. **Process to convert to STL format:** The process of transforming the CAD model into a format with computed individual "slices" or layers.
3. **Manipulation of STL file:** The STL file is used to define the orientation and generate supports for the overhang features.

4. **Machine setup:** This process encompasses a variety of tasks, such as configuring building settings and parameters, implementing powder recycle and machine cleaning procedures and establishing hardware setup protocols.
5. **Printing:** Manufacturing step layer-by-layer.
6. **Extraction:** Once the component has been built, it needs to be removed from the supporting structure or build platform. Also, support structures are separated from the part in this step.
7. **Post-processing:** Additional processes applied to the printed part. They can be either thermal, mechanical or chemical.

AM has the capability to be utilized across a wide range of material classes, such as metals, ceramics, polymers, composites, and biological systems. Metal AM is a production process that involves the creation of solid metallic objects through the bonding of metal sheets to form a 3D structure, joining powders with a liquid bonding agent or by consolidating metal powders or wire through the use of a concentrated heat source. The heat sources include laser, plasma, electron beam, or electric wire arc. The different metal AM technologies can be classified in five categories [1, 3]:

- **Powder bed fusion**: The powder bed is generated through the process of distributing powder across the predefined work surface area, in which thermal energy selectively fuses regions of the powder bed. An extra layer of powder is evenly distributed over the designated work surface, followed by a repetition of

the procedure to produce a cohesive three-dimensional object.

- **Binder jetting**: A liquid bonding agent is selectively deposited to join powders layer by layer. The powder is spread in a work surface in a similar manner than powder bed fusion technologies.

- **Material extrusion**: Process where material is selectively dispensed thought a nozzle. Usually in Metal Material Extrusion, material is composed of metallic powder is homogeneously dispersed in a polymeric cartridge which is heated up to be deposited through the nozzle.

- **Directed energy deposition**: DED is a AM process whereby a heat source is utilized to fuse metal by melting it simultaneously as it is being deposited. The metal, in the form of either powder or wire, is dragged or transported through a feeding system until it reaches a deposition head nozzle that is aligned with the beam source responsible for melting the metal.

- **Sheet lamination**: AM process in which the 3D object is built by bounding successively metal sheets.

According to the AMPOWER report [4], in 2022 the market size for Metal AM surpassed 3 billion EUR, encompassing suppliers sales from systems, material and

part manufacturing. This represents a growth of 21.2% compared to the previous year figure. According to suppliers predictions, the Metal AM market is expected to experience a growth rate of 26.1% in 2027, resulting in an overall market size of 9.66 billion EUR in that year. Furthermore, the projected growth of the material market is expected to increase from 6852 tons in 2022 to over 42000 tons also by 2027 [4]. Table 1.1 [4] collects the distribution of alloy weights for the total feedstock consumption in 2022 and the forecast for 2027. At present, steel is the primary material feedstock with a consumption rate of 27% of the total, followed by Ti alloys and Ni-based alloys, which account for 26% and 21%, respectively. According to predictions, steel is expected to maintain its dominance as the primary metal material feedstock for metal additive manufacturing, accounting for over 40% of the market share by 2027. The consumption of steel in tons is expected to rise from 1122 in 2022 to 13722 in 2027 [4].

Table 1.1
Distribution of alloys weight of total feedstock consumption in 2022 and forecast for 2027.

Material	2022	2027
Copper & bronze	3%	4%
Cobalt alloys	12%	6%
Titanium alloys	26%	19%
Nickel alloys	21%	17%
Steels	27%	43%
Aluminum alloys	10%	8%
Others	1%	2%

Furthermore, it should be noted that the metal feedstock utilized in AM has different formats, including powder, wire and sheet in metals. Thus, it is crucial to select the

appropriate material and format for each specific AM technology. According to the AMPOWER report [4], metal powder bed fusion technology is currently holding the largest market revenue among all metal and polymer AM technologies, accounting for 39% of the total sales in 2022. This figure is expected to rise to 45% by 2027. In 2022, the second and third positions are occupied by polymer powder bed fusion with a market share of 14% and polymer filament material extrusion with 12%. These numbers highlight the importance of powder bed fusion (PBF) technology and the use of metal powder as a feedstock material in the field of AM.

1.2 Additive Manufacturing pros and cons

The evident trend of Metal AM expansion is founded on various potential advantages for the industrial sector:

1. AM is a non-traditional manufacturing process that minimizes the need for machining and finishing operations in the production of a final component. This reduction in post-processing requirements results in a lower buy-to-fly ratio.
2. The production of complex or customized shapes can be accomplished within a brief timeframe without the necessity of tooling, as opposed to forging or casting, which usually entails a design and manufacturing process spanning several months.
3. The production of functionally graded materials can be promoted through this

process, as evidenced by sources [5, 6]. Metal AM presents an opportunity to efficiently investigate novel alloys.

4. AM has been reported to utilize 90% fewer raw materials as compared to conventional manufacturing techniques [7, 8].
5. AM technology has proven to be beneficial in the repair of pre-existing parts. AM has the capability to compete with conventional repair techniques and facilitate until now unattainable repairs in specific scenarios. The significant benefits of this possibility are the expenses and recuperation of mechanical performance [9, 10].

In spite of the benefits previously mentioned regarding AM, there exist various limitations and concerns associated with the present level of technological maturity.

1. The primary challenge associated with adopting AM technology is the significant capital investment required for the acquisition, installation, and maintenance of the equipment. Additionally, the cost of metal feedstock, is significant.
2. The maximum size that can be covered for each AM technology or machine is constrained by its dimensions. Moreover, the pace of construction is relatively slow, making it unfeasible for large components [11].
3. The combination of the initial 2 limitations results in a comparatively elevated costs per spare component. According to the AMPOWER report [4], the estimated cost of producing a steel part varies depending on the manufacturing

process. Production of a steel part with a volume of 100 cm^3 by PBF is estimated to cost between 150-300 EUR, around 100 EUR by binder jetting, 400-550 EUR by powder-DED, and below 100 EUR by wire-DED [4].

4. There exists a variation in both dimensional accuracy and surface roughness across different technologies, which is often correlated with the corresponding cost of the technology. This is particularly critical in parts that require high performance against fatigue, and application of post-treatment is needed to reduce the surface roughness.
5. The complete elimination of defects, such as porosity, microcracks, or inclusions, presents a significant challenge.
6. The microstructure of a printed object is significantly influenced by various factors such as the printing parameters, the printing strategy, as well as the size and geometry of the object. The potential variability in chemical composition among batches of raw materials, coupled with the aforementioned issue, may result in microstructural heterogeneities within the component at both micro and macro levels [12, 13].
7. The lack of repeatability and reproducibility of parts is attributed to the absence of reliable standards designed for additive manufacturing, together with the combination of the features outlined below.
8. The development of strong closed-loop process control algorithms and procedures is not trivial and still in progress [14, 15].

1.3 Industrial applications of metal Additive Manufacturing

The AMPOWER report [4] has categorized the present metal AM market into various industry sectors, including automotive, aeronautics, defense, space, medical, dental, energy, oil and gas, industrial, tooling and molding, part manufacturing suppliers, academia, and others. In 2022, the revaluation of total system sales amounted to 1.18 billion EUR. The space industry has leaded the list by generating sales worth 168 million. Other industries with significant sale numbers are: automotive (85 million), aeronautics (104 million), defense (102 million), medical (119 million), industrial (132 million), and tooling and molding (77 million). It is expected that these figures will continue to increase in coming years due to the research and development efforts aimed at constructing bigger machinery, attaining greater efficiency, developing robust printing parameters, and designing novel alloy compositions [4].

Based on the data analysis, it is predicted that by 2027, the industrial sector will hold the highest percentage share, followed by the space and automotive sectors, respectively, occupying the second and third positions. This is coherent with the expected growth in the steel demand for metal AM, regarding its large use in the automotive and industrial sectors. In order to meet the foreseeable future demands, it will be necessary to develop novel steel grades that are better suited to satisfy the requirements of the different industry sectors, especially industrial, automotive, tooling, rail

and naval, oil and gas, energy, defense, research and consumer goods.

1.4 Gas atomization

Gas atomization is a widely employed technique in which a gas is utilized to disperse a molten stream, resulting in the production of finely spherical metal powder particles. The fundamental concept underlying this procedure is the conversion of kinetic energy from a gas jet, characterized by high velocity, composed of nitrogen, argon, or helium, to a liquid metal stream operating at a pressure range of 10-40 bars. Consequently, the liquid metal stream undergoes a state of instability. The expansion of gas surrounding the molten substance induces a significant reduction in pressure, leading to the fragmentation of the liquid into droplets that ultimately form as metallic particles. This method yields powders that exhibit a high degree of sphericity and fineness, making them suitable for applications that necessitate dense packing and favorable flow properties, such as AM [16].

The gas atomization process commences with the melting the precursor raw materials within a tundish. Metal undergoes the process of melting when it is exposed to temperatures that exceed its designated melting point, and inert gas is injected in the melt to homogenize the liquid. Once the metal undergoes the process of melting, it exhibits a downward flow via a nozzle as a result of gravitational forces, overpressure

within the melting chamber, and the aspiration force generated by the gas jets positioned beneath the nozzle. The dispersion of metal occurs within the turbulent flow generated by the jets, whereby the majority of metal powder particles descend into a designated chamber positioned beneath the nozzle, commonly referred to as the tower collector. This phenomenon is particularly prominent for the larger particles within the metal powder. Nevertheless, certain fine powder particles are dragged by the gas and subsequently recirculated within the tower or accumulated within the cyclone collector, when present. Figure 1.1 [17] depicts a schematic representation of the process.

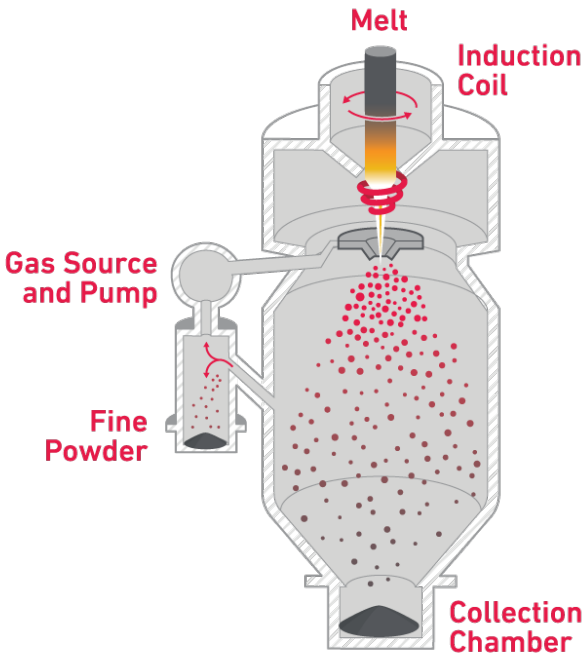

Figure 1.1: Sketch of gas atomization process.

The gas atomizer designs that are predominantly utilized in industrial settings include

close-coupled and free-fall configurations of nozzles. Figure 1.2 depicts a schematic illustration of both a free-fall atomizer and a restricted atomizer [18].

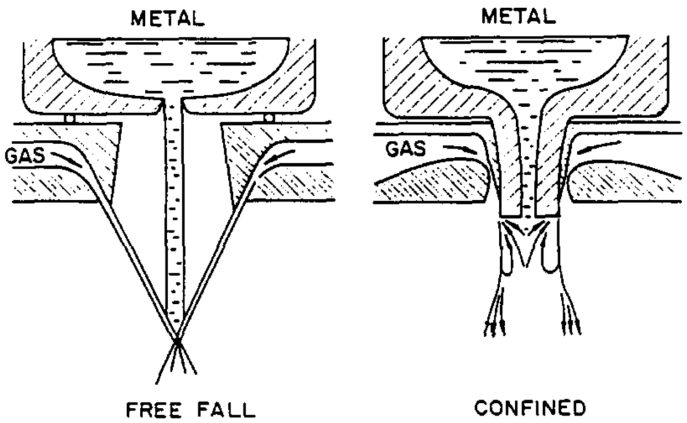

Figure 1.2: Schematic representation of the free-fall, and closed-coupled or confined atomization.

In close-coupled atomization, the gas exit is positioned adjacent to the melt nozzle exit. Conversely, in free-fall atomization units, the gas exit and melt nozzle exit are maintained at a variable distance ranging from 10 to 30 cm. In general, a confined or close-coupled atomization has the advantage of producing higher fine metal powder particles, due to the near closeness of the gas and melt streams, which facilitates efficient energy transfer [19]. Nevertheless, in cases where the aspirational force of metal is inadequate, it is possible for the metal to solidify and accumulate within the nozzle tip, so obstructing the atomization process, and this freeze-up or metal backflow is not typically observed during free-fall atomization.

The adequate choice of atomization parameters for a steel composition is paramount

as it directly influences the distribution of particle sizes in the powder (known as particle size distribution or PSD). This, in turn, dictates the efficiency of powder yield during atomization for a specific technology. Foe example, in the context of L-PBF, the presence of powder particles over 60 microns or those below 15-20 microns in size is considered undesirable. The most relevant atomization parameters that influence the PSD are [20]:

1. **Atomizing pressure:** One of the parameters with a strong influence on the PSD is the input pressure of the gas. In general, an increase in atomizing pressure tends to result in a reduction in powder size. However, it is worth noting that certain exceptional circumstances may arise, particularly at high pressure levels.
2. **Melt overpressure:** The increase in melt overpressure rises the melt flow, leading to a corresponding increase in the ratio between the melt flow and gas flow. In other words, the ratio or mass of melt is greater in comparison to the provided ratio or mass of gas. Thus, increasing the melt overpressure commonly results in the production of a coarser powder.
3. **Width of metal and gas nozzles:** As previously explained, the dimensions of the nozzles contribute to regulate the ratio at which molten material and gas are discharged. Therefore, by expanding the diameter of the gas nozzle, the flow rate of gas is increased, resulting in the production of finer particles of powder. In contrast, increasing the diameter of the metal nozzle leads to a rise in the

ratio of mass to metal liquid, resulting in the production of coarser particles.

4. **Melt superheating:** The process of melt superheating is employed to achieve the complete melting of metal precursor raw materials and the homogenization of the final composition prior to atomization. A higher melt superheating contributes to an accelerated melting of the raw materials, hence reducing the duration of the atomization process. Nevertheless, too high temperatures can lead to the volatilization of significant alloying elements in steel, such as C, Mn, Al, Ti or Si. Furthermore, the increment of the melt superheating has an impact on the PSD, resulting in a decrease and a narrowing of it.
5. **Atomizing gas:** Various inert gases can be employed as atomizing gas, with nitrogen, argon, and helium being the most prevalent options. Nitrogen is generally favored due to its comparatively lower cost. Argon is commonly utilized as the inert gas when atomizing materials can that react with nitrogen or nitrides are unwanted. The utilization of helium incurs significant costs, nevertheless, its elevated thermal conductivity serves to augment the pace of cooling for particles, hence facilitating the formation of amorphous microstructures. In relation to the PSD, when comparing atomization conditions with equal mass ratios of metal and gas flow, helium produces the most refined and tightest distribution of powder particles. Conversely, argon results in a coarser and wider distribution, while nitrogen falls in between. The observed tendency can be attributed to the molecular weight of the gases, with helium being the lightest and

argon being the heaviest. However, different figures can be obtained comparing atomization conditions in terms of gas volume ratio.

Furthermore, the atomization process determines other powder properties, including its density, morphology, flowability, spreadability, compressibility indexes, as well as its ability to absorb moisture. These final powder features define the powder quality for AM processes, since they significantly influence the processability by AM and the level of reproducibility of the resulting additively manufactured parts. However, the control of powder quality through the atomization parameters is a field of research, and additionally, the design of nozzles and atomization units has a significant impact on the quality of the powder.

1.5 Laser-Powder Bed Fusion

The L-PBF technique employs a laser beam with a power that can range between 0.1 and 1 kW [21] which acts as the energy source for the selective melting of the powder particles that usually measure between 15 to 63 microns size. This is achieved through the use of a mirror system that scans over a predetermined path, as defined by a 3D model file. Following the completion of the scanning layer, the build platform undergoes controlled downward movement via a piston, with the distance defined as the layer thickness. Simultaneously, the powder dispensed platform moves upward to ensure the homogeneous distribution of the new powder layer through a recoater.

This process is repeated until the part is completed, which ends covered by loose powder, which is extracted and collected by either brushing or a vacuuming, and subsequently sieved to be re-used. Figure 1.3 [22] shows a representation of the L-PBF process.

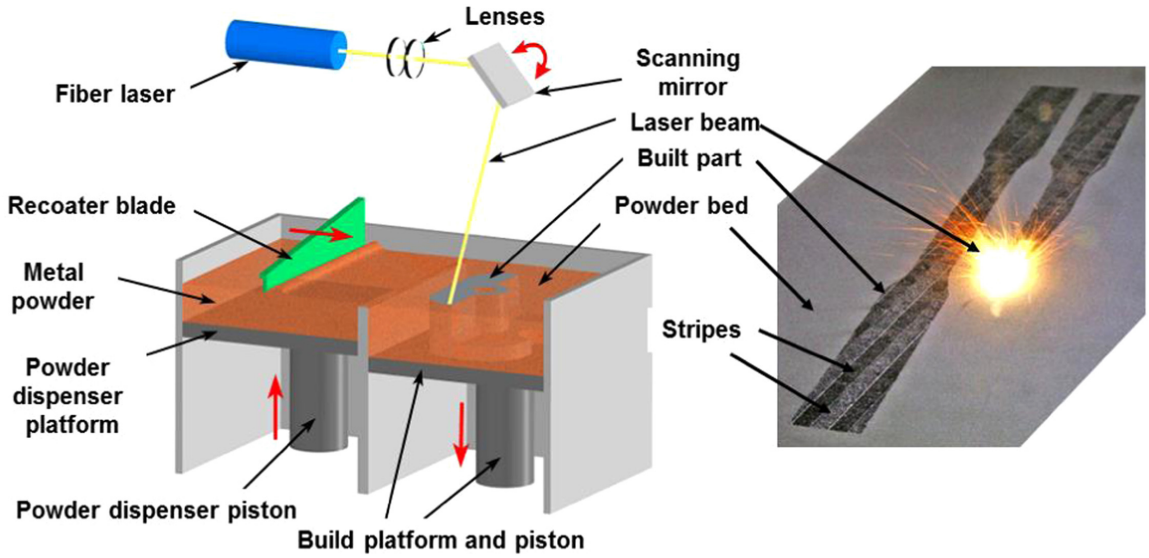

Figure 1.3: Sketch of L-PBF process.

In order to mitigate oxidation during the printing process, it is common to maintain an inert atmosphere (argon or nitrogen) within the printer chamber. Furthermore, it is possible to preheat the build platform prior to and during printing in order to reduce the cooling rates and residual stresses that may arise during the process. This technology is capable of achieving a geometrical tolerance of 40 microns and a minimum dimension size of 200 microns. L-PBF is a commonly employed AM technique that finds extensive application in diverse fields such as engineering for production of lightweight machine parts, complex geometric components, fuel cells, architectural

designs, as well as medical and dental applications. [23]

The major printing parameters utilized in the L-PBF process include the gas atmosphere, laser power, speed, hatch distance and the layer thickness. A sketch of the definition of these major printing parameters is represented in Figure 1.4 [24].

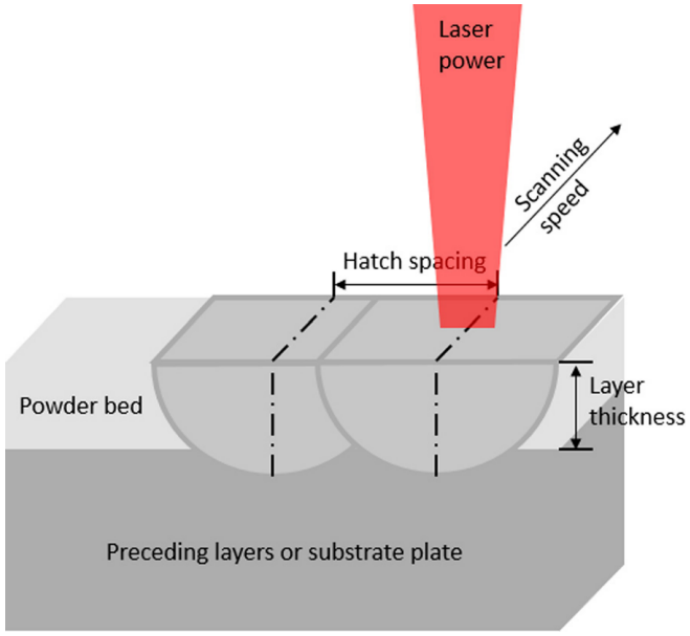

Figure 1.4: Sketch of the main printing parameters of L-PBF.

The combination of these parameters determine the amount of energy applied to the system:

The linear energy density (LED) is a metric that characterizes the amount of energy transferred per unit of distance. It is typically denoted in units of Jules per millimeter J/mm. Equation 1.1 provides the formula to determine the value of LED:

$$LED = \frac{P}{v} \tag{1.1}$$

where P is the laser power, and v is the laser speed.

The volumetric energy density (VED) is a metric that characterizes the amount of energy transferred per unit of volume of material. It is commonly expressed in J/mm^3. Equation 1.2 presents the general formula:

$$VED = \frac{P}{v \cdot h \cdot t} \tag{1.2}$$

where h is the hatch spacing, and the t is the layer thickness.

Both the LED and VED are key indicators of the quality of the printed parts. Therefore, the initial stages of developing a process window should involve the optimization of the LED and VED. Furthermore, the laser emission mode, beam shape and spot size are three additional important parameters to consider, which are not often changed in the printer machine. Other important process parameters in L-PBF are:

1. **Printing chamber atmosphere:** Most often, it is either argon or nitrogen. Its objective is to avoid oxidation during the process. The usage of nitrogen is sometimes beneficial because fully dense samples can be obtained at lower VED values than when using argon. This is thought to be due to the higher thermal conductivity of nitrogen in comparison with argon. However, nitrogen is more reactive than argon and can enter in solid solution in the steel and/or form nitrides.
2. **Flow rate:** It is calibrated to drag the spatter out of the printing zone. A strong

flow rate can remove the powder onto the printed bed, and cause flow turbulence, supposing different flow conditions at different locations of the printing bed.

3. **Packing density:** It is defined as the volume ratio between the volume occupied by the total number of parts printed together at the same printing bed and the total volume available in the printing bed. When the packing density of a printing job is high, the risk of spatter to fall onto a printed layer that can affect to the incoming layers is higher. A reasonable value for the packing density is below 15%.

The laser path or printing strategy is as well a determining factor to ensure the quality and integrity of the printed part. There exists a variety of strategies that are available for implementation, and the study of these strategies constitutes a field of research itself. Nevertheless, there are four widespread strategies, which are: stripes, chessboard, total fill and meander. These strategies are represented in Figure 1.5 [25].

Every strategy has its own benefits and drawbacks. Table 1.2 presents an overview of the advantages and disadvantages associated with each strategy. The selection of a scanning strategy should take into account the dimensions and geometry of the component.

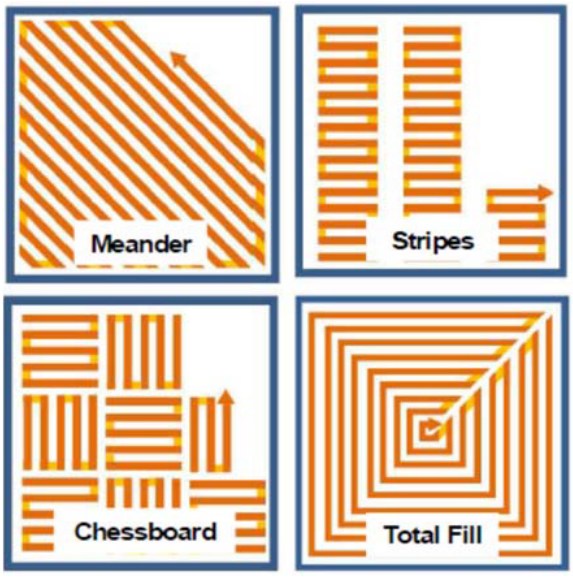

Figure 1.5: Representation of the four most widespread printing strategies in L-PBF.

Table 1.2
Pros and Cons associated with each scanning strategy.

Meander	Rapid and effective. It is well-suited for components with small layer sections.	Distribution of heat is not consistent.
Strategy	Pros	Cons
Stripes	Uniform thermal distribution across the layer. It is suitable for components with larger cross-sections	Slow
Chessboard	Improvements beyond the traditional stripe pattern	Slower than stripes
Total fill	High-quality surface finish	Bad densities

1.6 Directed Energy Deposition

The DED process involves utilizing a beam source, commonly a high-powered laser such as fiber, Nd:YAD, disk or CO_2, that focuses on a particular region. This region

is where the feedstock, in the form of either powder or wire, is concurrently supplied through a nozzle that is directed towards this area. In comparison to the L-PBF technique, that utilizes a powder metal bed selectively melt by a laser with an optical and mirror system, this printing method involves the simultaneous delivery of metallic feed at focused laser energy. This is achieved through the use of a movable robotic-arm computer numerical control (CNC) unit that holds the laser head and the feeder nozzle and manages the X-Y-Z movement [23].

The powder-based DED process involves the use of a high-powered laser to melt either the substrate or a specific region within an inert atmosphere. Concurrently, gas is used to drag and inject the powder into the melt created by the laser beam. The optimal distribution of powder particles for this technology is within a range of 50 to 100 microns [26, 27]. However, it is worth noting that powders of both finer and coarser particle sizes may also be utilized, although a reduction of deposition efficiency may result from small particle size due to the dispersion of fine powder by the carrier gas [26]. On the other hand, coarse powder may increase the surface roughness and decrease geometrical tolerances. This technology has the ability to manufacture and repair large-scale components, and create functionalized materials or in-situ alloying. Nonetheless, the main drawbacks are a relatively-low precision and accuracy, specially when compared with L-PBF, with rougher printed parts surface. Furthermore, it may not be well-suited for the production of small or complex-shape components.

Similar to L-PBF, the major parameters that impact the manufacturing integrity in DED are analogous to those in L-PBF, which are laser power, laser speed and, instead of layer thickness, the laser spot size. The interdependence of these parameters has been demonstrated to control the energy input per unit of traveled distance, also referred to as energy density, usually expressed in J/mm^2 . The simplified equation to calculate this energy is presented at equation 1.3:

$$E = \frac{P}{v \cdot d} \tag{1.3}$$

where P is the laser powder, v is the laser velocity and d is the laser spot. The magnitude of this energy is a key indicator of the melt pool size [28]. Additionally, the hydrodynamics of the molten pool, which are crucial in determining the quality of the printed component, are primarily governed by this energy [29, 30]. Nevertheless, there are other important process parameters that also affect the quality and integrity of the component to a lesser extent, such as such as:

1. **Shielding and Carrier gas flow**: DED commonly employs argon or helium as carrier and shielding gases to establish a safeguarding atmosphere, although, nitrogen can also be used. The appearance of porosity in the printed component can be caused by an excessive flow of gas, due to the entrapment of this gas within the melt pool. However, insufficient flow rates may fail to prevent oxidation within the melt pool.

2. **Overlapping**: Insufficient overlapping distance between laser tracks may result in lack of fusion porosity, which is attributed to incomplete bonding between the adjacent tracks [15]. Typically, a range of 30 - 50% overlap is considered optimal to prevent issues of inadequate fusion [31, 32].
3. **Powder flow rate**: The rate at which the powder is fed in the DED process has a direct impact on the geometry of the resulting melt pool. In order to achieve a constant melt pool geometry, it is essential to keep a uniform powder feed rate [9]. However, it should be noted that a high powder feed rate may cause a reduction in the effective incidence of the laser beam per particle, leading to lower heating of the powder particles and thus unmelted powder. Conversely, a low feed rate may result in overheating of the powder particles and even the previously deposited layers [32].
4. **Nozzle geometry**: Various nozzle types are utilized in DED process, typically made of copper or brass to enhance heat extraction. These nozzle types have the capacity to alter the behaviour of the powder feed and its interaction with the laser beam. Coaxial nozzles are characterized by an annular outlet cone that is structured as a cone within another cone. The powder passes through the region between these two cones. Another variant is the three or four beam nozzle, which comprises a single metallic part featuring three or four apertures for the injection of powder. These nozzles are capable of handling larger particle sizes [32]. Finally, the extreme high-speed laser material deposition (EHLA)

enables high deposition velocities by melting a significant amount of powder prior to its arrival at the melt pool [33]. The material growth during printing, the stability of the process and the deposition efficiency are influenced by the type and angle of incidence of the nozzle [34, 9].

5. **Laser beam shape**: Although there are emerging new possibilities for beam shaping, the two main laser intensity distributions are Gaussian and top-hat shapes. When the laser's focus is located above the surface, its intensity follows a Gaussian distribution. On the contrary, if the laser's focus is located at the surface level, its intensity conforms to a top-hat distribution. The Gaussian distribution is commonly preferred in order to prevent the likelihood of key-hole formation [35].
6. **Working distance**: The working distance refers to the spacing between the tip of the nozzle and the surface of the substrate. The calibration of the working distance is based on the convergence of the powder cone that is injected though the nozzle, and the focal point or focal distance that determines the beam shape. In order to ensure consistency in the melt deposition process during 3D printing, it is essential to maintain a consistent working distance. This can be achieved by adjusting the robotic arm to move upwards by the same distance as the height of the printed material or track. Otherwise, differences in the convergence point of the powder and the focal point of the laser may arise, causing variations in the working distance. These variations in the working distance, in consequence, may

result in inconsistent molten pools due to differences in the powder deposition and laser spot size. The aforementioned factors may culminate in a significant quality deterioration of the printed part, characterized by excessive heating and low deposition rates [36, 37, 34].

1.7 Microstructures and defects in Laser-Powder Bed Technologies

Steels manufactured in L-PBF and DED technologies go through a series of thermal cycles, including: (1) rapid heating due to the absorption of the laser energy, (2) fast solidification of the melted region after the laser incidence, (3) significant temperature gradients, (4) accumulated heat and (5) reheating and cooling caused from the laser incidence in the adjacent tacks and/or layers that can re-melt and re-solidify previously deposited material [38, 39, 40]. Although heat cycles depend on many process factors, non-equilibrium thermodynamics govern the physics of microstructure development in L-PBF and DED [23]. As a result, it is not completely known yet how the process parameters affect the microstructure and properties of AM printed parts. The thermal history described above influences different features of the steel microstructure processed by L-PBF and DED, such as:

1. **Solidification structures**: The solidification conditions define the temperature gradient and the solidification velocity, which determine the solidification

structures according with the associated solidification theory [41]. The solidification structures typically found in L-PBF and DED are: cellular, cellular dendritic, columnar dendritic, and equiaxed dendritic. A description of the solidification structures will be given in Section 1.11.1.2.

2. **Grain size:** The cooling rates inherent to the L-PBF and DED processes are typically extremely high due to the limited area heated by the laser. Consequently, steels produced by these AM technologies yield finer microstructures and smaller heat-affected zone (HAZ) compared to their conventionally manufactured counterparts [41, 42]. Furthermore, grain can be also refined by the presence of phases that act as inoculants, or by solid phase transformation. Thus, in general, the ultimate tensile strength (UTS) and yield strength (YS) of the parts produced through L-PBF and DED processes exhibit higher values as compared to their homologous produced by conventional manufacture [43, 44, 37, 45]. Nonetheless, a reduction in the total elongation (TE) may be observed as a result of the grain refinement, and the presence of defects within the material.
3. **Texture:** The melt pool flow dynamics, characterized by the rapid solidification and complex thermal cycles, induce heat flow in multiple directions, which results in possible preferential orientations of grain growth and phase evolution. This phenomenon ultimately leads to anisotropy in mechanical properties at various locations [46, 47, 48].

4. **Segregation**: The rapid solidification rates of L-PBF and DED lead the formation of non-equilibrium microstructures and extremely fine solidification structures. Certain constituents may exhibit tendency to segregate from or towards the liquid phase during solidification, thereby producing micro-segregation inside the solidification structures.
5. **Phase stability:** The fast cooling rates during solidification can hinder the formation of some phases present in equilibrium. On the contrary, re-heating can act as an intrinsic heat treatment (IHT) promoting solid phase transformations during the printing process.
6. **Inclusions:** Despite using a protective atmosphere in AM, microstructures exhibit spherical oxides raging from nanometers to few microns. However, these oxides differ from the irregular and large oxide inclusions observed in conventional manufacturing processes [49]. Moreover, the presence of S, which is usually coming as an impurity from the raw material, has the potential to generate sulfides.

Anisotropy is often observed in steels printed by L-PBF and DED. This anisotropy is typically evidenced by mechanical properties analyzed in specimens printed with different orientations relative to the building direction. For example, tensile properties, and especially the UTS and YS of printed steels exhibit dissimilarities when subjected to testing in the direction parallel or perpendicular to the building direction. The reason for this are that a significant number of steels present an epitaxial

microstructure and crystallographic texture oriented parallel to the building direction, so that strength is higher in this direction [50, 51]. However, in many cases, UTS and TE are lower in specimens printed parallel to the building direction, which is attributed to weak interfactial layers and porosity alienation perpendicular to the tensile direction [40, 43] . In contrast, printed specimens oriented perpendicular to the building direction show higher UTS and TE [52, 53]. These results indicate that preferential location of defects has higher impact in the mechanical properties than some microstructural features, such as crystallographic texture.

The typical defects observed in steel produced by L-PBF and DED that impact in the integrity and mechanical properties of the steel printed parts are:

- **Gas porosity**: It refers to the presence of gas entrapped during the melting process, typically spherical in shape. In addition, when high laser energy is applied spherical or irregular porosity known as key-hole is formed due to sublimation of part of the material [54].

- **Lack-of-fusion (LOF):** It refers to porosity with irregular shape caused by unmelted powder. The origin of this LOF can be inadequate printing parameters with low VED that is not sufficient to melt all powder in the layer, or presence of spatter in the powder layer that hinders the complete meting of the material within the layer.

- **Delamination**: It refers to the phenomenon of adjacent layers separating from each other as a result of incomplete melting between them [55].

- **Balling**: It is a phenomenon that arises from the Plateau-Rayleigh[1] instabilities, resulting in the discontinuity of the melt pool and the formation of separate spherical islands [56, 57]. This phenomenon can be ascribed to the elevated viscosity of the liquid, resulting in an inadequate wetting of the powder surface by the liquid. Consequently, the particles of the powder exhibit a tendency to form agglomerates as a result of surface tension, leading the balling. The adjustment of the laser speed can control the process of balling [58].

- **Cracking:** The formation of cracks in AM responds to two physical phenomena: cracking occurring during the solidification (or hot cracking), and cracking caused by residual stressed due to fast solid phase transformations during rapid cooling (also called cold cracking).

1.8 Commercial Steels in Additive Manufacturing

Currently, a limited range of steel materials is employed in AM processes. The different phases that can be present in the steel matrix such as austenite, ferrite and

[1]The Plateau–Rayleigh instability is a phenomenon in fluid dynamics that explains the reasons and mechanisms behind the fragmentation of a falling stream of fluid into smaller packages, which possess equivalent volumes but reduced surface areas.

martensite, along with the multiple precipitation carbides, intermetallics or inclusions, provide a significant range of microstructural diversity with the corresponding mechanical properties. The steel powders that are currently in highest demand in the AM market based on their developed or promising outputs are:

1. **Austenitic stainless steels:** 316L, which is the steel most often used in AM, and 304L
2. **Precipitation hardening stainless steels:** 17-4PH, 15-5PH, 17-7PH and PH 13-8Mo
3. **Maraging steels:** mainly 18Ni300, but also 18Ni250 and 14Ni200
4. **Duplex stainless steels:** 2205, 2207, 2507, 2707, 3207, 1.4091 and SAF2705
5. **Martensitic stainless steels:** 410, 420, 440C and 440B
6. **Ferritic stainless steels:** 430, 430L and 434
7. **Low alloy steels:** 4140, 4340, DP600, 4630, 4365, 4605, 8620, 42CrMo4, 5120, 20MnCr5, SAE 52100 and SCM415
8. **Carbon bearing tool steels:** H13, H11, D2, M2 and P20
9. **Oxide dispersion-strengthened steels:** PM2000
10. **Pure Iron**

The following is an overview of the most studied commercial steel powders for L-PBF and DED. It includes: austenitic stainless steels (SS), precipitation-hardening (PH) martensitic SS, maraging steels and carbon-bearing tool steels.

1.8.1 Austenitic Stainless Steels

Austenitic SS are a highly popular group of industrial materials in AM. They are also the most commonly employed class of steel in AM due to their exceptional printing ability, corrosion resistance, energy absorption, ductility and bio-compatibility. These properties render them suitable for employment in a diverse range of industrial sectors, including biomedical, aerospace, defense, oil and gas, petrochemical and automotive [49]. The main two austenitic SS compositions in the powder market are 304L and specially 316L, which is the most used steel in AM and the first to be printed with a relative density higher that 99.9% [59, 60]. Compared to conventional cast and hot rolled steels subjected to lower cooling rates, the microstructure and phase transformations of these steels in L-PBF and DED are quite different. The microstructure of these steels is typically fully austenitic [61], although some $\delta-$ferrite may be present, particularly in DED-produced steels, where there is a stronger segregation of Cr and Mo to the solidification cell boundaries [62, 63]. The grain size is significantly smaller in comparison to those produced through traditional methods and grains exhibit a columnar morphology oriented along the building direction [64, 65, 66, 67, 68]. Typically, a strong crystallographic texture is observed in these steels in the <001> direction also parallel to the printing direction.

The tensile properties of parts produced by L-PBF and DED exhibit a remarkable

combination of strength and elongation, with comparable ductility values to the counterparts produced by conventional methods and higher YS and UTS. The YS and UTS of 316L produced by L-PBF and DED range between 450-590 MPa and 640-700 MPa, respectively, in the as built state, and TE between 36-59%. In contrast, tensile properties of conventional products are in the range of 165-365 MPa of YS, 450-555 MPa of UTS and 30-43% of TE [69, 70].

1.8.2 Duplex Stainless Steels

Duplex SS are identified by their microstructure, which comprises a similar fraction of $\delta-$ferrite and austenite. This microstructure is characterized to offer notable mechanical strength, fair ductility and exceptional resistance to corrosion, particularly in regard to pitting and crevice corrosion [71]. The aforementioned properties exhibit suitability for employment in corrosion-resistant scenarios within the oil and gas industry, petrochemical, construction, marine and desalinization sectors [72], a specific example of such deployment is in the offshore oil and gas infrastructures [73]. The equilibrium between the ferritic and austenitic microstructure can be attained by employing comparable amounts of austenite-stabilizing elements such as Ni (and N in "superduplex"), as in austenitic SS. Additionally, Cr as ferrite-stabilizing element is added in concentrations ranging from 22 to 26 wt.%. The major difficulty associated

with duplex SS pertains to their phase transformations, wherein the process significantly influences the microstructure and phase evolution, leading to possible formation of several detrimental phases, such as the sigma intermetallic Cr-rich phase [74]. The 2507 superduplex grade and the 2205 grade are the most extensively researched duplex stainless steels in AM. Dense samples with a relative density exceeding 99.5% have been successfully produced [75]. However, microstructures show notable dissimilarities between L-PBF, which is mainly ferritic [75], and DED, where a more significant amount of austenite is formed [76]. The main cause of the microstructural differences can be attributed to the different cooling rates inherent to both techniques [49]. Thus, the development of time/temperature post-heat treatment is usually required for these steels. Table 1.3 presents a comparison of the tensile properties of the two steels as reported in literature, in relation to the conventional product. It can be noted that, regardless of the heterogeneity of the microstructure, steels that are as-printed exhibit higher strength while showing a decrease in elongation. By applying an appropriate heat treatment, it is possible to achieve tensile properties that are comparable to those of traditional products. However, a wrong selection of heat treatment can result in a reduction of the tensile properties.

Table 1.3
Tensile properties (UTS, and TE) of duplex steel. AB: as built, HT: heat-treated.

Alloy	UTS (MPa)	TE (%)	Source
2205 Conventional	650-880	25	[77]
2507 Conventional	580-800	30-40	[78]
2205 L-PBF AB	870-940	10-12	[79]
2205 L-PBF HT	620-770	21-28	[79]
2507 L-PBF AB	1030-1320	8-14	[79]
2507 L-PBF HT	800-920	2-43	[79]

1.8.3 Martensitic Stainless Steels

Martensitic SS are steels with adequate properties to apply in scenarios where high levels of strength, wear and corrosion resistance are required, such as bearings, pumps, blades, valves, or shafts [49]. The main martensitic SS grade that has been investigated in AM is the 420 medium carbon martensitic SS, which is widely used due to its high hardenability and good corrosion resistance properties. This steel grade has been successfully printed to fabricate fully dense samples thought DED [80, 81], and L-PBF [82]. The major limitations of this steel grade are its poor ductility and anisotropic microstructure and properties. The microstructure of as-printed material is significantly influenced by the printing parameters used. For instance, in the DED process, the microstructure after printing comprises typically a mixture of martensite and δ-ferrite. On the other hand, in L-PBF, some austenite fraction may be also retained [49] and reverted by rearrangement of carbon between martensite and austenite during the IHT of the process [83]. Table 1.4 illustrates the importance of heat treatment enhancing the tensile properties of 420 grade processed through

AM. However, these tensile properties in AM do not attain the values obtained in conventional product.

Table 1.4
Tensile properties (YS, UTS, and TE) of 420 SS. AB: as built, HT: heat-treated.

Alloy	YS (MPa)	UTS (MPa)	TE (%)	Source
Conventional	1300	1600	14	[49, 84]
L-PBF AB	835-865	1025-1075	2.3-2.7	[85]
L-PBF HT	930-979	1490-1550	6.1-6.5	[85]

1.8.4 Precipitation Hardening Martensitic Stainless Steels

PH martensitic SS have exceptional mechanical strength and corrosion resistance. These steel grades are either fully martensitic or austenitic-martensitic [86]. The two main PH martensitic SS variants used in AM are 17-4PH and 15-5PH both of which are classified as "fully martensitic". Whilst certain carbides may be formed, the PH mechanism of these steel grades is primarily driven by Cu precipitates within the microstructure that undergo nucleation and growth during the ageing step. Although the microstructure of 17-4PH and 15-5PH is typically mainly martensitic[87], and it is common to obtain retained austenite in these steels processed by AM [88, 89]. This is because upon the end of the process of solidification, austenite remains as the predominant phase, and during the subsequent cooling, not all austenite undergoes transformation into martensite, leading to a wide range of potential retained

austenite content [23]. The significant diversity of microstructures observed in the as-printed state of these steels, including ferrite, martensite, austenite, MC carbides and precipitates [90], as opposed to other steel grades, can be attributed to various factors:

1. The martensite finish temperature is slightly higher than ambient temperature. Thus, the microstructure is significantly impacted by variations in both the chemical compositions and printing parameters. Regarding the chemical composition, the content of N holds significant importance, as it is a strong austenite-stabilizing element. Steel powders that are atomized under N have the potential to hold high N contents. The final microstructure after printing is influenced by the quality of the raw steel powder and its chemical composition [91, 92, 93, 94].
2. The presence of chemical inhomogeneities caused by microsegregation can result in the formation of regions that are rich in austenite stabilizing elements. These regions may have a martensite starting and/or finishing temperatures that are below the room temperature [95].
3. The martensitic transformation is hindered by residual stresses and small solidification cells [93, 96].
4. The IHT has the potential to cause local recrystallization, particularly in areas with smaller grain sizes [97].

A post-heat treatment is necessary to achieve homogenization of the microstructure in these steels. The complete decomposition or transformation of retained austenite cannot be achieved solely through the aging of the as-printed material [98]. Typically, achieving the desired microstructure necessitates a multi-step heat treatment to homogenize it. The post-heat treatment process comprises a series of steps which include an initial solution, quenching steps and aging [99]. To determine the adequate post-treatment, the material specifications and requirements must be considered, such as its microstructure, corrosion resistance or mechanical properties. Tensile properties can be very different depending on the post-treatment, table 1.5 compares the conventional product after standard H900 treatment with reported values for 17-4PH steel produced by L-PBF under different conditions.

Table 1.5
Tensile properties (YS, UTS, and TE) of 17-4PH steel. AB: as built, S: solution treatment, A: aging treatment.

Alloy	TS (MPa)	UTS (MPa)	TE (%)	Source
Conventional (H900)	1050-1170	1310-1380	10-15	[49]
L-PBF AB	500	1170	7-9	[100]
L-PBF A	1100	1370	12-13	[100]
L-PBF S+A	1050-1200	1200-1300	7-11	[100]

1.8.5 Maraging Steels

Maraging steels belong to the category of martensitic steels (no stainless). Maraging steels are also classified as a type of tool steels that are free of carbon [74]. The microstructure after quenching is characterized by a relatively soft and malleable martensitic framework, which is strengthened by the precipitation of intermetallic phases during the ageing process [101].

The maraging steel that is commonly utilized in AM is the 18-300 variant [46, 101, 102, 103, 104]. This particular steel is highly suited to AM processing and has the ability to produce samples that are free of cracks, with relative densities exceeding 99% [101, 105, 106, 107]. The microstructure of maraging steels produced through conventional methods is predominantly martensitic. However, maraging steel processed by AM exhibits a microstructure characterized by the presence of blocks of martensite laths and retained austenite [108]. These laths are predominantly located within small solidification cells with a size that ranges 0.3-2.0 microns in L-PBF [46, 101, 105, 103, 104, 108], whereas in DED the solidification cells have an averaged size of 5 microns [109, 108, 110]. The presence of retained austenite is attributed to the micro-segregation during the solidification process of elements that stabilize austenite, which leads to their accumulation on the interdendritic/intercellular regions. Hence, the weight percentage of austenite present in the microstructure as

printed may vary from 6 to 11% [103, 111, 108]. The as built microstructure in L-PBF shows no precipitates. On the contrary, the as-printed microstructure in DED shows a considerable concentration of NiAl intermetallics, with the exception of the uppermost layer [108, 110]. This observation suggests that the precipitation occurs during the IHT of DED process, whereas the IHT in L-PBF is not sufficient for precipitation. This phenomenon explains the higher levels of hardness measured in DED specimens (360-420 HV10) in comparison to L-PBF specimens (310 HV10), despite the fact that the microstructure is finer in L-PBF [108].

Maraging steels present a relatively low crystallographic texture when compared to other steel grades in AM. This is due to the transformation of previous austenite grains into several martensitic blocks with different crystallographic orientations [101, 112]. In the case of maraging steels, it is usual to employ a multi-step post heat treatment process to achieve a homogeneous microstructure that meets the desired specifications. This process involves an initial solution treatment that promotes the austenitization of the material, followed by a quenching step to transform it into martensite, and a final aging step to induce precipitation. Nevertheless, it has been observed that although austenite can be eliminated from the microstructure of AM maraging steel by solution and quenching, it results in a coarser martensitic microstructure than the initial as built state [103, 113]. Conversely, in cases where aging is directly applied, the austenite is not removed, but instead increases through the process due to austenite reversion of the metastable martensite [114, 103, 108]. Regarding the

tensile properties, the YS and UTS of non-aged maraging steel produced through AM are comparable to or slightly higher than those of conventional counterparts [105, 103, 106]. However, aged maraging steels exhibit similar YS and UTS than conventional products, but poorer levels of TE. Tensile properties are summarized in table 1.6.

Table 1.6
Tensile properties (YS, UTS, and TE) of 18Ni-300 maraging steel. AB: as built, S: solution treatment, A: aging treatment.

Alloy	YS (MPa)	UTS (MPa)	TE (%)	Source
Conventional S	760-895	830-1170	6-17	[103, 106, 107]
Conventional A	1790-2070	1830-2100	5-11	
L-PBF AB	815-1080	1010-1205	6-12	[106, 113]
L-PBF S	800-970	950-1100	10-14.5	[105, 106, 103]
L-PBF A or S+A	1750-2000	1850-2217	1-5	[106, 104, 113, 114]

1.8.6 Carbon-bearing tool steels

Carbon-bearing tool steels are a type of steels with medium or high C content that are comprised of elements that have the affinity to form carbides, for example Cr, W, Nb, Mo or V. The excellent hardness, wear resistance and resistance to high-temperature softening of these steels render them suitable for tooling applications, such as the production of drills, molds, hobs, etc. [49]. Commonly, this type of steels undergoes a heat treatment in order to attain a dispersion of carbides of various sizes to enhance their wear resistance and hardness, particularly when exposed to high temperatures

[115]. The targeted microstructure of these steels is composed of a martensitic matrix with carbides dispersed throughout, which are formed during tempering. The as-quenched, or as built microstructure consists of a martensitic matrix supersaturated in carbon, and tempering facilitates the precipitation of carbides, which in turn enhances the ductility of the material [74]. These steels offer high strength but low toughness in the as built condition, resulting in poor processability in AM and a propensity for cracking. Process parameters need careful development and adjustment to mitigate the risk of failure during the printing process [116].

The hot working tool steel H13 is the most commonly used carbon-bearing tool steel in AM [49]. After the optimization of the printing parameters, it is reported to be printed with no cracks using DED technology [117, 118, 119] and L-PBF by heating the build platform during printing at temperatures above 100°C [120, 121, 122, 123]. The microstructure of H13 steel in AM is characterized by solidification cells or dendrites, consisting of martensite with retained austenite in the intercellular or interdendritic regions. This is similar to PHSS, martensitic SS, and maraging steels microstructures, and is also attributed to microsegregation during solidification and the IHT of the AM process [74]. The solidification cells/dendrites have sizes in the range of 0.5 to 2.0 microns in L-PBF [120, 124, 125, 123] and 2 to 30 microns in DED [126, 127, 128]. In contrast to other martensitic steels, the as built microstructure may contain a relatively elevated concentration of carbide precipitates [120, 121, 125, 128, 117, 119].

This is more noticeable in the DED process, as the influence of the IHT is more pronounced, resulting in a greater concentration of carbides rich in Cr and V [129].

The prevention of cracking in L-PBF involves the reduction of thermal gradients in order to mitigate residual stresses [123]. As martensite initiation temperature for H13 is approximately 300 °C [74], the microstructure acquired thought preheating at temperatures below 200 °C is analogous to the microstructure obtained without preheating, characterized by the presence of martensite, retained austenite, and carbides. On the contrary, a bainitic microstructure can be attained by preheating at 400 °C [23].

The tensile properties of H13 as built in L-PBF have been reported to be notably inferior to those achieved though conventional routes [120, 121, 122]. Following the heat treatment, the material produced by L-PBF exhibits comparable strength. However, the elongation of the H13 steel in L-PBF is significantly lower due to the presence of internal defects [120, 121, 122]. On the other hand, the tensile properties of H13 as built in DED are similar to those of the conventional material. This is because the IHT enables the fresh martensite to be tempered during the printing process [117].

Additional significant carbon-bearing tool steels in AM include H11 and high-speed steel M2. H11 shows a comparable microstructure to H13, but with reduced V content to enhance toughness in detriment of strength and wear resistance [115]. Meanwhile, M2 comprises supersaturated martensite, retained austenite and M_2C carbides within its microstructure [130]. The application of preheating temperatures exceeding 200 °C

is required to prevent cracking during the L-PBF printing process. Nonetheless, the mechanical properties (hardness and tensile properties) are lower than those of the conventional product [116]. Table 1.7 gathers the reported mechanical properties of H13 and M2 steel, and compares them with those of their conventionally produced counterparts.

Table 1.7
Tensile properties (YS, UTS, TE and Rockwell-C hardness) of H13 and M2 carbon-bearing steels. AB: as built, HT: heat treated, BP: build platform preheating.

Alloy	TS (MPa)	UTS (MPa)	TE (%)	HRC	Source
H13 Conventional	1569-1650	1930-1990	9-12	40-53	[121, 128]
H13 L-PBF AB		1000-1200	0.8-1.9	54	[131]
H13 L-PBF HT	1580	1860	2.2	51	[132]
H13 L-PBF BP(100°C)	1150-1275	1550-1650	1.5-2.3		[120]
H13 L-PBF BP(200°C)	835	1620	4.1		[121]
H13 L-PBF BP(400°C)	1073	1965	3.7		[121]
H13 DED AB	1288-1564	2033-2064	5-6	55	[128]
M2 Conventional		1600	1.5	65	[116]
M2 L-PBF HT		1300	0.7	64	[116]

To provide an overview of the mechanical properties of this section of commercial steels for AM, Figure 1.6 illustrates the relationship between the UTS and the TE that are obtained using commercial steel powders in L-PBF and DED technologies. The plot includes both the as built and heat treated conditions, and the green region outlines the mechanical properties that are intended to cover with the design of novel High Mn steels for AM.

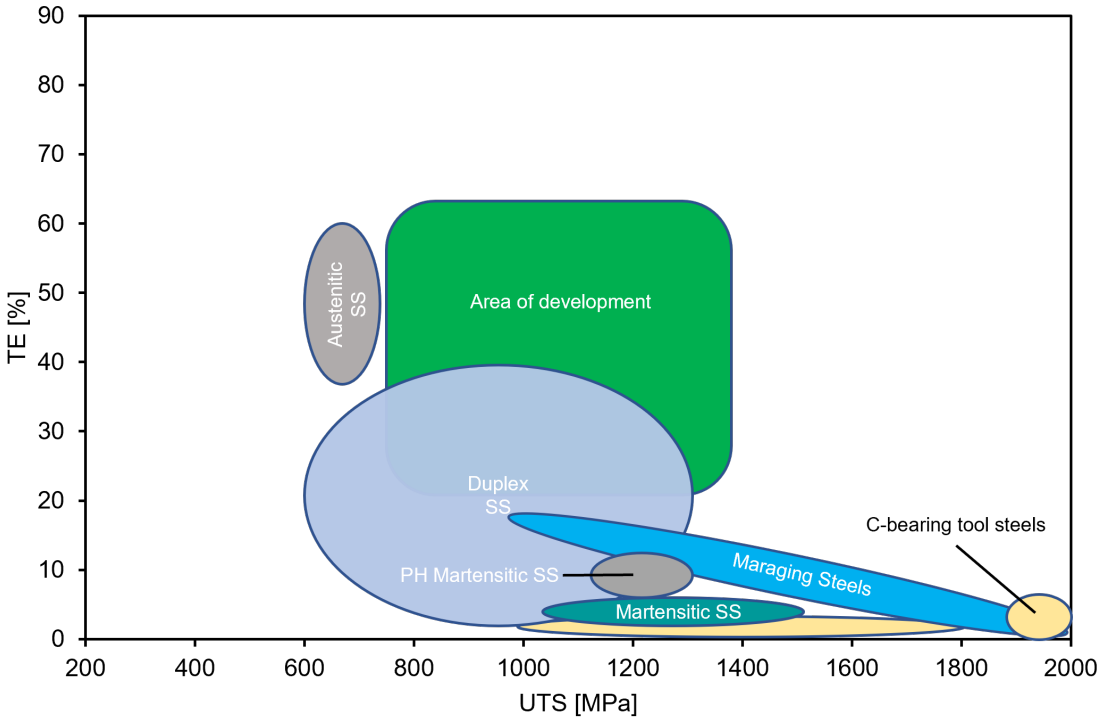

Figure 1.6: Overview of tensile properties of available commercial steel powders discussed in Section 1.8, after being printed by L-PBF or DED. The UTS and TE represented include as built and heat treated conditions.

1.9 Fe-Mn steel system and High Mn steels

The discovery of manganese steels is attributed to Sir Robert Hadfield in 1882 [133]. According to Hadfield's research, steels presented an increased brittleness within the range of 2.5-7.5 wt.% of Mn content. However, when the manganese content was raised above 10 wt.%, the steel showed greater toughness. Hadfield conducted further research on these steels and later filed the first Mn-steel patent based on a steel with a nominal composition of Fe-12Mn-1.2C wt.%, with a Mn/C ratio of 10 to 1, which was obtainable through ferro-alloys [134]. The present-day designation for this

composition is “Hadfield’s Manganese steel” or “Hadfield steel” [134, 135].

After this, there has been a persistent effort towards the advancements of Mn-steels and High Mn-steels owing to their recognized high work-hardening, and exceptional ductility-strength balance and low cost [135]. These advancements are pertained to Advanced High Strength Steels (AHSS), a class of steels that covers a large group of steel families that are widely used by automakers and other industries due to their light-weighting ability, which helps to reduce fuel consumption and mitigate pollution.

AHSS are also known for their good tensile properties and can serve as a cost-effective alternative to expensive alloying elements like Ni or Cr, by using Mn. The first generation of AHSS comprises the following steel grades: dual-phase (DP), complex phase (CP), martensitic (MART) and transformation induced plasticity (TRIP).

The second generation of AHSS includes the austenitic SS, twinning-induced plasticity (TWIP) steels and High Mn Fe-Mn-Al-C low density steels. The mechanical properties and weight reduction potential of second generation AHSS are superior to those of first generation. However, the industrialization of TWIP and High Mn steels is a costly process due to their High Mn content and significant amount of alloying elements, particularly Al, Si and C that causes several challenges during production, such as poor hot ductility, high affinity for oxygen at high temperatures, high segregation of elements, formation of brittle and undesired phases, etc [136, 137]. The development of a third generation of AHSS was motivated by the different limitations

of first and second generations. Mechanical properties of the third generation of AHSS aim to fall in between first and second generations while minimizing processability issues and reducing costs as compared to second generation. The third generation of steels comprises quenching and partitioning (Q&P) steels, medium manganese steels, and carbide-free bainitic (CFB) steels [138, 136].

Given that austenitic SS are widely used in AM industry, TRIP, TWIP and High Mn Fe-Mn-Al-C low density steels have a high potential in AM due to their remarkable strength and ductility, and the high austenite content, especially of the last two. In addition, the differences and particularities of AM processing routes can potentially resolve the conventional issues that have hindered the industrialization of these steels.

1.9.1 TRIP steels

The TRIP effect refers to the phenomenon of martensitic transformation occurring during plastic deformation. The impact of this phenomenon in steel is primarily determined by alloying constituents: C, Al, Si and Mn. Upon the application of stress to these steel grades resulting in elastic and further plastic deformation, the metastable austenite enriched in C undergoes transformation into martensite. The TRIP phenomenon enhances the work-hardening and strength of the steel through deformation, mostly in the "neck" region where higher strain is faced. Consequently, deformation is halted in this region, thereby delaying necking [138].

The conventional compositional range of TRIP steels is 0.1-0.4 wt.% C, less than

2.5 wt.% Mn, less than 2.2 wt.% Si and less than 2.0 wt.% Al. Chemical composition combinations inside the aforementioned ranges are designed to target a microstructure that consists of retained austenite that is embedded within a matrix of ferrite, bainite, martensite, or a combination thereof. This microstructure is capable of achieving a range of tensile properties that fall within 500-1050 MPa range of UTS and 10-30% range for TE [139]. However, High Mn steel developments have reported TRIP as unique contribution to strain hardening in compositions with contents of Mn around 20 wt.% [140, 141]. It is important to note that the TRIP deformation mechanism can be also present in other steel grades, including Q&P, CFB and medium Mn steels.

1.9.2 TWIP steels

TWIP steels exhibit outstanding mechanical properties such as elevated strain hardening, large TE and great UTS. These properties, render them as potential materials for weight reduction in various industrial applications such as auto, shipbuilding, oil and gas industries or structural applications [142]. The austenitic microstructure of TWIP steels is primarily responsible for their high strain-hardening. This phenomenon is often attributed to the reduction of the dislocation mean free path, described as a dynamic Hall-Petch type relationship, which occurs due to the rising fraction of deformation twins during plastic deformation. These twins are known to form new crystal orientations and thus new interfaces that act as grain boundaries

which imply strong obstacles to dislocation glide [142]. Figure 1.7 ilustrates the dynamic Hall-Petch effect [143], which is responsible for the strain hardening mechanism observed in TWIP steels. The dislocation main free path is depicted as the width of an untwinned grain in the scenario shown in Figure 1.7a, whereas in Figure 1.7b, it is constrained to the space between two twins that formed due to stress.

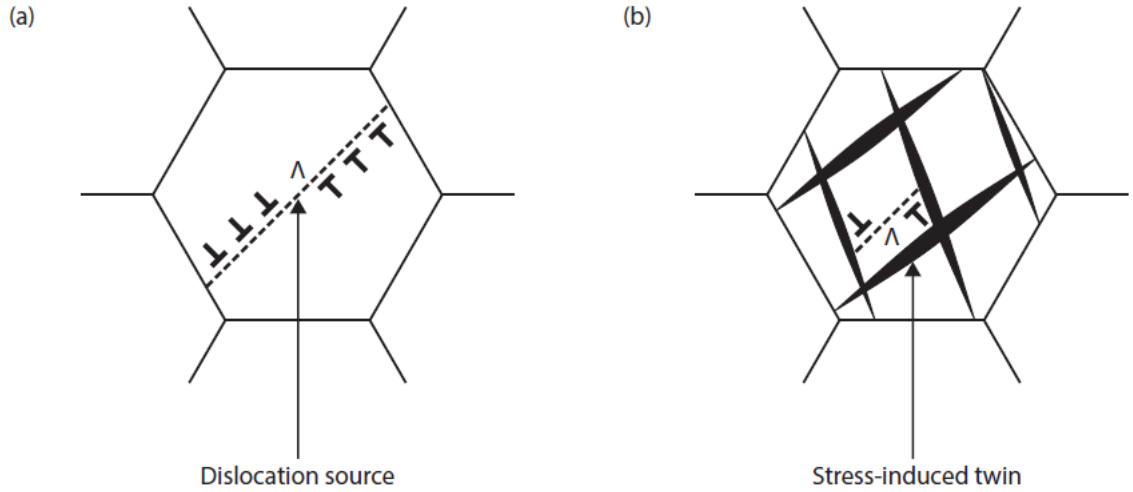

Figure 1.7: Sketch of the TWIP effect and dynamic Hall-Petch effect, where the dislocation main free patch is shown in (a) an unstressed grain, and (b) stressed grain.

The chemical composition of these steel grades consists of Mn within the range of 20-30 wt.%, C $<$ 1 wt.%, Al $<$ 3 wt.%, Si $<$ 3 wt.%, and the potential addition of secondary elements such as Cr, Cu, Nb, N, Ti or V [142, 144]. The appropriate choice of chemical composition holds significant importance as it determines the attainment of the austenitic matrix and the prevalence of mechanical twinning as the principal deformation mechanism.

The stacking fault energy (SFE), which is defined as the energy associated with the

formation of a disruption of the stacking sequence of an FCC lattice after passing of a Shockely partial dislocation, has been widely accepted as the key parameter governing the plastic deformation mechanism. SFE values below 15 mJ/m^2 lead stress-induced phase transformation, or TRIP-effect, intermediate SFE values ranging from 15-45 mJ/m^2 are typically associated with mechanical twinning, while SFE values exceeding 45 mJ/m^2 commonly result in dislocation glide and share banding [142]. Thus, the targeted SFE for TWIP steels should fall between 15-45 mJ/m^2 and it is influenced by the presence and amount of alloying elements. Manganese is a special element since it has the ability to decrease the SFE up to concentrations of 14 wt%, beyond which the SFE increases [145]. Then, addition of Al and Cu increases linearly the SFE, while Si and Cr slightly reduce it [146, 144].

Attending to this, the mechanical properties of steel compositions defined as TWIP range between 800-1100 MPa UTS, and 55-80% TE [139].

1.9.3 High Mn Fe-Mn-Al-C low density steels

High Mn steels are a type of Fe-Mn-Al-C low density steels characterized by an austenitic matrix with the optimal presence of second phases.

Development of Fe-Mn-Al-C steels started during the 1950s as substitute for Fe-Cr-Ni steels [147]. These steels offer a strong potential for employment in lightweight applications, rendering them particularly appealing for utilization in structural applications and the automotive industry [148]. Moreover, it is noteworthy that these steels

show other interesting properties such as remarkable strength and toughness, even when subjected to cryogenic temperatures [147, 149, 150, 151], good fatigue and oxidation resistance at room and elevated temperatures [147, 150, 152, 153, 154], as well as high energy absorption [148, 149, 147]. These properties are of significant value to various industries, including oil-and-gas, aerospace, defence, or chemical.

The reduction in weight of these steels is attributed to the incorporation of elements possessing lower density than iron. Equation 1.4 provides a linear approximation of the correlation between the presence of Mn, Al and C and the reduction in density of austenite [139]. Furthermore, the incorporation of other optional alloying elements with low density, such as Si (2.3 g/cm^3), may be considered for enhancing the reduction in weight.

$$\rho_{austenite}\ (g/cm^3) = 8.15 - 0.101(wt.\%Al) - 0.41(wt.\%C) - 0.0085(wt.\%Mn) \quad (1.4)$$

The classification of Fe-Mn-Al-C low density steels is based on their respective Mn, Al, and C content, which has a significant impact on the microstructure and matrix phases during hot working temperatures [139]. Table 1.8 presents a summary of the chemical composition ranges for each steel category, along with the corresponding attainable tensile properties.

Table 1.8
Common ranges of chemical compositions and tensile properties of the four different categories of Fe-Mn-Al-C low density steels.

Characteristic Vs Steel type	Ferritic	Ferrite-based duplex	Austenite-based duplex	Austenitic
Al (wt.%)	5-9	3-7	5-10	5-12
Mn (wt.%)	<5	2-12	5-30	12-35
C (wt.%)	<0.05	0.05-0.5	0.4-0.7	0.6-2.0
UTS (MPa)	200-600	400-950	600-1300	600-1200
TE (%)	10-40	10-40	15-65	35-100

The ferritic type is composed of small amounts of Mn and C, with the aim of achieving an elongated δ-ferrite microstructure at high processing temperatures. The presence of other phases at room temperature, such as $\alpha-$ferrite, B2-ordered ferrite, FeAl, or DO_3-ordered structure, is also possible depending on the amount of Al. The ferrite based duplex aims to achieve a microstructure mainly consisting of $\delta-$ferrite and austenite at hot working temperatures. The fraction of $\delta-$ferrite in this microstructure exceeds 50%. The austenite's stability at room temperature is not high due to the relatively small o medium presence of austenite-stabilizing alloying elements. The two remaining classifications pertain to High Mn Fe-Mn-Al-C steels, which are classified as austenitic and austenite based duplex. The austenite stability at room temperature is significantly high in both steels due to the substantial presence of Mn and C in the chemical composition. This results in a fully austenitic microstructure for austenitic and formation of some δ-ferrite in the austenite based duplex. Furthermore, high levels of Al present in both steels can result in the precipitation of a specific type of carbide known as "κ". The literature commonly refers to these steels

as "Triplex" due to their potential combination of austenite, ferrite and κ-carbide phases [139].

This review demonstrates that High Mn steels show significant potential for the AM industry. These steels are addressed to cover a gap where high toughness and exceptional combinations of UTS and elongation are required (e.g., UTS $>$ 800 MPa and TE $>$ 50%), together with low density. In such cases, these steels represent a better alternative to other steel solutions currently available in the AM market (Sections 1.8.1 - 1.8.6). Furthermore, these types of steels have the potential to replace costly Austenitic SS, providing superior performance at a lower cost.

Although TWIP steels exhibit great potential for AM, this research will focus on High Mn Fe-Mn-Al-C low density steels, as they offer a wider range on tensile properties and have high Al contents that enhance their oxidation resistance, which is an interesting property in AM to avoid the need for surface post-processing. The subsequent sections present an examination of the evolution of microstructural phases, mechanisms of strengthening, and the process of industrialization pertaining to High Mn Fe-Mn-Al-C low density steels, with a specific emphasis on High Mn austenitic Fe-Mn-Al-C low density steels. This steel is expected to have a more homogeneous microstructure after printing as compared to High Mn austenitic-based duplex steels, and considering that most commercial steels require a post-processing after printing, the development of new steel grades that do not require such treatment is beneficial.

1.9.3.1 Microstructure of High Mn Fe-Mn-Al-C low density steels

The microstructures of austenite-based duplex and austenitic low density steels are characterized by a combination of an austenitic matrix and a different fraction of $\delta-$ferrite. The microstructure of hot-rolled austenitic Fe-Mn-Al-C comprises equiaxed austenitic grains. Upon cooling or prolonging annealing temperatures, precipitation of a type of κ-carbide occurs [155, 156].

Other phases that can be formed are $\alpha-$ferrite (or ordered B2 and/or $D0_3$), and $\beta-$Mn phase in compositions or regions rich in Mn [155]. The nucleation of $\beta-$Mn phase occurs at the austenitic grain boundaries and it is detrimental for ductility and toughness. The precipitation of $\alpha-$ferrite occurs at the grain boundaries or austenite, or at the $\delta-$ferrite/austenite grain boundaries [157]. At lower temperatures, α-ferrite can undergo a transformation to ordered B2 or DO_3 [158]. If nanosized B2 phase is formed, the material strength can be increased, although, this mechanism is not well understood yet [159, 160].

The $\kappa-$carbide is a phase that possesses a perovskite structure, referred to as $E2_1$. The theoretical stoichiometric composition is represented by $(Fe,Mn)_3AlC$, wherein the Al atoms are situated at the corner positions of the cubic cell, while the Fe and Mn atoms are located at the center of the faces. The C atom, on the other hand, is positioned at the interstitial site of $(\frac{1}{2}, \frac{1}{2}, \frac{1}{2})$ [161, 162]. However, in reality, a metastable $(Fe,Mn)_3Al,C_x2$ (where $x < 1$), is formed through spinodal decomposition of austenite

[163, 164]. This non-stoichiometric carbide, is commonly denoted as κ' in the literature or intragranular κ'-carbide [163]. However, another type of $\kappa-$carbide, known as intergranular κ^*-carbide [165, 166, 167], can be distinguished as being formed at the grain boundaries. The mechanism of formation and their respective contribution to the mechanical properties are significantly different.

The $\kappa'-$carbide precipitates intragranularly in a homogeneous and coherent manner within the austenitic grains matrix. The precipitation sequence can be described as follows [168, 169, 158]: $\gamma \rightarrow \gamma' + \gamma'' \rightarrow \gamma' + SRO \rightarrow \gamma' + \kappa'$, where SRO means short range order of atoms.

Intergranular κ^*-carbides are precipitated in a heterogeneous manner at the boundaries of austenite grains in a lamellar structure when subjected to annealing. This precipitation reaction can be defined as either $\gamma \rightarrow \gamma + \kappa^*$ or $\gamma \rightarrow \gamma + \kappa^* + \alpha$ [170, 171].

A significant increase in yield strength can be achieved with formation of fine intragranular $\kappa'-$carbides, but the opposed effect occurs if these carbides coarsen [172, 147, 173]. On the contrary, the presence of κ^*-carbides has been shown to lead always to a reduction in ductility [172, 149]. With regard to the chemical composition, intragranular $\kappa'-$carbides are formed when contents of Al and C are higher than 6.2% and 1.0% respectively [139] or higher than 7.0% and 0.7% [174]. In contrast, intergranular κ^*-carbides may precipitate at relatively lower levels of Al and C (5.5% and 0.7%) than κ'-carbides [139]. Thus, it is important to keep precise control

over the process in order to prevent undesired precipitation of these carbides.

1.9.3.2 Strengthening mechanism of austenitic High Mn Fe-Mn-Al-C low density steels

Considering the solution and quenching condition, the yield strength of austenitic Fe-Mn-Al-C low density steel is enhanced by the dissolution of Mn, Al, and C in the austenite [175, 176]. Furthermore, grain refinement provides an additional mechanism for strengthening these steels. In addition, the precipitation hardening of fine phases, particularly κ'-carbides, can be employed. These carbides significantly hinder the movement and ordering of dislocations during deformation [173, 177, 149, 147]. In austenitic Fe-Mn-Al-C low density steels having a SFE ranging from 20-50 mJ/m^2, the deformation mechanism mainly consists of a preliminary stage of planar glide, followed by mechanical twinning [178]. An increase in SFE results in a delay of mechanical twinning to higher levels of stress or even a complete suppression thereof. The mechanism of planar glide deformation, devoid of any cross-slip observation, has been identified in these steels that form a slip band Taylor-lattice structure[1], regardless of the presence of κ-carbides-carbides in their microstructure. The microstructure of these steels is commonly considered to include either fully developed κ-carbides, SRO, or long range order (LRO) clustering. Their presence is believed to interact with

[1]The Taylor lattice represents one of the earliest forms of low energy dislocation structure (LEDS). It consists of an equilibrium array wherein alternating rows of positive and negative edge dislocations are placed. Specially, the arrangement is such that each dislocation is surrounded by four nearest neighbors, all of which possess a sign opposite to that of the given dislocation.

dislocations, resulting in a reduction of the barrier for trailing dislocations, which is known as the glide plain softening hypothesis [179, 180]. The increase of strain results in a corresponding rise in the number of slip bands and their intersections, leading to a prominent refinement of the microstructure. The mechanism behind the dynamic refinement and its resulting work hardening effect remains ambiguous and subject to discussion. Two main hypotheses have been proposed to account for this phenomenon, named as micro band induced plasticity (MBIP) and slip band refinement-induced plasticity (SRIP), which can be also referred to as dynamic slip band refinement (DSBR) [179, 180].

1.9.3.3 End-use properties of austenitic High Mn Fe-Mn-Al-C low density steels

This section will provide an overview of a set of end-use properties that are relevant to High Mn Fe-Mn-Al-C steels, with a particular emphasis on the austenitic grade.

- **Stiffness**:The Young's modulus is an essential material property for certain structural components of automobiles such as the body-in-white. It has been observed that the Young's Modulus of High Mn Fe-Mn-Al-C low density steels is generally lower compared to other Advanced High Strength Steels (AHSS) [177, 181]. The decrease in stiffness is attributed to the incorporation of Al [182]. The weight reduction capability of low-density steels is dependent upon

the values of both Young's Modulus and density. Thus, it is necessary to take into account the specific stiffness, which is the Young's modulus normalized by density. The values of specific stiffness are comparable to those of traditional steels [139]. Additionally, it has been noted in literature that the introduction of Si and Cr can enhance the stiffness of Fe-Mn-Al-C low density steels [183].

- **Impact toughness**: High Mn low density steels exhibit an excellent combination of mechanical strength and fracture toughness, rendering them highly suitable for structural applications [184]. These steels have higher values of impact toughness in comparison to AHSS, while demonstrating values comparable to those of austenitic SS. Specifically, the austenitic Fe-Mn-Al-C low density steel shows cases of Charpy V-notch toughness at room temperature of 200 J/cm^2 [151, 150]. The impact toughness of High Mn low density steels is affected by the formation of κ-carbides, which can induce brittleness and a reduction of ductility and subsequent loss of impact toughness [184, 150].

- **Specific energy absorption**: The concept of specific energy absorption refers to the amount of deformation energy per unite of volume that is absorbed at a particular temperature and strain rate, typically within the range of 10^2 to 10^3 s^{-1}. This property is very important in the design of parts that require weight reduction, such as land or aerial vehicles. The austenitic Fe-Mn-Al-C low density steel presents a specific energy absorption of approximately 0.5 J/mm^3,

which is significantly greater than that of conventional deep drawing steels, such as DC04, IF steels and HC300LA. These steels are commonly utilized in the production of automotive bodies and frame structures, and typically provide specific energy absorption values ranging from 0.16-0.25 J/mm^3 [149, 185, 186].

- **Fatigue**: Austenitic Fe-Mn-Al-C low density steels exhibit fatigue resistance comparable to TWIP steels, surpassing that of austenitic SS (such as 304L) but lower than that of martensitic Cr steels[153, 187, 188]. The impact of κ-carbide on fatigue resistance remains insufficiently comprehended, with favorable and unfavorable cases [189].

- **Weldability**: Despite the fact that welding of Fe-Mn-Al-C low density steels is feasible, there exists not much of literature about this topic. The main challenge in weldability for these steels is the formation of heterogeneous crystallographic nucleation with the melt, which results in a mixture of elongated and textured dendrites with equiaxed structures [190, 191]. Additionally, the rise in Mn vapour pressure that occurs with increasing temperature can result in significant Mn evaporation [192], and there is a risk of hot cracking susceptibility [193, 194].

- **Oxidation Resistance**: The elevated levels of Al in High Mn Fe-Mn-Al-C low density steels facilitate the growth and development of uninterrupted oxide layers of Al_2O_3 or $FeAl_2O_4$, thereby conferring superior resistance to oxidation

in comparison to conventional steels [195, 154, 196, 197, 198]. This level of oxidation resistance is similar to that of austenitic SS [195].

- **Corrosion Resistance**: The passive Al_2O_3 film formed by the elevated levels of Al in High Mn low density steels enhances their corrosion resistance to levels equivalent to or surpassing those of conventional high strength steels [177]. Inside the Fe-Mn-Al-C low density steels, the austenitic grade shows greater corrosion resistance as compared to the austenite based duplex owing to the fact that the initial stages of corrosion, which typically manifest in the form of pitting, tend to occur selectively in the ferrite grains [199]. Nonetheless, the corrosion resistance of austenitic Fe-Mn-Al-C low density steel is comparatively inferior to that of austenitic SS [200, 201, 202].

- **Formability**: The capacity of a material to undergo the intended or final deformation form without experiencing necking failures is referred to as its formability. This is one of the primary constraints hindering the utilization and industrialization of High Mn Fe-Mn-Al-C low density steels [177, 149, 203, 204]. Despite this, the characteristics of AM processes and their capacity to fabricate the final geometry directly without forming operations, offer a promising resolution to broaden the scope of High Mn Fe-Mn-Al-C low density steels for additional applications.

1.9.4 Industrialization challenges of High Mn steels

Despite the significant potential of High Mn steels, such as TWIP and Fe-Mn-Al-C low density steels in various industrial applications, their utilization still remains limited. The short application of these steels can be attributed to the difficulties encountered in their large-scale production. The elevated Mn content and its associated high vapour pressure render the processing of liquid metal exceedingly difficult. Furthermore, the elevated levels of Al present in High Mn low density steels give rise to a number of challenges [177, 205, 206, 176, 207, 208], including:

- The occurrence of intensive reactions between the melt and the refractory materials, casting products, or covering materials can lead to deviations from the intended chemical composition.

- The precipitation of Al_2O_3 within the liquid steel has the potential to result in obstruction of the nozzles in the course of the process of continuous casting.

- The formation of Al-oxides that are heavy and dense may pose a potential hazard due to their susceptibility to chemical reactions with the surrounding atmosphere.

- Certain types of Al oxides, particularly those containing Mn and Fe, have the potential to develop during the high-temperature processing phase and can have

adverse effects on the final product. These oxides are challenging to remove once formed.

- Elevated levels of Mn and Al have the potential to induce significant macrosegregation, resulting in the development of fragile phases or fracturing during hot working due to localized reduction of the solidus temperature.
- The precise management and control of κ-carbides precipitation and other phases precipitation at every stage of the process requires the use of various steps, including annealing, aging treatments, and fast cooling rates in conjunction.
- Very narrow casting and hot rolling process window to avoid cracking and cold rolling is not feasible.

Thus, the conventional processing of High Mn steels is hindered by several factors, thereby necessitating alternative processing routes such as AM as a viable solution.

1.10 High Mn steels in Additive Manufacturing

The unique mechanical properties and potential applications of High Mn steels have attracted significant attention in the field of AM. AM technologies have the potential to overcome the industrial limitations of conventional production. However, the existing literature on this topic remains limited. The majority of the published studies

centered on the Fe-Mn-Al-C system deal with materials that exhibit either TWIP or TWIP strain hardening mechanism [209, 210, 211, 212, 213, 214, 215, 216]. Extensive research carried out between RWTH Aachen University and the Fraunhofer Institute for Laser Technology ILT (Aachen) was conducted on the Fe-21Mn-xAl-0.3C (wt.%) steel system utilizing both L-PBF and DED processes [212, 209, 211, 210, 214, 215]. The variation of Al in the range from 0-2 wt.%, customizes the SFE, which governs the strain hardening mechanism and the mechanical properties. The reported values for YS fall within the range of 200-500 MPa, while UTS ranges from 550-900 MPa and TE from 20-35% when using DED. These compositions have SFE values below 35 mJ/m^2, which is typical for TRIP and TWIP strain hardening mechanisms. The study of the influence of Al in L-PBF was conducted up to 5 wt.%, which increases the SFE to 48 mJ/m^2. This wider steel composition range enables a broader range of tensile properties measured in the as built condition: YS between 500-700 MPa, UTS ranging from 700-1000 MPa and TE from 30-50%.

The microstructure in as built state is predominantly austenitic, with the possibility of some ferrite in the alloys with the highest aluminum concentrations, as reported by [215, 209]. The austenitic grains follow epitaxial growth, exhibiting a columnar structure along the building direction. A slight crystallographic texture was observed along this direction [209, 215], that can explain the tensile properties anisotropy along different directions [211]. The addition of Al within the range of 4-5 wt.% promotes the nucleation of ferrite. This phenomenon can result in a transformation from an

elongated fully austenitic microstructure to a more refined and randomized texture consisting of both austenite and ferrite [215]. Formation of (Mn, Si, Fe) and Al oxides, as well as Mn sulfides was observed in both L-PBF and DED microstructures. The sizes of these inclusions were found to vary, ranging from nano to submicron size in L-PBF and submicron to micron size in DED. The presence of these inclusions implies a potential hazard in terms of risk of cracking caused by residual stress [210]. Mn microsegregation was measured at the solidification cell structure scale with 2.5-6.0 wt.% variation between the cell core and boundary [209, 210].

Another TWIP steel system that has been investigated in L-PBF is Fe-22Mn-0.6C-0.25V-0.25Si-0.2Cr, which possesses a fully austenitic microstructure characterized by columnar grains and a texture aligned with the building direction [213]. The material's tensile properties reached a YS of 600 MPa, and UTS of 900 MPa, and a TE of 35% in its as built state. Upon subjecting the steel to a heat treatment at a temperature of 1050 °C for a duration of 1 hour, the TE can be increased twofold to 70%. However, the YS and UTS suffer a reduction, with values of 300 and 800 MPa, respectively. In addition, the Fe-10Mn-1.6Al-0.4C-0.7V martensitic steel system was investigated in L-PBF, yielding a remarkable UTS of 1625 MPa and a fair TE of 7.8% [216].

Nevertheless, the aforementioned high manganese steel systems investigated in AM have not the elevated levels of Mn, Al and C required for high weight reduction. To the best of the author's knowledge, there is only one recent study published on

the development of an austenitic low density steel Fe-30Mn-9Al-1Si-0.5Mo-0.9C [217]. The reported tensile properties were promising, notwithstanding the presence of solidification microcracks oriented in the building direction throughout the entire cross-sectional area, characteristic of hot-cracking. The microstructure of the as-printed material is fully austenitic and composed of cellular solidification structures. These structures give rise to elongated grains that are aligned along the building direction. The presence of noticeable segregation of Mn and Si was detected in the solidification cellular-dendritic structures, as well as in the boundaries of the melt pool. Elevated levels of Al were detected in areas with lower concentrations of Mn and Si. So, the main microstructural drawbacks of AM (macro and micro segregation, in conjunction with hot cracking) occur in this High Mn Fe-Mn-Al-C low density steel.

The current thesis aims to explore the design and development of novel austenitic Fe-Mn-Al-C low density steels. The objective is to overcome the constraints of traditional manufacturing techniques and produce near net-shape components with the design flexibility that offers AM. However, hot cracking and micro segregation become new challenges.

1.11 Alloy design for Additive Manufacturing

This section provides a review and analysis of the general solidification theory, combining alloy design-oriented tools. The aim is to tackle the limitations encountered

conventionally manufactured of low-density steels, specifically High Mn Fe-Mn-Al-C steels, and mitigate the emerging challenges associated with AM. These challenges primarily involve the formation of undesirable phases due to solidification microsegregation and hot cracking.

1.11.1 General Solidification Theory

In the context of processes characterized by a moving melt pool, such as welding or AM, the size and morphology of grains, the occurrence of micro and macro segregation, and the formation of defects like cold and hot cracking are all influenced by the behavior of solidification. In the end, these factors determine the properties of the final product. Therefore, it is crucial to comprehend the factors that influence the formation of solidification microstructure [218].

Based on the similarities between welding and AM, solidification behavior was reviewed in the context of directional solidification (in one direction), focusing on the relationship between temperature gradient in the liquid phase (G) and growth rate (R) at the solid-liquid interface (S/L). Specifically, this review focused on the impact of these factors on the redistribution of solid, microsegregation, and the size and morphology of the solidification structure.

1.11.1.1 Solute Redistribution

Following the process of nucleation, the solid material undergoes growth through the mechanism of atoms diffusion from the liquid phase to the solid phase at the S/L interface. In the context of a planar S/L interface, S. Kou establishes four distinct cases for solute redistribution [219].

- **Case I:** Diffusion occurs in both solid and liquid, resulting in reaching a state of equilibrium during solidification. During the process of solidification, the amount of solid increases. However, it is important to note that the solid composition remains always uniform, thereby preventing any segregation of solute.

- **Case II:** Complete diffusion takes place in the liquid, while no diffusion in the solid. By growing the solid phase, the solute is drawn away into the liquid (when partition coefficient is less that 1, and opposite case when above 1).

- **Case III:** Liquid exhibits complete diffusion while solid, only limited diffusion. This implies that certain solutes have the ability to undergo back diffusion into the solid phase. When the partition coefficient is less than 1, the solute that diffuses back increases the concentration of the solute in the solid that has already been formed. As the rate of back diffusion increases, the degree of solute segregation decreases, thereby approaching Case I of solid redistribution. Conversely, a decrease in back diffusion results in an increase in solute segregation

and a closer approximation to Case II behaviour.

- **Case IV:** The diffusion in the liquid is limited, while there is no diffusion in the solid. Due to restricted diffusion in within the liquid, the solute that is not incorporated into the growing solid, accumulates in a solute-rich layer in the S/L interface, while the overall composition of the liquid phase remains unchanged. Consequently, the layer enriched with solute progresses forward reaching a steady state until the end of the solidification, when the liquid solute content experiences a rapid increase.

In a general sense, it can be concluded that there is no solute segregation in Case I, solute segregation is maximal in Case II, and intermediate in Cases III and IV. In both laser based AM technologies (L-PBF and DED) the cooling rates during solidification are extremely fast limiting solute diffusion and causing segregation of solute during solidification. Thus, these AM processes would approximate better to solidification Cases II, III and IV.

1.11.1.2 Solidification Modes

The S/L interface, or solidification interface, exhibits a planar nature under equilibrium conditions. However, in AM or welding processes, the liquid phase experiences supercooling, resulting in alternative solidification modes. These modes consist of cellular solidification, columnar-dendritic solidification, an intermiddle cellular-denfritic,

and equiaxed-dendritic solidification. The degree of undercooling and subsequent solidification mode are determined by the previously defined established variables G and R. A decrease in the temperature gradient G leads to an increase in supercooling, while an increase in the growth rate R results in an increase in supercooling. Figure 1.8 [219, 220] serves as an illustration of how the ratio G/R influences the mode of solidification.

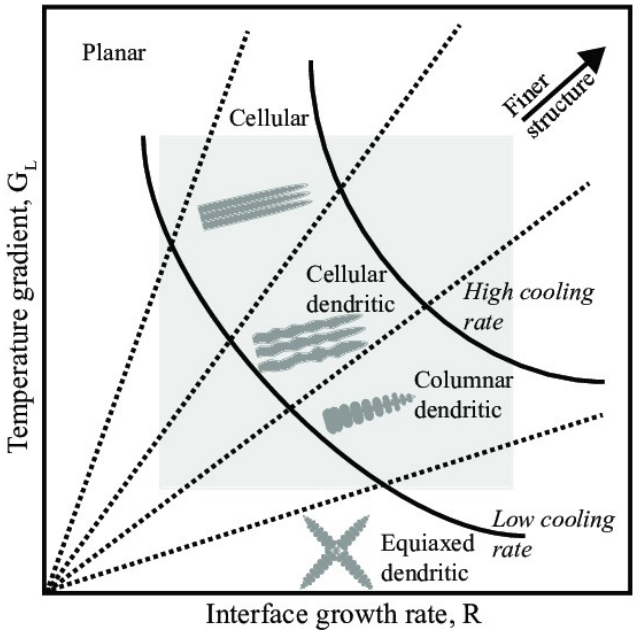

Figure 1.8: Effect of G and R on the morphology and size of solidification structure.

Furthermore, the product $G \cdot R$ denotes the cooling rate. As the product increases, the cellular spacing or secondary dendritic arm spacing becomes more refined. Thus, the size of the solidification structure is determined by product $G \cdot R$.

The process of solute redistribution during cellular or dendritic solidification leads to the segregation of solute at a microscopic level, occurring across the cells or dendrite

arms. The phenomenon being referred to is commonly known as microsegregation. As depicted in Figure 1.9 [219], the placement of volume elements is such that they are oriented along the centerlines of adjacent cells or secondary dendrite arms [219]. Additionally, the S/L interface within this volume is planar, allowing for the analysis of microsegregation based on the examination of four distinct cases of solute redistribution, as described in Section 1.11.1.1.

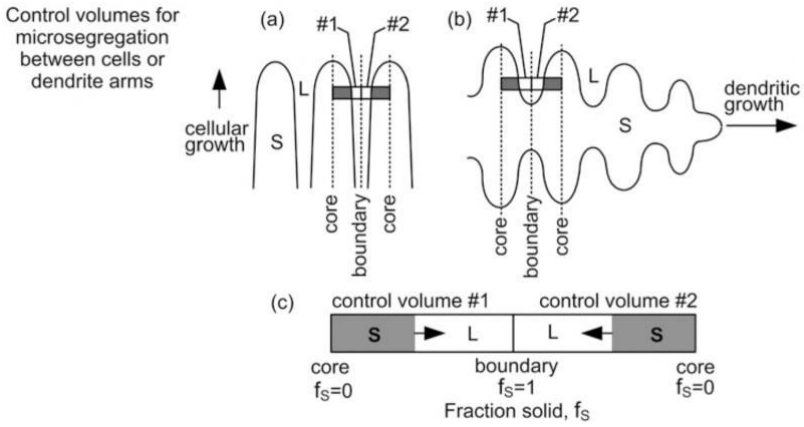

Figure 1.9: Control volumes for solute redistribution applied to analysis of microsegregation: (a) cellular solidification; (b) dendritic solidification; (c) control volumes enlarged.

1.11.1.3 Columnar to equiaxed transition

The columnar to equiaxed transition (CET) is a phenomenon that takes place when equiaxed grains begin to grow in the constitutionally undercooled liquid located ahead of the solid columnar front, thereby impeding the growth of the columnar structure. An equiaxed grain structure is characterized by the nucleation of randomly oriented

crystals that grow in all directions [221]. Equiaxed grains are commonly preferred in various manufacturing processes due to their ability to enhance the material's isotropy and strength through the Hall-Petch effect of finer grains [222, 223].

1.11.1.4 Control the solidification mode in laser-Additive Manufacturing

Based on the principle of solidification, it is possible to potentially control the transition from columnar to equiaxed solidification by controlling the printing parameters. This can be achieved by enhancing supercooling through the reduction of the temperature gradient at the solidification front (G) and by increasing the velocity of the S/L interface (R) [224]. Various methods have been reported in the literature for achieving CET through the manipulation of laser process parameters in AM. These methods include adjusting the energy density [225, 226, 227, 228], modifying the laser beam shape [229, 230], changing the laser spot diameter [231], or modifying the scanning strategy [225, 232, 233]. Furthermore, the enhancement of grain refining can be achieved by regulating solidification supercooling through the process of remelting previously printed layers [234, 235, 236]. However, it is widely acknowledged that the control of G and R, is more challenging in welding and AM than in other manufacturing processes, such as casting [237]; while the homogeneity of CET varies across different regions of the melt pool [238]. Furthermore, effectively managing printing conditions to manipulate the G and R is often impractical for various alloy systems, additive manufacturing hardware, and complex geometries of near net shape parts,

where heat accumulation can occur [69, 239, 240]. Therefore, it is essential to implement a more practical methodology for the control of microstructure by means of grain refinement. In order to enhance the process of grain refinement in printing, recent research has focused on investigating novel alloys that facilitate heterogeneous nucleation by creating nucleation sites during solidification in the printing process [234].

1.11.2 Steel-design oriented CALPHAD tools

This section addresses the potential of calculation of phase diagrams (CALPHAD) to boost steel development, as well as indicate the specific CALPHAD-oriented tools employed in the design of steels for AM.

1.11.2.1 The CALPHAD method

The CALPHAD method, which was initially formulated by Larry Kaufman in 1970, has been widely employed in the investigation and development of materials [241]. The CALPHAD method is a modeling technique that aims at defining the Gibbs energy of distinct phases through the integration of theoretical physics-based and empirically-based thermodynamic models. CALPHAD models are structured within thermodynamic databases that are self-consistent. These databases can be disseminated and utilized by various software tools, as well as integrated into computational

materials design tools that operate at multiple scales. The application of CALPHAD modeling has demonstrated significant efficacy in the field of Integrated Computational Materials Engineering (ICME) methodologies, particularly in the context of materials design, with a specific emphasis on alloy systems. One of the primary difficulties encountered in CALPHAD modeling pertains to the development of thermodynamic databases that accurately represent the materials' properties under varying conditions of composition, temperature, pressure, and configuration. The development of extensive thermodynamic databases comprising multiple components is a significant undertaking within the CALPHAD community. In fact, numerous companies have emerged, offering multicomponent thermodynamic databases as a primary component of their product offerings. Furthermore, with the continuous expansion of the materials data environment [242], there is an increasing demand and potential for the utilization of CALPHAD modeling in materials design.

1.11.2.2 Databases

This investigation employed the thermodynamic and mobility commercial databases, TCFE12 and MOBFE5, developed by Thermo-Calc Software AB for steel and Fe-base alloys [243]. The thermodynamic database contains a total of 30 elements. These elements have recommended composition limits that are sufficiently broad for most of the High Mn Fe-Mn-Al-C low density steel compositions. For instance, the recommended composition limits include up to up to 10 wt.% for Al, 7 wt.% for C,

30 wt.% for Mn, 5 wt.% for Si, 3 wt.% for Ti, or up to 5 wt.% for N. The mobility database encompasses a total of 27 elements, which consist, of the following phases of interest among others: BCC-A2, FCC-A1, FE4N-LP1, Cementite, HCP-A3, and Liquid. Furthermore, this database includes evaluated self-diffusion data for various elements, as well as evaluated data for several alloy systems, including Al-Fe, Fe-C, Fe-N, Fe-Mn-C, and Fe-Mn-Si among others in the BCC-A2 phase, Fe-Mn, Fe-N, Fe-C, Fe-Mn-C, and Fe-Mn-Si in FCC-A1 among others, as well as Fe-Mn in the liquid phase.

The CALPHAD-based calculations were performed using Thermo-Calc 2023a, DICTRA, and TC-Python software tools also developed by Thermo-Calc Software AB [243].

1.11.2.3 Scheil-Gulliver Models

The Scheil-Gulliver solidification theory [244, 245] models the solidification process in situations characterized by rapid solidification conditions. There exists empirical evidence supporting the validity of the assumptions made in these models within the context of AM applications. For example, it was observed that the solidification paths predicted by the Scheil-Gulliver theory and a diffusion simulation, which took into account the kinetic behavior of Inconel 625 in AM, exhibited a strong agreement [246]. The strong agreement observed between the Scheil-Gulliver model and the diffusion simulation suggests that the rapid cooling rates employed in the AM process can be

accurately approximated using the Scheil-Gulliver solidification theory.

The present model assumes that the solid-liquid interface is in a state of thermodynamic equilibrium. It further assumes that the diffusion of all elements in the liquid phase occurs at an infinitely rapid rate. Conversely, the diffusion of all elements in the solid phase is negligible, except for carbon (C) and nitrogen (N), which are classified as "fast diffusers" and are computed to diffuse infinitely fast even in the solid phase. Scheil-Gulliver model is implemented in Thermo-Calc software and simulations consider a gradual cooling from a temperature at which the alloy is liquid. The determination of the equilibrium quantity and composition of solid and liquid phases occurs when the temperature decreases below the liquidus temperature. The first calculated solid phase is eliminated from the system, and for the following calculation step at a lower temperature, only the quantity and composition of the liquid phase are utilized. The equilibrium quantity and composition of the solid and liquid phases are once again determined, and subsequently, the solid phase is withdrawn from the system for the next stage. The aforementioned procedure is repeated iteratively until the absence of any remaining liquid phase. The present model is representative of Kou's Case II solute redistribution of unidirectional solidification presented at Section 1.11.1.

The Thermo-Calc software also allows the implementation of a second Scheil-Gulliver

model that incorporates back diffusion in the primary solid phase. This model provides a more accurate representation of Kou's Case III scenario of solute redistribution. The present model integrates a kinetic term to account for the back diffusion of all components within the primary solid phase, specifically the FCC or BCC phase in the context of steel. This is achieved by utilizing thermodynamic and mobility databases. In addition to the computation, it is essential to specify the cooling rate. Rapid cooling rates limit the time available for back diffusion, resulting in outcomes similar to the original Scheil-Gulliver method. Conversely, an extremely low cooling rate allows for nearly complete back diffusion, leading to solidification calculations that are comparable to equilibrium. Furthermore, besides the cooling rate, it is necessary to define the effective size of the solidification domain (Figure 1.9). The size of the domain dendrites, known as the secondary dendrite arm spacing (SDAS), is frequently associated with the cooling rate [247, 248]. This is because the SDAS represents the region where liquid is commonly trapped during the solidification process, and consequently, it is linked to micro-segregation [249, 250]. The correlation between the SDAS and the cooling rate is commonly expressed by equation 1.5, wherein λ_2 represents the SDAS measured in micrometers (μm), $\dot{T}$ denotes the cooling rate measured in Kelvin per second (K/s), and the constants a and b are specific to the material.

$$\lambda_2 = a \cdot \dot{T}^{-b} \tag{1.5}$$

The assumptions for this back diffusion model are the following: (1) The diffusion of all elements within the liquid phase is characterized by an exceptionally high rate of movement, (2) the diffusion of individual elements within the primary solid phase is determined by analyzing kinetic data, cooling rate, and domain size, (3) the diffusion of elements classified as "fast diffusers" (C and N) exhibits an endless rapid movement within the solid phase, extending beyond the primary phase to encompass all phases, and (4) the interface between the solid and liquid phases is in a state of thermodynamic equilibrium.

The integration of non-equilibrium solidification models with the CALPHAD method enables prediction of materials behavior under rapid cooling conditions, such as those found in laser-based AM processes. This approach facilitates the identification of segregation patterns at the scale of solidification structures, determination of the specific solidification pathway, and characterization of the resulting phases.

1.12 Aim of this research

The primary goal of this project is to develop new High Mn steel grades that are suitable for metal AM and meet the existing and future material demand and requirements of the major industrial sectors mentioned in section 1.3. Five specific objectives were defined in order to accomplish the general objective:

1. To select High Mn steels that are suitable for AM from theoretical perspective.

2. To produce the steel powders and validate their processability in L-PBF.
3. To evaluate the static properties of the steels designed in the context of current market gaps, and propose and validate complementary alternatives.
4. To evaluate the steel processability in another AM technology, such as powder-DED.
5. To assess the material's performance in a use case.

In order to achieve these specific objectives, a set of tasks has been identified and will be addressed in this thesis.

1. To select a set of compositions for the novel steel family based in thermodynamic calculations.
2. The production of steel powders for AM processing and evaluation and validation of powder quality.
3. To ensure quality of the 3D printed parts by developing the AM process window for each of the selected steel compositions.
4. To analyze the microstructure of the 3D printed steel and mechanical properties in the as built state.
5. To investigate the influence and the potential effects that different heat treatments could have on the microstructure and mechanical properties of the steels under study.
6. To examine the performance of the steels on a NNS printed sample, simulating

a possible end-use application.

Chapter 2

Materials and Methods

In this chapter, an overview of the employed materials, equipment, experimental techniques, and methodology is provided. In order to achieve the development of new High Mn Fe-Mn-Al-C low density steels suitable for AM, the specifications of different steel powders, as well as the processing and testing equipment, are first discussed. The experimental procedure is then described in detail.

2.1 Materials production

This section outlines the production process of steels in AM, beginning with the production of powder as the feedstock material for L-PBF and DED. Subsequently, the equipment used in both AM methodologies is described.

2.1.1 Powder production: Atomization

Spherical metallic powder is produced by the gas atomization technique, utilizing the AUG 3000 equipment manufactured by Blue Power shown in Figure 2.1. During the gas atomization process, the metal feedstock, which is composed of different ferroalloys that are adjusted to achieve the nominal composition once mixed, is subjected to an Ar inert atmosphere and inductively heated to temperatures ranging from 150 to 300 °C above the steel liquidus temperature inside an alumina crucible. This temperature is maintained for a period of 60 minutes. Upon complete melting of the composition, a stopper rod is opened to facilitate the liquid steel to flow in a laminar manner. This flow is subsequently impacted by the injection of gas through a nozzle at a pressure of 20 bar, resulting in the formation of fine liquid droplets that solidify rapidly to produce the metallic powder. The atomizing gas used was nitrogen that can be preheated up to a temperature of 300 °C. The resultant powder exhibits a particle size distribution that is predominantly below 250 microns. The tower collector recovers the coarser powder, while the cyclone collector recovers the finer powder, which is carried along by the gas flow.

Figure 2.1: AUG 3000 atomization unit used in this research.

2.1.2 Processing of powders by Laser-Powder Bed Fusion

A Trumpf TruPrint 1000 machine shown in Figure 2.2, was used to study the austenitic Fe-Mn-Al-C low density steels in L-PBF technology. The machine is equipped with an continuous fibre laser with a maximum power of 200 W and a laser spot diameter of 55 μm.

The printing jobs were executed on a baseplate made of 316L material, with a diameter of 100 mm. The overall print capacity of the equipment is equivalent to the product of the baseplate's surface area and a vertical distance of 100 millimeters. A design of experiments (DoE) was conducted to determine the optimal printing parameters for austenitic Fe-Mn-Al-C low density steels. The DoE included modifications of the laser power, laser speed, and hatch distance to investigate the most favorable

process conditions. Table 2.1 presents the printing ranges that were studied. Furthermore, a consistent printing approach was maintained by utilizing a meander strategy with a 90° alteration in orientation for each layer.

Figure 2.2: TruPrint 1000 L-PBF machine used in this research.

Table 2.1
Range of studied printing parameters in TruPrint 1000.

Process parameter	Range
Laser power	150 - 200 W
Laser speed	300 - 1100 mm/s
Hatch distance	0.07 - 0.11 mm
Layer thickness	0.02 mm
Printing atmosphere	N_2

2.1.3 Processing of powders by Directed Energy Deposition

The Trumpf D70 focusing laser head system, equipped with a Trumpf TruDisk 4002 disk laser boasting a maximum power of 4000 W and a wavelength of 1030 nm, was utilized to produce DED steel samples. The laser head was mounted on a KR 210 R3100 ultra KUKA robot, which facilitated its movement in a Cartesian space system (x, y, z). The effective workspace of the system is comparable to a cylinder with a diameter of approximately ⌀4 m and a height of 4 m.

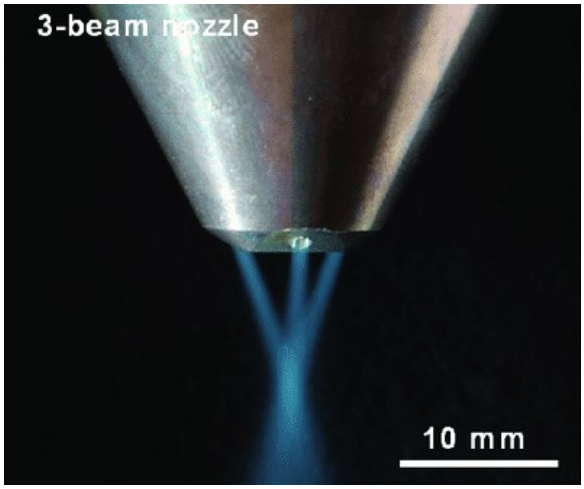

Figure 2.3: Powder gas jets of the three beam nozzle in powder-DED.

The Medicoat powder hopper is utilized to supply powder, which is then transported by Ar carrier gas and subsequently introduced into the melt pool through a SO12 3-beam nozzle. Figure 2.3 [251] shows the operational powder jet of this type of nozzle in powder-DED.

In addition, the laser beam undergoes collimation through the application of focal collimating lenses, which possess the capability to adjust the spot size from a diameter of ⌀0.8 mm at the focal point, with a Top-Hat laser intensity distribution, to an unfocused diameter of ⌀4 mm, characterized by a Gaussian laser intensity distribution shape. In addition, Ar gas is introduced into the molten pool as shielding gas to prevent oxidation during the printing process. Figure 2.4 shows an image of the DED equipment.

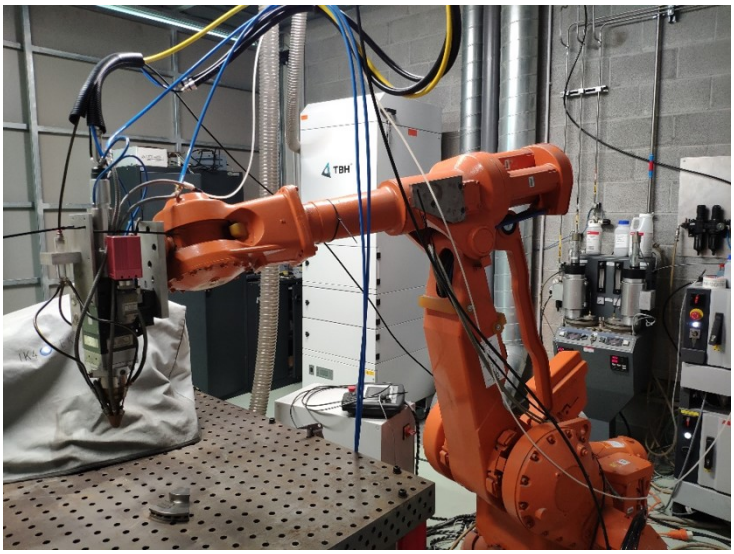

Figure 2.4: DED equipment used in this research.

The process parameters were developed using a similar DoE approach as in L-PBF, with modifications made to the printing parameters outlined in the Table 2.2.

Table 2.2
Range of studied printing parameters in DED system.

Process parameter	Range
Laser power	700 - 1600 W
Laser speed	20 - 30 mm/s
Laser spot	2 mm
z - displacement	0.6 - 1.2 mm
Shielding gas	Ar
Shielding gas flow	10 l/min
Carrier gas	Ar
Carrier gas flow	4 l/min
Powder feed rate	9 - 20 g/min
Laser beam shape	Gaussian
Working Distance	16 mm
Dwell time between layers	30 s
Baseplate material	316L
Printing strategy	zig-zag

2.2 Methods

This section describes the experimental techniques employed to characterize the gas atomized powders and additive manufactured parts of High Mn Fe-Mn-Al-C low density steels. The software, databases and models used for CALPHAD calculations are as well described.

2.2.1 Chemical analyses

The powders' chemical composition was determined through various analytical techniques. C and S were analyzed using the combustion method with a LECO CS744 instrument, and O and N were analyzed using the inert gas fusion technique with a

LECO ON736 instrument, following the standard ASTM 1019. The remaining elements were analyzed using inductively coupled plasma optical emission spectroscopy (ICP-OES), following the standard ISO 11885:2007. The gravimetric method outlined in the ISO 439:2020 is employed to measure the silicon content when it surpasses 0.8–1 wt.%.

2.2.2 Classification and measurement of powder particles based on size

The powders were classified into three fractions based on their particle size utilizing a commercially available CFS 5/HD-S Plus Netzsch air classifier. In this equipment, powder from the atomizer is dispersed by clean gas, inside a classifier wheel. This classifier wheel is optimized to produce fine particle size cut with high yield. Three different powder fractions were classified with these cuts: Fraction 1 (F1) for the powder particles collected that have a size below 20 μm. Fraction 2 (F2) for the powder particles collected that have a size ranging from 20 to 60 μm. Lastly, fraction 3 (F3) is representative of powder particles that have between 60 and 150 μm. Powder fraction F2 is used for L-PBF technology, and powder fraction F3 for powder-DED. The particle size distribution (PSD) of the various powder fractions was assessed using laser diffraction with the Malvern Mastersizer 3000 instrument, following the ASTM B822 standard.

2.2.3 Density measurements in printed material

The density of printed cubes was determined using Archimedes' method, employing an AMTAST FA2104J digital density balance in accordance with the ASTM B311-22 standard. Three independent measurements were done for each cube, and averaged.

2.2.4 Microscopy

This section will provide an overview of the various microscopy techniques employed and the required preparation methods utilized for the characterization of both powders and printed samples.

2.2.4.1 Metallographic observations in powders

The microstructure of powders was analyzed by field emission gun – scanning electron microscopy (FEG-SEM). This examination was conducted using a ZEISS Ultra Plus equipment or, alternatively, an FEI Verios 460L SEM at the University of Connecticut. The latter is an ultra-high resolution Schottky emitter SEM, capable of capturing images with ultra-high resolution at low energy even on insulating samples without the need for a conductive coating. In order to achieve this objective,

powders were prepared by mounting, grinding, and polishing using established metallographic techniques. In an alternative approach, the incorporation of powders into nickel electro-deposits was carried out, following the methodology proposed by Field and Fraser [252]. Subsequently, twin-jet electropolishing was employed to expose and examine the internal microstructure of the samples. A comprehensive examination was conducted using scanning transmission electron microscopy (STEM) on an FEI Talos F200X microscope that was outfitted with a Super-X silicon drift detector (SDD) energy-dispersive X-ray spectrometry (EDXS) system at the University of Connecticut. The specimens utilized in STEM studies were prepared using the focused ion beam (FIB) lift-out technique within the FEI Helios Nanolab 460F1 dual beam FIB-SEM instrument.

2.2.4.2 Metallographic observations in printed material

Printed cubes were selected according to their relative density for further metallographic characterization. Samples were cut parallel to the building direction at the mid-section of the cubes using the Buehler IsoMet High Speed precision saw. Then one half of the cube was embedded in conductive PhenoCure resin, ground and polished following standard processes as per ASTM E3-11(2017). Macro- and micrographs of the samples were acquired by light optical microscopy (LOM) using a ZEISS AxioVert A1 MAT to evaluate the presence of internal defects such as pores and cracks.

The internal microstructure of the builds was examined by SEM and high-angle-annular-dark-field scanning transmission electron microscopy (HAADF-STEM) on thin foil samples cut parallel to the build direction and then twin-jet electropolished to perforation. The STEM analyses were performed on the electron-transparent regions around the perforations, whereas SEM was performed on the smooth areas of the foils away from the holes. This approach was adopted because such samples were free of mechanical damage and gave high-quality images and EBSD data. For the builds, backscattered electron (BSE) images were acquired, rather than SE images, to better reveal the grain structure.

Further examination was conducted using atom probe tomography (APT[1]) on an LEAP 5000 XR atom probe that was equipped with the IVAS software offered by CAMECA for the data analysis at Ghent University. The specimens utilized in APT studies were prepared using the FIB lift-out technique within the FEI Scios 2 dual beam FIB-SEM instrument from ThermoFisher Scientific.

[1]APT is a highly advanced method used for analyzing materials. It provides a wide range of capabilities for imaging in three dimensions and measuring the chemical composition at the atomic level. The technology offers exceptional resolution, with depths being resolved at approximately 0.1-0.3 nm and lateral measures at 0.3-0.5 nm. The specimen is constructed in the shape of an extremely pointed apex. The cooled tip is subjected to a high direct current voltage ranging from 3 to 15 kV. The tip's extremely small radius and the application of high voltage result in the generation of a significantly elevated electrostatic field (tens V/nm) at the surface of the tip, situated immediately below the atom evaporation point. When subjected to laser or high-voltage pulsing, the surface experiences atom evaporation through field effect, resulting in near-complete ionization. These ionized atoms are then directed towards a position-sensitive-detector with exceptionally high detection efficiency. The detector enables the simultaneous measurement of: The measurement of the time-of-flight (TOF) of ions involves determining the duration between the initiation of a laser or voltage pulse and the subsequent arrival of the ions on the position-sensitive-detector. This TOF measurement enables the determination of the mass-to-charge ratio of the ions. 2) The determination of the (x,y) coordinates of the ion's impact on the detector is achieved by monitoring both the x-y position and the sequential arrival of ions on the position-sensitive detector. This enables the reconstruction of the initial position of the atoms on the tip.

2.2.5 Diffraction analyses

The following section provides a description of the different diffraction-based characterization methods employed in both powder and printed components.

2.2.5.1 Electron Backscatter Diffraction

Electron Backscatter Diffraction (EBSD) maps were obtained from electropolished samples using an EDAX TEAM EBSD system installed on the Verios 460L SEM for the powder material, at the University of Connecticut and an AztecHKL EBSD system installed on the AURIGA SEM for the printed component at Universitat Politècnica de València.

2.2.5.2 X-Ray Diffraction

The phase constitution of powder and printed cubes was determined by X-Ray diffraction (XRD) using a Bruker D2 Phaser diffractometer equipped with Cu-Kα radiation using a time step of 6 s, a step size of 0.04° and within the 20 – 141.5° 2θ angle range. Diffrac.EVA 4.3 software from Bruker was used to identify the diffracted phases and the Rietveld refinement analysis was performed by TOPAS V6.0 software to determine the phase fractions by Hill and Howard relationship [253]. The reference phases information was obtained from Crystallographic Open Database (COD) with

identification (ID) COD1525442 (austenite), COD7204904 (ferrite), COD9015794 (DO3), COD1539509 (Ti-carbonitride) and from the Materials Project database version v2022.10.28 with the ID mp-22793(κ-carbide), and mp-1330(Al-nitride).

2.2.6 Mechanical testing

This section defines the mechanical testing instruments employed for evaluation of the mechanical properties of printed components.

2.2.6.1 Hardness

The hardness measurements were conducted using the Wilson VH1150 instrument, in accordance with the ASTM-E9217 standard. A minimum of five measurements were taken on the sample in order to determine the average Vickers hardness value.

2.2.6.2 Tensile

Tensile tests were carried out using an Instron-5882 machine equipped with a video extensometer INSTRON 2114 and capable of applying a maximum load of 100 kN. The tests were conducted in accordance with the ASTM-E8/E8M standard, where the deformation velocities applied are 0.6 mm/min until 1% of deformation, and 9 mm/min beyond that.

The specimens were printed in the vertical direction with the longitudinal dimensional parallel to the 3D-printing building direction. The dimensions of the specimens considered the ASTM-E8/E8M rectangular subsize geometry are represented in Figure 2.5, where overall length (L) was 100 mm, thickness (T) was 6 mm, width (W) was 6 mm and the gauge length (G) was 25 mm.

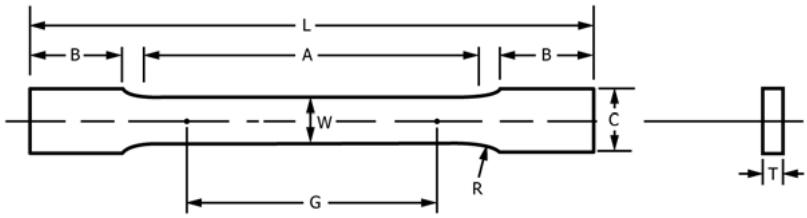

Figure 2.5: Dimensions of rectangular subsize tensile specimens as defined by the ASTM E8/E8M standard.

2.2.6.3 Compression

Compression tests were conducted in the lattice strcutures using a 250 kN universal dynamic testing machine, equipped with compression platens. The experiments were conducted under controlled conditions, with displacement being the independent variable and a constant speed of 5 mm/min being applied. Compression platens were attached to the machine, as seen in Figure 2.6.

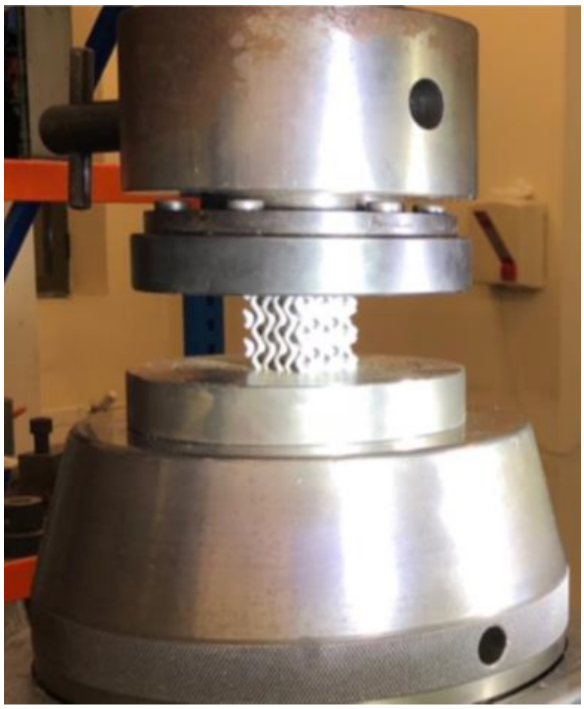

Figure 2.6: Compression test set-up for lattice structures.

The elastic response of the lattices under compression was analyzed by comparing the the maximum absorbed energy in the elastic domain, and the maximum elastic stress and strain of each lattice. In addition, the energy absorption before material densification was studied with the purpose of comparing the maximum level of ductility of the material and the failure pattern in each tested lattice geometry.

Furthermore, real-time monitoring was conducted in selected cases to observe the deformations occurring on one of the faces of the specimen while applying the test load. The video image correlation system is capable to generate a mesh on the specimens and ascertain real-time measurements of deformations at various points on the specimen. These recordings were made to capture the deformations in relation to

the applied load. Figure 2.7 depicts the configuration of the image correlation video system, along with a snapshot of the data collecting process captured by the program during the AM lattice compression test.

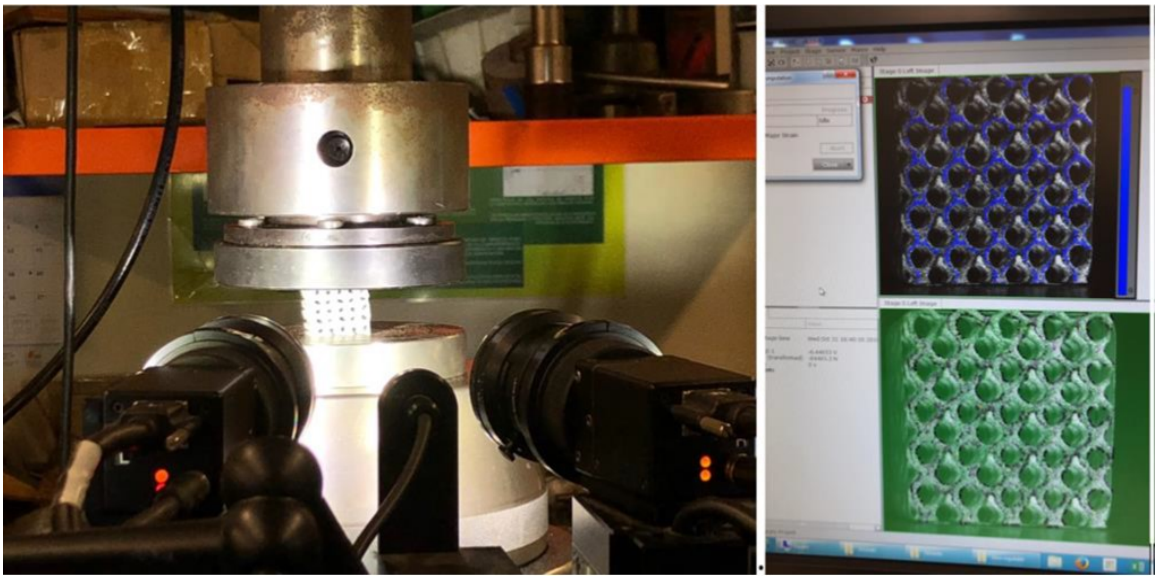

Figure 2.7: Video-correlation set-up during compression test.

In order to complete the results of the tests, conventional video recordings were as well conducted when image video-correlation was not done. The purpose of these recordings was to capture the mechanical response throughout the testing process.

2.2.6.4 Impact Toughness

Impact toughness tests were performed utilizing an IBERTEST PIB-30-MDA Charpy pendulum with a maximum load capacity of 300 J, following the ASTM-E23 standard. Measurements were performed by producing Charpy samples in L-PBF in accordance

with the ASTM E23 standard. The specimens were printed with a V-notch positioned at the midpoint of their height. The dimensions of the specimens were a cross-sectional area of 10 x 10 mm^2 and a height of 55 mm.

2.3 Methodology

Initially, steel compositions were designed based on thermodynamic calculations, and then steel powder of selected compositions were fabricated by gas atomization. These atomized powders require characterization in relation to quality for AM processes. This includes the evaluation of powder particle density and morphology through the use of LOM and SEM microscopy. Furthermore, the examination of powder microstructure is conducted through the utilization of advanced microscopy and diffraction techniques, with the aim of understanding the microstructure evolution of the material under fast solidification.

The powders were used as raw material in the L-PBF and DED technologies. Then, to define the process window of each steel for each technology, a DoE was employed that encompassed the parameters specified in Table 2.1 (for L-PBF) and Table 2.2 (for DED). Appendix A details the parameters used to define the process window in L-PBF for all developed High Mn Fe-Mn-Al-C low density steels. These parameters serve to define a processable process window, with some adequate set of printing parameters for steels. The specimens utilized to determine the process window in AM

of the steel materials under investigation consisted of cubic shapes measuring 1 cm x 1 cm x 1 cm in L-PBF, and parallelepiped shapes measuring approximately 5 cm x 0.2 cm x 1-2 cm in DED. An example of a CAD file is shown in Figure 2.8.

After the samples were printed, they were visually inspected to identify the presence of surface defects or cracks. Subsequent density measurements were conducted using Archimedes' method in order to evaluate the relative density of various samples and anticipate the potential existence of internal defects or cracks. Later, destructive analyses were conducted in the densest cubes for further characterization. These analyses included the assessment of cross-section density using LOM, measurements of hardness, and determination of interstitial content (specifically, C, O, and N), to examine the potential occurrence of decarburization during printing or oxidation. The purpose of this characterization process is to identify an optimal set of printing parameters. These parameters will then be used to further analyze the material's microstructure and mechanical properties. The aim is to establish the relationship between the material chemistry, the printing process, microstructure and its resulting properties.

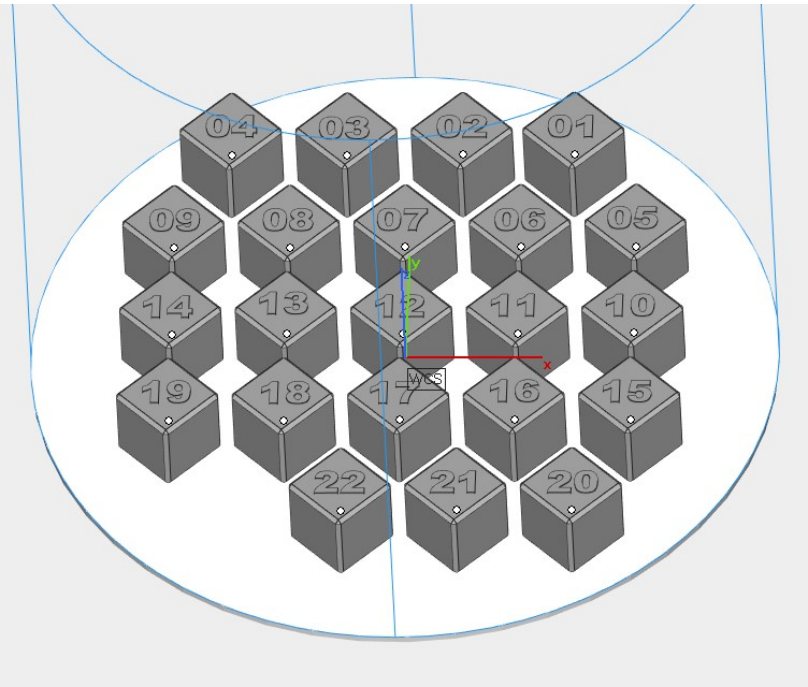

Figure 2.8: DoE CAD in TruPrint 1000.

Chapter 3

Alloy design to prevent hot cracking

Hot cracking (HC) is a persistent problem in metallurgical manufacturing for certain steels grades, and it occurs in practically all production processes involving solidification, including casting, welding, and additive manufacturing [254, 255, 256, 257]. In welding, HC refers to the appearance of shrinkage cracks during the solidification of weld metal but may also refer to both solidification cracking (SC) and liquation cracking (LC) caused by successive welds or in the heat affected zone (HAZ). SC refers to cracking developed in the weld metal and can occur in a wide range of areas and directions, but the most common types are longitudinal collinear cracks from the intersection of grain growth with opposite sides of the melt, and "flare" cracks, which are also longitudinal, but tilted to the thickness direction. LC stands when cracking occurs in the high-temperature zone of the HAZ or in previously deposited weld metal

during a subsequent run. LC may occur in a number of sites and orientations, but it is most prevalent at the fusion zone of a weld between the confluence of grains (related to segregation). Both types of HC happen when the available supply of liquid weld metal is insufficient to cover the voids between solidifying weld metal created by shrinkage stresses, obstruction of liquid or narrow channels between solidifying grains [258, 259]. Several HC theories have sought to explain the causes of this phenomena; these ideas have their roots in casting and have evolved in close accordance with the physical reality of the welding process [260]. One of the most comprehensive theories is the "Borland or Generalized theory" [261], which was established in 1960 and divides solidification into four stages: Initial phase of solidification in which dendrites are widely spread and surrounded by significant quantities of liquid. A second phase during which solidification cracks heal. A third stage designated as the critical temperature range or critical solidification range. During this phase of dendrite growth, interdendritic networks become isolated, fracture healing is no longer viable, and HC occurs. And the four stage is the end of solidification. Later, this theory was extended by dividing stage three into two: 3H, in which solidification is susceptible to cracking due to the presence of thin liquid films along the grain boundaries; and 3L, in which solidification is not susceptible to crack initiation, but is vulnerable to crack propagation due to the presence of liquid droplets along the grain boundaries. HC may be regulated in welding by modifying the bead pattern, managing the strain on the solidification pattern, and adjusting the material composition, as the composition

determines the theoretical solidification range of the weld metal and the other parameters to the kinetics. Invariably, different weld metals have a variety of solidification temperatures. Low melting point elements may be rejected by solidifying dendrites, resulting in a thin layer of liquid that persists at low temperatures and is thus located at a considerable distance from the main pool of liquid metal. This film cannot bear the contraction strain, and a fracture forms if it cannot be supplied effectively from the weld pool [258]. Several criteria have been devised to evaluate, based on the chemistry of a steel grade, its susceptibility to HC [262, 263, 264]. In addition, Kujanpaa et al. correlated the content of delta ferrite with the total crack length in austenitic and austenitic/ferritic stainless steels, proposing a Cr/Ni ratio between 1.48 and 1.95 and an optimal delta ferrite content between 5 - 20% in the austenitic weld matrix to prevent HC [265]. These strategies could be employed in additive manufacturing: the printing approach can control the solidification processes by, for example, altering the cooling rate by preheating the substrate, while the material composition approach can control the solidification range and phases formed using the CALPHAD method [266, 267].

This research is focused on the second approach for the development of a steel grade that exhibits resistance to HC in L-PBF, regardless of the prevailing printing conditions. This development involved a CALPHAD-based alloy design of raw materials, followed by powder production and L-PBF printing trials. HC tendencies were evaluated in L-PBF samples, while the solidification microstructure and microsegregation

were evaluated in the metal powder, rather than the L-PBF samples. The reasons for using the steel powder instead of the L-PBF sample lie in the fact that the microstructure of L-PBF samples is influenced by the IHT caused by the adjacent printed tracks and layers, which in turn modifies the initial solidification microstructure. In contrast, the steel powder particles retain their initial solidification microstructure, and although the solidification mechanism of the metal droplets differs from that of welded tracks, it can serve as a useful approximation for assessing microstructural differences during solidification, which may clarify the presence or absence of HC in L-PBF.

3.1 CALPHAD-based alloy design

Thermodynamic calculations were carried out using the TC-Python module of the Thermo-Calc 2023a software with the TCFE12 and MOBFE5 commercial thermodynamic and kinetic databases for steels. The system size was defined as 1 mole, and simulations were performed at 10^5 Pa standard-state pressure (1 bar). Calculations yield information on solidification paths, phase formation temperatures, phase fractions, phase compositions, and segregation of alloying elements. The Scheil-Gulliver model described in Section 1.11.2.3 was implemented to predict the solidification paths as well as phase constitution of the alloys. C and N were defined as "fast diffusers" in the model, so that the diffusion of these elements is considered to be

infinitely fast in the solid phase. This is a reasonable approach for ultra-fast solidification rates of powder atomization and L-PBF, and it was used to predict the hot cracking susceptibility (HCS) susceptibility of FeMnAlC steels.

Scheil-Gulliver solidification with solute back diffusion simulations were additionally employed to predict the HCS of High Mn Fe-Mn-Al-C low density steels under this condition. The four HCS criteria adopted in this investigation are explained below.

1. **The solidification interval (ΔT):** It is defined as the temperature range between 0.01 and 0.99 fraction of solid during solidification.
2. **The Crack Susceptibility Coefficient (CSC):** The CSC model is based on the idea that there are key time periods during solidification when the structure is most susceptible to cracking. It was first introduced by Clyne and Davies [268] in order to describe the impact of alloy composition on hot tearing. Later, Yan and Lin [269] compiled from various sources experimental observations of HC, and redefined a new experimental CSC, defined as the ratio between the cracking length for that alloy and the maximum cracking length in the alloy system studied, to express a probability to occur. The CSC used in this study refers to the original criteria defined by Clyne and Davis in Equation 3.1.

$$CSC = \frac{t_V}{t_R} \tag{3.1}$$

where t_V is the vulnerable time period during solidification, when the material

is susceptible to cracking, and t_R is the time relaxation period when stress relief processes take place.

Following Clyne and Davies' method, cooling rates were evaluated under three distinct thermal conditions: mode 1 with a constant cooling rate, $\frac{\delta T}{\delta t}$ is constant; mode 2 with a constant heat flow, $\frac{\delta Q}{\delta t}$ is constant; and mode 3 with a heat flow proportional to the square root of time, $\frac{\delta Q}{\delta t} \propto t^{-1/2}$.

Clyne and Davies [268] came to the conclusion that mass and liquid feeding happens easily at liquid volume fractions between 0.6 and 0.1, hence the time spent in these ranges was classified as time relaxation (time available for the stress relief process). At extremely low liquid volume fractions, the material is too susceptible to fracture. The authors selected a liquid fraction between 0.1 and 0.01 as the vulnerable regime and defined the time spent as the time during solidification when the casting is susceptible to fracture.

3. **The Brittle Temperature Range (BTR):** In welding, the BTR range is defined at the end of the solidification, where HC can take place [270]. Regarding some of the HC theories such as the "Shrinkage-brittleness" or the "Technological strength", strain growth occurs in the solidifying weld pool due to thermal contraction inside the material and the contribution of any additional external stress. HC will occur if strain exceeds a critical level (inside a solidifying weld pool within the BTR). The less deep and wide the BTR, the higher HC resistance [260]. The BTR will be assumed to be defined in the same way as

t_V.

4. **Hot Cracking Coefficient (HCC):** The HCC criterion considers the solidification interval ΔT, and the CSC at the same time by combining them. It is defined as:

$$HCC = \Delta T \cdot CSC \tag{3.2}$$

3.1.1 Selection of the base steel system

The HCS models were computed using the base composition that was chosen according to the guidelines provided by I. Kalashnikov et al. [172]. This selection aimed to prevent the formation of $\beta-$Mn and $\kappa-$carbides in FeMnAlC systems with High Mn content, thereby minimizing the risk of brittle failure. Additionally, isotherm calculations were performed to maximize the stability of the FCC phase as a function of temperature. The composition of the base material chosen is Fe-28Mn-7Al-0.8C (wt.%) and the impact of P and Si on HC of this steel was studied in L-PBF, using computational calculations accompanied by experimental validation. Both P and Si are commonly encountered in raw materials used in steelmaking. P is known to be a detrimental element for HC in Mn steels and often comes with Mn-containing raw materials as an impurity [271, 272]. However, Si is found to be sometimes beneficial and sometimes detrimental to avoid HC [262, 264, 272], and it must be synergistically considered with the rest of alloying elements. It should be noted that the gain of N during the atomization process was estimated to be 0.02 wt.%, and this value was

taken into account in the calculations as part of the base material composition.

The P content was varied from 0 to 0.2 wt.% in increments of 0.01 wt.% and the Si content from 0 to 4 wt.% in increments of 0.2 wt.%. For this mapping, the Scheil-Gulliver model, and the Scheil-Gulliver model with solute back diffusion in the primary phase were used for comparison. These models were described in Section 1.11.2.3 and are representative of Modes II and III of solution redistribution during solidification (Section 1.11.1.1), and reasonable approaches for the rapid cooling rates of L-PBF, where solid diffusion is limited and solidification lays closer to Scheil than to equilibrium [273].

3.2 Calculation of hot cracking susceptibility

The solidification interval and the relaxation and vulnerability times that are used for the CSC, HCC and BTR criteria are determined from the Scheil-Gulliver solidification calculations. The calculation process is exemplified in Figure 3.1 for the three thermal modes using the base Fe-28Mn-7Al-0.8C-0.02N (wt.%), where the relaxation time t_R represents the time between the formation of 0.4 and 0.9 mole fraction of solid and the vulnerability time t_V is the time between the 0.9 and 0.99 mole of the solid fraction. The solidification range is defined between 0.01 and 0.99 solid mole fraction. Data trimming below and above this range helps to eliminate both the influence of high solidification start temperatures due to the formation of minor primary phases

or precipitates (AlN in the present case), and the impact of low solidification end temperatures due to convergence issues at the end of the calculation.

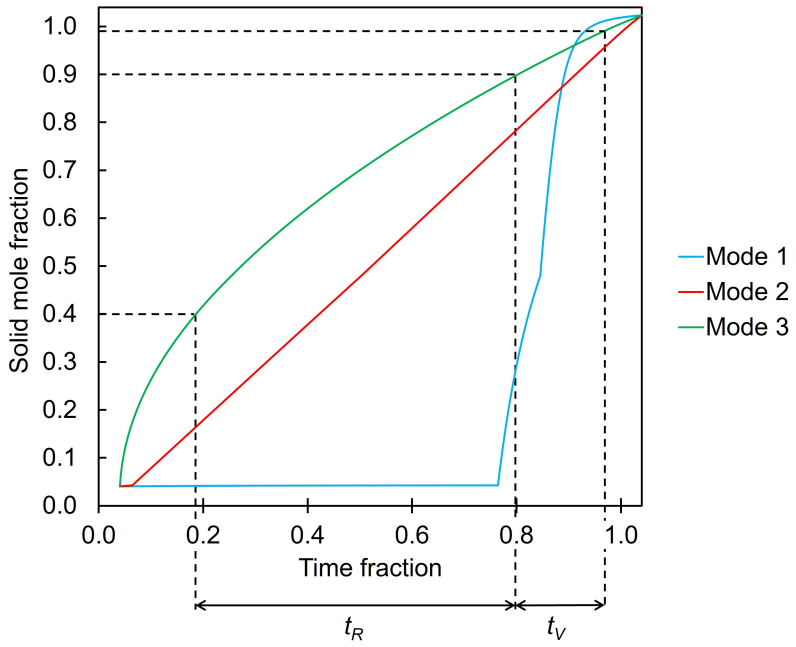

Figure 3.1: Example of the determination process for the relaxation and vulnerability times from the Scheil-Gulliver calculation for the three different thermal conditions.

Figure 3.2 shows heat maps considering the three different HCS criteria (CSC, HCC, BTR) calculated from Scheil-Gulliver solidifications for each of the thermal modes for the Fe-28Mn-7Al-0.8C-0.02N composition having Si contents up to 4.0 wt.% and P contents up to 0.20 wt.%. Figure 3.2a corresponds to the CSC criteria, Figure 3.2b to the HCC criteria and the Figure 3.2c to the BTR criteria. From left to right, HCS maps are shown for calculations according to the thermal mode 1, thermal mode 2 and thermal mode 3 for the three criteria presented.

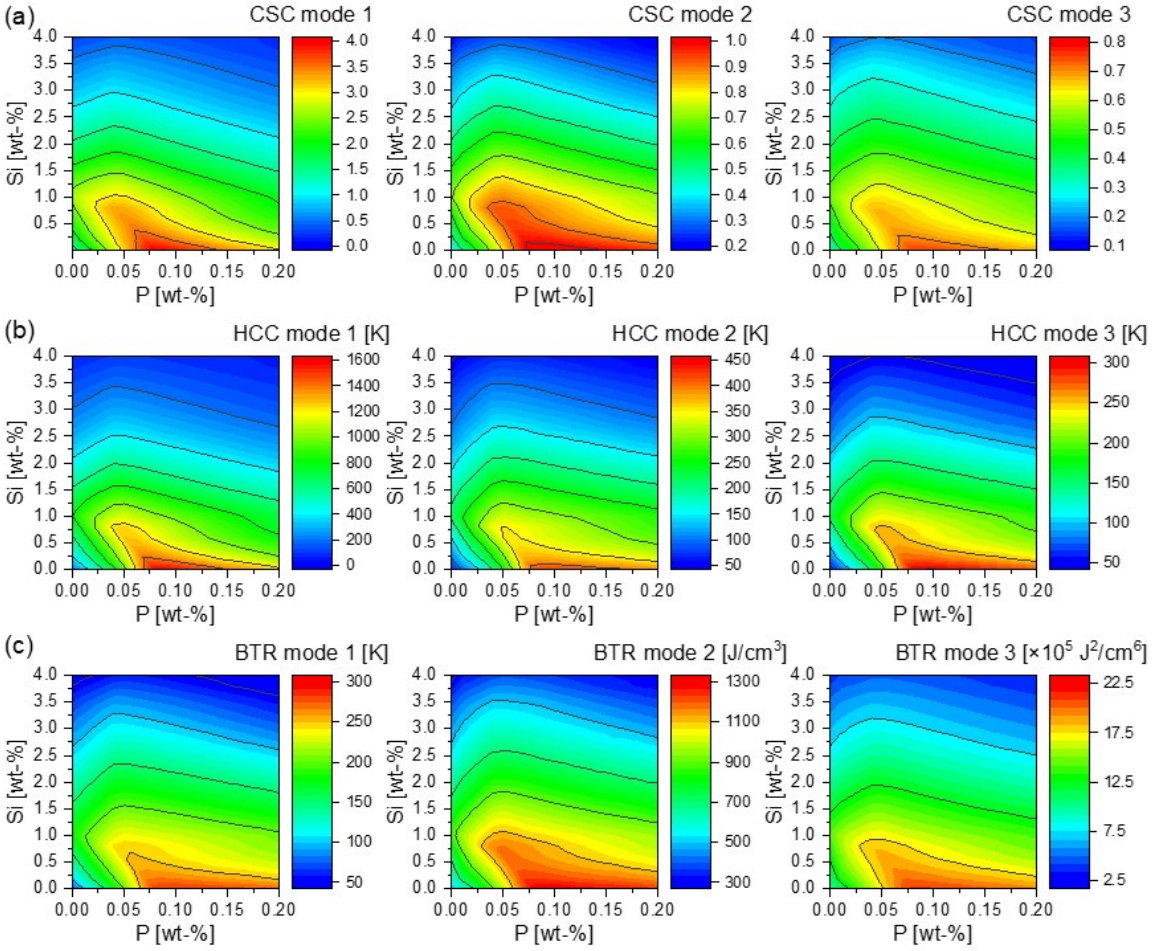

Figure 3.2: Calculated heat maps of HCS criteria for the High Mn low density reference steel composition Fe-28Mn-7Al-0.8C-0.2N varying the content of P from 0 to 0.2 and Si from 0 to 4 wt.% using the Scheil-Gulliver solidification model. Calculations were done according to the (a) CSC criterion, (b) HCC criterion and (c) BTR criterion under thermal mode 1 (left), mode 2 (center) and mode 3 (right).

Each of the three thermal modes and the three HCS criteria (CSC, HCC and BTR) yield similar results, where phosphorous values above 0.04 wt.% lead to a strong increase in the HCS meaning a high risk of HC during solidification, while silicon shows a bell curve, where low silicon values offer low HCS, then the HCS increases reaching itS maximum around 1 wt.% of Si and decreases again for higher silicon contents. This increase of the HCS at initial increments of Si could be explained by the

reported solidification problems of fully austenitic SS grades, where fully austenitic microstructures may generate large liquid films at the austenite-austenite solidification boundaries, that are enlarged in presence of Si, resulting in an easy activation of intergranular solidification cracking [265, 274]. This may be worsened by the presence of solutes with low melting point such as S or P, which segregate during solidification and intensify the HCS [275]. Nonetheless, when Si content increases, more ferrite is formed and a reasonable quantity of delta ferrite evenly distributed in the austenitic matrix is favorable for avoiding HC [265, 276]. This is because ferrite can dissolve more P and S that austenite, so they are retained in the solute rather than being available to form liquid films along the grain boundaries. The presence of even a small fraction of ferrite rises the grain boundary area, so that any liquid film that forms spreads over a larger region and cannot form a continuous liquid film [277]. The minimum content of Si to prevent HC by forming ferrite in austenitic steels varies between compositions [278]. For the second and third thermal modes, the effect of Si and P on the CSC and HCC criteria are comparable, as both are defined based on the heat flow, although mode 3 is less restrictive than mode 2, indicating a lower likelihood of HC but still with the same tendency. Nonetheless, each criterion and thermal mode indicates a safer HC region with a high P content (> 0.06 wt.%) when the Si content is raised beyond 2.0 - 2.5 wt.%. Nevertheless, high contents of Si aimed at avoiding HC can lead to the formation of brittle phases that promote cold cracking in the material.

These HCS findings were then validated using the Scheil-Gulliver with Back Diffusion solidification model, indicating that the Scheil-Gulliver solidification model is an acceptable approximation for instances involving fast cooling rates. For this model, the SDAS was measured in 1 µm in cross sections of powders of sizes between 20-60 μm used for L-PBF, and the cooling rate was calculated in 5000 K/s from Equation 1.5, where the specific material's constants a and b were estimated in 43.7 and 0.44 respectively, based on the the austenitic steel composition Fe-10Mn-15Ni-0.62C constants provided by O Volkova et al. [279].

Six compositions were selected to conduct the printing experiments based on the HCS calculations shown in Figures 3.2 and 3.3. The compositions are coded as FeMnAlC-(HP)-(xSi), where the suffix -HP is used when the P content is above 0.01 wt.% and the suffix -xSi is used to indicate the amount of Si targeted when the amount is above 0.25 wt.%. These are: FeMnAlC, FeMnAlC-HP, FeMnAlC-HP-2Si, FeMnAlC-1Si, FeMnAlC-2Si and FeMnAlC-4Si.

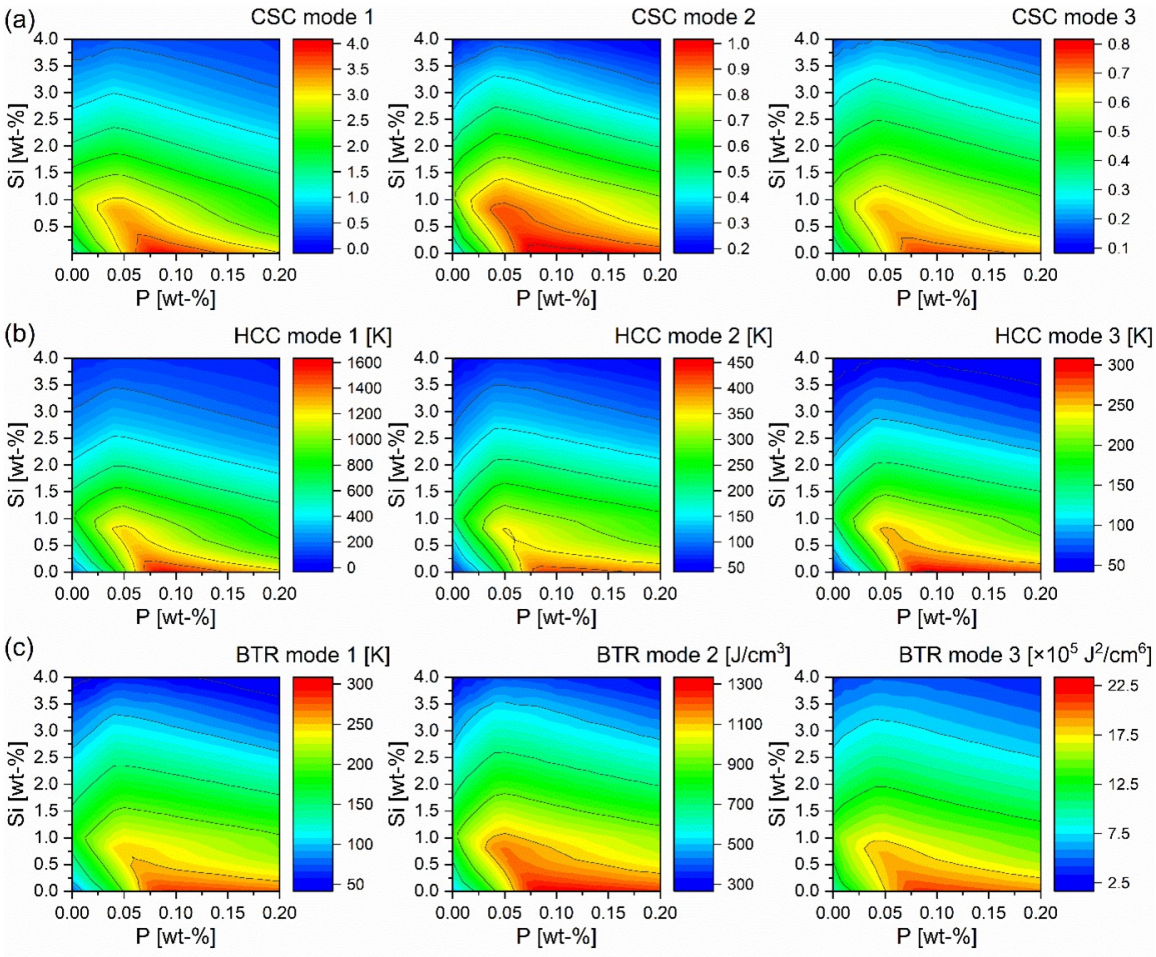

Figure 3.3: Calculated heat maps of HCS criteria for the High Mn low density reference steel composition 28Mn-7Al-0.8C-0.2N varying the content of P from 0 to 0.2 and Si from 0 to 4 wt.% using the Scheil-Gulliver with back diffusion solidification model. Calculations were done according to the (a) CSC criterion, (b) HCC criterion and (c) BTR criterion under thermal mode 1 (left), mode 2 (center) and mode 3 (right)..

3.3 Powder production

Six FeMnAlC steel powder compositions with comparable Mn, C, and Al contents but varied Si and P levels were produced by nitrogen atomization from a combination of different ferroalloys i.e., Fe ingots with 99.7 wt.% purity, Fe-75Si (wt.%), Al with

99.7 wt.% purity, Mn with 99.8 wt.% purity, Fe-78Mn (wt.%) and graphite. Fe-78Mn has higher S and P impurities than Mn and it was used for the high P content steels, while Mn alone was incorporated into the compositions with limited amounts of P. Their target and final chemical compositions are shown in Table 3.1. The experimental contents of O and N were derived from the atomization process and impurities of these elements existing in the raw materials, while S and P were derived solely from the raw materials.

Table 3.1

Target and measured chemical compositions of powders with size between 20-60 μm (fraction F2) of High Mn Fe-Mn-Al-C low density steel with different contents of Si and P, in wt.%.

Material		C	S	P	Si	Mn	Al	N	O
FeMnAlC	Target	0.80	<0.01	<0.01	<0.05	28.0	7.00		
	Measured	0.88	<0.01	<0.01	0.01	29.5	6.62	0.03	0.04
FeMnAlC-HP	Target	0.80	<0.01	0.07	0.25	28.0	7.00		
	Measured	0.80	<0.01	0.06	0.20	28.7	6.77	0.01	0.03
FeMnAlC-HP-2Si	Target	0.80	<0.01	0.07	2.00	28.0	7.00		
	Measured	0.84	<0.01	0.07	1.72	26.8	6.18	0.01	0.01
FeMnAlC-1Si	Target	0.80	<0.01	<0.01	1.00	28.0	7.00		
	Measured	0.76	<0.01	<0.01	1.03	28.8	7.69	0.02	0.07
FeMnAlC-2Si	Target	0.80	<0.01	<0.01	2.00	28.0	7.00		
	Measured	0.77	<0.01	<0.01	2.09	28.5	7.63	0.02	0.07
FeMnAlC-4Si	Target	0.80	<0.01	<0.01	4.00	28.0	7.00		
	Measured	0.79	<0.01	<0.01	3.78	26.1	7.73	0.02	0.05

Representative 10th, 50th, and 90th percentiles of the particle size distribution, D10, D50 and D90, respectively, of the steel powders produced are given in Table 3.2 for each of the powder fractions F1, F2, and F3.

Table 3.2
D10, D50 and D90 percentiles of the FeMnAlC steel powder size distributions of different powder size fractions.

Powder fraction	D_{10} (μm)	D_{50} (μm)	D_{90} (μm)
F1 (<20 μm)	4.83	10.11	18.01
F2 (20-63 μm)	20.39	32.83	53.17
F3 (63-150 μm)	51.30	88.70	148.00

3.4 HCS during L-PBF printing process

The as-built density cubes produced with the six powders are shown in Figure 3.4. The reference FeMnAlC composition as well as the two steels containing high P content were printable under the different examined conditions, and all cubes were successfully printed without any failure during the printing process (Figure 3.4a-c). As silicon is added to the composition (FeMnAlC-1Si, FeMnAlC-2Si, and FeMnAlC-4Si), the process window becomes more restricted, and more cubes are stopped during the process to prevent the whole construction from failing. The reason of this failure is the impact of the samples with the powder recoater, which might harm it. The primary cause of this printing failure is high energy densities, which cause molten material to concentrate on the border due to heat and mass transport, resulting in thick solidified regions at the edges [280]. For the cubes printed using the FeMnAlC-1Si powder, printing conditions 7 and 8 with high VED values and a laser power of 175 W failed (Figure 3.4d), while condition 2 with a higher VED than 7 but a lower laser power is still printable. All high VED printing conditions (1, 2, 7, 8, 10, 15, 16)

failed for the cubes printed with FeMnAlC-2Si powders (Figure 3.4e), where condition 12 corresponds to the maximum VED feasible. For FeMnAlC-4Si, all printing conditions failed except condition 11, with a moderate VED, that could be printed close to its total height before failure occurred (Figure 3.4f). FeMnAlC-HP-2Si has a comparable Si content to FeMnAlC-2Si, nevertheless, the process window is not restricted as no cube had to be stopped during the printing process. Note that the details of all process conditions are given in Appendix A.

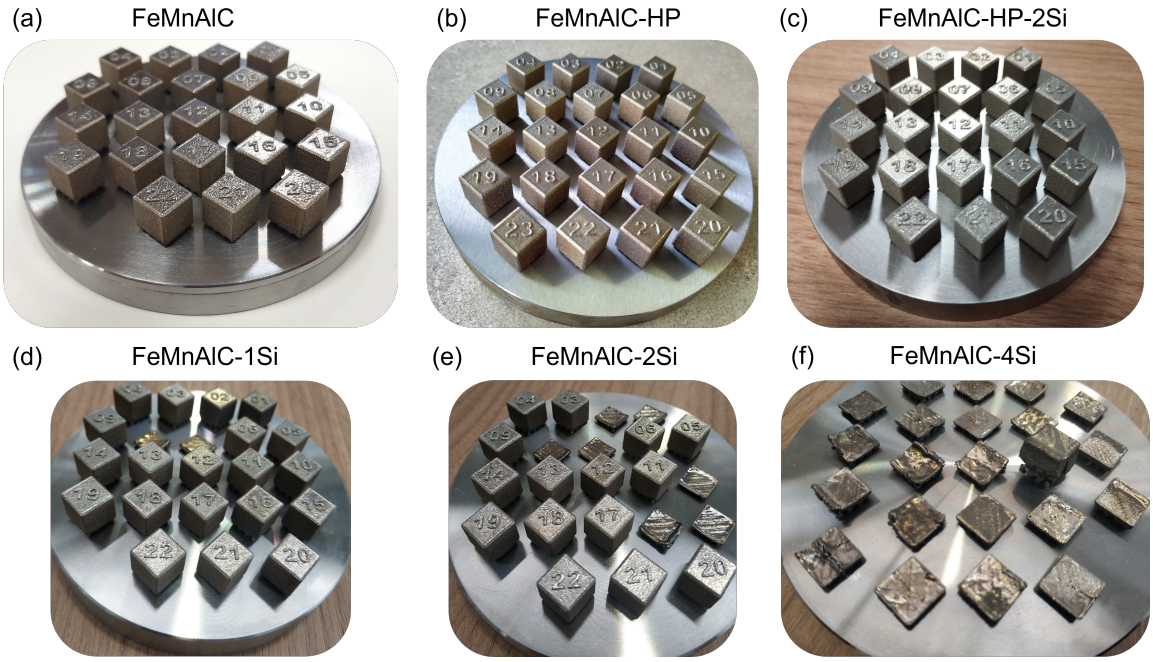

Figure 3.4: As-built density cubes printed using the (a) FeMnAlC, (b) FeMnAlC-HP, (c) FeMnAlC-HP-2Si, (d) FeMnAlC-1Si, (e) FeMnAlC-2Si, and (f) FeMnAlC-4Si.

Figure 3.5 shows cross sections of the density cubes for the six investigated alloys. HC is observed in FeMnAlC-HP, FeMnAlC-HP-2Si and FeMnAlC-1Si in Figures 3.5b-d, respectively. The cracks in the FeMnAlC-4Si composition (Figure 3.5f) are related

to residual stresses, as they are long cracks (>1 mm) that are transverse and parallel to the building direction, and it is possible to find fully dense regions in between them. In this sense, HC is expected to occur uniformly over the whole section, as in the case of the FeMnAlC-HP, FeMnAlC-1Si, and FeMnAlC-HP-2Si materials. In the meantime, FeMnAlC and FeMnAlC-2Si materials show no signs of HC, as shown in Figures 3.5a and Figure 3.5e.

Table 3.3 lists the solidification interval of the compositions in Table 3.1 computed from the Scheil-Gulliver solidification model, together with the HCC criterion calculated according to the three thermal modes. Both the target and the final chemical compositions of powders were used for the calculations, given that small deviations from the target have an impact on the HCC values. The HCC criterion was chosen above the other two represented in Figures 3.2 and 3.3 in order to simplify representation, since all three yield comparable results, and because this criterion not only takes into consideration the other two, but also the solidification interval. According to calculations, FeMnAlC-HP, FeMnAlC-1Si and FeMnAlC-HP-2Si alloys have stronger propensity to HC than the other three compositions, with higher HCC values and solidification interval. The minimum HCC values for these measured compositions are 709, 217 and 162 K for modes 1, 2 and 3, respectively. Besides, FeMnAlC, FeMnAlC-2Si and FeMnAlC-4Si target and measured compositions, with no apparent HC, have the lowest HCC and solidification interval values, indicating lower HCS. The maximum HCC values for the alloys without hot cracks are 403, 137 and 104 K

for thermal modes 1, 2 and 3, respectively.

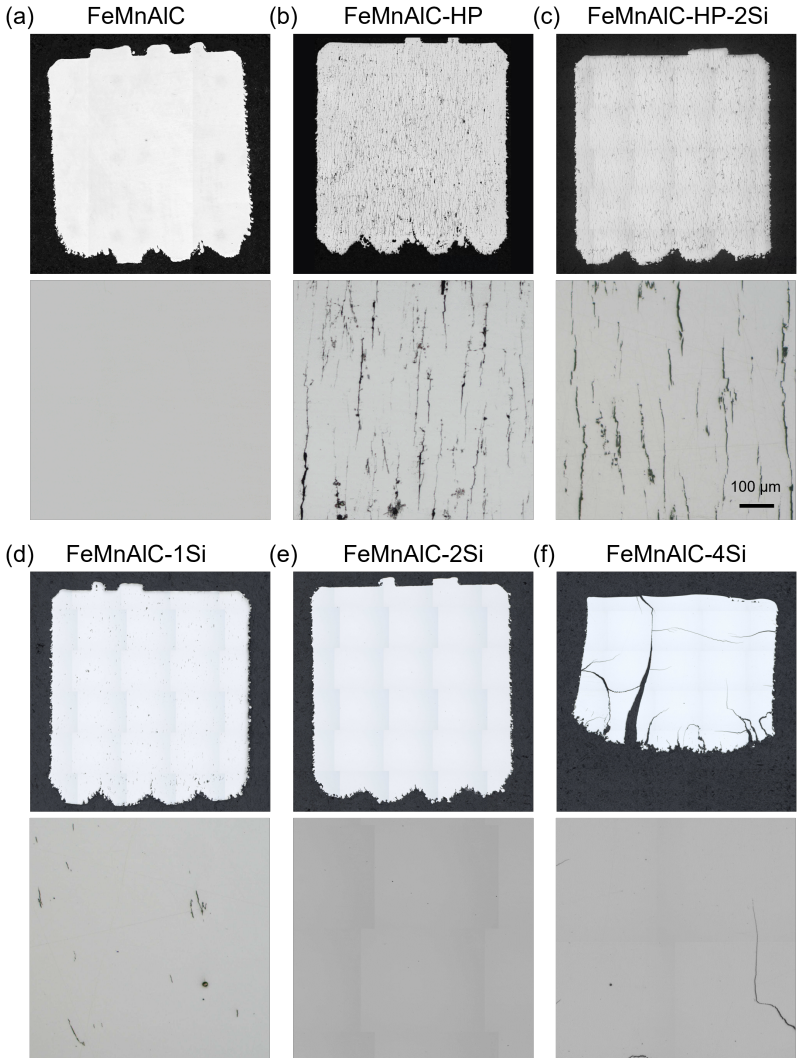

Figure 3.5: Cross section at two magnifications of the L-PBF printed dense cubes for (a) FeMnAlC, (b) FeMnAlC-HP, (c) FeMnAlC-HP-2Si, (d) FeMnAlC-1Si, (e) FeMnAlC-2Si, (f) FeMnAlC-4Si.

Furthermore, the cracks are the longest in the FeMnAlC-HP material, followed by the FeMnAlC-HP-2Si, and finally the FeMnAlC-1Si alloy (see Table 3.3 and Figure 3.5). According to the HCC calculated with modes 2 and 3 in Table 3.3, the ranking of

susceptibility of these alloys to HC is FeMnAlC-HP>FeMnAlC-HP-2Si>FeMnAlC-1Si, which is in good agreement with the lengths of the cracks observed. However, calculations according to mode 1 indicate that FeMnAlC-HP-2Si alloy would be less susceptible to HC than FeMnAlC-1Si. Therefore, thermal modes 2 and 3 predict better HCS than mode 1 for the alloy compositions here analyzed. According to the results, HCC values greater than 217 and 162 K calculated using modes 2 and 3, respectively, lead to HC, while HCC numbers below 137 and 104 K in modes 2 and 3, respectively, are safe against HC. It is noteworthy the "healing" effect that Si may have in high P compositions, as reflected by the shorter cracks found in the FeMnAlC-HP-2Si alloy as compared to the FeMnAlC-HP. Careful alloy design and elaboration could be conducted to mitigate or even avoid HC in materials containing high levels of impurities, thereby reducing the cost of raw materials and avoiding complex secondary metallurgy operations such as dephosphorization.

Finally, the HCC under the three thermal modes was calculated for the FeMnAlC composition reported in literature [217], and the results are collected in Table 3.3. Both the reported experimental and theoretical compositions show ΔT and HCC values exceeding the previously defined threshold to prevent HC. Indeed, the length of the cracks reported in the FeMnAlC reference composition from literature [217] is comparable to that measured in the FeMnAlC-1Si alloy, and the HCC under modes 2 and 3 is as well similar i.e., 217 Vs 238 K and 162 Vs 176 K, respectively. Conversely, the HCC under thermal mode 1 was 241 K lower in the FeMnAlC-1Si alloy, and

ΔT 3 K higher. These observations support the hypothesis that the HCC calculated under thermal modes 2 and 3 predicts accurately HCS in High Mn Fe-Mn-Al-C low density steel grades.

Table 3.3
Calculated solidification interval (ΔT), HCC in the 3 thermal condition modes, and length of hot cracks measured in the alloys investigated. Calculations were done considering the Scheil-Gulliver solidification model in both the target and measured compositions.

Material	Composition	ΔT, K	Mode 1, K	Mode 2, K	Mode 3, K	Cracks' length
FeMnAlC	Target	172	221	68	56	–
	Measured	187	371	90	73	No cracks
FeMnAlC	Target	385	1412	379	274	–
-HP	Measured	360	1278	333	246	100-300 μm
FeMnAlC	Target	328	553	207	150	–
-HP-2Si	Measured	348	709	250	182	50-250 μm
FeMnAlC	Target	303	794	210	159	–
-1Si	Measured	309	787	217	162	10-60 μm
FeMnAlC	Target	274	425	140	107	–
-2Si	Measured	274	403	137	104	No cracks
FeMnAlC	Target	226	71	49	37	–
-4Si	Measured	237	125	70	52	No HC cracks
FeMnAlC	Target	277	976	188	142	–
paper[217]	Measured	306	1028	238	176	5-50 μm

3.5 Microstructure development during solidification

The solidification structure can be studied in powders given that there is no IHT, as it is the case for most of the layers in L-PBF processed materials. For this reason, both the powders used as feedstock in L-PBF (20-63 μm), designated as F2, and

the smallest fraction of powders (<20 μm), designated as F1 were characterized to understand how the materials solidify. The influence of the cooling rate was analyzed by comparing the microstructures of F1 and F2 powders from the same batch, since F1 powders solidify faster than F2 because they have smaller PSD [281].

Figure 3.6 (a) and (b) show the X-ray diffractogram of the F1 and F2 fractions of the powders, respectively, and Figure 3.6 (c) shows the X-ray diffraction data of the density cube 11 thereby produced. All powders are mainly austenitic with some fraction of ferrite that increases with the content of P and Si. Table 3.4 collects the corresponding results in terms of weight percent of phases after Rietveld refinement of XRD data.

The evolution of ferrite can be spotted by looking at the highest diffraction peak of Fe-BCC at a diffraction angle of 44° and in the results shown in Table 3.4. The fraction of ferrite is similar in powder fractions F1 and F2 for most of the High Mn Fe-Mn-Al-C low density steel compositions, except in the FeMnAlC-HP-2Si powders, where the ferrite content in F1 (12 wt.%) is higher than in F2 (3 wt.%), meaning that ferrite is stabilized at higher cooling rates. The fraction of ferrite in L-PBF dense cube samples decreases in comparison with the reference powders. Indeed, the fraction of ferrite becomes marginal in most compositions and only the FeMnAlC-2Si and FeMnAlC-4Si printed cubes show well-defined Fe-BCC diffraction peaks. Nevertheless, the fraction of ferrite in the FeMnAlC-2Si and FeMnAlC-4Si cubes is also smaller in comparison to the reference powders. The Fe-FCC austenitic phase of all

High Mn Fe-Mn-Al-C low density steel compositions shows crystallographic texture along the (2 0 0) plane, which is represented by the diffraction peak around 49.5°. The relative intensity of this diffraction plane increases in all High Mn Fe-Mn-Al-C low density steels as compared to the reference powder, where no texture is detected. This texture component is particularly strong in the materials with high P content, where the first peak of austenite (∼42.5°) is almost erased as a consequence. The stronger texture in these compositions may be related to the pronounced HC observed and the longer solidification intervals that can lead to longer columnar grains along the building direction, which are detrimental for this cracking [282].

The FeMnAlC-4Si powders show diffraction peaks other than austenite and ferrite, most probably due to a Si-rich phase, such as the ordered DO3. This ordered BCC phase can be formed in high-Si steels and it is hard but brittle [283, 284, 285]. The DO3 phase shares diffraction planes with Fe-BCC, superposing the diffraction peaks, but it has other superlattice diffraction peaks that are forbidden for Fe-BCC (i.e., 31°, 52.° and 55°), such that both phases can be differentiated and calculated. Quantification of the DO3 phase in Table 3.4 shows that it is dependent on the cooling rate and increases from 18 wt.% in F2 to 31% in F1. The L-PBF cube of this composition is the only sample that shows more diffraction peaks than the powder located at 41°, 48°, 70° and 84°; which match with the ordered precipitate (Fe,Mn)3AlC (so-called κ–carbide) typical of the High Mn FeMnAlC low density steel family. According to Choo et al. [286], the formation of this carbide is due to spinodal decomposition of

austenite, which could be driven also by the IHT of L-PBF process. The content of Si in this steel is sufficient to significantly increase the ferrite fraction. C has low solubility in ferrite and is expelled from this phase, thereby enriching the austenite and facilitating the precipitation of κ–carbide. It is well known that these carbides increase the strength of High Mn Fe-Mn-Al-C low density steels due to their coherency with the austenitic matrix and hardness [287]. However, when carbides are formed between grains, mechanical properties are deteriorated [287, 172]. This, together with the presence of the brittle DO3 phase, can be the reasons for failure of FeMnAlC-4Si cubes during printing and the concomitant cracking. It is noteworthy that the accuracy of quantification using the Rietveld refinement technique is 2 wt.%, and that phases that are in a smaller amount may not be detected by the XRD technique.

	F1			F2			Cube			
Alloy	γ	α	DO3	γ	α	DO3	γ	α	DO3	κ-carbide
FeMnAlC	bal.	<2	–	bal.	<2	–	bal.	<2	–	–
FeMnAlC-HP	bal.	<2	–	bal.	<2	–	bal.	<2	–	–
FeMnAlC-HP-2Si	bal.	13	–	bal.	3	–	bal.	<2	–	–
FeMnAlC-1Si	bal.	4	–	bal.	3	–	bal.	<2	–	–
FeMnAlC-2Si	bal.	9	–	bal.	6	–	bal.	6	–	–
FeMnAlC-4Si	bal.	22	31	bal.	19	18	bal.	20	35	13

Table 3.4

Weight percent of phases present in the F1 and F2 fractions of the powders and L-PBF cubes produced of FeMnAlC-xP-ySi compositions, as determined by Rietveld refinement of XRD data, where the error of the technique is estimated in ± 2 wt.%. γ denotes austenite, α ferrite and κ kappa-carbide.

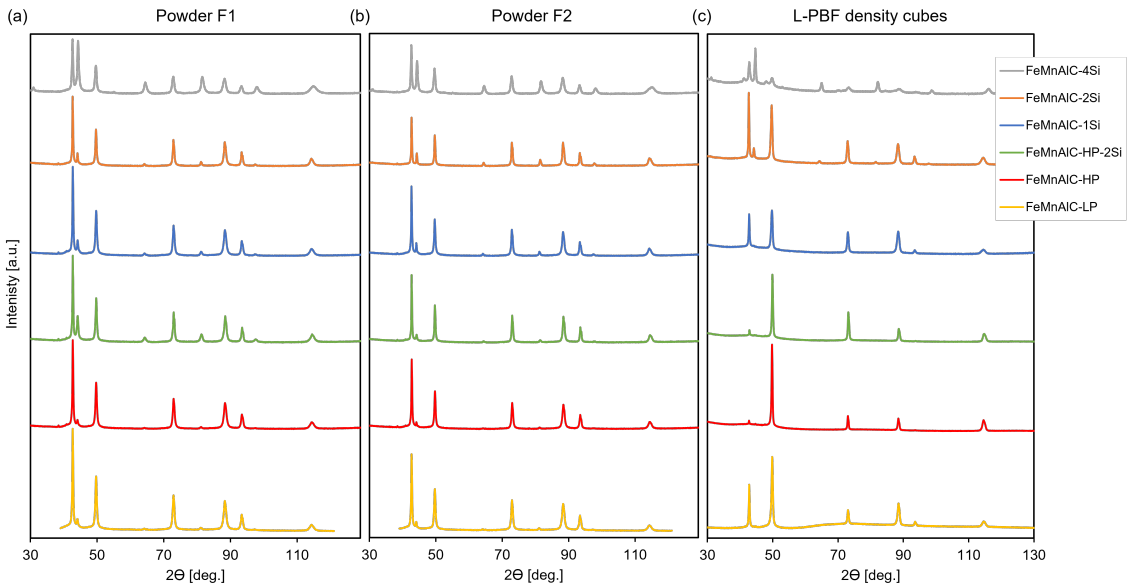

Figure 3.6: XRD data of FeMnAlC-xP-ySi (a) F1 powders, (b) F2 powders and (c) L-PBF cubes with laser parameters 11: 175 W and 700 mm/s.

Finally, the low content of ferrite found in the FeMnAlC-HP, FeMnAlC-1Si and FeMnAlC-HP-2Si powders and printed materials agrees with calculations and theory. Si, and P extend the last stage of solidification, forming thin liquid films responsible for HC. This issue can be solved by the nucleation of ferrite, which shortens the solidification interval, as it is proved in the FeMnAlC-2Si composition.

In this regard, Figure 3.7a shows the solidification path of the FeMnAlC and FeMnAlC-HP measured compositions in Table 3.1.

Figure 3.7a reflects that not only the total solidification interval increases in approximately 200 °C, but that the majority of this increment occurs at the vulnerability time, thereby increasing the chances of forming thin liquid films along the grain boundaries that lead to HC. Figure 3.7b illustrates the evolution of the solidification interval ΔT

as a function of the Si and P contents. The solidification interval increases with the Si content up to ∼1 wt.% when the P content is below 0.07 wt.%. However, when the Si content is higher than 1.0 wt.%, the solidification interval begins to decrease gradually for P levels below 0.07 wt.% and rapidly for higher amounts of P. This is explained by the fact that higher amounts of Si promote the formation of ferrite, which is able to dissolve greater quantities of P than austenite and solidification concludes earlier.

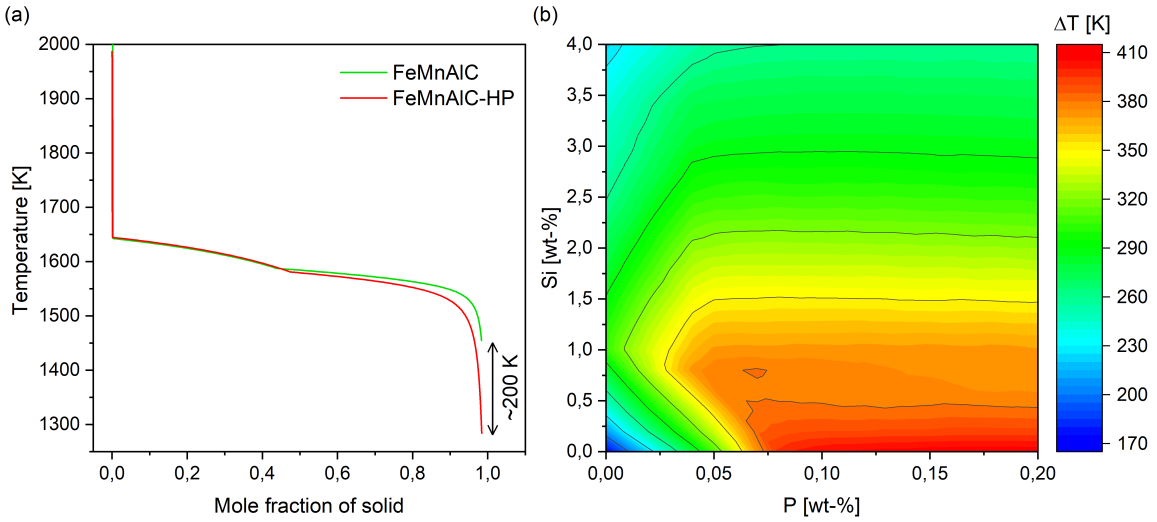

Figure 3.7: Calculation of Solidification interval with Scheil-Gulliver model. (a) Representation of the evolution of mass fraction of solid with temperature for FeMnAlC and FeMnAlC-HP compositions. (b) Evolution of the complete solidification interval for different contents of Si and P.

Secondary electron (SE) SEM images in Figure 3.8 show that the powders of both alloys have a spherical morphology, while most of the powder particles have some smaller particles or satellites attached to the surfaces.

The SE SEM images obtained from electropolished cross sections reveal different microstructures in the two alloys. For FeMnAlC-2Si, well developed dendrites are observed, with occasional pockets of a different phase at the dendrite boundaries. For the FeMnAlC-4Si, however, a more complex structure was observed with an undulating morphology on the electropolished surface. The EBSD inverse pole figure (IPF) maps from these samples revealed corresponding differences in the grain structure with larger, more equiaxed grains in the FeMnAlC-2Si and more complex grain morphologies in the FeMnAlC-4Si. This can be related to the phase distributions as shown in the corresponding maps. The grains are predominantly (93%) austenite in the FeMnAlC-2Si, with small grains and pockets of ferrite at the grain boundaries. For the FeMnAlC-4Si, there is a much higher volume fraction of ferrite (28%) and this is distributed throughout the microstructure. These microstructural observations in FeMnAlC-2Si powder are in agreement with the XRD observations that can explain the formation of brittle phases that lead to cracking.

To determine the effect of P content, the microstructures of powders of the FeMnAlC and FeMnAlC-HP steels were compared in Figure 3.9a-d and e-h, respectively. SE SEM images show that here again the powder particles of both alloys have a spherical morphology, but there are fewer satellites attached to the surfaces as compared to the powders of FeMnAlC-2Si and FeMnAlC-4Si. The SE SEM images from the electropolished cross sections suggest that the grain structures are very different in the FeMnAlC and FeMnAlC-HP powders, and this is revealed more clearly in the

EBSD inverse pole figure (IPF) maps from the center of the electropolished powders. The FeMnAlC sample exhibits a well-defined equiaxed grain structure, and the corresponding phase map shows that this is a single-phase (100% austenite) structure. For the FeMnAlC-HP, however, a more complex grain morphology is exhibited due to the presence of fine ferrite pockets at the austenite grain boundaries. However, the distribution along the grain boundaries is less uniform than in the FeMnAlC-2Si powder, and fine grains of austenite coexist inside the ferritic domains. Further analysis of these features was performed by STEM as described below.

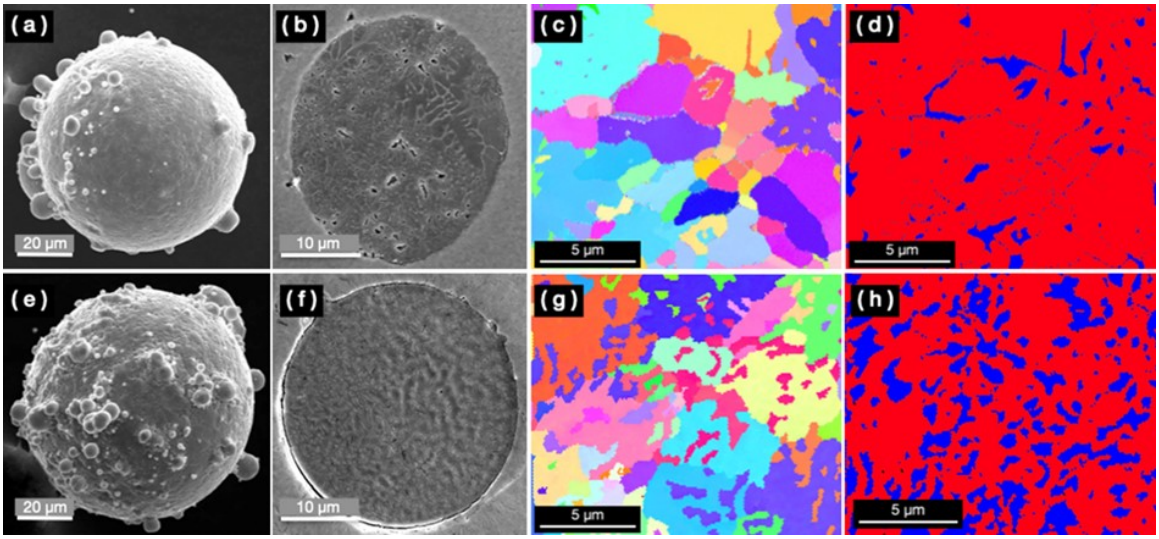

Figure 3.8: SEM data from F2 powders of (a-d) FeMnAlC-2Si, and (e-h) FeMnAlC-4Si. (a) & (e) SE images of surface morphology, (b) & (f) cross-sectional SE images of powder microstructure, (c) & (g) EBSD IPF maps, and (d) & (h) EBSD phase distribution maps.

STEM data obtained from the FIB-cut specimens from FeMnAlC and FeMnAlC-HP are shown in Figures 3.10 and 3.11, respectively. In the FeMnAlC, there is evidence

of P and S segregation to grain boundaries and in particular to triple junctions (Figure 3.10a). There are also fine inclusions (<100 nm in diameter), and the character of these is revealed more clearly at higher magnification (Figure 3.10b and Figure 3.10c). Most of the inclusions within the grains are enriched in Al and N, whereas those at the grain boundaries are rich in Mn and O. Occasional more complex features are present such as in Figure 3.10c where there is evidence for P and S segregation to one side of an Al- and N-rich inclusion.

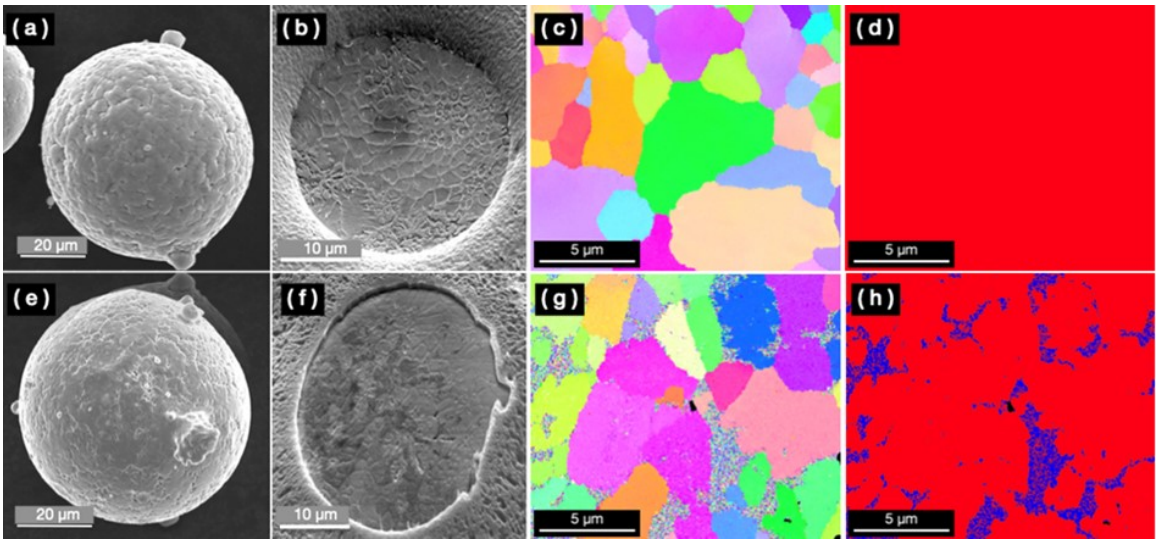

Figure 3.9: SEM data from F2 powders of (a-d) FeMnAlC, and (e-h) FeMnAlC-HP. (a) & (e) SE images of surface morphology, (b) & (f) cross-sectional SE images of powder microstructure, (c) & (g) EBSD IPF maps, and (d) & (h) EBSD phase distribution maps.

The FeMnAlC-HP specimens exhibit somewhat different effects. The P segregation to grain boundaries and triple junctions appears to be more extensive (Fig. 3.11a), such that there is a continuous distribution of P along the boundaries. This is not accompanied by S segregation as was observed in FeMnAlC, but instead there is evidence for

segregation of Mn to the boundaries. Unlike the P (and the S in FeMnAlC), the Mn is not confined to the boundary plane but instead there appears to be a gradient in the Mn concentration. Moreover, the only inclusions observed in FeMnAlC-HP are those that are rich in Al and N (Figure 3.11b). These are coarser than the corresponding inclusions in FeMnAlC, and they exhibit a well-defined tabular morphology. Two examples are shown in Figure 3.11b and these are oriented parallel and perpendicular to the habit plane of the inclusions.

The presence of significant P and Mn segregation at the grain boundaries, resulting in highly concentrated regions of these elements, may indicate the formation of thin layers comprising the final fraction of liquid metal that solidifies in L-PBF. These regions would be unable to withstand the strain caused by contraction and, if not sufficiently filled by the weld pool, lead to crack formation.

Additionally, Si segregation was not observed in the FeMnAlC composition (Figure 3.10), whereas some Si was detected at the solidification boundaries in the FeMnAlC-HP composition (Figure 3.11a). The reason may be attributed to resolution, since the Si content in the FeMnAlC composition is of 0.01 wt.%, as opposed to the 0.20 wt.% in the FeMnAlC-HP, allowing for the detection of a Si gradient in the latter.

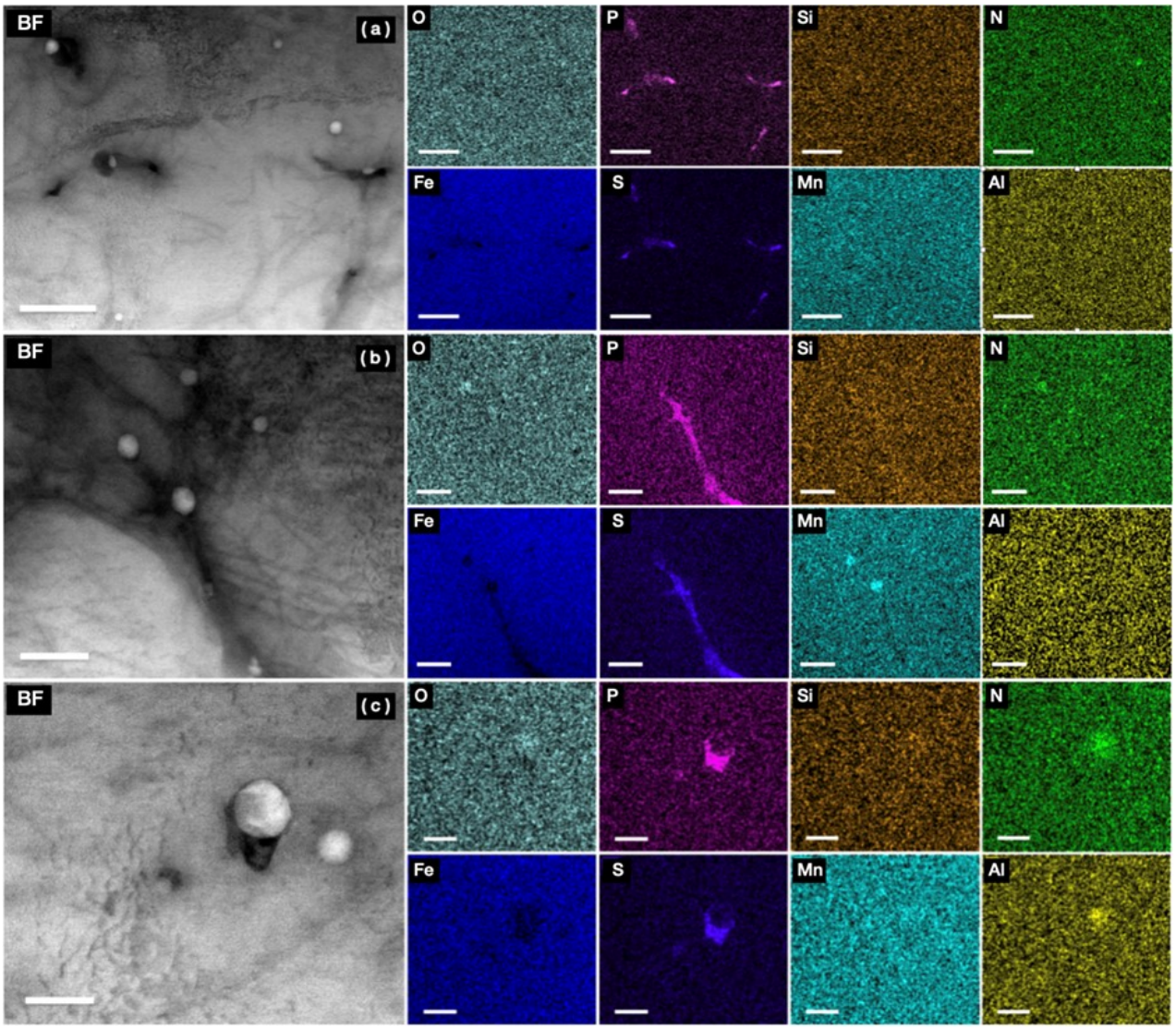

Figure 3.10: STEM data from FIB-cut sections of FeMnAlC-LP F2 powder particles. Each panel comprises a bright field (BF) image and a corresponding set of normalized X-ray intensity maps from an EDXS spectrum imaging experiment on the same area. Scale bars correspond to: (a) 500 nm, (b) 200 nm, and (c) 100 nm.

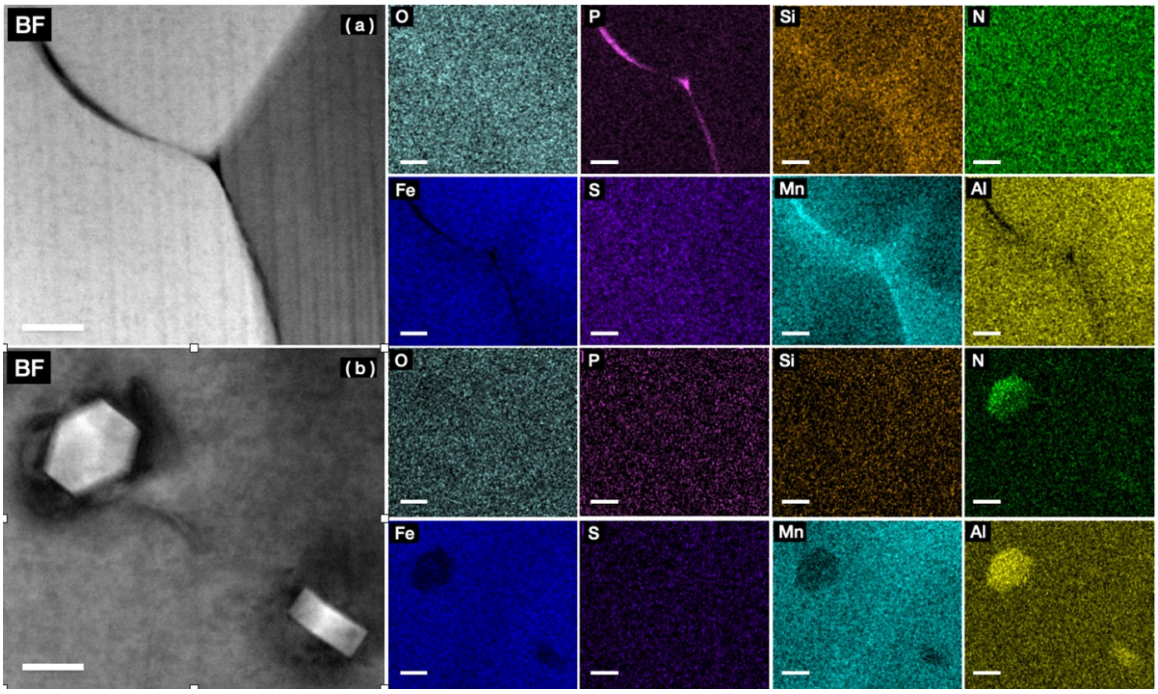

Figure 3.11: STEM data from FIB-cut sections of FeMnAlC-HP F2 powder particles. Each panel comprises a bright field (BF) image and a corresponding set of normalized X-ray intensity maps from an EDXS spectrum imaging experiment on the same area. All scale bars correspond to 100 nm.

3.6 Microstructure during L-PBF process

The microstructure of two of the studied High Mn Fe-Mn-Al-C low density steels (FeMnAlC and FeMnAlC-2Si) was investigated in L-PBF. These compositions were chosen due to their combination of Si and P content, which was resistant against hot and cold cracking.

The XRD measurements presented in Figure 3.6 and Table 3.4 show that in both cases microstructure is mainly austenitic, with a slight increase in the ferritic phase upon the addition of Si.

The SEM images (Figures 3.12 and Figure 3.13) disclose the type of solidification structures present in the L-PBF samples. The FeMnAlC steel exhibits elongated solidification cells, as depicted in the Figure 3.12a, which displays distinct colonies of solidification cells that have been intersected by various planes, resulting in the exposure of different section and, consequently, distinct shapes. Figure 3.12b presents a micrograph capturing the cross-section of a cellular cell colony at higher magnifications. The micrograph reveals that the diameter of the cellular cells is measured in less than 1 μm.

More complex and heterogeneous solidification structures are shown in Figure 3.13 for the FeMnAlC-2Si L-PBF cubes. The solidification structures exhibit a recurring pattern at regular intervals of 20 μm along the building direction, which matches with the layer thickness process parameter. This pattern is observed in Figures 3.13(a-b)

at a magnification of x1500. Micrographs captured at a magnification of x3000 in Figures 3.13(c-d) reveal that the solidification cells inside the layer thickness have a cell morphology similar to those reported in the FeMnAlC composition, with a comparable diameter of 1 μm. Nevertheless, the solidification structures exhibit a transition towards a dendritic-type morphology as they approach the boundaries of the layer thickness.

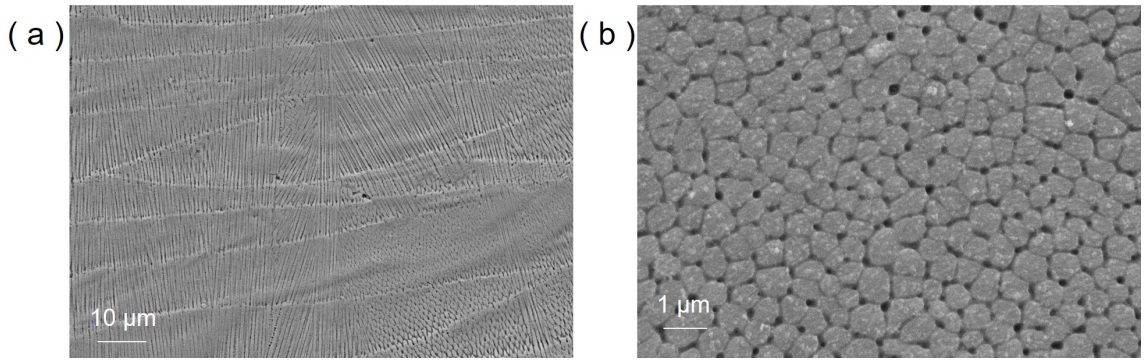

Figure 3.12: SEM images of FeMnAlC L-PBF sample at different magnifications (a) x3000 and (b) x10000.

The analysis of the matrix grain size and morphology was conducted using EBSD for the same two compositions: FeMnAlC (Figure 3.14 a-b) and FeMnAlC-2Si (Figure 3.14 c-d). The band contrast image in the EBSD maps was superposed onto the Inverse Pole Figure (IPF) oriented in the building direction (Figure 3.14 a & c) and the transverse direction (Figure 3.14 b & d).

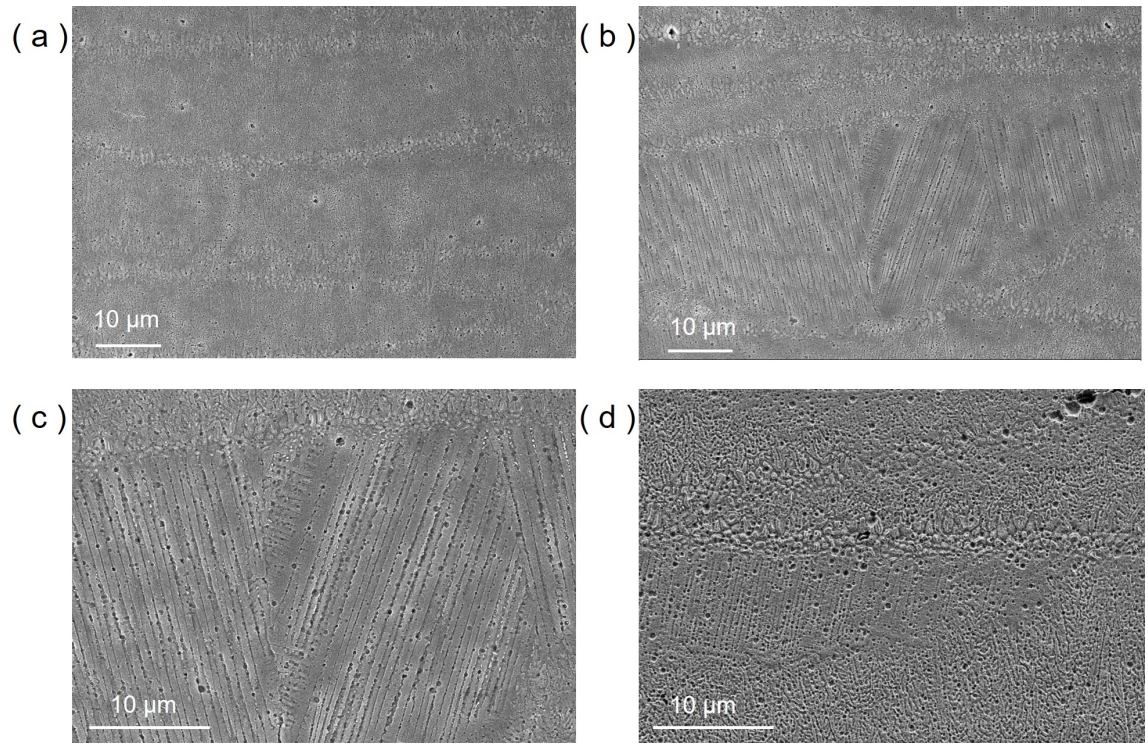

Figure 3.13: SEM images of FeMnAlC-2Si L-PBF sample at different magnifications (a-b) x1500 and (c-d) x3000 and different locations capturing the different solidification cells.

The FeMnAlC steel exhibits epitaxial growth of the austenite, resulting in the formation of columnar grains that are aligned along the building direction and cross several melt pools. This alignment is a characteristic commonly observed in laser AM processes. In the FeMnAlC-2Si steel, most of the austenitic grains show a columnar shape that extends inside the melt pools, with their orientation predominantly aligned in the transverse direction. Within the coarse grains, there are finer grains of few microns in length that are aligned in the building direction. These smaller grains seem to originate from the beginning of the melt pool, suggesting that these

variations in morphology and size are attributed to thermal variations during solidification inside the melt pool.

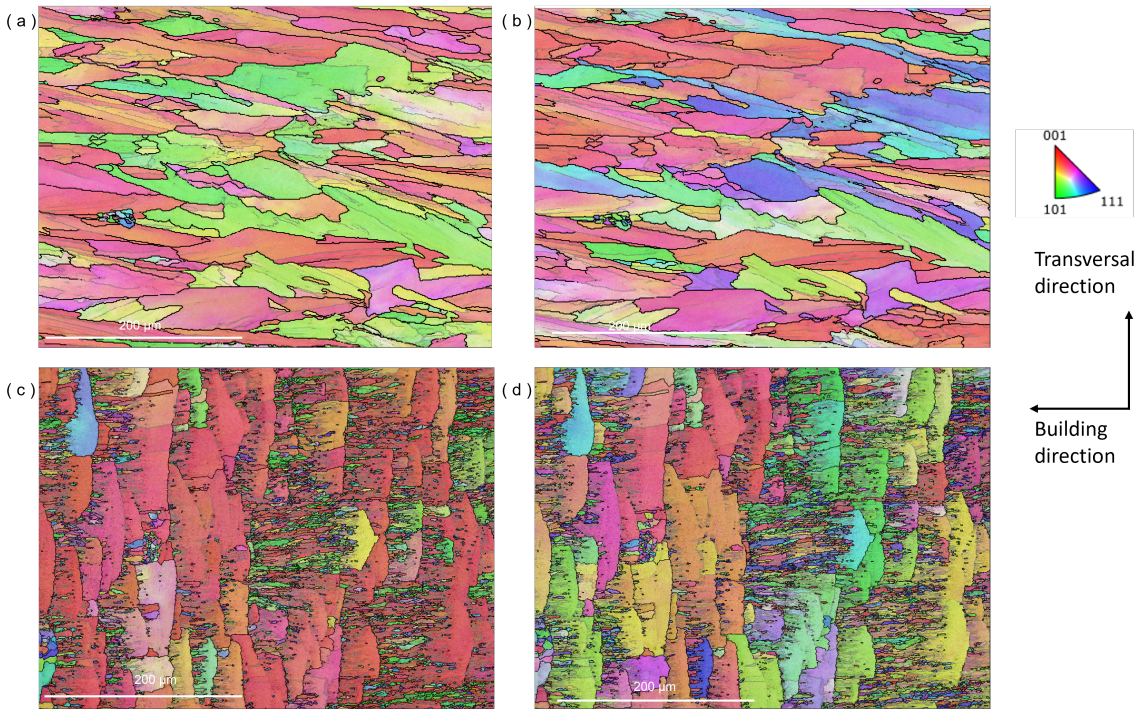

Figure 3.14: EBSD maps for FeMnAlC steel (a-b) and FeMnAlC-2Si steel (c-d) superposing the IPF at the direction parallel to the building direction (a & c) and parallel to the transversal direction (b & d), onto the band contrast.

The pole figures (PF) of the principal crystallographic planes for FCC crystal structures (100), (110) and (111) show the crystallographic texture of FeMnAlC (Figure 3.15a) and FeMnAlC-2Si (Figure 3.15b). Both materials present a predominant texture in the (100) planes along the building direction, although in FeMnAlC is less strong and slightly tilted few degrees. In addition, texture of (100) planes in the FeMnAlC steel is also oriented parallel to the normal direction, which is consistent

with the scanning strategy used during the printing process with 90° rotation between layers. The latter texture component could be mitigated or even eliminated by using a 67° rotation strategy between layers, which randomizes in the parts the texture generates in each layer due to the laser technology [288]. It is noted here that a 90° rotation was maintained in this thesis to reinforce texture development such that isotropy improvements obtained solely by alloy design in Chapter 4 are easily evidenced.

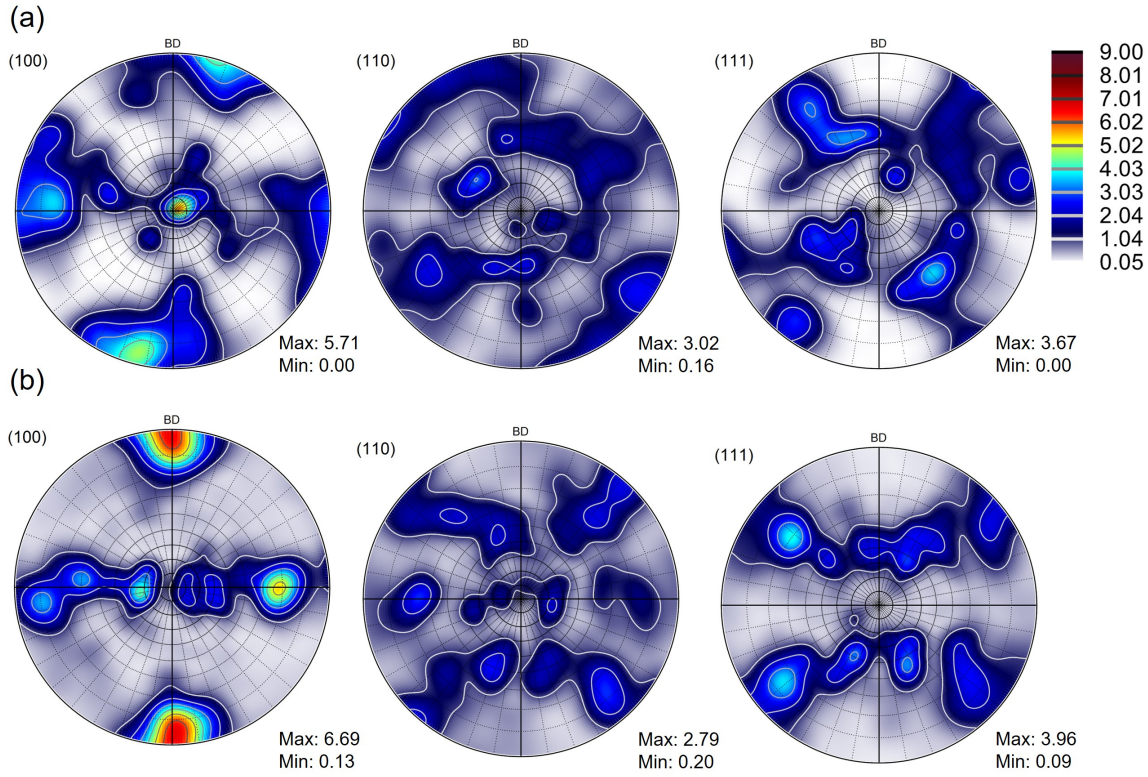

Figure 3.15: Pole Figures of the crystallographic planes (100), (110) and (111) in the materials (a) FeMnAlC and (b) FeMnAlC-2Si. Note that BD refers to the building direction.

3.7 Summary and conclusions

This chapter involved the implementation of the CALPHAD approach for the prediction of HCS in High Mn Fe-Mn-Al-C low density steels, followed by gas atomization and L-PBF processing of selected compositions and the subsequent evaluation of their microstructure, microsegregation, and HCS. The following conclusions can be drawn:

1. AM is a reliable alternative to conventional metallurgy, to fabricate small, thin, or complex shape compounds in High Mn Fe-Mn-Al-C low density steels.
2. Experimental results show that HC is likely to occur in steel grades if the composition is not specifically tailored, causing vertical cracks along the building direction that can extend across the entire cross section. The occurrence of HC in High Mn Fe-Mn-Al-C low density steels can be predicted with HCS criteria determined from the solidification curve calculated using the CALPHAD method. Among all the HCS criteria here evaluated, the HCC in thermal modes 2 and 3 are the most accurate, and a threshold has been proposed to prevent HC in high Mn Fe-Mn-Al-C low density steels.
3. Solidification microstructures studied in the powders support the differences in the solidification curves calculated by CALPHAD: P and S segregate into the liquid during solidification, forming film regions enriched with these elements at the solidification boundaries, which are a potential risk of HC. Also, P promotes

the formation of ferrite leading to more complex grain morphology. In addition to that, Si also promotes the ferrite formation. This ferrite formation seems to concentrate between the dendrite boundaries forming pockets of ferrite. The formation of ferrite by additions of Si around 2 wt.%, can dissolve the P content to prevent HC, although higher additions of Si may increase the risk of cold cracking by formation of brittle phases.

4. This generalist approach enables its extension to other materials that suffer from HC in AM, in order to prevent it.

Chapter 4

Alloy design for grain refinement

Because of the directed heat flow during solidification and fast solidification, AM of metallic materials utilizing powder bed fusion processes, such as L-PBF, generally result in a microstructure of columnar grains [289, 290, 291, 292]. Coarse columnar grains, on the other hand, may reduce material resistance to HC [293, 294, 295], fracture toughness, and cause anisotropy [290, 238, 296]. Tensile strength and total elongation for such microstructures, for example, are claimed to be different when specimens are taken parallel to the printing direction (aligned with columnar grains) than when specimens are taken perpendicular to the printing direction [297, 298]. As a result, grain nucleation during cooling from the liquid plays an important role in determining the final grain size distribution, especially if the material has no solid state phase transformations, i.e., there is no possibility for grain refinement by thermal or

thermo-mechanical treatments. Thus, grain refinement during solidification becomes an important mechanism to improve toughness, isotropy and HC resistance of alloys to be used in L-PBF [299]. According to the principle of solidification, it may be feasible to manage the CET by adjusting the printing conditions. To obtain equiaxed dendritic solidification structures, this approach aims at minimizing the temperature gradient at the solidification front and increasing the cooling rate, or more precisely, the velocity of the solid/liquid interface [224]. By adjusting laser process parameters, CET has been accomplished using a variety of methods reported in the literature, for example: tuning the energy density [225, 226, 227, 228], the laser beam shape [229, 230], the laser spot diameter [231] or the scanning strategy [225, 232, 233]. In addition, regulating solidification supercooling by remelting previously printed layers helps to facilitate grain refining [234, 235, 236]. Nevertheless, it is known that CET is more difficult in welding and similar processes than in casting [237], that it is not homogeneous at different parts of the melt pool [238], and that manipulating the thermal gradient and solidification front velocity requires extensive management of printing conditions and is frequently inapplicable to multiple alloys systems, additive manufacturing hardware [69, 239], or near net shape parts with complex geometries and shapes, where heat can accumulate [240]. Hence, a more pragmatic approach for microstructure control through grain refining is necessary. As an alternate strategy for grain refinement during printing, new alloys have been studied to increase heterogeneous nucleation by generating nucleation sites during printing [234]. Successful

alteration of the solidification conditions, leading to grain refinement in AM has been reported by modifying the feedstock powder via *ex-situ* addition of inoculant-forming nanoparticles [294, 300] or pre-alloying the powder with inoculant-forming elements for incorporation *in-situ* during solidification [225, 301]. In metallurgy, the term "inoculants" denotes deliberate elements employed in the treatment of molten metal during alloying or casting procedures, to induce alterations in its microstructure, and ultimately improve the mechanical and physical properties of the resultant alloy, for example, increasing the alloy's strength by forming a microstructure of finely dispersed grains. Nevertheless, the practical challenges of incorporating these nanoparticles *ex-situ* into the feedstock powder, their cost, and safety issues must be taken into account [238]. A further benefit of L-PBF for inoculation is that it is difficult to include these particles using conventional production techniques, such as casting or classical powder metallurgy, while avoiding non-homogeneous dispersion or excessive grain growth. The quick solidification of L-PBF in a relatively small melting pool over a big printing bed may overcome these issues [302].

The utilization of inoculants within the steelmaking industry plays an important part in the improvement of steel alloy properties. The efficacy of these inoculants relies on several variables, such as their thermal stability, wettability, solubility, size, and lattice mismatch with the matrix phase. Oxides, commonly used as inoculants, exhibit commendable thermal stability and solubility; however, their effectiveness is limited by their relatively low wettability with the molten metal. Conversely, carbides and

nitrides generally exhibit higher wettability than oxides, but they typically have lower heat stability and solubility. When considering the effect of lattice mismatch, it is evident that oxides, nitrides, and carbides have the potential to induce varying outcomes in ferritic or austenitic steel matrices, by altering the nucleation and growth of crystal phases, which in turn have an effect on the final microstructure and mechanical properties of the steel. Therefore, the careful selection and precise control of inoculants in steelmaking processes are important to tailor the microstructure and, consequently, the final performance of steels for the different industrial applications. In Fe-based alloys, the solidification and transformation modes that arise during cooling may be divided into three classes: ferrite mode, ferrite/austenite mode, and austenite mode [303]. In the ferrite and austenite modes, solidification is completed in the single-phase state of the ferrite and austenite phase, respectively, and then any other phase is formed through solid-state transformation. In the ferrite/austenite mode, after crystallization of the primary ferrite crystal, the triple phase state consisting of the L+α+γ phases is formed through a peritectic reaction, meaning that austenite forms together with ferrite from the liquid phase.

Ti-containing inoculants, carbides, nitrides, carbonitrides, and oxides, are proven to promote grain refinement in ferritic steels processed by L-PBF [290, 238, 298, 299]; which solidify in the ferrite mode. Besides, TiC or Ti(C,N) are also effective heterogeneous nucleation agents for controlling grain development in 316L stainless steel in ferrite/austenite mode [302, 304]. However, there is a general agreement that when

the structures solidify in the austenite mode, Ti(C,N) is not an effective nucleant, and solidification occurs primarily by the columnar growth of austenite dendrites, both under slow and rapid cooling [303, 305, 306, 307]. In the latter case, titanium oxides are proved to be effective inoculants, where spinel particles are the most potent nuclei for austenitic grains followed by olivine and finally corundum particles, while Ti(C,N) are not effective at all [305].

The goal of this chapter is to evaluate the grain refining efficacy of TiC and Ti(C,N) inoculants over AlN, generated *in-situ* in pre-alloyed High Mn Fe-Mn-Al-C low density steel powders containing varying amounts of Ti. Using thermodynamic calculations, the solidification paths of the different steels were related to their microstructure, potential refinement, and crystallographic texture. Ti was selected due to the comparatively acceptable refining results of *ex-situ* TiC additions on 316L steel powder [304, 302], as well as the demonstrated effectiveness under the ferrite/austenite solidification mode.

4.1 CALPHAD-based inoculant calculations

To examine the formation of TiC or Ti(C,N) for potential refinement of the austenitic grains in L-PBF, a pseudo phase diagram of Fe-28Mn-7Al-0.8C-0.02N-xTi low density steel composition was calculated and it is shown in Figure 4.1. The nitrogen content utilized in this calculation is a representative value that we should anticipate to find

in the powder, based on experimental measurements performed in prior FeMnAlC atomized compositions (Table 3.1 of Chapter 3).

Under equilibrium conditions, the solidification path of the matrix in Figure 1 proceeds through the ferrite/austenite mode, where a ceramic particle is firstly formed in the liquid (AlN or Ti(C,N)), then ferrite nucleates and finally austenite is formed coexisting with the ceramic, ferrite and the liquid until full solidification. AlN is the first phase to form prior to ferrite and austenite, both in the absence of and in the presence of relatively low amount of Ti. Nevertheless, when Ti concentration exceeds 0.55 wt.%, AlN is replaced by Ti(C,N) as the first forming phase. AlN and Ti(C,N) coexist and are formed before ferrite and austenite at Ti levels between 0.1 and 0.55 wt%, while AlN is generated before Ti(C,N).

To study the influence of both the nature of precipitates and the solidification path, four powders with different Ti contents were chosen: (1) the reference composition with no Ti (FeMnAlC), where only AlN may be formed, (2) a composition with 0.2 wt.% of Ti (FeMnAlC-02Ti), where both AlN and Ti(C,N) should coexist and be formed, (3) a composition with 0.5 wt.% of Ti (FeMnAlC-05Ti), where both AlN and Ti(C,N) should coexist and be formed with dissolution of the AlN before the end of solidification, and (4) a composition with 2.0 wt.% of Ti (FeMnAlC-2Ti), where only Ti(C,N) and no AlN should form. The purpose of these compositions is to assess the effect of a greater Ti concentration on the nature precipitates, as well as the volume and size of Ti(C,N) precipitates and their efficacy as grain refiners.

In order to examine the microstructural evolution of the different steel compositions during non-equilibrium solidification, Scheil-Gulliver calculations were performed to simulate the rapid cooling rates of gas-atomization powder production and laser-based additive manufacturing techniques, where C and N were defined as fast-diffusers due to their high diffusivity in solid steel. The chemical composition was the same as that specified for equilibrium calculation, but with the four levels of Ti defined and a realistic O-contamination value of 0.04 wt.% (Table 3.1). Most of the O in the powder concentrates on the surface, resulting in the formation of superficial oxides. This implies that smaller powder particles, characterized by a larger specific surface compared to bigger particles, exhibit relatively higher O-content. However, these oxides can be found inside the bulk of the printed material.

Figure 4.2a shows the development of mass fraction of solid with the decrease in the temperature for the four compositions, whereas Figure 4.2b depicts the first phases that solidify before the formation of ferrite, when the temperature decrease associated with the formation of solid fraction is rapidly reduced (and becomes close to a plateau in Figure 4.2b). At this early stage, where precipitates begin to form and the temperature drops without a plausible increase in the solid phase, FeMnAlC and FeMnAlC-02Ti exhibit similar solidification paths, whereas in the FeMnAlC-05Ti and the FeMnAlC-2Ti, the final fraction of solid at this early precipitation stage is higher, 0.53 and 2.18 wt.%, respectively.

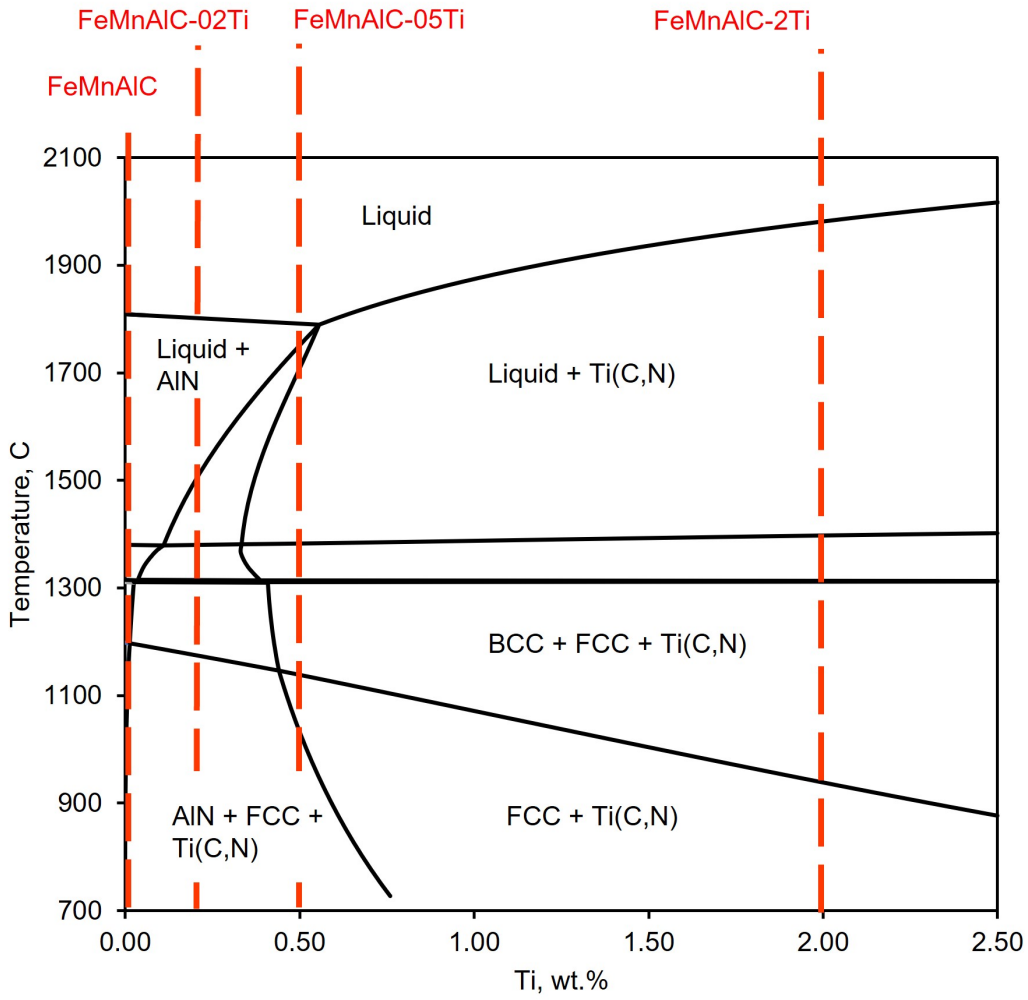

Figure 4.1: Calculated pseudo-phase diagram of the system Fe-28Mn-7Al-0.8C-0.02N-xTi up to 2.5 wt.% of Ti. Dashed lines indicate the studied compositions with the different levels of Ti (0, 0.2, 0.5 and 2.0) in wt.%.

Table 4.1 compiles the Scheil-Gulliver-calculated weight percentages for the different phases formed after solidification. This approach predicts that a greater proportion of ferrite will form during solidification when Ti is present. In accordance with equilibrium calculations (Figure 4.1), AlN is still formed in the FeMnAlC-05Ti, and some Ti(C,N) is formed already in the FeMnAlC-02Ti. The increment of the total amount of precipitates and more precisely in Ti(C,N), explains the higher fraction of solid

formed during solidification before ferrite or austenite nucleate as shown in Figure 4.2b. Lastly, the proportion of Al-oxides is predicted to be independent of the quantity of Ti itself, but rather dependent on the levels of O and Al. No other oxide is predicted to be formed.

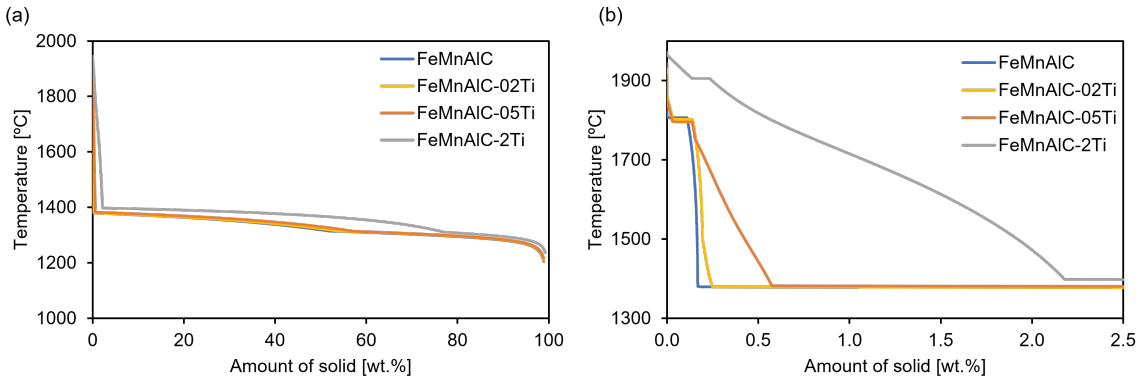

Figure 4.2: Scheil-Gulliver solidification calculations for the four different Fe-Mn-Al-C steel compositions: (a) the evolution of mass fraction of solid in wt.% with the decrease in temperature during solidification and (b) a zoom of the first stages of solidification before austenite and ferrite start to form.

Table 4.1
Mass fraction of the different solid phases in wt.% calculated at the end of the solidification with the Scheil-Gulliver model for the four High Mn Fe-Mn-Al-C low density steel compositions.

Alloy	γ, wt.%	α, wt.%	Al_2O_3, wt.%	AlN, wt.%	Ti(C,N), wt.%
FeMnAlC	bal.	51.67	0.09	0.09	–
FeMnAlC-02Ti	bal.	53.20	0.09	0.11	0.21
FeMnAlC-05Ti	bal.	56.39	0.09	0.07	0.58
FeMnAlC-2Ti	bal.	73.54	0.09	–	2.38

4.2 Powder production

Fe-28Mn-7Al-0.8C-xTi low density steel powders were fabricated in a lab-scale atomization equipment AU3000 Blue Power as described in Section 2.1.1. In order to produce the different Ti-containing High Mn low density steel compositions, a variety of ferroalloys were combined and melted at a temperature of 1800 °C. The ferroalloys included: Fe ingots with a purity of 99.7 wt.%, Al with a purity of 99.7 wt.%, Mn with a purity of 99.8 wt.%, Fe-70Ti (wt.%) and graphite.

The target and final chemical compositions of the steels produced are presented in Table 4.2. The experimental amount of O and N come from the atomization process and the presence of these elements in the raw materials. On the other hand, S, P, and Si are exclusively derived from the raw materials.

Table 4.2
Target and measured chemical compositions of powders with size between 20-60 μm (fraction F2) of High Mn Fe-Mn-Al-C low density steels with different contents of Ti, in wt.%.

Material		C	S	P	Ti	Mn	Al	Si	N	O
FeMnAlC	Target	0.80	<0.01	<0.01	<0.05	28.0	7.00	<0.10		
	Measured	0.88	<0.01	<0.01	0.01	29.5	6.62	0.01	0.03	0.04
FeMnAlC-02Ti	Target	0.80	<0.01	<0.01	0.20	28.0	7.00	<0.10		
	Measured	0.83	<0.01	<0.01	0.19	28.2	6.99	0.14	0.02	0.05
FeMnAlC-05Ti	Target	0.80	<0.01	<0.01	0.50	28.0	7.00	<0.10		
	Measured	0.82	<0.01	<0.01	0.46	28.1	7.00	0.14	0.03	0.08
FeMnAlC-2Ti	Target	0.80	<0.01	<0.01	2.00	28.0	7.00	<0.10		
	Measured	0.87	<0.01	<0.01	1.92	27.9	6.31	0.12	0.03	0.03

The typical 10th, 50th, and 90th percentiles of these powders size distributions, D10,

D50 and D90, are similar to those of FeMnAlC-Si shown in Chapter 3 at Table 3.2, with values of 17.8, 29.9, and 50.8 μm, respectively in the powder fraction F2.

4.3 Microstructure development during solidification

The effects of different Ti contents in the starting powders, and the role of Ti-rich precipitates in microstructure refinement, were evaluated by comparing data from Ti-free (FeMnAlC), low and moderate Ti (FeMnAlC-02Ti and FeMnAlC-05Ti) and Ti-rich (FeMnAlC-2Ti) compositions. SE SEM images from the powder surfaces (not shown) confirmed that all four powders exhibit spherical morphologies, and that very few satellites are attached to the powder particle surfaces. Higher magnification SE SEM images and EBSD data from the electropolished cross-sections reveal rather different microstructures in the four alloys (Figure 4.3). For the Ti-free FeMnAlC powder (Figure 4.3a), precipitates appear as white spots distributed homogeneously across the electropolished surfaces. The morphology of the electropolished surface revealed in the higher-magnification SE SEM image is consistent with the alloy having equiaxed grains uniform in size with clear grain boundaries, and the EBSD data show that this microstructure is austenitic. The FeMnAlC-02Ti powder in Figure 4.3b exhibits a dendritic microstructure with a low volume fraction of ferrite and no evidence of grain refinement. For the FeMnAlC-05Ti powders (Figure 4.3c), finer austenite grains are observed surrounded by small pockets of ferrite. For the FeMnAlC-2Ti

powder shown in Figure 4.3d, however, a much larger number of Ti-rich precipitates is observed throughout the microstructure. The austenite grain size is correspondingly finer, with these grains being surrounded by a higher volume fraction of ferrite grains.

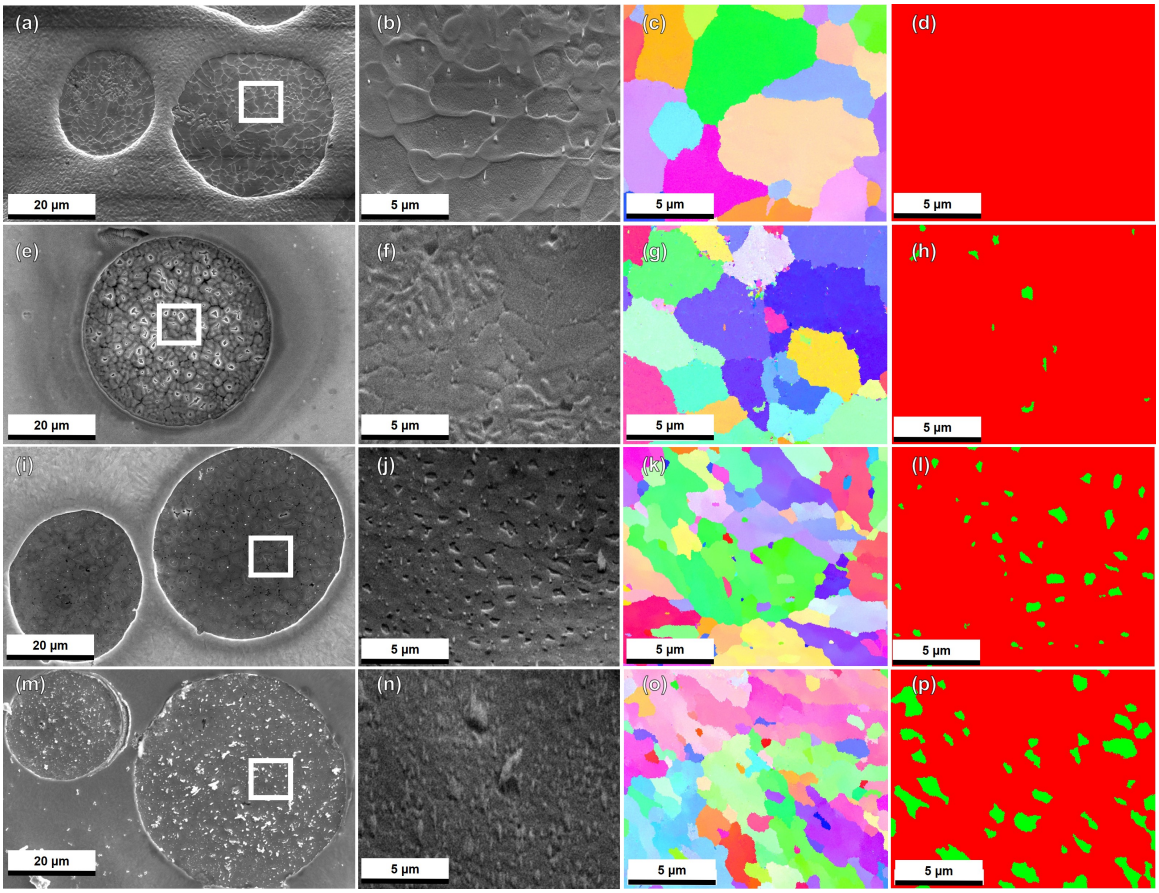

Figure 4.3: SEM data from electropolished cross sections of powders of (a-d) FeMnAlC, (e-h) FeMnAlC-0.2Ti, (i-l) FeMnAlC-0.5Ti, and (m-p) FeMnAlC-2Ti. (a) & (e) & (i) & (m) cross-sectional SE images powder microstructure, (b) & (f) & (j) & (n) SE SEM images at higher magnifications of powder microstructure, (c) & (g) & (k) & (o) EBSD IPF maps, and (d) & (h) & (l) & (p) EBSD phase distribution maps, red-austenite, green-ferrite.

STEM data obtained from electron-transparent regions in the foils from each powder are shown in Figure 4.4. The bright-field images reveal the details of the grain structures along with the distributions and morphologies of the precipitates. In the Ti-free FeMnAlC powder shown in Figure 4.4a, most of the precipitates are Al-rich and roughly equiaxed with diameters of <100 nm. However, a few Ti-rich precipitates are observed, possibly due to contamination during the pre-alloying process. In FeMnAlC-0.2Ti (Figure 4.4b), there is clear evidence of the coexistence of Ti(C,N) and AlN precipitates mainly at the austenite grain boundaries. Similar groups of precipitates are found in FeMnAlC-0.5Ti, and the location of the Ti(C,N) at the matrix grain boundaries is revealed clearly in Figure 4.4c. For the FeMnAlC-2Ti, no Al-rich precipitates are observed, and the elemental maps reveal a much higher volume fraction of Ti-rich precipitates, as shown in Figure 4.4d.

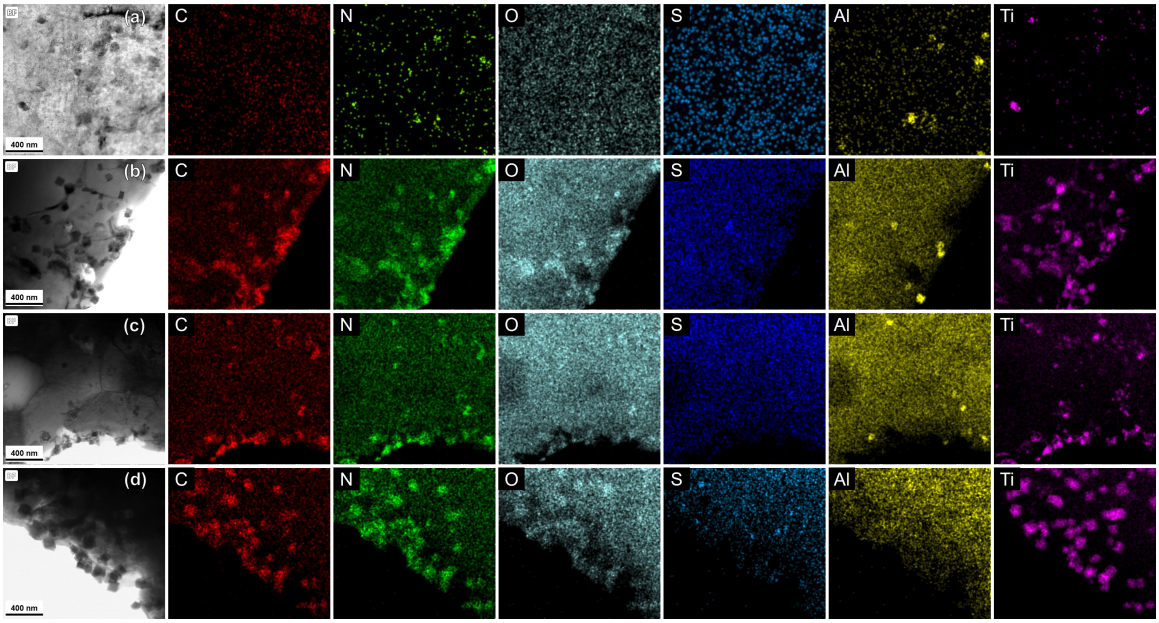

Figure 4.4: STEM data from twin-jet electropolished sections of (a) FeMnAlC, (b) FeMnAlC-0.2Ti, (c) FeMnAlC-0.5Ti, and (d) FeMnAlC-2Ti powder particles. Each panel comprises a bright field (BF) image and a corresponding set of normalized X-ray intensity maps from an EDXS spectrum imaging experiment on the same area. Scale bars correspond to 400 nm in all images.

4.4 Production of L-PBF samples

Figure 4.5 shows the as built density cubes created with the four powders. When moderate concentrations of Ti are added to the composition (0.2 wt.% in FeMnAlC-02Ti and 0.5 wt.% in FeMnAlC-05Ti), the process window narrows, and some cubes are stopped to prevent the whole structure from failing. This failure is due to the effect of the samples with the powder recoater, which might be detrimental. Due to heat and mass transmission, high energy densities lead molten material to concentrate on the boundary, resulting in thick patches of solidified material [280]. To prevent

the powder recoater from hitting these thick material patches producing non-uniform powder layers or even carryover of material, the printing process of the affected cubes is stopped. For the cubes produced using FeMnAlC-02Ti and FeMnAlC-05Ti powders, conditions 7 and 8 with high VED values and a laser power of 175 W failed, however condition 2 with a greater VED than condition 7 but a lower laser power is still printable. Nevertheless, no cubes had to be stopped when printing the FeMnAlC-2Ti, even if the amount of Ti is four times higher than that of FeMnAlC-05Ti. Note that printing conditions are detailed in Appendix A.

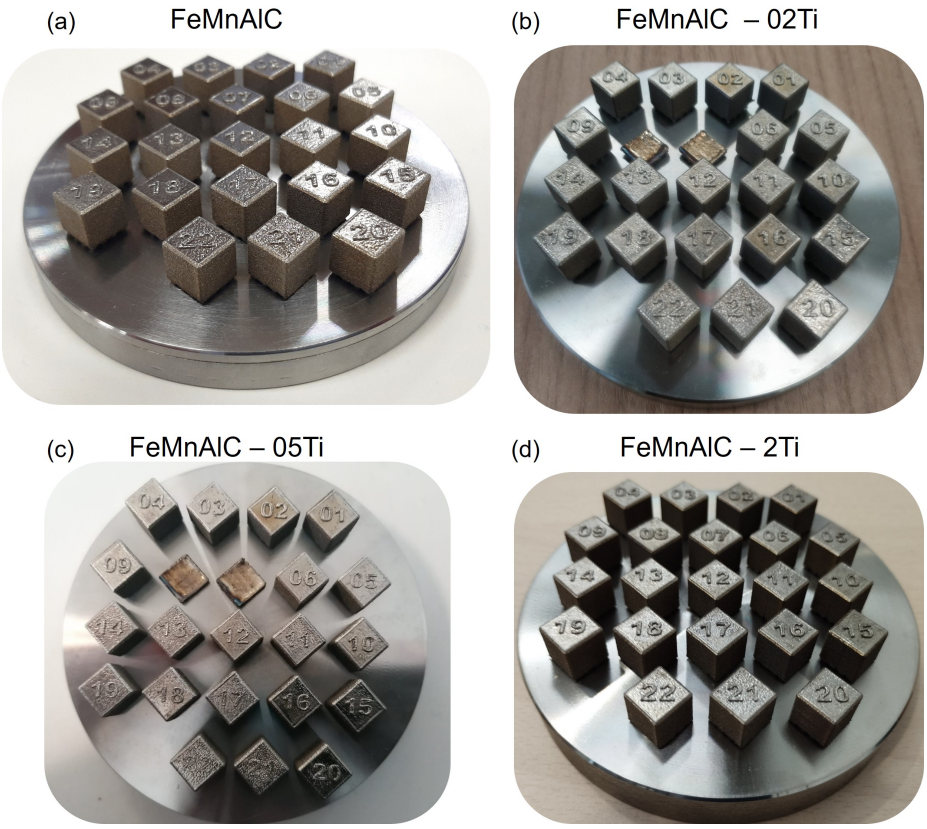

Figure 4.5: Density cubes printed using the steel powders (a) FeMnAlC, (b) FeMnAlC-02Ti, (c) FeMnAlC-05Ti, (d) FeMnAlC-2Ti.

Figure 4.6 shows cross sections of the density cubes for the four investigated alloys. Fully dense cubes (relative density >99.9%) are obtained with all powders. However, cubes built using the FeMnAlC-2Ti material show large cracks nucleating at the sharp angles of the base of the cubes. This is due to the fact that these notched areas are prone to stress accumulation that can eventually lead to fracture. To avoid this issue, a stress-relieving heat treatment may be performed before handling the samples, or alternatively, the supporting structures might be modified to eliminate acute angles. For complex shape geometries, however, effective mitigation of cold cracking becomes difficult or impossible. Thus, alloys free of this cracking problem are preferable to allow processability at industrial scale.

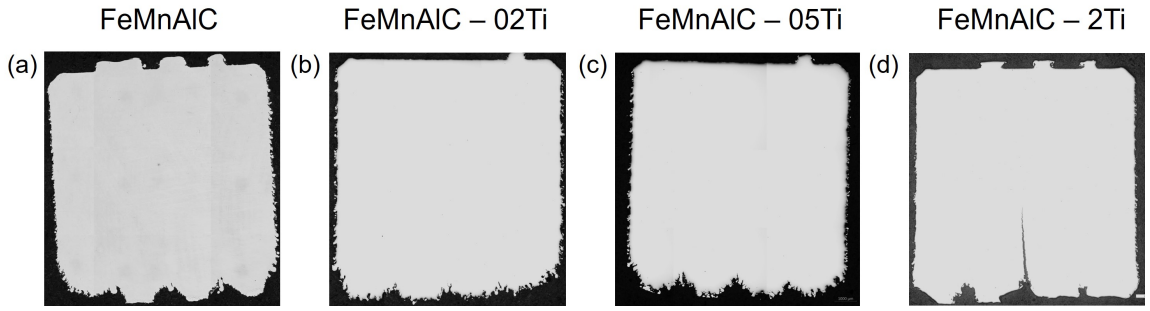

Figure 4.6: Cross section of the L-PBF printed dense cubes printed using (a) FeMnAlC, (b) FeMnAlC-02Ti, (c) FeMnAlC-05Ti and (d) FeMnAlC-2Ti powders.

4.5 Microstructure development during L-PBF process

The microstructure of the High Mn Fe-Mn-Al-C low density steel printed cubes with different contents of Ti was analyzed to study the influence of Ti on the final microstructure in L-PBF samples.

First, the microstructure in both powders and printed material of the various compositions was analyzed by XRD, considering that powder shows the solidification structure whereas printed materials are subjected to both solidification and the influence of IHT during L-PBF process. Moreover, powders of different fraction sizes were studied to examine the effect of cooling rate on microstructure, since smaller powder particles solidify quicker than larger ones. Figure 4.7 shows the measured spectra of the four compositions in powder fractions F1 and F2, as well as in density cubes, while Table 4.3 provides the phase quantification of the spectra. In all powders, the main diffraction peaks are due to austenite. In addition, ferrite was identified in FeMnAlC-05Ti and FeMnAlC-2Ti powders, where diffraction peaks from different planes of ferrite are detected. Also, in the FeMnAlC and FeMnAlC-0.2Ti powders the first ferrite diffraction peak at 44^{o} was identified. Nevertheless, ferrite was not detected in cubes printed using the FeMnAlC and FeMnAlC-02Ti powders, and its content decreases in the cubes printed with the FeMnAlC-05Ti and FeMnAlC-2Ti steels, as compared to their respective reference powders. Moreover, powders and cubes printed using

the FeMnAlC-2Ti composition, show peaks other than ferrite and austenite at angles 35.5°, 42°, 61° and 77°, enabling the identification and quantification of Ti(C,N). XRD measurements prove that an increment of Ti up to 2 wt.% increases the fraction of Ti(C,N) as predicted by CALPHAD (Table 4.1). This shows that the L-PBF as built microstructure differs significantly from the fresh microstructure after solidification, given that the IHT during L-PBF promotes austenite reversion.

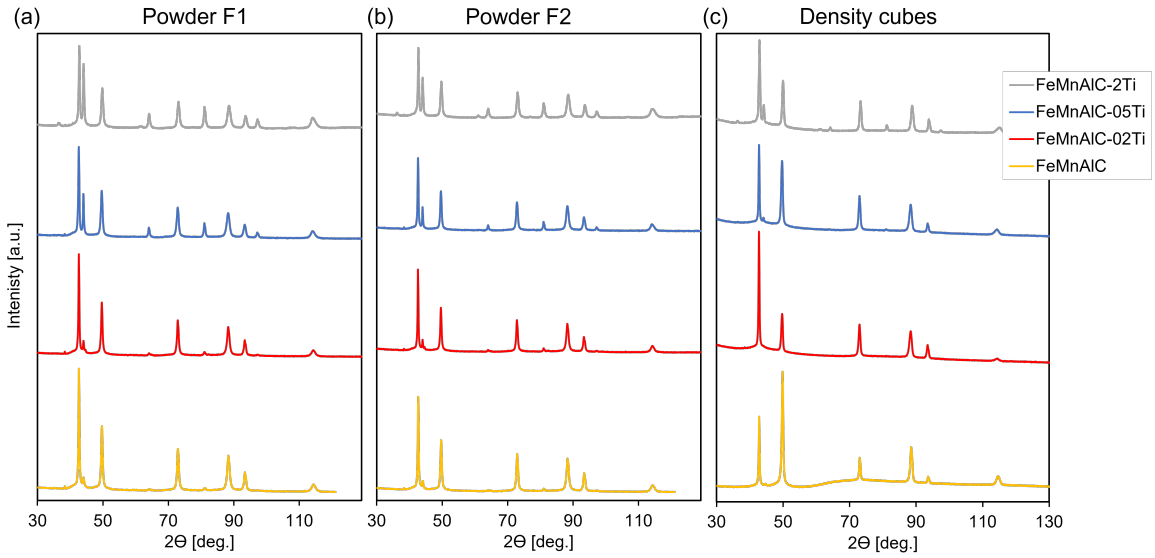

Figure 4.7: XRD data of FeMnAlC-xTi (a) F1 powders, (b) F2 powders and (c) L-PBF cubes.

The efficiency of Ti as a inoculant driven agent for grain refinement was evaluated by EBSD in the three compositions with Ti: crack-free FeMnAlC-02Ti and FeMnAlC-05Ti; and FeMnAlC-2Ti in a region far from the cold crack. Figure 4.8 shows the EBSD maps, in which the band contrast images are superposed onto the IPF oriented in the building direction (Figure 4.8a, c & e) and the transverse direction (Figure 4.8b,

d & f), where black lines are drawn to represent boundaries with misorientation higher that 15°.

Table 4.3
Quantification of phases (in wt.%) present in the F1 and F2 fractions of the powders and L-PBF cubes produced of FeMnAlC-xTi compositions, as determined by Rietveld refinement of XRD data, where the maximum error of the technique is estimated in ±2 wt.%. γ denotes austenite, and α ferrite.

	F1			F2			Cube		
Alloy	γ	α	others	γ	α	others	γ	α	others
FeMnAlC	bal.	<2	<2	bal.	<2	<2	bal.	<2	<2
FeMnAlC-02Ti	bal.	2	<2	bal.	2	<2	bal.	<2	<2
FeMnAlC-05Ti	bal.	13	<2	bal.	7	<2	bal.	2	<2
FeMnAlC-2Ti	bal.	27	2	bal.	19	2	bal.	7	2

The FeMnAlC-02Ti steel (Figure 4.8a-b) shows columnar grains that are slightly tilted relative to the building direction. This is comparable to the reference FeMnAlC composition (Figure 3.14a-b) where it is likely that the epitaxial growth follows a similar pattern. However, there may be variations coming from differences in the powders' optical and thermo-physical properties, and the printing parameters, particularly the laser powder and scanning speed, which results in varying energy inputs. In contrast, the FeMnAlC-05Ti and FeMnAlC-2Ti compositions (Figure 4.8c-f) exhibit a combination of columnar grains within the melt pool, with dimensions ranging from 1-2 times the layer thickness. In the spaces between the columnar grains there is a region of finer equiaxed grains. This region, which is more evident in FeMnAlC-05Ti steel than FeMnAlC-2Ti, may coincide with the initiation (bottom) of the melt pool or the layer, meaning that columnar grain growth is blocked by the CET zone, and

that grains are not able to cross the melt pools like in the case of FeMnAlC and FeMnAlC-02Ti.

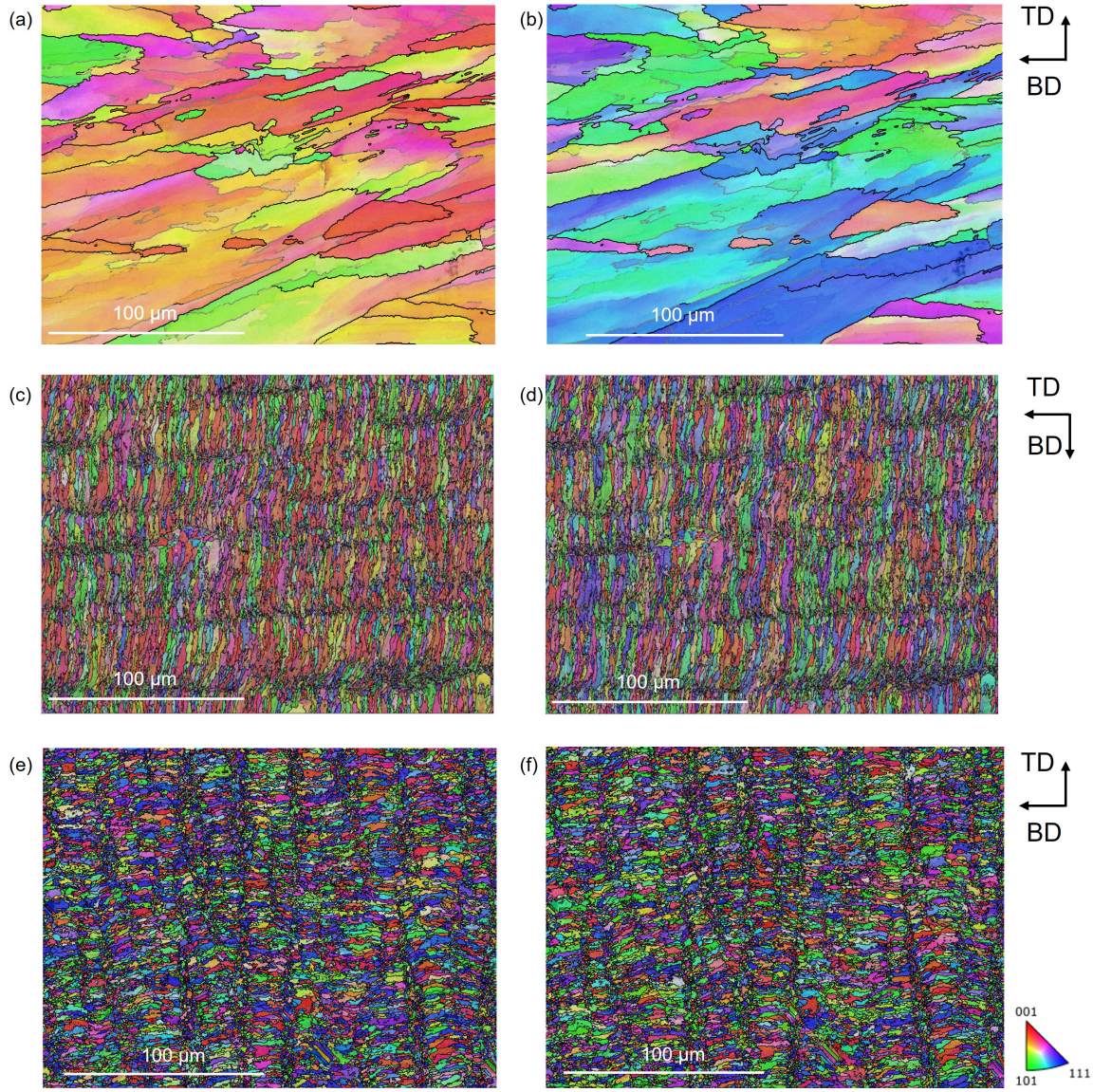

Figure 4.8: EBSD maps at x500 magnification in the center of the L-PBF samples for FeMnAlC-02Ti (a-b), FeMnAlC-05Ti (c-d), and FeMnAlC-2Ti (e-f) superposing the IPF at the direction parallel to building direction (a, c & e) and parallel the transversal direction (b, d & f), onto the band contrast.

The austenitic columnar grains in the FeMnAlC-05Ti and FeMnAlC-2Ti steels

presents a refinement of approximately 10 times the size in FeMnAlC and FeMnAlC-02Ti steels, thus demonstrating the effectiveness of Ti(C,N) as a grain refiner for these steel family. Table 4.4 collects the grain size quantification from EBSD maps, where the average grain size is approximated by the equivalent diameter, and the standard deviation is the error. The average grain size was calculated in 25.4 ± 23.9 μm for FeMnAlC steel, while the average grain size was refined up to 2.2 ± 1.7 μm in the FeMnAlC-05Ti composition and 3.9 ± 2.6 μm in the FeMnAlC-2Ti composition. The high standard deviation is due to the presence of smaller grains between the large ones. In the case of FeMnAlC-02Ti, smaller grain size was measured as compared to FeMnAlC grains, although there is no strong evidence of grain refinement, since the size of the map is not large enough to capture a statistically representative number of grains.

Table 4.4
Grain size quantification from EBSD maps, where the average grain size is approximated by the equivalent diameter, and the standard deviation is the error.

Alloy	Grain size (μm)
FeMnAlC	25.4 ± 23.9
FeMnAlC-02Ti	16.8 ± 21.6
FeMnAlC-05Ti	2.2 ± 1.7
FeMnAlC-2Ti	3.9 ± 2.6

Representative BSE SEM image and EBSD data from selected builds are presented in Figure 4.9 for a more detailed analysis of the effect of Ti at the melt pool level. For the Ti-free FeMnAlC sample (Figure 4.9a-c) there are coarse columnar grains that propagated through the melt pool boundaries, with no ferrite observed in the

EBSD data. Very similar microstructures are observed in the FeMnAlC-0.2Ti samples (Figure 4.9d-f). However, when the Ti content is increased to 0.5 wt.%, the BSE SEM images and the IPF maps reveal different features; the grain structures are much finer and more equiaxed, but the ferrite content is still low (Figure 4.9g-i). When the Ti content is further increased to 2 wt.% in Figure 4.9j-l, the BSE SEM images reveal a slightly finer grain structure, but the EBSD data show the emergence of a large volume fraction (≈15%) of ferrite. These fractions of ferrite detected are equivalent to the XRD observations in weight percentage (Table 4.3). The ferritic grains represented in red (Figure 4.9c, f, i & l), show an equiaxed shape and seem to concentrate at the boundaries of the melt pool, where the thermal condition and the local elemental segregation may be favorable for ferrite to form at these areas.

Crystallographic texture of austenitic grains was analyzed by PF. Figure 4.10 represents the PF of the main crystallographic planes (100), (110), and (111) in printed cubes of compositions FeMnAlC-02Ti (Figure 4.10a), FeMnAlC-05Ti (Figure 4.10b), and FeMnAlC-2Ti (Figure 4.10c). Similar to FeMnAlC (Figure 3.15a), both compositions with different additions of Ti experienced a propensity of preferential orientation of (100) planes along the building direction (BD). However, the intensity of this texture is strongly reduced in the FeMnAlC-05Ti and FeMnAlC-2Ti compositions, thereby demonstrating the potential of grain refinement in achieving randomly oriented grains, which in turn promotes isotropy. FeMnAlC-2Ti shows even lower degree of texture than FeMnAlC-05Ti. Perhaps the formation of higher fraction of ferrite

contributes the randomization of the texture.

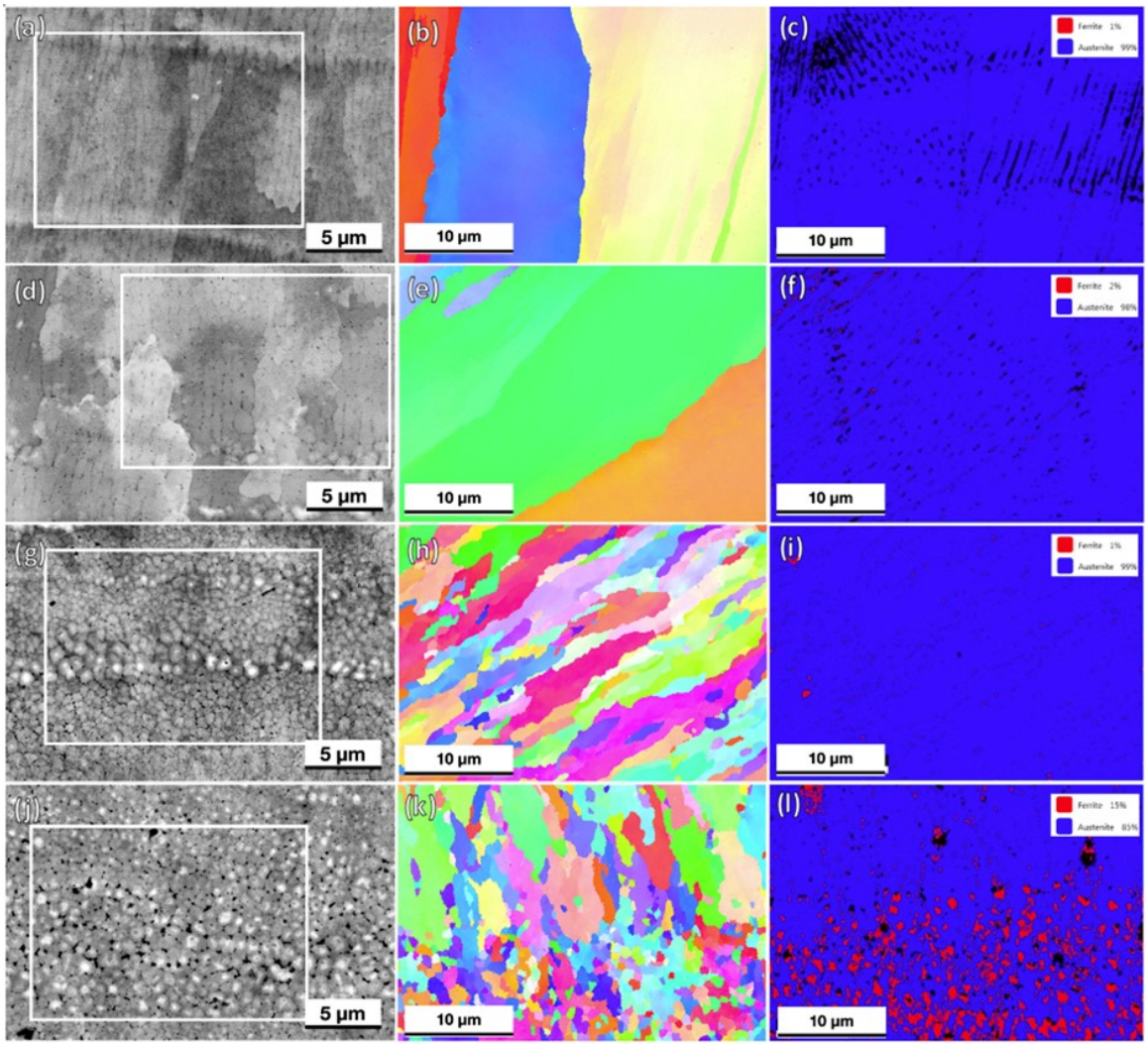

Figure 4.9: SEM data from printed parts of (a-c) FeMnAlC, (d-f) FeMnAlC-0.2Ti, (g-i) FeMnAlC-0.5Ti, and (j-l) FeMnAlC-2Ti. (a) & (d) & (g) & (j) BSE images of the cross-section microstructure, (b) & (e) & (h) & (k) EBSD IPF maps, and (c) & (f) & (i) & (l) EBSD phase distribution maps.

STEM studies on the electropolished foils reveals further details of the microstructure as shown in Figure 4.11 and Figure 4.12; these include high-angle annular dark field (HAADF) images and STEM EDXS maps from selected builds for each composition.

In the Ti-free FeMnAlC printed cube shown in Figure 4.11a, all the precipitates are Al-rich, and none of the Ti-rich precipitates was found. As the Ti content is increased to 0.2 wt.%, Ti-rich precipitates are observed along the columnar grain boundaries and these coexist with Al-rich precipitates (Figure 4.11b).

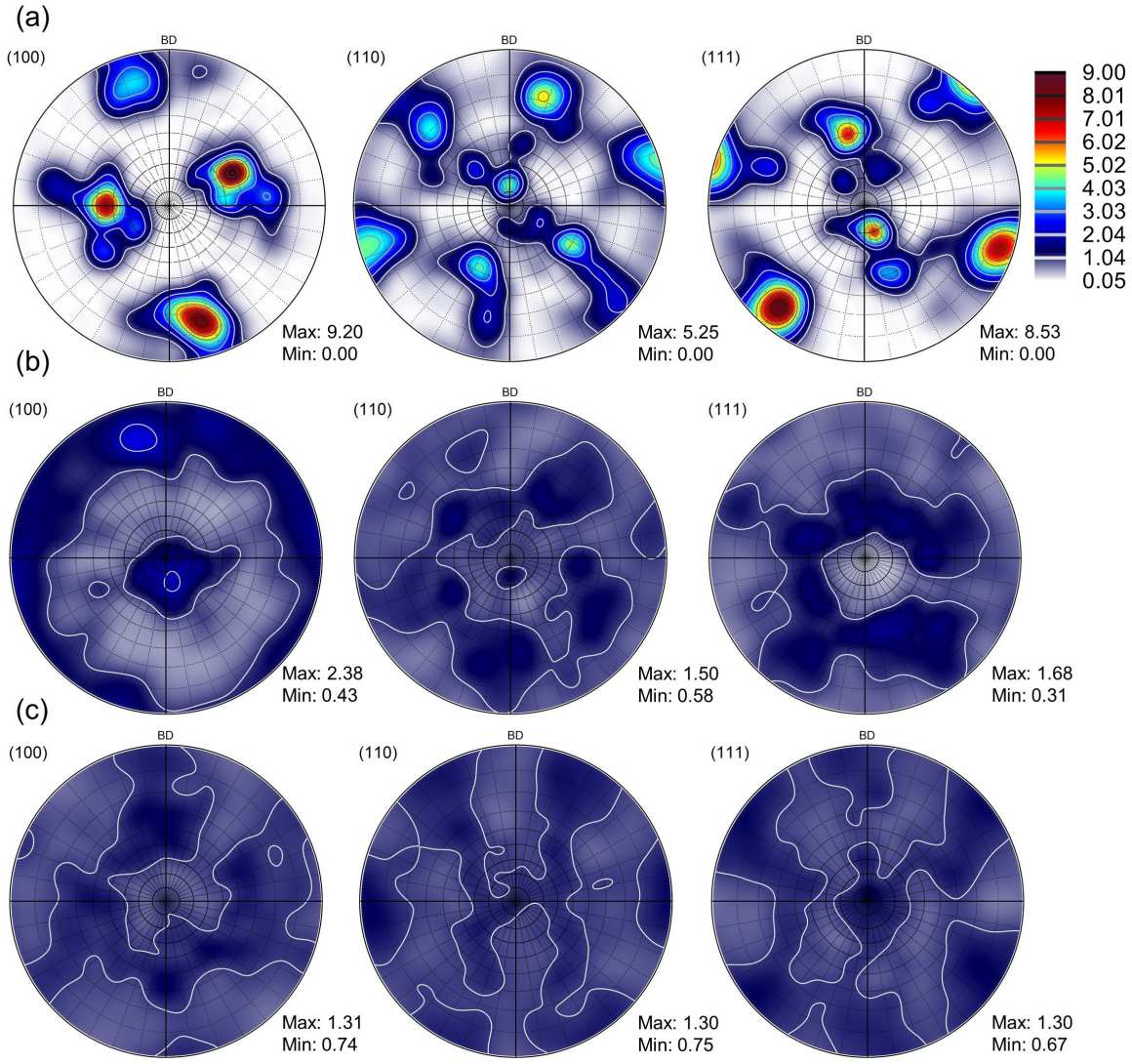

Figure 4.10: Pole Figures of the crystallographic planes (100), (110) and (111) in the L-PBF samples of composition (a) FeMnAlC-02Ti, (b) FeMnAlC-05Ti, and (c) FeMnAlC-2Ti. Note that BD refers to the building direction.

.

For the FeMnAlC-0.5Ti cube in Figure 4.12a, the STEM data show finer and more equiaxed grain structures with some precipitates within the grains in addition to those formed on the boundaries. When the Ti content is increased to 2 wt.%, no Al-rich precipitates are observed in the printed samples and instead a very high density of Ti-rich precipitates is present (Figure 4.12b). This is consistent with the results from the corresponding powders. We observe that the sizes (<100 nm) of the precipitates in the printed parts are smaller than those (<300 nm) in the corresponding powders. There is some evidence for the segregation of sulfur in each of these parts, and in each case, this appears to be co-located with the precipitates.

These microstructural analyses and results are in agreement with the CALPHAD calculations and show evidence that the major grain refinement is caused during the solidification by formation of Ti(C,N) inoculants.

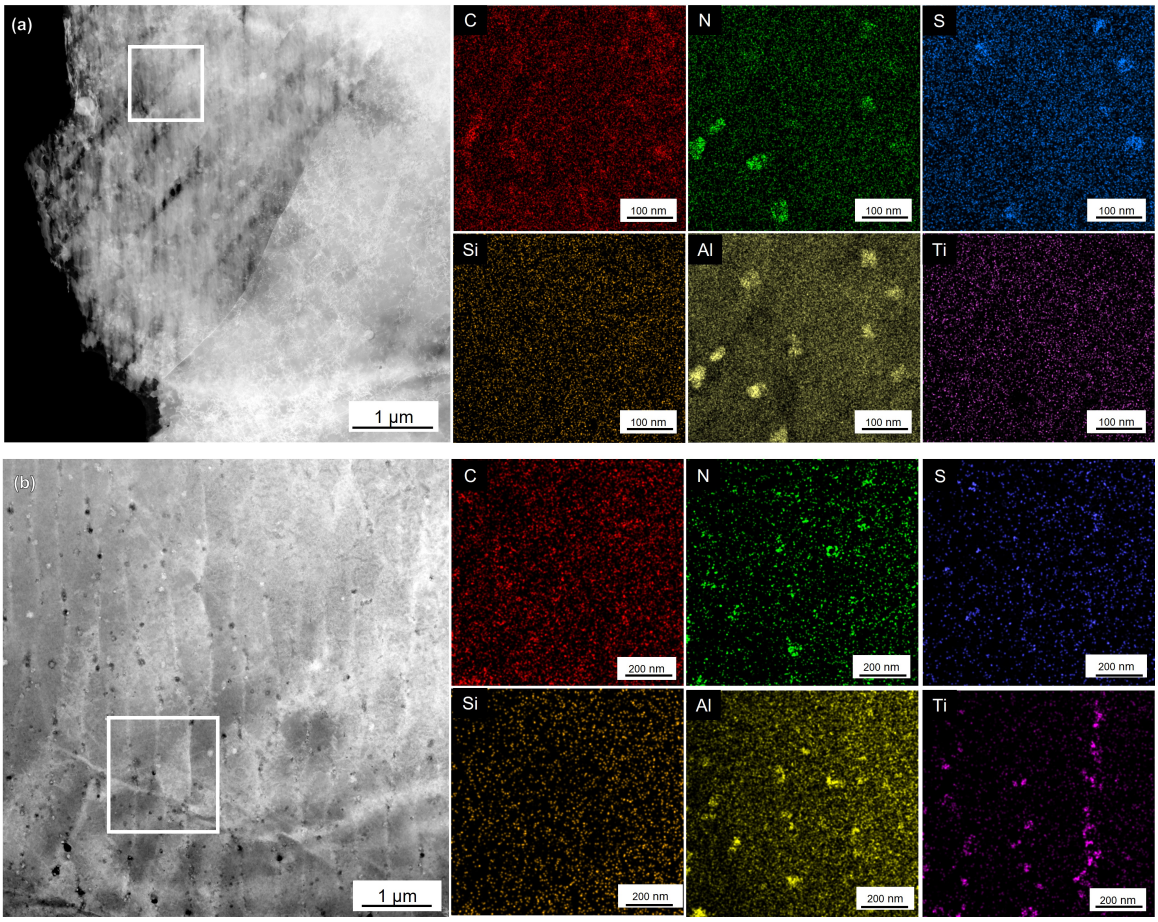

Figure 4.11: STEM data from twin-jet electropolished samples of (a) FeMnAlC and (b) FeMnAlC-0.2Ti of printed parts. Each panel comprises a HAADF image and a corresponding set of normalized X-ray intensity maps from an EDXS spectrum imaging experiment on the selected area.

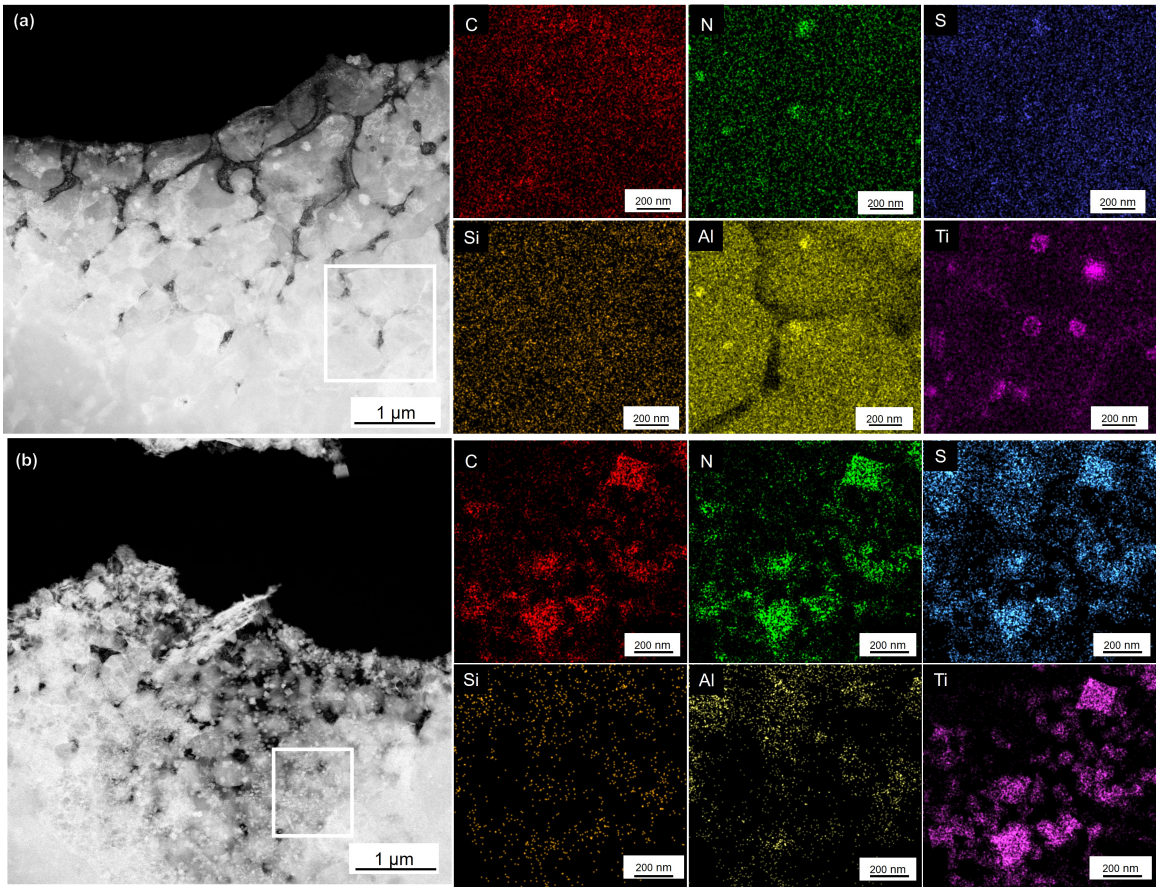

Figure 4.12: STEM data from twin-jet electropolished samples of (a) FeMnAlC-0.5Ti and (b) FeMnAlC-2Ti of printed parts. Each panel comprises a HAADF image and a corresponding set of normalized X-ray intensity maps from an EDXS spectrum imaging experiment on the selected area.

4.6 Summary and conclusions

The influence of adding Ti into a FeMnAlC steel composition investigation was motivated by CALPHAD calculations, which predict that the addition of Ti could induce a modification in the primary phase that is formed during solidification, hence potentially serving as inoculant. The four compositions with different levels of Ti present good quality for AM. Furthermore, these additions of Ti have been confirmed to modify the microstructure of the powders, by increasing the ferrite fraction (specially in FeMnAlC-2Ti) and reducing the matrix grain size. However, the austenitic grains show consistent epitaxial shape and size until 0.2 wt.% of Ti, and evidence of grain refinement and more equiaxed shape is not plausible until 0.5 wt.% of Ti.

The precipitates observed in the powder through experimental techniques, are consistent with the predictions made by the CALPHAD method. In the absence of Ti, only precipitates rich in Al are formed. However, when Ti is added into the composition, precipitates rich in Ti coexist with the Al-rich precipitates, up to a certain value. Beyond it, the Al-rich precipitates disappear (FeMnAlC-2Ti). The distribution of AlN in the microstructure was found to be homogeneous. However, Ti(C,N) exhibited a concentration near the grain boundaries, particularly in cases where grain refinement was observed.

Fully dense crack-free samples were successfully printed in L-PBF using FeMnAlC, FeMnAlC-0.2Ti, and FeMnAlC-0.5Ti steels. However, it was observed that samples

printed with FeMnAlC-2Ti showed cold cracks, which were found to originate at the sharp angles of the cube base.

The differences in microstructure were confirmed by XRD analyses, wherein the additions of Ti lead to an increment in the fraction of ferrite. However, this increment is lower when compared to the powder samples. This observation is likely attributed to the influence of the IHT, since cooling rates in L-PBF are higher than in powder atomization process, and the fine powder (F1) which cools down faster than F2 fraction, shows higher ferrite fraction.

EBSD maps obtained from the printed samples provide evidence of grain refinement in the matrix, which was observed in the FeMnAlC-05Ti and FeMnAlC-2Ti powders. These additions of Ti in the steel achieve a reduction in grain size by one order of magnitude, as well as a randomization of the crystallographic texture. The lack of grain refinement evidence with 0.2 Ti wt.% could indicate that a minimum amount of Ti(C,N) is necessary to achieve a significant grain refinement effect.

The HAADF images and STEM EDXS maps in the printed parts show comparable findings regarding the presence and distribution of precipitates when compared to those observed in the powder. Nevertheless, it is worth noting that finer Ti(C,N) where found in the printed part than in the powder, which could suggest that these precipitates may have undergone dissolution and subsequent re-precipitation during L-PBF process.

Chapter 5

Towards industrialization

In this chapter, the mechanical properties of the High Mn Fe-Mn-Al-C low density steels developed for AM are studied. These properties refer to their response to applied forces or loads, which are essential in industry for predicting the behavior of materials under different conditions.

5.1 General mechanical properties

5.1.1 Mechanical hardness

The mechanical hardness of several High Mn Fe-Mn-Al-C low density steels was evaluated in order to anticipate and assess differences in their mechanical behavior. In order to evaluate the homogeneity of hardness in samples produced using L-PBF, an initial micro hardness test was conducted throughout the whole cross section of a dense cube sample. Figure 5.1 shows the evolution in microhardness for the FeMnAlC reference composition, where the hardness homogeneity along the cross section is evident, with values around 300 HV regardless of the specific place being tested.

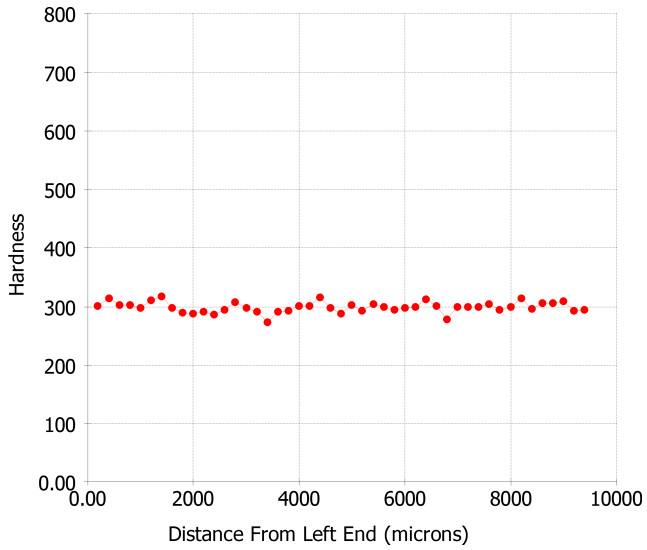

Figure 5.1: Microhardness evolution in FeMnAlC L-PBF dense cube cross section.

In order to evaluate the mechanical hardness of the different Fe-Mn-Al-C low density steels, a series of 7 Vickers hardness measurements were taken throughout the cross section of L-PBF cubes printed with different parameters (energy input), using a load of 10 kg. The resulting values were then averaged to get a representative estimate of hardness. Figure 5.2 shows the hardness of dense cubes printed under different L-PBF conditions for three compositions: FeMnAlC, FeMnAlC-1Si, and FeMnAlC-2Si, where hardness values remain consistent regardless of the printing conditions. This characteristic is significant as it demonstrates the resilience of the microstrucutre against variations in printing conditions and solidification velocities and profiles. Similar hardness values are observed for both FeMnAlC and FeMnAlC-1Si, independently of the printing parameters. It is worth to mention that some HC occurs in the FeMnAlC-1Si composition, which might result in a reduction in hardness due to the presence of internal cracks. In contrast, fully dense FeMnAlC-2Si cubes experience an increase in hardness of around 50 HV as compared to the FeMnAlC counterparts for each set of printing conditions. Furthermore, hardness was also measured on the sole cube that could be successfully printed using FeMnAlC-4Si powder until the completion of the printing process (Figure 3.5f) exhibiting several long cracks. Hardness measurements were conducted in regions distant from fractures and yielded an average value of 515 HV10, which supports the hypotheses that residual stresses and cold cracking are responsible for the brittle fracture observed in this composition. In addition to

its impact on HC, the influence of Si on solution hardening in steels has been recognized [308].

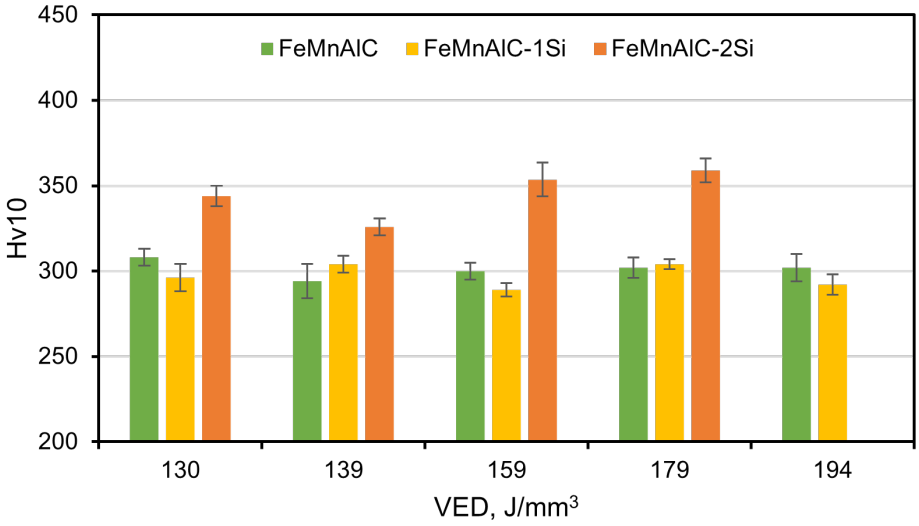

Figure 5.2: Vickers hardness HV10 of L-PBF dense cubes printed under different conditions for compositions FeMnAlC, FeMnAlC-1Si, and FeMnAlC-2Si.

The hardening effect of titanium was investigated in a similar manner. The hardness of several sets of L-PBF dense cubes, which were printed using differed parameters, were evaluated for the three levels of titanium investigated in Chapter 4. Figure 5.3 displays the hardness values measured from dense L-PBF cubes under different printing conditions. Hardness increase was observed with the addition of different levels of Ti to the reference composition (FeMnAlC). Even the small addition of 0.2 wt.% of Ti in FeMnAlC-02Ti leads to increased hardness. This may be attributed to two factors: a slightly reduced grain size and the precipitation strengthening of Ti(C,N) in addition to AlN. Nevertheless, a significant increase in hardness (about 50 HV10)

was measured in the FeMnAlC-05Ti composition, where the grain size is reduced by a factor of 10 in comparison with the reference composition (Table 4.4). In contrast, the hardness of FeMnAlC-2Ti is lower in comparison to FeMnAlC-05Ti. The difference in hardness is particularly greater at high VED printing conditions ($> 200 J/mm^3$). Regarding than the size of grains and Ti(C,N) precipitates are comparable between these two steel composition, the lower hardness observed in the FeMnAlC-2Ti as compared to the FeMnAlC-05Ti may be attributed to the larger amount of ferrite in the microstructure (Figure 4.7 and Table 4.3), and this ferrite fraction becomes larger at high printing VED values. This implies that the most favorable addition of Ti for this specific steel grade is closer to 0.5 wt.% in order to provide optimal hardening properties and prevent the risk of cold cracking.

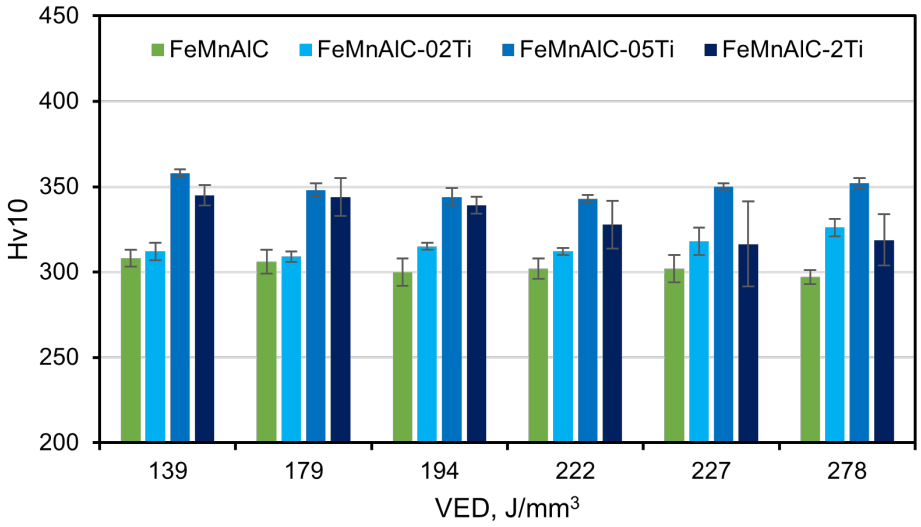

Figure 5.3: Vickers hardness HV10 of L-PBF dense cubes printed under different conditions for compositions FeMnAlC, FeMnAlC-02Ti, FeMnAlC-02Ti and FeMnAlC-2Ti.

Finally, the combined hardening effect of Ti and Si in the FeMnAlC steel composition was studied. To explore this effect, a new composition, denoted as FeMnAlC-2Si-05Ti, was produced by adding 2 wt.% of Si and 0.5 wt.% of Ti into the reference composition FeMnAlC. The hardness of FeMnAlC-2Si and FeMnAlC-05Ti exhibited similar values, with an approximate increase of 50 HV10 compared to the reference composition of FeMnAlC (Figure 5.2 and Figure 5.3). The incorporation of both elements in those amounts results in a linear increment of 50 HV10, hence leading to a total increase of 100 HV over the reference composition of FeMnAlC (Figure 5.4).

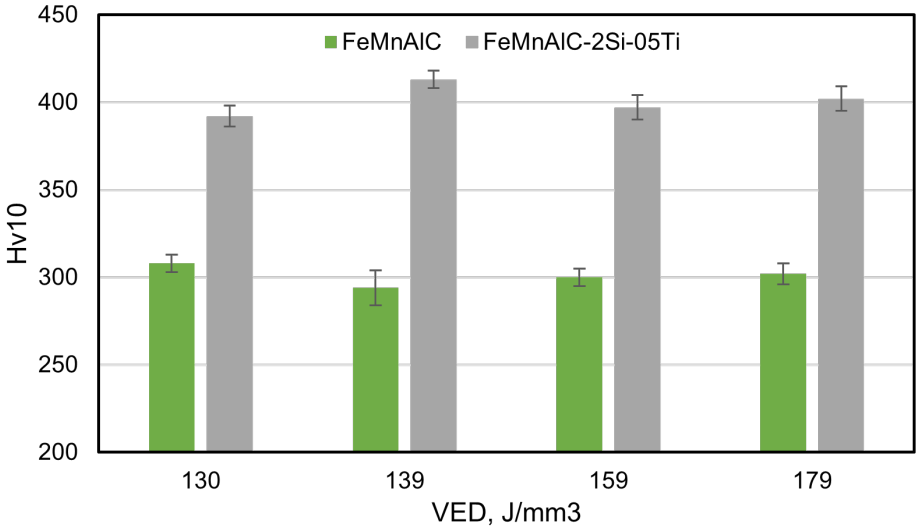

Figure 5.4: Vickers hardness 10 of L-PBF dense cubes printed under different conditions for compositions FeMnAlC and FeMnAlC-2Si-05Ti.

Table 5.1 presents a summary of the hardness values for different grades of High Mn Fe-Mn-Al-C steels, together with the corresponding measured density. The hardness and density values correspond to the average value obtained from measurements performed on the dense cubes printed with different parameters, together with the

standard deviation of these measurements.

The density values of all High Mn Fe-Mn-Al-C low density steels studied in L-PBF were found to be below 7.0 g/cm^3, and the additions of Si and Ti lead to further reduction in density, reaching a minimum value of 6.70 g/cm^3 in the FeMnAlC-2Si-05Ti grade.

Table 5.1
Hardness and density values of the different Fe-Mn-Al-C low density steels studied in L-PBF.

Alloy	Hardness (HV10)	Density (g/cm^3)
FeMnAlC	301 ± 4	6.97 ± 0.02
FeMnAlC-1Si	296 ± 6	6.92 ± 0.01
FeMnAlC-2Si	348 ± 14	6.85 ± 0.01
FeMnAlC-02Ti	314 ± 6	6.88 ± 0.02
FeMnAlC-05Ti	351 ± 6	6.83 ± 0.01
FeMnAlC-2Ti	332 ± 12	6.80 ± 0.01
FeMnAlC-2Si-05Ti	400 ± 9	6.70 ± 0.01

5.1.2 Tensile properties

The investigation of the tensile properties of the different High Mn Fe-Mn-Al-C low density steels was conducted in the as built state to determine the level of strength and ductility response of these steels in accordance with the ASTM E8/E8M standard. Figure 5.5 depicts a representation of the CAD file with an image presenting the printed samples that remain still attached to the build platform.

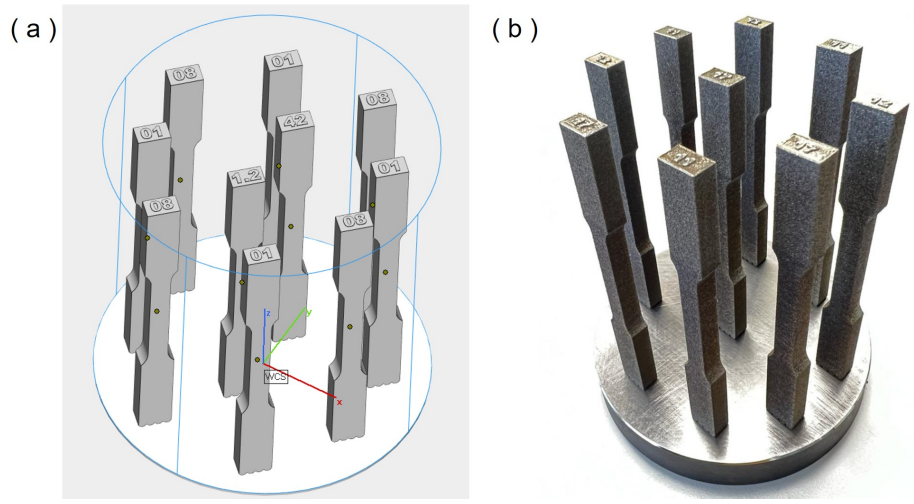

Figure 5.5: Rectangular subsize ASTM E8/E8M tensile specimens (a) designed by CAD and (b) printed in L-PBF.

5.1.2.1 Tensile properties of FeMnAlC steel printed by L-PBF

The FeMnAlC steel was subjected to testing under two printing conditions, parameters 11 and 17, with VED values of 139 and 130 J/mm^3, respectively, that are considered optimum in terms of printing density and process productivity. Each condition was evaluated using a total of three specimens. Figure 5.6 shows the tensile curves obtained in samples printed using an energy of 139 J/mm^3 (in blue), and the curves obtained under a printing energy of 130 J/mm^3 (in orange).

The tensile curves exhibit consistency, particularly in terms of yield and ultimate strength, both for the same printing parameters and among similar optimal printing parameters (see Figure 5.6). The overall elongation exhibits the maximum relative variability of 5%. This variability translates into a coefficient of variation between

10-12% in the total strain. The as built state of FeMnAlC exhibits very promising tensile properties, characterized by strength values of YS ranging from 570-600 MPa and UTS from 740-760 MPa, as well as an exceptional ductile behavior, with a TE response of 42-47%. The observed tensile properties suggest that the material has the potential to exhibit excellent energy absorption behavior. The multiplication of the UTS and the TE yields an early indication of the material's capacity to absorb energy, resulting in encouraging values approximately to 35000 MPa·%.

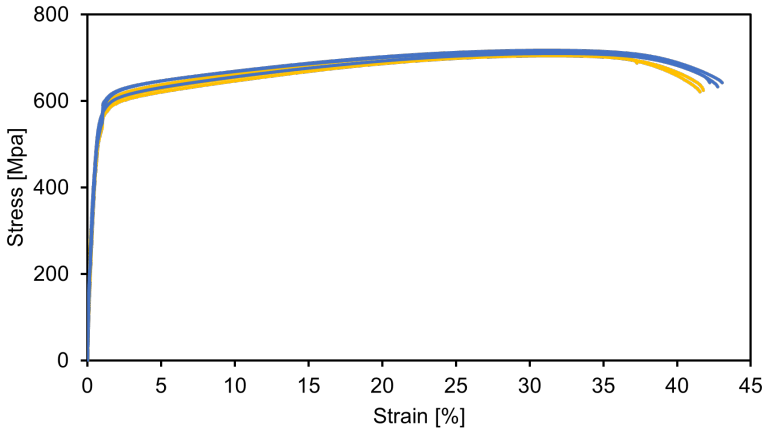

Figure 5.6: Tensile curves of as built FeMnAlC steel in L-PBF printed with a VED value of 139 J/mm^3 in blue and 130 J/mm^3 in orange.

The fracture surfaces shown in Figure 5.7 exhibit the presence of a micromechanism characterized by ductile behavior. This is observed in regions containing microscopic micro-holes, which indicate the occurrence of ductile mechanisms.

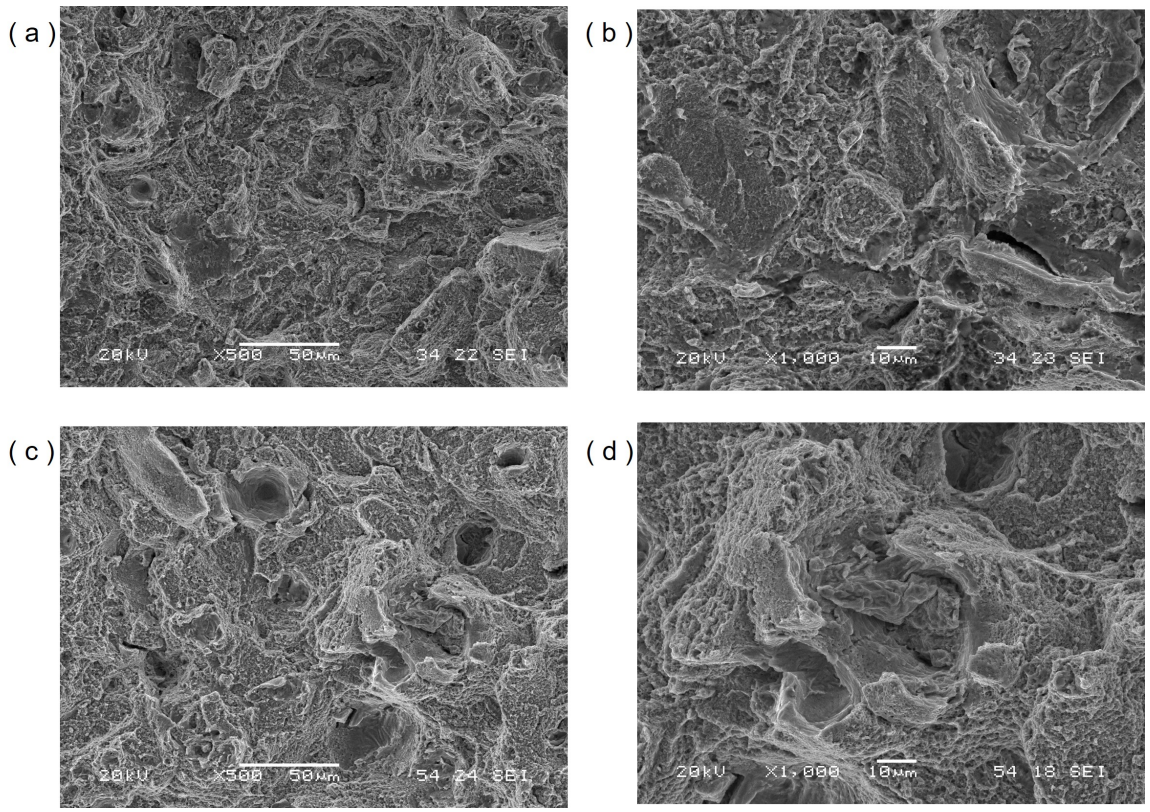

Figure 5.7: Fracture surface of L-PBF tensile specimens of FeMnAlC steel printed under (a-b) 130 J/mm^3 and (c-d) 139 J/mm^3 VEDs. Images were taken at different magnifications (a, c) x500 and (b,d) x1000.

5.1.2.2 Tensile properties of FeMnAlC-2Si steel printed by L-PBF

The hardening effect of Si, as seen in Figure 5.2, was also tested in the FeMnAlC-2Si tensile specimens. This composition was chosen because the formation of hot and cold cracks is prevented. Specimens were printed using the same parameters employed in FeMnAlC steel, characterized by VED values of 130 and 139 J/mm^3.

Figure 5.8 illustrates the tensile behavior of FeMnAlC-2Si steel. Tensile strength

remains also consistent among sister specimens, and specimens with different energy printing parameters. When comparing these results with the tensile curve of FeMnAlC steel presented in Figure 5.6, it becomes evident that the addition of Si has a strengthening impact, leading to an increase in both YS and UTS by approximately 200 MPa. However, it is worth noting that this enhancement in tensile strength is accompanied by a reduction in the TE, which is decreased to 16-20%.

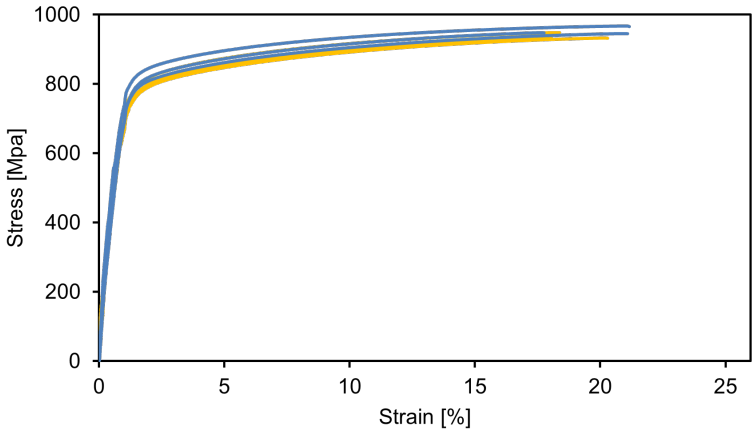

Figure 5.8: Tensile curves of as built FeMnAlC-2Si steel in L-PBF printed using a VED value of 130 J/mm^3 in blue and 139 J/mm^3 in orange.

Figure 5.9 shows the fracture surface at different magnifications of two samples of FeMnAlC-2Si tensile specimens printed using energies of 130 J/mm^3 (Figure 5.9a-b) and 139 J/mm^3 (Figure 5.9c-d). The fracture surfaces exhibit the presence of a micromechanism characterized by a combination of ductile and brittle behaviour. This is observed in regions containing microscopic micro-holes, which indicate the occurrence of ductile mechanism. Additionally, areas displaying quasi-cleavage and secondary cracking are observed indicating the presence of brittle micromechanisms.

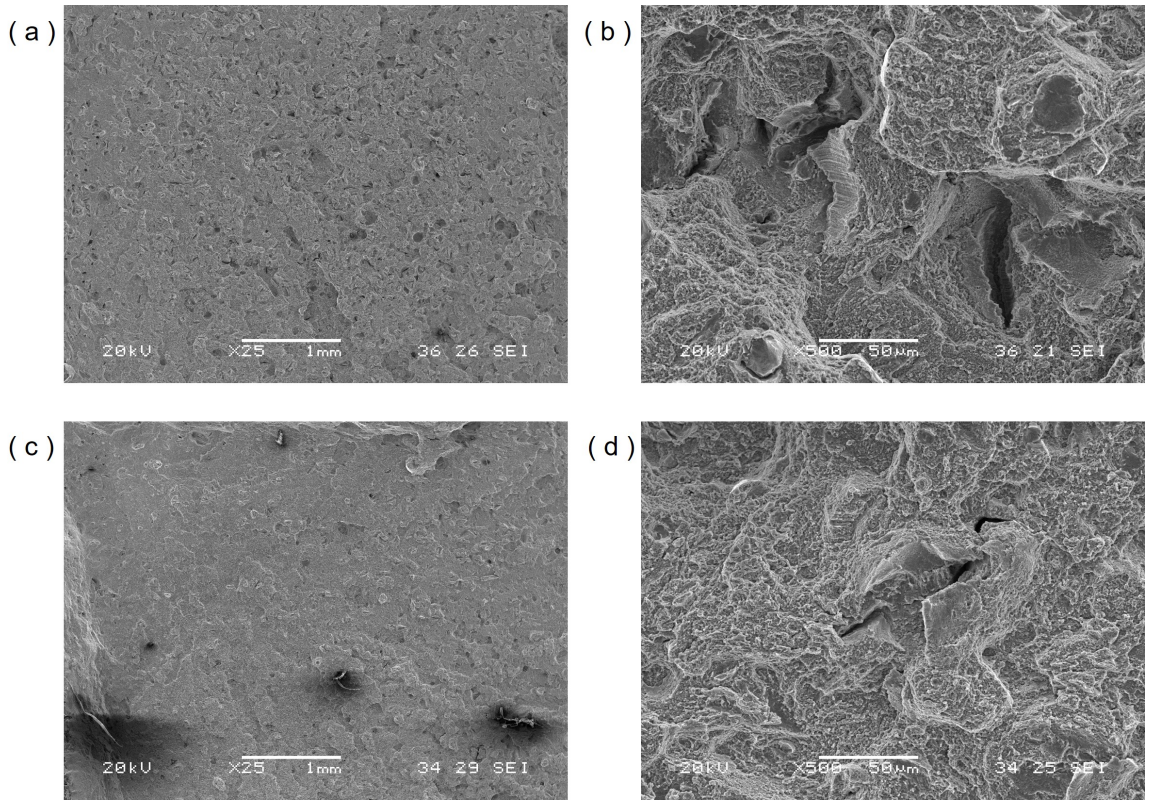

Figure 5.9: Fracture surface of L-PBF tensile specimens of FeMnAlC-2Si steel printed using VED of (a-b) 130 J/mm^3 and (c-d) 139 J/mm^3. Images were taken at different magnifications (a, c) x25 and (b,d) x500.

Fracture mechanisms are consistent in both samples indicating that it is predominately governed by the material, with no observed variations with the printing conditions.

5.1.2.3 Tensile properties of FeMnAlC-05Ti steel printed by L-PBF

Furthermore, the strengthening effect of Ti additions FeMnAlC steel was investigated through tensile tests in FeMnAlC-05Ti steel. In order to assure good density values

and prevent failure during the printing process of this composition, it was necessary to limit the laser power to 150 W. It should be noted that even though denser samples were obtained with higher VED values compared to the VED values employed in FeMnAlC and FeMnAlC-2Si compositions, the aforementioned laser power restriction was still necessary.

The tensile behavior of FeMnAlC-05Ti exhibits similarities to that of FeMnAlC-2Si (Figure 5.10). Tensile strength shows a significant increment of 200 MPa, but with a reduction in the TE to a range of 20-25%. This ductility performance is slightly better to that of FeMnAlC-2Si.

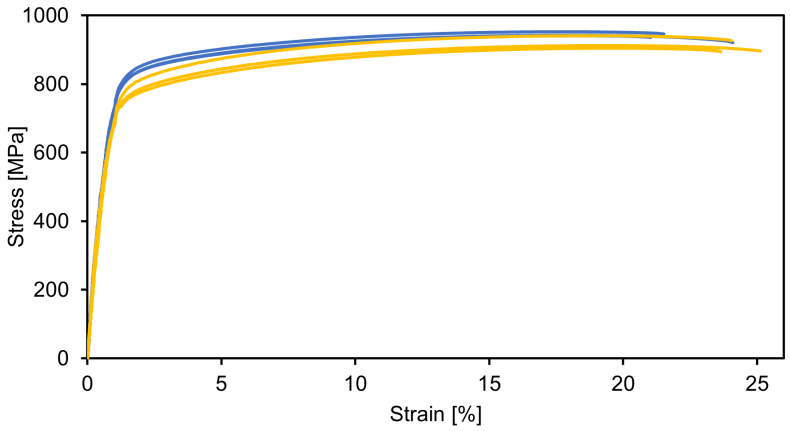

Figure 5.10: Tensile curves of as built FeMnAlC-05Ti steel in L-PBF printed with a VED value of 167 J/mm^3 in blue and 278 J/mm^3 in orange.

The fracture surfaces of FeMnAlC-05Ti steel presented in Figure 5.11 show a completely ductile behavior characterized by nucleation, coalescence and micro-hole

growth, with no signs of brittle failure, on contrary to observations in FeMnAlC-2Si composition (Figure 5.9).

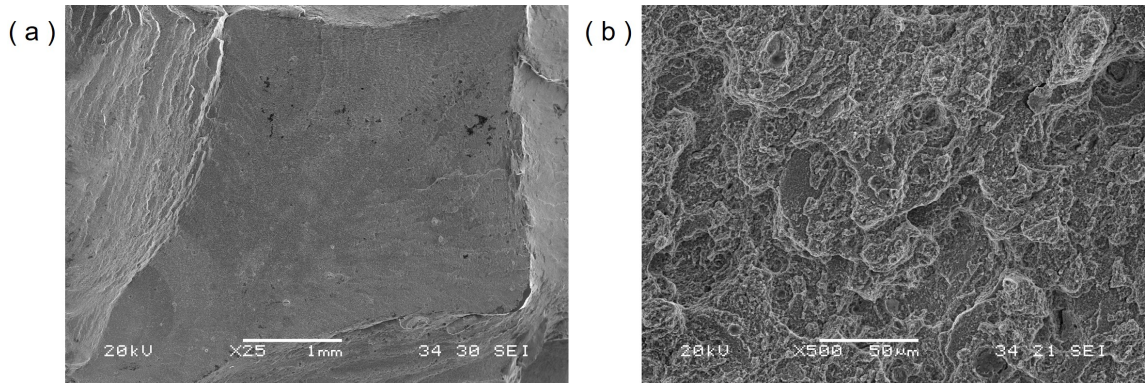

Figure 5.11: Fracture surface of L-PBF tensile specimens of FeMnAlC-05Ti steel at different magnifications (a) x25 and (b) x500.

5.1.2.4 Tensile properties of FeMnAlC-2Si-05Ti steel printed by L-PBF

The investigation of the strengthening mechanism resulting from the incorporation of Si and Ti into the FeMnAlC alloy composition was conducted by carrying out of tensile tests in the FeMnAlC-2Si-05Ti composition. Tensile curves are shown in Figure 5.12. Samples were fabricated using VED values of 139 J/mm^3 (in color blue in Figure 5.12) and 278 J/mm^3 (in color orange in Figure 5.12). Comparable tensile results are obtained in all specimens and confirm an increase in both YS and UTS by 400 MPa in comparison to the reference FeMnAlC composition. This increase might be attributed to a linear combination of solid solution strengthening from Si and the grain refinement resulting from the additions of Ti. Nevertheless, the TE experiences

an important drop and lies within the range of 4-6%.

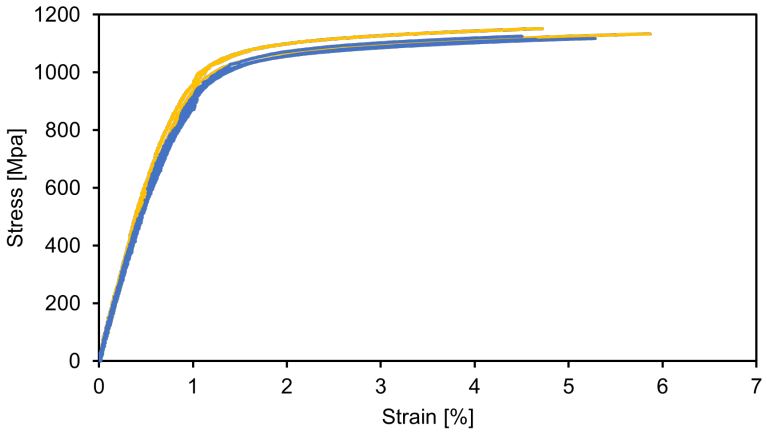

Figure 5.12: Tensile curves of as built FeMnAlC-2Si-05Ti steel in L-PBF printed using a VED value of 139 J/mm^3 in blue and 278 J/mm^3 in orange.

Fracture surfaces of this steel are shown in Figure 5.13. The fracture mechanism is similar to the one observed in FeMnAlC-2Si composition (Figure 5.9) characterized by a combination of ductile and brittle behavior.

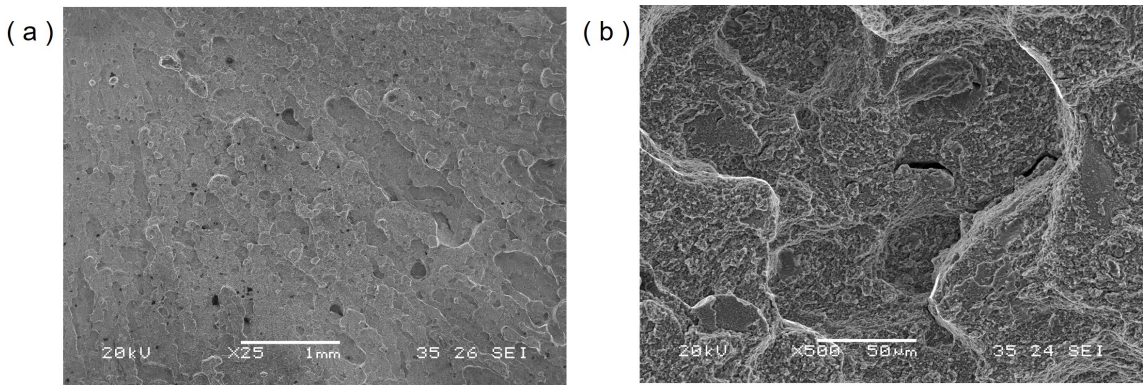

Figure 5.13: Fracture surface of L-PBF tensile specimens of FeMnAlC-2Si-05Ti steel printed at different magnifications (a) x25 and (b) x500.

5.1.2.5 Strain hardening mechanisms in High Mn Fe-Mn-Al-C low density steels

The tensile curves reveal an interesting phenomenon in the FeMnAlC-2Si, FeMnAlC-05Ti, and FeMnAlC-2Si-05Ti compositions, wherein the UTS is nearly reached before failure, which is different from the typical behaviour observed in the steel tensile curves. In contrast, the composition of FeMnAlC exhibits a tensile curve that follows a more conventional pattern, characterized by a decrease in strength after the UTS is reached i.e., necking, until failure occurs. The reason behind this remains unclear and falls outside the scope of this work; nonetheless, one hypothesis could be linked to the deformation mechanism and the presence of small grains in these steels. The strain hardening mechanism in High Mn Fe-Mn-Al-C low density steels remains a subject of ongoing debate in literature. The two main theories are: the microband induced plasticity (MBIP) theory and the slip band refinement induced plasticity (SRIP) theory [180, 179, 309]. Nevertheless, both hypotheses agree on the formation of co-planar glide deformation within the grains, and no presence of mechanical twinning [180].

At a microstructural level, it is possible that slip bands, which are unable to propagate across individual grains [309], could accumulate rapidly at grain boundaries and hinder further deformation beyond the UTS. Nevertheless, a deeper investigation of the deformation mechanisms of these steels would be necessary to disclose the strain

hardening mechanism observed.

The tensile properties of the four High Mn Fe-Mn-Al-C low density steels are compiled in Table 5.2. Both FeMnAlC-2Si and FeMnAlC-05Ti steels in the as built condition, have a UTS above 900 MPa while keeping ductility values around 20%, which is not covered with current steels in the market (Section 1.8). In addition, the FeMnAlC composition can compete with 316L (Section 1.8.1) since it provides similar YS and TE but with UTS higher than 700 MPa which is not reached with 316L. Furthermore, the FeMnAlC composition offers lower density and cost associated with alloying elements. These characteristics position this steel as a real alternative to replace 316L in many applications.

Table 5.2
Tensile properties of the different Fe-Mn-Al-C low density steels studied in L-PBF.

Alloy	YS (MPa)	UTS (MPa)	TE (%)
316L	450-590	640-700	36-59
FeMnAlC	570-590	735-755	42-47
FeMnAlC-2Si	725-770	935-960	16-20
FeMnAlC-05Ti	700-750	920-950	20-25
FeMnAlC-2Si-05Ti	885-925	1120-1150	4-6

5.2 In-use properties

The FeMnAlC composition was selected from the High Mn Fe-Mn-Al-C low density steels under investigation in order to conduct a deeper examination of additional mechanical properties. These properties are closely associated with specific applications, such as thermal stability, impact toughness, and energy absorption through lattice structures.

The selection of the FeMnAlC composition was based on its microstructural homogeneity in terms of phases, solidification structures size and morphology, grain size, morphology, and potential to become a candidate steel to substitute 316L in some applications by offering similar elongation, higher strength, and lower density and cost. Homogeneity is a crucial material characteristic in AM as it ensures consistent properties in a printed component with large dimensions or complex geometries, when variations in energy and solidification conditions may exist across different regions of the sample. Furthermore, this composition has notable similarities to 316L, serving as a valuable point of comparison for assessing the performance of this material in relation to these more specific features.

5.2.1 Thermal Stability of FeMnAlC steel printed by L-PBF

Various heat treatments were investigated in the FeMnAlC steel in order to assess their potential for modifying the L-PBF as built microstructure and, consequently, the mechanical properties of the steel. The temperatures investigated ranged from 250 to 850 °C, covering an extended range in which κ-carbides can be formed. In order to account for dynamic effects, various holding time periods were also examined. Ultimately, two cooling steps were considered: one involving exposure to ambient air, and the other involving rapid cooling in water. These quenching aims to keep the microstructure obtained at the end of the heat treatment.

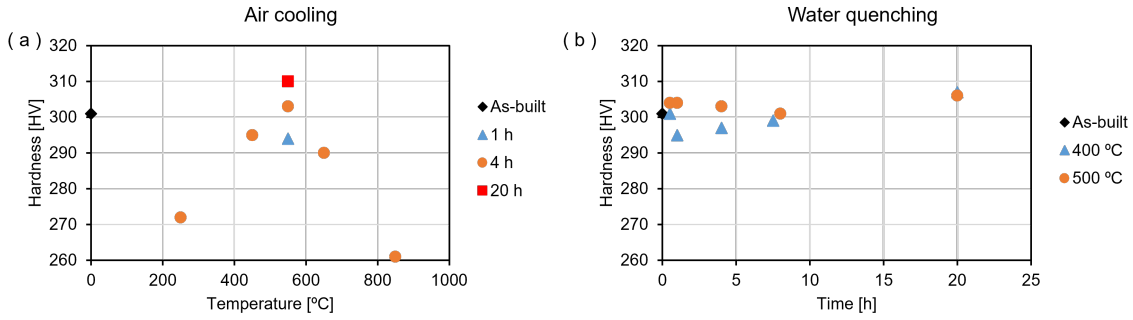

Figure 5.14: Hardness HV10 measurements on FeMnAlC L-PBF samples submitted at different time-temperature heat treatments and cooled in (a) air and (b) water quenching.

Figure 5.14 displays the hardness measurement conducted on FeMnAlC L-PBF samples, with one set cooled in air (Figure 5.14a) and another set cooled using water quenching (Figure 5.14b). The heat treatments that were subjected to cooling in

ambient air include a wider range of temperatures ranging from 250 to 850 °C for a duration of 4 hours. Hardness exhibits a rather consistent level, particularly within the temperature range of 400-700 °C. However, a drop in hardness of less than 40 HV10 is observed at temperatures of 250 °C and 850 °C. The observed highest drop in hardness took place at 850 °C and could be attributed to the transformation of austenite into softer ferrite.

The heat treatment experiments using water quench cooling focused at temperatures with no hardness drop in Figure 5.14a, aiming to evaluate the possible hardness increase by the precipitation of κ-carbides within or between the austenitic grains. Therefore, different periods of time ranging from 1 hour to 20 hours were employed throughout the heat treatments conducted at temperatures of 400 and 500 °C. Results indicate that hardness levels exhibit a notable degree of stability at both temperatures and all periods of time tested, with values around 300 HV. This implies the absence of any indication of precipitation, and the microstructure exhibits minimal modification at these temperatures, as observed for a maximal duration of 20 hours. In order to validate the stability of mechanical properties under these specific temperature conditions, a series of tensile tests were conducted on ASTM E8 size specimens following heat treatments at 400 and 500 °C for a duration of 4 hours. The resulting tensile data are compiled in Table 5.3, demonstrating the consistency and resilience of the tensile properties at these temperatures. The observed decrease in the YS can

be attributed to factors such as partial recovery or recrystallization of the microstructure, and the Bauschinger effect[1] that increases the YS in the as built condition, if the material is submitted to compression residual stresses above the original YS during printing.

Table 5.3
Tensile properties of Fe-Mn-Al-C low density steels studied in L-PBF in the as built condition and after heat treatment at 400 and 500 °C for 4 h.

Alloy	YS (MPa)	UTS (MPa)	TE (%)
FeMnAlC as built	570-590	735-755	42-47
FeMnAlC 400 °C	555-565	720-741	42
FeMnAlC 500 °C	550-575	745-751	42-43

After subjecting the FeMnAlC L-PBF samples to heat treatments, a microstructural evaluation was conducted to understand the stability of the mechanical properties after heat treatment. Following a preliminary microscopy investigation, with no plausible microstructural differences observed, microstructure differences were studied at the nanoscale between an as built sample and a sample that underwent a 4-hours heat treatment at 500 °C using APT.

[1]The "Bauschinger Effect" is a phenomenon observed in materials science, specifically within the domain of mechanical behavior of materials. It describes a peculiar deviation from expected elastic behavior when materials undergo cyclic loading, especially in the context of plastic deformation. When a material is subjected to plastic deformation, its YS increases and becomes more resistant to further deformation. However, the Bauschinger Effect reveals an intriguing aspect: if the direction of the applied stress is reversed after yielding, the material demonstrates a reduced yield strength in the opposite direction. This reduced yield strength is a consequence of residual stress and microstructural changes in the material due to the initial deformation. It underscores the material's memory of past stresses, indicating a history-dependent behavior.

Two lamellas with similar dimensions were lift out from both samples perpendicular to the direction of the solidification cellular structures (Figure 5.15a). This extraction strategy was employed to facilitate the investigation of microsegregation at the solidification boundaries, and the possible association of κ-precipitation.

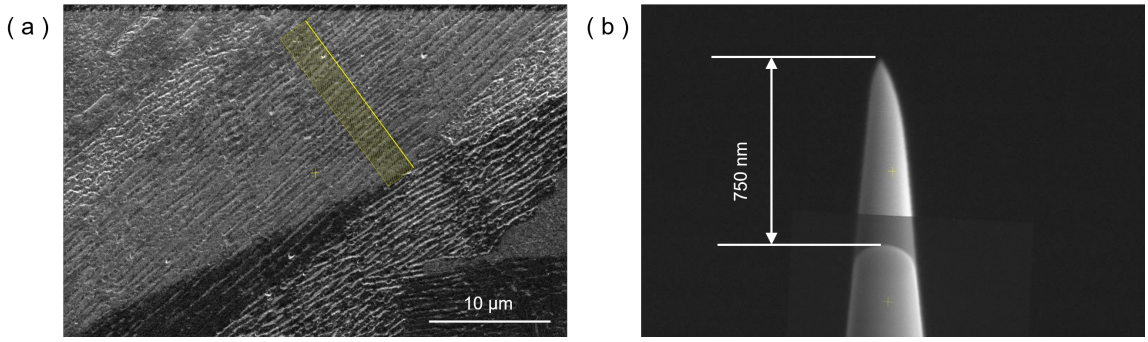

Figure 5.15: (a) SEM micrograph of the size of extraction of material by FIB lift out for APT examination, (b) SEM micrograph of an APT tip with a radius of curvature below 50 nm obtained after FIB annular milling.

Figure 5.16a depicts the microsegregation profile of FeMnAlC steel as it is produced by L-PBF. On the other hand, Figure 5.16b illustrates the microsegregation profile after to subjecting this material to a heat treatment at a temperature of 500 °C, which was held for 4 hours. Micorsegregation of Mn and C was detected at the solidification boundaries in the as built sample. This microsegregation profile is stronger at the solidification boundary after heat treatment, with a sharp increase of Mn and C at this location.

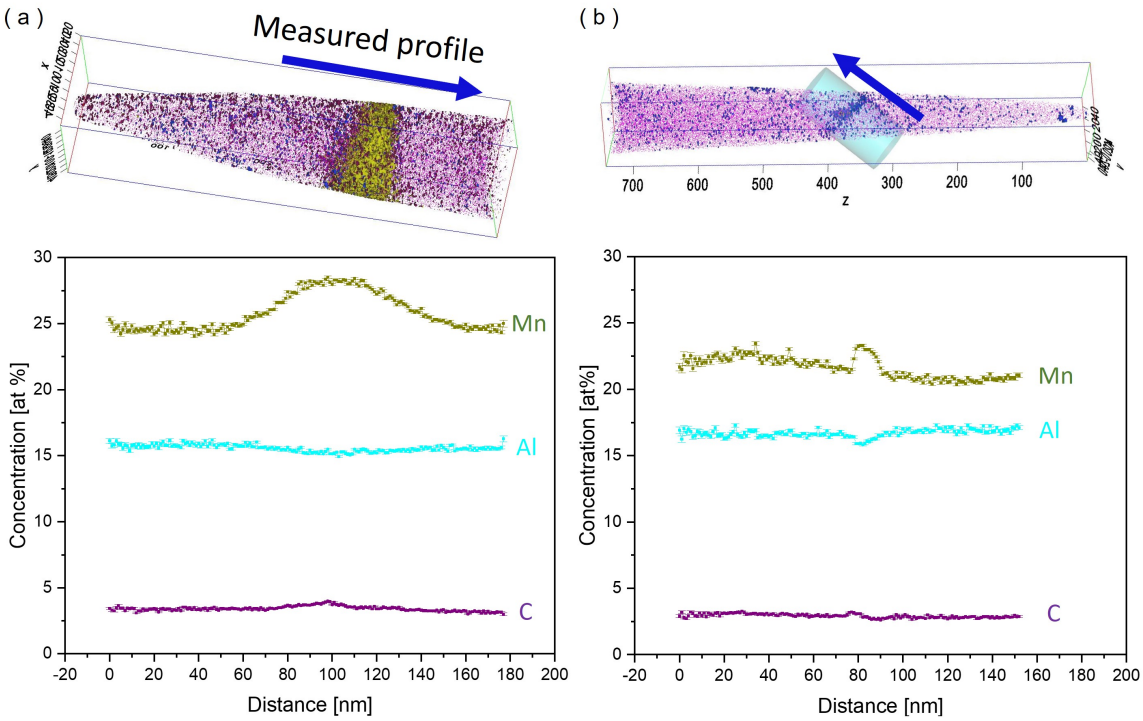

Figure 5.16: Chemical concentration profile along one axis perpendicular to the solidification cell structures of FeMnAlC steel L-PBF samples (a) as built and (b) heat treated at 500 °C for 4 hours.

In addition to the observed microsegregation patterns, the elemental distribution in both samples shows certain degree of uniformity at the nano-scale, with the only distinction of the presence of C-rich regions in the heat treated sample, as it was captured in Figure 5.17. However, no evidence of phase development or precipitation was observed after the heat treatment.

The observed elementary and microstructural uniformity and similarity could explain the stability of mechanical properties after the heat treatments studied.

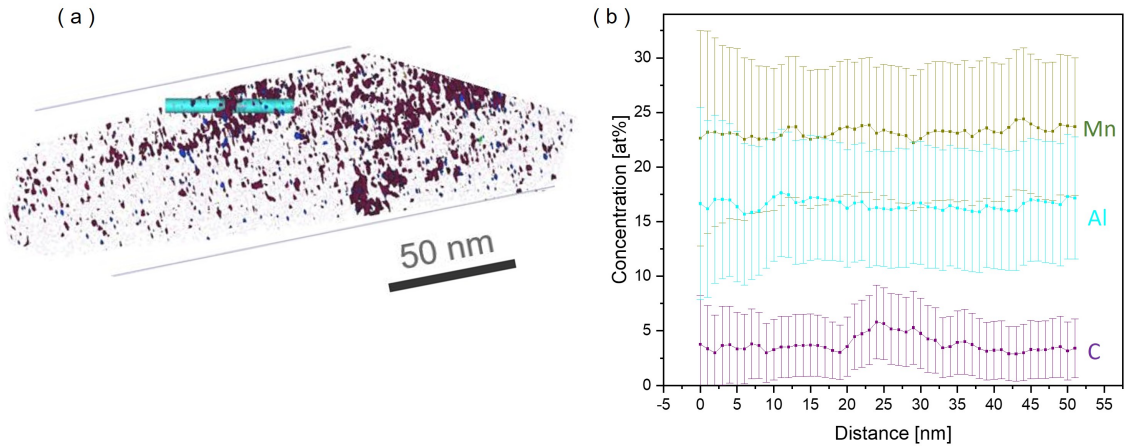

Figure 5.17: Chemical concentration profile along one C-rich region FeMnAlC steel L-PBF sample heat treated at 500 °C for 4 hours.

5.2.2 Impact toughness of FeMnAlC steel printed by L-PBF

Impact toughness of FeMnAlC steel was investigated in the as built condition using Charpy-V specimens. Figure 5.18 depicts a representation of the CAD file and an image presenting the printed samples that remain still attached to the build platform.

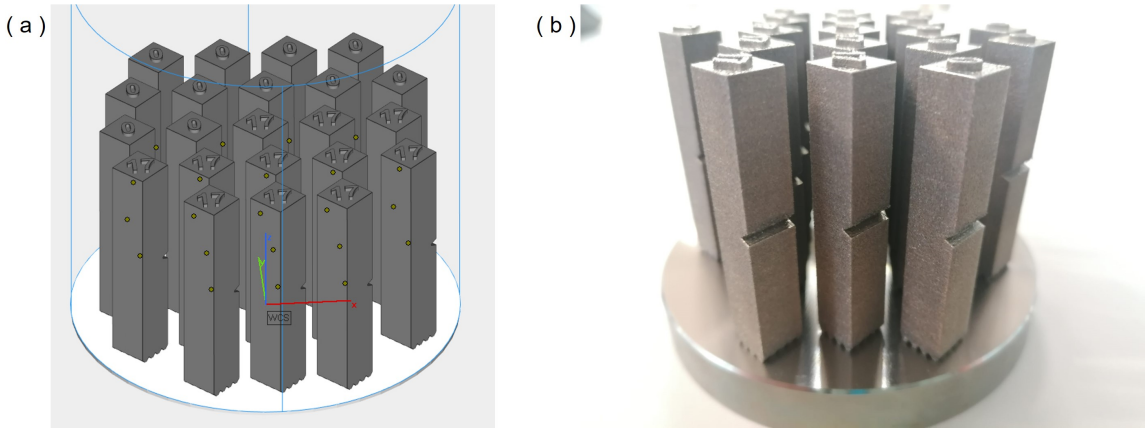

Figure 5.18: Charpy ASTM E23 specimens (a) designed by CAD and (b) printed in L-PBF with FeMnAlC steel.

Charpy V-notch (CNV) toughness was evaluated at various temperatures ranging from room temperature to -70 °C, with three measurements taken at each temperature. Figure 5.19 shows the mean value per temperature together with the corresponding standard deviation. Furthermore, for the purpose of examining cryogenic temperatures, a total of three samples were subjected to immersion in liquid nitrogen and afterwards measured at a temperature of -196 °C. The results demonstrate significantly low ductile-to-brittle transition temperatures, since CVN toughness experiences a typical decrement as temperature decreases. However, this drop is progressive from 20 ºC to -70 °C (34 J to 26 J), suggesting that the transition could occur between -70 °C and -196 °C, where the CVN toughness further decreases to 13 J.

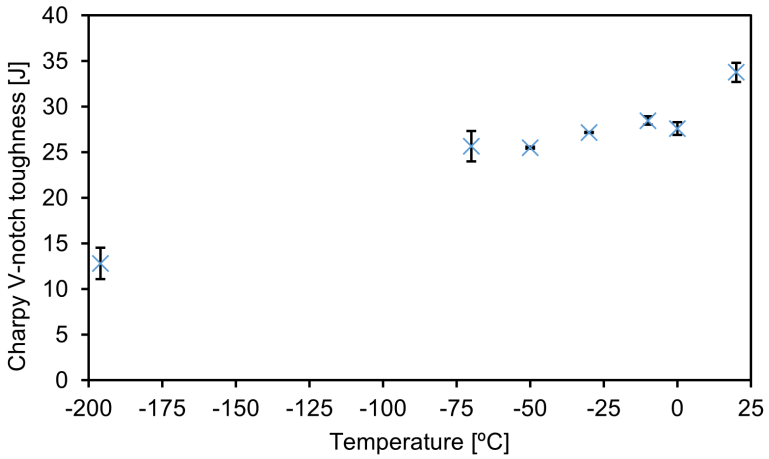

Figure 5.19: CVN toughness of FeMnAlC steel in L-PBF at different temperatures from room temperature to cryogenic.

The examination of the fracture surface of the Charpy specimens at the different testing temperatures was conducted in order to understand the material's deformation mechanism and the transition from ductile to brittle behavior. Figure 5.20 displays representative images of the fracture surface of FeMnAlC material tested at the different temperatures. Figure 5.20 demonstrates that the fracture operating micromechanism is ductile, regardless of the test temperature until -70 °C. This behavior is defined by the nucleation, coalescence, and development of microholes. At -196 °C fracture micromechanism is a mixture ductile-brittle. Therefore, the prevailing deformation mechanism in FeMnAlC remains ductile, even when subjected to cryogenic temperatures. This characteristic makes FeMnAlC an interesting material for potential applications in low-temperature and cryogenic environments.

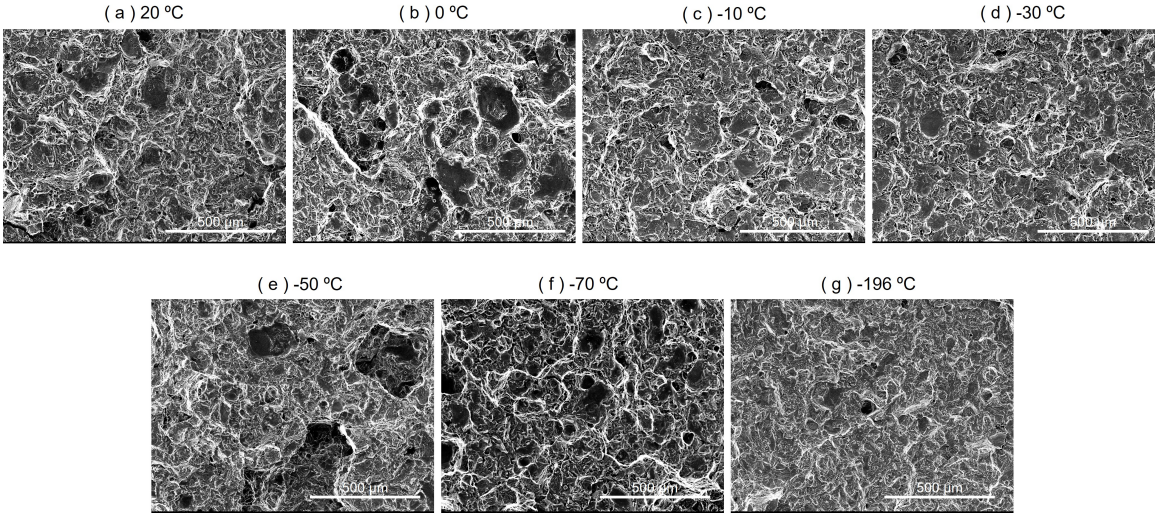

Figure 5.20: Fracture surfaces of Charpy FeMnAlC steel specimens printed in L-PBF tested at (a) room temperature, (b) 0 °C, (c) -10 °C, (d) -30 °C, (e) -50 °C, (f) -70 °C and (g) -196 °C.

5.2.3 Compression with lattice structures of FeMnAlC steel printed by L-PBF

In AM, lattice structures represent a transformative approach to material design and utilization, characterized by their repetitive, open-cell configurations of nodes and struts. These complex geometries, achievable through advanced AM techniques, offer a unique combination of strength, reduced weight, and material efficiency. Their applications extend across various fields, specially in aerospace, automotive, and biomedical industries, where they enable the creation of components with optimized mechanical properties, such as improved strength-to-weight ratios and enhanced thermal management capabilities. The most prevalent lattice geometries are cubic-based lattice structures (e.g., BCC or FCC), diamond-based lattice structures and gyroid-based lattice structures.

This analysis focused on the mechanical response to compression of FeMnAlC steel in three different lattice structures from the 3 most used types: a double diamond (DD) lattice structure, a double gyroid (DG), and the BCC cubic-based lattice structures. The DD and DG geometries, where printed using different lattice densities. The lattice density represents the proportion of volume occupied by the lattice structure relative to a solid structure with identical dimensions, and was the variable that was adjusted for each shape. The range of densities explored was between 20% and 30%. For the BCC structure only a density of 20% was used. Furthermore, two

lattices were printed for each geometry, hence ten lattices were fabricated in total. Compression tests were conducted as described in Section 2.2.6.3, where some of which involved capturing the data by video-correlation of images.

Figure 5.21a depicts the CAD file of all lattices whose dimensions are embedded in a cube with a side of 30 mm^3, together with their respective orientations during the L-PBF printing process. Out of the total of 10 lattices that were produced; 5 of them were manufactured in a top bed and 5 in a bottom bed. Figure 5.21b shows the lattice samples after L-PBF printing that were subjected to compression tests.

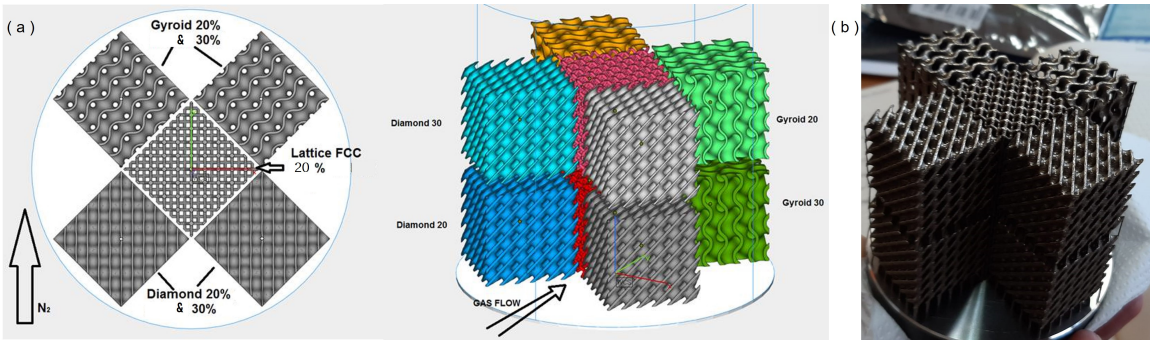

Figure 5.21: Lattice structures (a) CAD representation of the different lattices and their location in the L-PBF machine and (b) printed in L-PBF

The lattice samples were assigned alphanumeric codes (DD1-20%, DD2-20%, DG1-20%, DG2-20%, BCC1-20%, BCC2-20%, DD1-30%, DD2-30%, DG1-30%, and DG2-30%). Table 5.4 provides a summary of the codes, geometries, and the volume occupied by the 10 lattices. Furthermore, it is worth noting that the orientation of the compression test direction was consistently parallel to the building direction in L-PBF in all lattices.

Table 5.4
Specification of the different lattice structures and their codification.

Code	Geometry	Volume occupied (%)
DD1-20%	Double diamond (DD)	20
DD2-20%	Double diamond (DD)	20
DG1-20%	Double gyroid (DG)	20
DG2-20%	Double gyroid (DG)	20
BCC1-20%	BCC	20
DD1-30%	Double diamond (DD)	30
DD2-30%	Double diamond (DD)	30
DG1-30%	Double gyroid (DG)	30
DG2-30%	Double gyroid (DG)	30
BCC2-20%	BCC	20

The maximum load, deformation, and energy absorption inside the elastic domain was determined from compression curves for each lattice structure. Figure 5.22 illustrates the process of extracting these values from the compression curve. Initially, the curve exhibits an elastic slope, which is then followed by a progressive stress increment or plateau during the plastic deformation phase. By the end, the "densification" stage is reached, wherein the lattice cells collapse completely, resulting in an increase in load without any further deformation [310]. The determination of the maximum energy absorbed (E_{tot}) by the lattice structure involves the computation of the integral of the curve up to the point of densification strain (D_d)[311, 310, 312]. The determination of the maximum elastic energy (E_e), the specific elastic energy ($E_{e,s}$), and the maximum elastic load (P_e) is performed using a similar methodology, but limited to the point of maximum elastic strain (D_e).

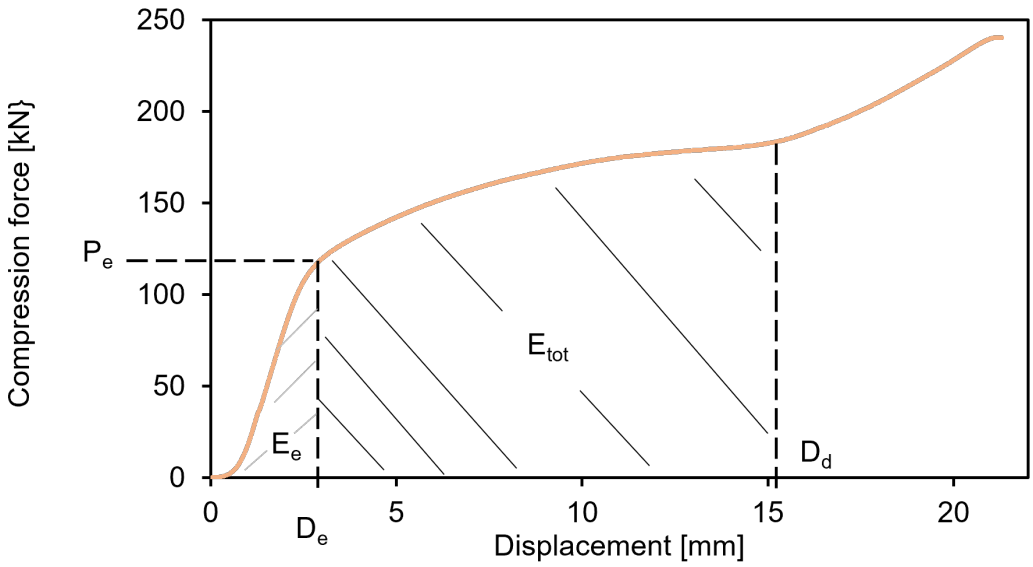

Figure 5.22: Representation of extraction of lattice results from compression test curves.

Based on the finding shown in Figure 5.23, the DD geometry provides better energy absorption results compared to both the DG and BCC structures. Decreasing the volume percentage of the lattice structures results in an increased weight reduction. However, it also leads to a decrease in the overall energy absorbed. Understanding the specifications of a component is essential in determining the level at which weight reduction may be achieved. The quantification of compression results is collected in Table 5.5. Data demonstrates that the DD lattice structure exhibits better performance, showing the strongest resistance to compression load through the elastic domain, as well as resistance to densification.

Figure 5.23 presents a comprehensive comparison of compression test curves, enabling a straightforward evaluation of different lattice configurations with different density percentages and geometries. The FeMnAlC steel presents great ductility without any

sudden failure in all lattice structures. The robustness of the response of each lattice is clear, since lattices exhibiting identical shape and density percentages show similar results.

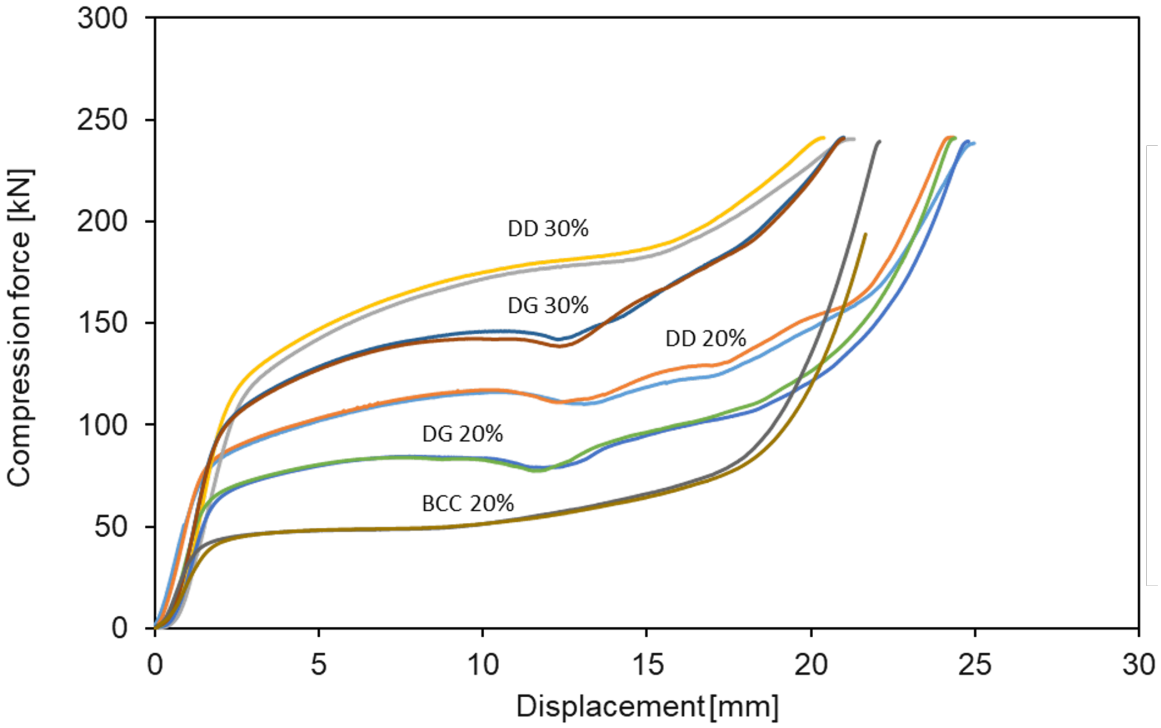

Figure 5.23: Comparison between all FeMnAlC lattices compression tests.

Figure 5.24 depicts representative images captured at the moment of plastification in the compression test, as obtained using video-correlation. The image showcases the three different lattice structures: DD (DD1-20%), DG (DG1-20%), and BCC (BCC1-20%). The analysis of video-correlation data reveals that the distribution of deformation inside the lattice structures is not uniform. The DD (Figure 5.24a) exhibits the greatest deformation localized at the oblique lines, while the DG (Figure 5.24b) shows

maximum deformation at the horizontal curves. In the case of the BCC structure (Figure 5.24c), the 90° joints are found to experience the highest levels of distortion.

Table 5.5
Compression results of FeMnAlC lattice structures printed in L-PBF.

Lattice	P_e (kN)	D_e (mm)	D_e (%)	E_e (J)	D_d (mm)	D_d (%)	$E_{e,s}$ (J/g)
DD1-20%	75.0	1.5	5.0	59.8	13.0	43.3	4.8
DD2-20%	75.0	1.4	4.8	49.7	12.0	40.0	4.0
DD1-30%	117.0	2.9	9.5	142.4	16.0	53.5	7.6
DD2-30%	119.0	2.6	8.6	135.1	15.0	50.0	7.2
DG1-20%	60.9	1.8	6	43.3	12.5	41.7	3.5
DG2-20%	58.1	1.5	5.1	34.5	12.0	40.0	2.8
DG1-30%	95.0	2.0	6.6	77.7	12.5	41.7	4.1
DG2-30%	97.6	2.1	7.0	88.4	12.5	41.7	4.7
BCC1-20%	37.7	1.3	4.3	22.3	11.0	36.7	1.8
BCC1-20%	37.2	1.6	5.2	25.8	11.0	36.7	2.1

Finally, the compression response of FeMnAlC steel was compared to that of 316L, which is well recognized as the main austenitic steel in AM and serves as a reasonable benchmark. In this comparative analysis, the double diamond lattice structure comprising 30% of the overall volume was chosen due to its greater mechanical performance.

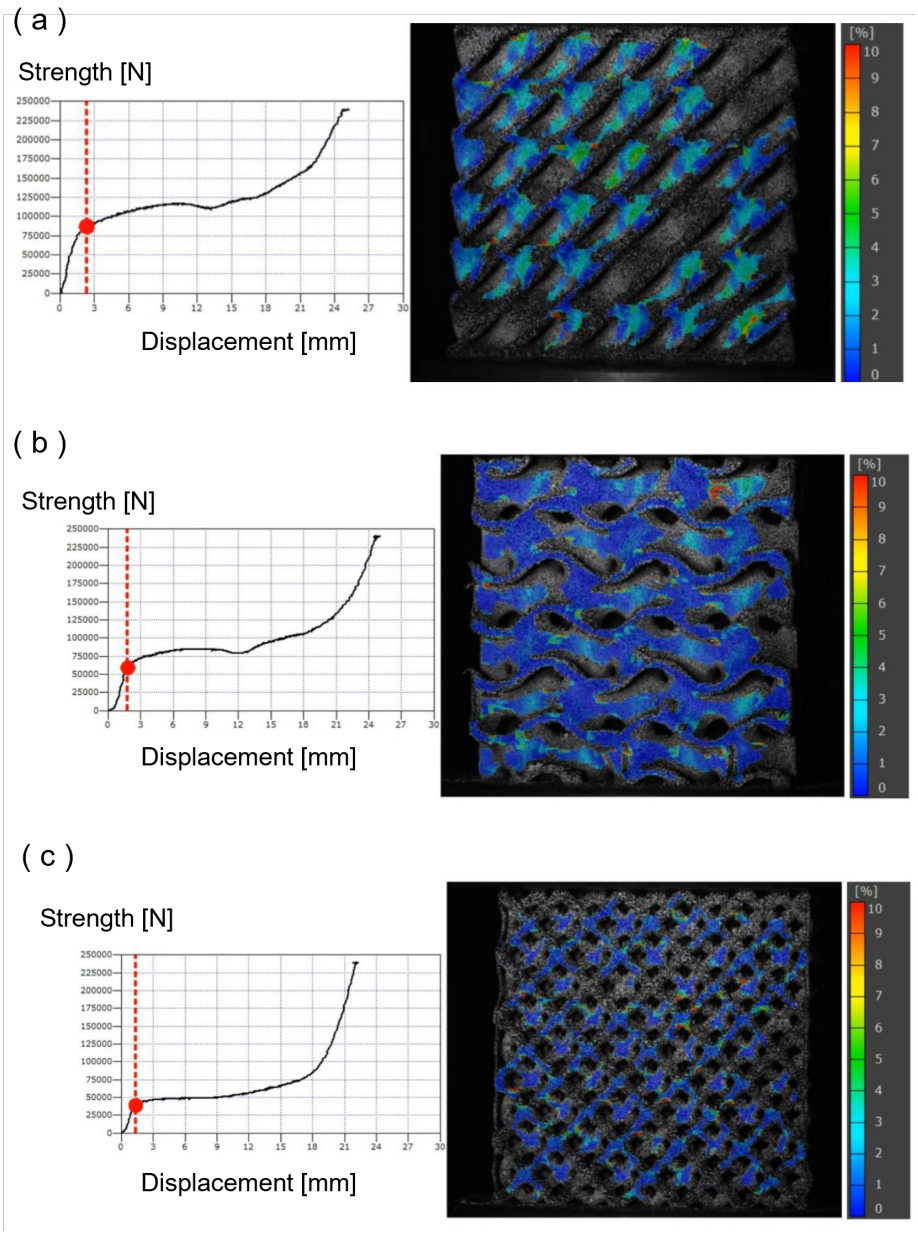

Figure 5.24: Representative video-correlation image of FeMnAlC deformation in L-PBF lattice a) double diamond, b) double gyroid and c) BCC structures.

The comparative mechanical lattice behavior in compression of FeMnAlC and 316L steels are shown in Figure 5.25. The results indicate that FeMnAlC exhibits superior mechanical properties compared to 316L steel. The FeMnAlC steel has a greater

elastic domain, with a maximum elastic load ranging from 117-119 kN and an elastic displacement of 2.6-2.9 mm (or 8.6-9.5% maximum elastic strain). In comparison, the 316L steel has a lower elastic domain, with a maximum elastic load of 81-84 kN and an elastic displacement of 1.2-1.4 mm (or to 4.0-4.7% of maximum elastic strain). (D_d) for both steels exhibits similarity, measuring at 15 mm or 50% strain. However, the FeMnAlC steel has a higher maximum energy absorption compared to the 316L steel, with approximate values of 2400 J and 1500 J, respectively. Furthermore, it is worthy to highlight that the density of FeMnAlC steel exhibits a reduction of about 12.5% compared to the density of 316L steel. This characteristic contributes to an enhanced specific energy absorption (E_s) or the ratio between absorbed energy and mass (128 J/g Vs 69 J/g).

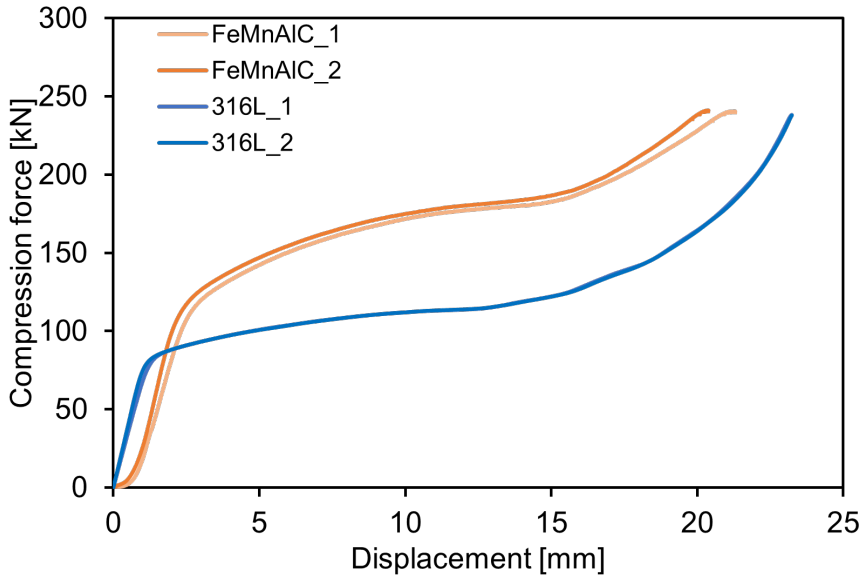

Figure 5.25: Compression test comparison of double diamond 30% lattice structures manufactured with FeMnAlC (orange) and 316L (blue) steels by L-PBF.

5.2.4 Compatibility of FeMnAlC steels with other 3D printing technologies: Powder-DED

The investigation of the compatibility of FeMnAlC steel with alternative AM technologies was conducted by experimentation using powder-DED technology, described in Sections 1.6 and 2.1.3. In order to determine the printing parameters, small walls with dimensions of 50 mm in length and a growth of 10-30 layers were printed. This was done to achieve a sample height of around 5 mm. No overlapping laser tracks were used in the xy plane, resulting in samples with thicknesses that closely approximate the size of the laser spot. A set of printing experiments was conducted using this specified geometry, where multiple samples were printed with varying parameters inside a process window that was determined for steels and was outlined in Table 2.2. Figure 5.26 illustrates and example of samples printed following this DoE.

The utilization of the DoE in conjunction with a characterisation methodology similar to the one outlined in Section 2.3 enables the identification of the optimal printing process window for this steel in powder-DED. After the determination of the best printing settings, the layer growth was monitored in order to ensure a good harmonization between the layer growth and the z-displacement of the robot.

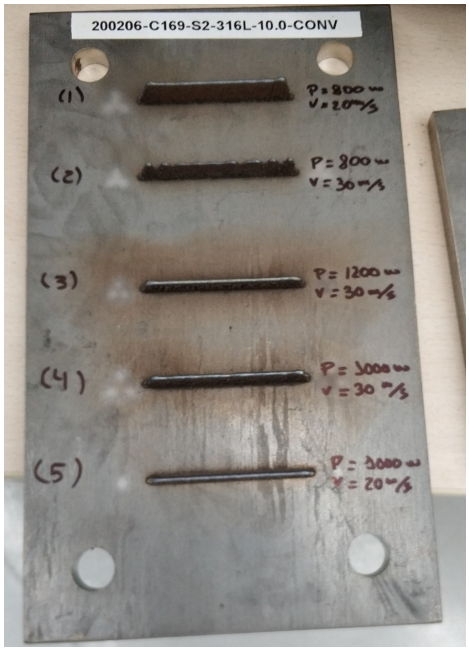

Figure 5.26: Photograph of the small walls printed using the DoE to develop the printing parameters of FeMnAlC steel in powder-DED.

5.2.4.1 Microstructure

The selected optimal parameters for FeMnAlC steel powder in DED process are 800 W of laser power, a laser speed of 20 mm/s, and a laser spot diameter of 2 mm with a Gaussian beam shape distribution. These parameters were chosen because they have produced fully dense samples without any loss of chemical elements. Figure 5.27a shows a representative LOM image of a FeMnAlC sample cross-section produced by DED. The image reveals the absence of any visible crack with a density above 99.9%. Figure 5.27b displays SEM images of cross sections at higher magnifications, revealing the solidification structures. The presence of heterogeneous distribution of cellular-dendritic (Figure 5.27b left) and columnar-dendritic (Figure 5.27b right) solidification

structures is visible indicating that they differ from the observed solidification structures in this steel printed in L-PBF, which exhibited exclusively cellular structures. One possible explanation for this difference in solidification structures observed in the same material but printed using different technologies is that the thermal gradient is reduced in powder-DED due to the significantly higher temperature that acquires the printing bed during the process compared to LPBF, resulting in the material entering the dendritic region (see Figure 1.8).

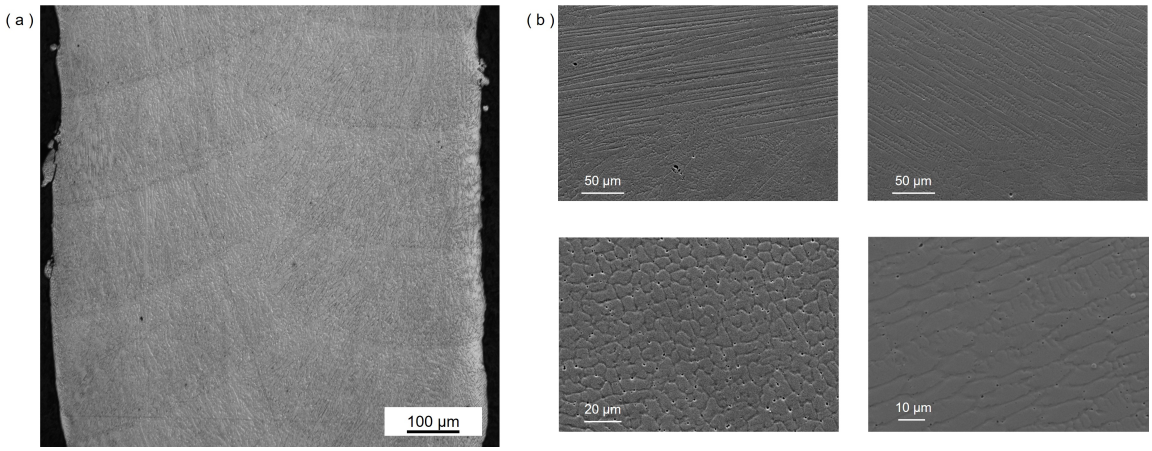

Figure 5.27: Cross-section of FeMnAlC steel powder produced by DED at different magnifications taken with (a) LOM and (b) SEM.

The equivalent diameter size of cellular-dendritic structures was measured in less than 10 μm, whereas the columnar-dendritic structures exhibited sizes ranging from 10 to 20 μm. This indicates that the solidification structures have larger dimensions in DED compared to L-PBF.

Similar to L-PBF, the microstructure observed in the DED samples of FeMnAlC was

mainly austenitic, as evidenced by the XRD measurement presented in Figure 5.28. The diffraction peaks detected exclusively correspond to the austenite phase.

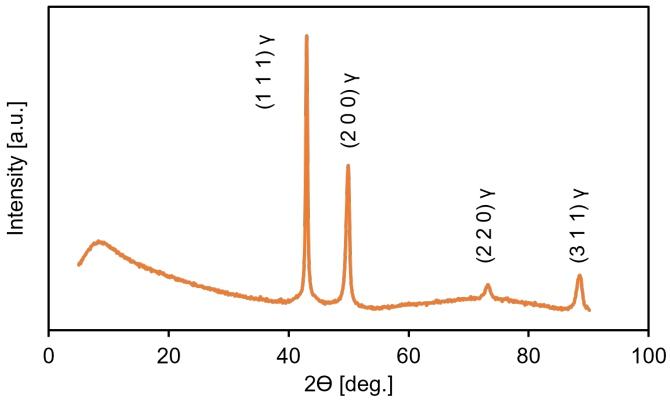

Figure 5.28: XRD diffraction patter of FeMnAlC processed by DED.

EBSD analyses were conducted in order to investigate the grain size and morphology of the austenitic grains. Figure 5.29 displays the EBSD maps with the IPF along the building direction of FeMnAlC steel samples produced by DED. This map was measured in a centralized area of the cross-section. The mainly austenitic microstructure measured by XRD was further corroborated by EBSD. However, in contrast to the epitaxial growth observed in L-PBF (Figure 4.13a-b), the austenitic grains in the DED process show a finer size and a more equiaxed morphology. The equivalent diameter method was used to determine the average grain size from EBSD maps, giving an average estimation of 16.3 $\pm$ 15.1 μm in the DED sample and 25.4 $\pm$ 23.9 μm in the L-PBF sample. The results obtained were unexpected, since it is known that

the cooling rate in the DED process is comparatively slower than L-PBF, and additionally, the printed layer, and the molten pool in DED is normally measured in millimeters, whereas the layer thickness in L-PBF is in the micrometer scale. Consequently, the grain size of steel processed in DED usually tends to be bigger that that in L-PBF.

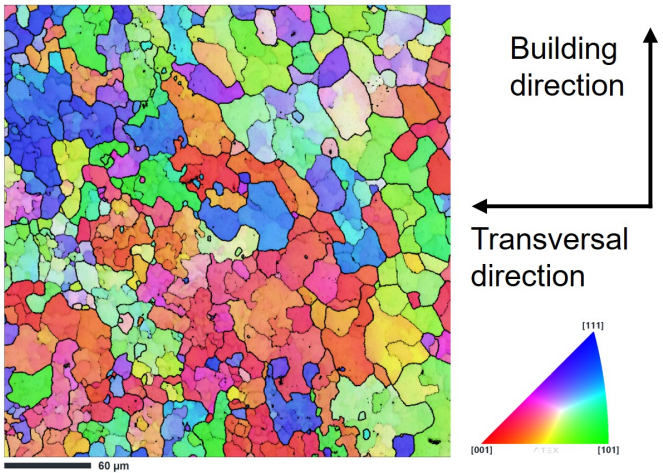

Figure 5.29: EBSD map of FeMnAlC steel sample printed by DED.

The crystallographic texture of FeMnAlC steel printed with DED was examined using PF analysis and compared with samples produced with this steel in L-PBF (see Figure 3.15a). According to the results presented in Figure 5.30, the equiaxed austenitic grains formed during the DED process contribute to the randomization of the crystallographic texture. This randomization is characterized by the absence of a predominant direction, as demonstrated by the significantly low maximum intensity measured at the (100) planes along the building direction (BD), as well as the the two orthogonal directions.

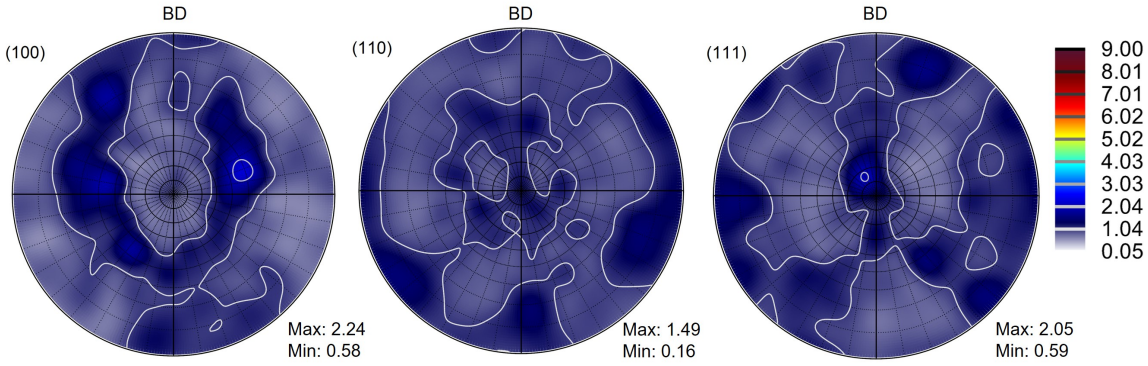

Figure 5.30: PF of FeMnAlC sample printed in DED. Note BD refers to the building direction.

In order to further explore the origin of this equiaxed grain structure, backscattered FEG-SEM images were acquired throughout the entire height of the samples. These images revealed the presence of equiaxed grains at every sample location, as illustrated in Figure 5.31b. However, the top part of the samples exhibits columnar grains aligned along the building direction, as depicted in Figure 5.31a. This particular grain morphology corresponds to the last printed layer. This observation indicates that the formation of equiaxed grains does not occur during the solidification stage of printing, but rather through the influence of IHT on the subsequent printed layers. The IHT in DED is more massive than in L-PBF, as a result of dimension of the melt pool and the laser power employed. The presence of columnar grains just in the upper part of the sample can be explained by this reason. Thus, grain refinement phenomenon in DED could be the result of a cyclic phase transformation occurring between ferrite and austenite at elevated temperatures, which is induced by thermal

cycling [313]. This thermal cycling inducing grain refinement by cyclic phase transformation has been already observed in AM, when a CrMnNi steel was fabricated in Electron Beam Melting (EBM) technology [314]. The cooling rates associated to the EBM process may be more comparable to those of DED than to those of L-PBF due to the elevated temperatures required in the powder bed [314, 315].

Further investigation into the crystallographic evolution of austenite grains during solidification and through the IHT is necessary to clarify the factors contributing to the formation of columnar and equiaxed grains in this steel in different AM technologies. This topic could potentially serve as the subject of a separate research work.

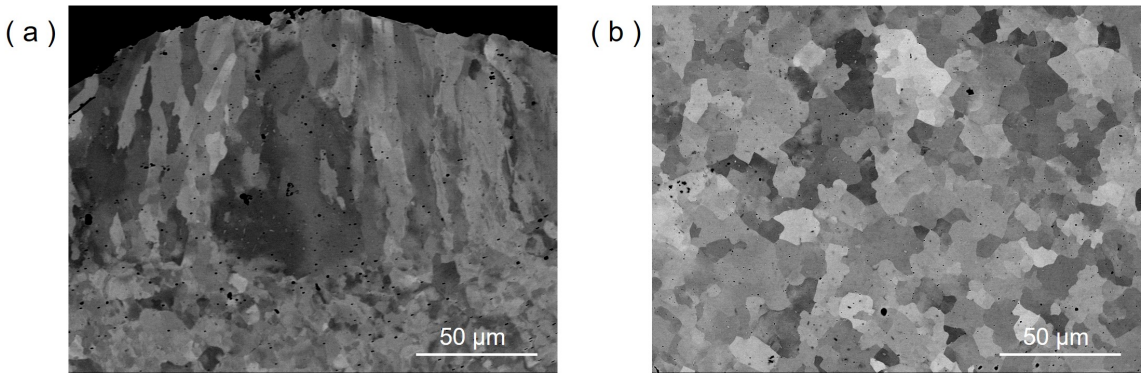

Figure 5.31: SEM-backscattered images taken at the cross section of FeMnAlC steel produced by DED at (a) the upper layer and (b) a representative middle-height section

5.2.4.2 Mechanical properties of FeMnAlC steel printed by Powder-DED

The mechanical properties of FeMnAlC steel were studied in order to evaluate its performance in specimens fabricated by DED process and compare it with the mechanical behavior observed in L-PBF printed specimens. The investigated mechanical properties included hardness, tensile properties, impact toughness, and their variation through heat treatments.

The tensile samples were extracted horizontally from printed walls, using the same ASTM E8/E8M subsize specimens as those used in specimens printed by L-PBF. This extraction is sketched in Figure 5.32. The only difference in the specimens was the thickness, which was constrained to around 2 mm, corresponding to the thickness of the wall. Nonetheless, this thickness remained within the range defined by the standard.

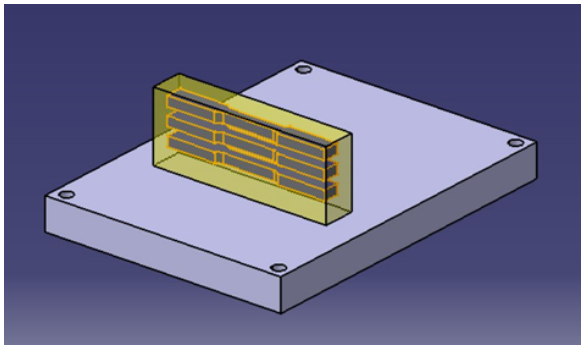

Figure 5.32: Extraction of horizontal tensile specimens in DED.

Various specimens were tested, and the resulting tensile curves are displayed in Figure

5.33. The level of variability observed in the tensile curves and tensile properties is greater in DED compared to L-PBF. In addition to the presence of scatter in the TE, there is also noticeable variation in the strength values (YS and UTS). The higher variation of tensile properties in DED as compared to L-PBF is thought to be due to the greater variability in the DED process technology itself. For instance the initial specimens were printed onto a substrate at a lower temperature. During the printing process, the substrate undergoes heating, which alters both the solidification conditions and the geometry of the melt pool. Consequently, the height of the melt pool shifts from the initial calibrated z-displacement of the robot. This variability in the DED process induces systematic errors during printing that can induce defects and microstructural and mechanical variability of printed compounds.

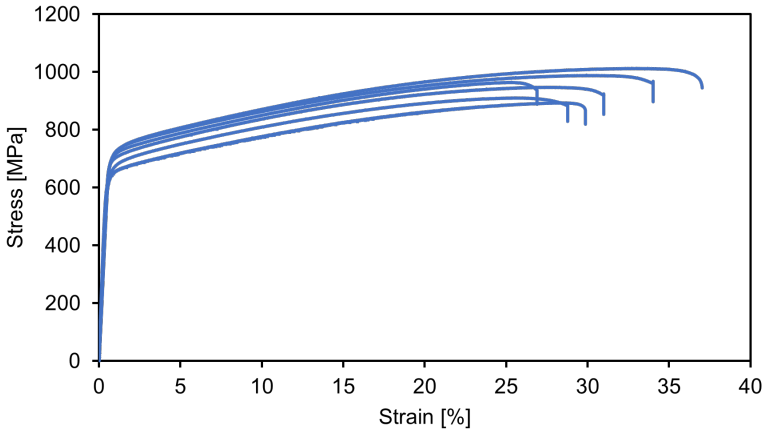

Figure 5.33: Tensile curves of as built FeMnAlC steel printed by DED.

In any case, the tensile properties obtained are comparable and beyond these obtained by LPBF. The majority of ductility values fall within the range of 30-35%, the YS

exceeds 600 MPa, while the UTS surpasses 900 MPa in all cases.

The higher tensile strength exhibited by FeMnAlC steel powder printed using DED as compared to specimens printed by L-PBF can be attributed to the observed finer and more equiaxed grain microstructure, and the Hall-Petch effect. Consequently, the mechanical properties can be explained through microstructural analysis.

The fracture surfaces of the tensile samples confirm the occurrence of ductile fracture characterized by nucleation, coalescence, and growth of micro-cavities. Figure 5.34 displays a representative fracture surface at different magnifications, revealing the micro-cavities, which confirms the ductile fracture mechanism.

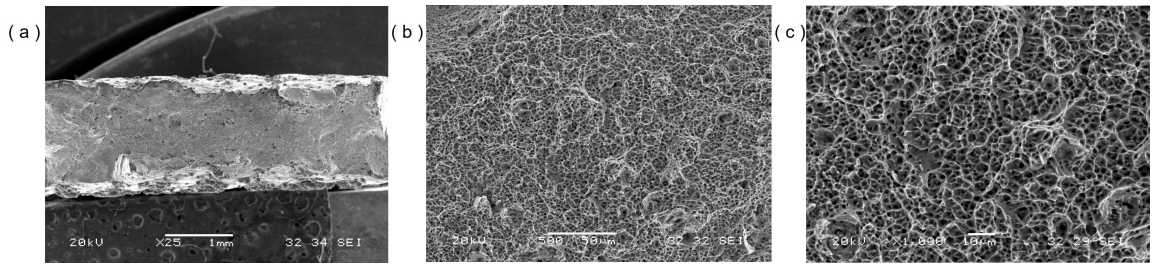

Figure 5.34: SEM images of fraction surface of tensile FeMnAlC specimens printed by DED at different magnifications (a) x25, (b) x500, and (c) x2000.

Impact toughness measurements were performed using Charpy specimens that were horizontally extracted from thin walls. The thickness of the Charpy specimens was also decreased to around 2 mm, which corresponds to the wall thickness. Samples were not extracted vertically, because it is not practical, and the notch was machined in one of the specimen's sides where cracks have longer distance to travel. It is important to note that this dimension is outside the ASTM E23 standard. Charpy

experiments were carried out at different temperatures in order to comparatively evaluate and determine the transition from ductile to brittle behavior.

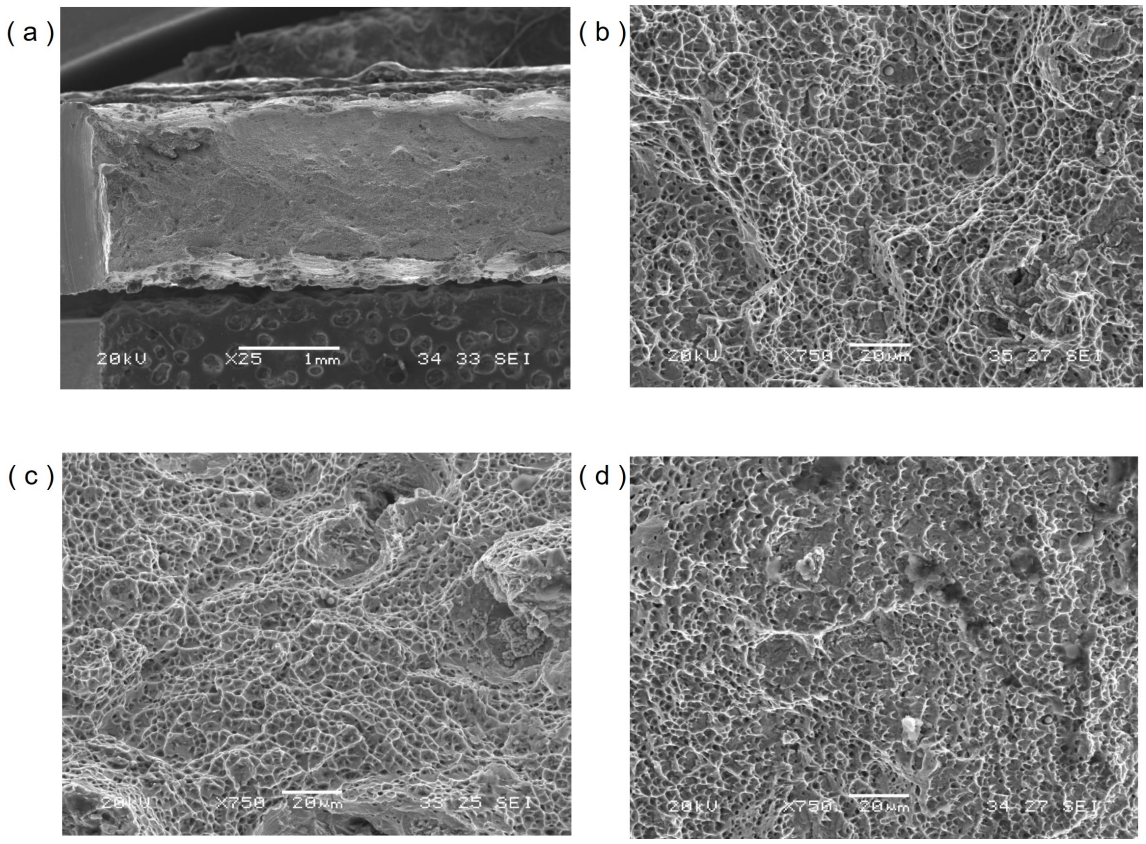

Figure 5.35: SEM images of fracture surfaces of Charpy FeMnAlC specimens printed by DED. Image (a) shows a representative fracture surface at low magnifications and fracture surfaces at higher magnifications (x700) are shown at the samples tested at (b) room temperature, (c) -20 °C, and (d) -60 °C.

Charpy measurements were conducted at ambient temperature, as well as at -20 °C and -60 °C, yielding consistent absorbed energy values of 11 J for a cross-sectional area of 2 x 10 mm^2. Also, an examination of the fracture surfaces were conducted on all the samples, as depicted in Figure 5.35. The findings of this study confirmed a

ductile fracture mechanism in all the temperatures tested, indicating that the ductile to brittle transition in FeMnAlC steel produced by DED occurs at temperatures lower than -60 °C.

5.2.4.3 Influence of heat treatments on mechanical properties

The impact of heat treatment on mechanical properties was conducted at a temperature of 500 °C, which was the subject of more comprehensive analysis in L-PBF samples. Hardness measurements were conducted on DED samples that were subjected to a temperature of 500 °C for time periods ranging from 1 to 48 hours and cooled in air. Measurements are provided in Figure 5.36, showing the mean hardness value and its corresponding standard deviation. This steel exhibits a harness stability for a duration of two days under a temperature of 500 °C. These results show similarities to the hardness observations in L-PBF specimens subjected to comparable heat treatments, where microstructure remains quite similar and explains the hardness consistency.

The impact of heat treatments on tensile properties was also examined in specimens heat treated at 500 °C for 4 and 16 hours. Figure 5.37 illustrates the tensile curves of ASTM E8/E8M subsize specimens that have undergone heat treatment for a duration of 4 hours (represented in blue) and 16 hours (represented by the orange curves). The steel samples exhibited a commendable uniformity in their tensile curves, with ductility values around 40 % and UTS above 1000 MPa with no surface finishing

treatment. The samples subjected to a 16-hour duration displayed slightly elevated tensile strength values, while the samples subjected to a 4-hour duration exhibited greater total elongation values. However, it is possible that the systematic errors and variability in the DED process may contribute to the observed differences in tensile properties.

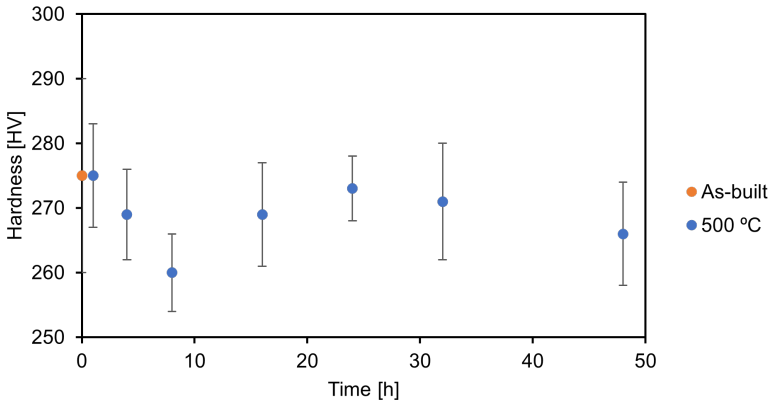

Figure 5.36: Averaged hardness values and standard deviations measured in FeMnAlC DED samples as built (orange) and subjected to 500 °C heat treatment for different times (blue).

Table 5.6 presents the measured range of these properties measured in FeMnAlC steel samples produced by DED as built and after the two heat treatments at 500 °C. These results show that this material offers YS values between 630-825 MPa, UTS around 1000 MPa and TE between 30-45 %. In addition, due to the particularity of the DED process, this steel undergoes a grain refinement that reduces anisotropy and enhances tensile strength. These features, in conjunction with the mechanical properties and their stability at moderate temperatures such as 500 °C, can hold significant

importance for numerous applications, where high strength and ductility values are required, or simply as an alternative to 316L (Section 1.8.1), or other commercial steels (Section 1.8.2 - 1.8.6).

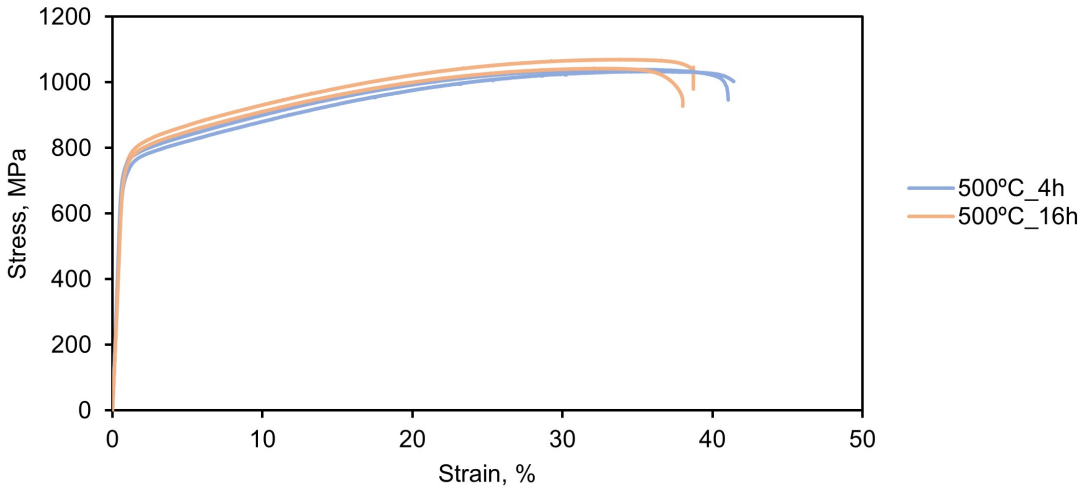

Figure 5.37: Tensile curves of FeMnAlC steel printed in DED and heat treated at 500 °C for 4 hours (in blue) and for 16 hours (in orange).

Table 5.6
Tensile properties of FeMnAlC steel printed by DED in the as built condition and after HT at 500 °C.

Alloy	YS (MPa)	UTS (MPa)	TE (%)
FeMnAlC as built	630-700	895-1015	27-37
FeMnAlC HT (500 °C - 4h)	785-800	1035-1040	41-44
FeMnAlC HT (500 °C - 16h)	810-825	1045-1070	38-39

5.3 Summary and conclusions

This section focuses on the examination of the mechanical properties of various High Mn Fe-Mn-Al-C low density steels in AM, and their response to external forces and loads, which is of great importance to the industry as it enables the prediction of material's behaviour under different conditions.

First, hardness tests were conducted on all the High Mn Fe-Mn-Al-C low density steels under study in order to investigate the impact of Si and Ti additions on strength of these steels. Most probably, the primary mechanism by which Si strengthens these steels is through solution hardening, whereas Ti additions contribute by grain refinement mechanism.

Out of all the studied steels, four compositions (FeMnAlC, FeMnAlC-05Ti, FeMnAlC-2Si, and FeMnAlC-2Si-05Ti) were chosen for the analysis of their tensile properties. Tensile properties of each of these four steels were evaluated under different printing parameters, demonstrating a resilient tensile behaviour regardless the printing parameters used. In addition, each steel shows attractive tensile properties, which fill gaps which were not covered by current commercially available steels for AM. FeMnAlC composition achieved better performance than 316L in terms of lower density and tensile properties: UTS values (above 700 MPa), and TE (over 40%). The FeMnAlC-05Ti and FeMnAlC-2Si steels exhibit UTS values of approximately 950 MPa, accompanied by TE values between 16-25%. Ultimately, FeMnAlC-2Si-05Ti

provide UTS values exceeding 1100 MPa and has the lowest density. However, it shows relative lower TE values of approximately 5%. The fracture failure in FeMnAlC and FeMnAlC-05Ti compositions is ductile, on the contrary, in FeMnAlC-2Si and FeMnAlC-2Si-05Ti steels a combination of ductile and brittle mechanism is observed in the fracture surface.

Among these steels, the FeMnAlC composition was chosen for more extensive characterization and analysis. The thermal stability of this composition was examined up to a temperature of 500°C for a duration of 20 h. It was found that there is no notable effect on the hardness or tensile properties. This characteristic was supported by microscopy observations, in which APT reveled that only minor changes in microstructure occur. The impact toughness of this steel was evaluated by V-notched Charpy tests, revealing a ductile fracture mechanism even at cryogenic temperatures. This characteristic makes this steel a promising candidate for such applications. Finally, the toughness of this steel was studied under compression tests using lattice structures, which are suitable for compression and energy absorption purposes. The performance of FeMnAlC steel was assessed with commercial 316L, resulting in almost twice higher specific energy absorption, with FeMnAlC absorbing 128 J/g compared to 69 J/g for 316L steel.

Last but not least, the FeMnAlC steel's compatibility with other AM technologies was demonstrated by DED, resulting in fully dense samples that show exceptional tensile properties (similar to those obtained by FeMnAlC-05Ti in L-PBF), impact

toughness resilience at low temperatures, and tensile and hardness thermal stability at temperatures up to 500 °C.

Chapter 6

Conclusions and future work

In this thesis a literature review was carried out to gather information of current steels available in the market for AM and explore the potential of High Mn Fe-Mn-Al-C low density steels to fill some of the mechanical and application gaps that are not covered with current commercial steels. The limitations and problems associated with these High Mn Fe-Mn-Al-C low density steels found in traditional production routes were detailed. It was also clarified that most of these constraints should not occur in laser-based AM technologies such as L-PBF, due to the inherent characteristics and physics of these processes. Nevertheless, other issues such as HC, cold cracking, and microsegregation were identified as new challenges.

This thesis demonstrates the feasibility of producing fully dense High Mn Fe-Mn-Al-C low density steels free of cracks by AM. This was achieved by employing a careful

alloy design assisted by CALPHAD calculations. A method to predict and prevent HC in this steel grade was successfully developed and demonstrated, and could be extrapolated to other steel families or alloys. Furthermore, the effectiveness of Ti(C,N) as inoculant in this particular steel family was demonstrated. CALPHAD calculations predict that additions of Ti in this High Mn Fe-Mn-Al-C low density steel grade modifies the solidification path. Upon the addition of certain amount of Ti, Ti(C,N) becomes the first solid phase that forms, instead of AlN, which is gradually removed from the microstructure. At intermediate levels of Ti, both ceramic phases coexist. Different levels of Ti additions were evaluated, and an optimum range that maximizes grain refinement while preventing cracking was determined.

Subsequently, the mechanical properties of High Mn Fe-Mn-Al-C low density steels were evaluated and compared to those of other commercially available steel grades such as 316L, to emphasize the potential of these steel grades in AM. Additionally, the microstructural analysis of each studied High Mn Fe-Mn-Al-C low density steel composition has contributed to understand the relationship between material-process-properties.

Finally, the compatibility of these steel grades with other AM technologies was demonstrated using the FeMnAlC composition in DED.

From an academic perspective, future work is focused in (1) understanding the basic principles behind grain refinement, and material strengthening, both related to alloying and processing, (2) evaluating, characterizing and understanding the deformation

mechanism of the different steels and the impact of process, microstructure and alloying.

Future industrial work is focused in enhancing the microstructural control of this steel system in AM, and evaluating further in-use properties relevant to different industrial applications:

Particularly, the basic mechanical evaluation here presented might be extended to include other compositions of interest, such as FeMnAlC-05Ti, FeMnAlC-2Si, and FeMnAlC-2Si-05Ti. This comprises the assessment of the resistance of mechanical properties and microstructure to changes in temperature, the impact toughness throughout a range of temperatures from room temperature to cryogenic temperatures, and the energy absorption capacity of lattice structures. Besides, the characterization of in-use properties should be extended to include other properties that are necessary for certain end-use applications in some industries. These in-use properties include but are not limited to fatigue, Young's and shear modulus, wear resistance, oxidation resistance, and material's isotropy, which can be measured from specimens extracted or printed at different orientations on the build platform. Furthermore, the compatibility of the additional High Mn Fe-Mn-Al-C low density steel grades studied in this thesis with other AM technologies, such as DED, should be confirmed.

For full industrialization these achievements need to be consolidated by producing a substantial amount of these steel powders in large-scale or industrial atomization units, and properties need to be evaluated using specimens printed in other L-PBF

machines or DED equipment. Finally, these High Mn Fe-Mn-Al-C low density steels need to be tested under real study cases to validate their performance on actual components used in industry.

References

[1] ASTM Standard. F2792. 2012. standard terminology for additive manufacturing technologies. *ASTM F2792-10e1*, page 24, 2012.

[2] Gulnaaz Rasiya, Abhinav Shukla, and Karan Saran. Additive manufacturing-a review. *Materials Today: Proceedings*, 47:6896–6901, 2021.

[3] William E Frazier. Metal additive manufacturing: a review. *Journal of Materials Engineering and performance*, 23:1917–1928, 2014.

[4] Maximilian Munsch, Matthias Schmidt-Lehr, and Eric Wycisk. *AMPOWER report 2023: Additive Manufacturing Market Report*. AMPOWER GmbH Co. KG, 2023.

[5] Fude Wang, Junfa Mei, and Xinhua Wu. Microstructure study of direct laser fabricated ti alloys using powder and wire. *Applied Surface Science*, 253(3):1424–1430, 2006.

[6] Kamran Aamir Mumtaz and Neil Hopkinson. Laser melting functionally graded composition of waspaloy® and zirconia powders. *Journal of materials science*, 42:7647–7656, 2007.

[7] Karen M Taminger and Robert A Hafley. Electron beam freeform fabrication for cost effective near-net shape manufacturing. In *NATO/RTO AVT-139 Specialists"Meeting on Cost Effective Manufacture via Net Shape Processing*, 2006.

[8] Alphons Anandaraj Antonysamy. *Microstructure, texture and mechanical property evolution during additive manufacturing of Ti6Al4V alloy for aerospace applications*. The University of Manchester (United Kingdom), 2012.

[9] Huan Qi, Magdi Azer, and Prabhjot Singh. Adaptive toolpath deposition method for laser net shape manufacturing and repair of turbine compressor airfoils. *The International Journal of Advanced Manufacturing Technology*, 48:121–131, 2010.

[10] Martin Hedges and Neil Calder. Near net shape rapid manufacture & repair by lens. In *Cost Effective Manufacture via Net-Shape Processing, Meeting Proceedings RTO-MP-AVT-139, Paper*, volume 13, 2006.

[11] Samuel H Huang, Peng Liu, Abhiram Mokasdar, and Liang Hou. Additive manufacturing and its societal impact: a literature review. *The International journal of advanced manufacturing technology*, 67:1191–1203, 2013.

[12] SM Kelly and SL Kampe. Microstructural evolution in laser-deposited multilayer ti-6al-4v builds: Part i. microstructural characterization. *Metallurgical and Materials Transactions A*, 35:1861–1867, 2004.

[13] PA Kobryn, NR Ontko, LP Perkins, and JS Tiley. Additive manufacturing of aerospace alloys for aircraft structures. Technical report, Air Force Research Lab Wright-Patterson AFB OH Materials and Manufacturing . . . , 2006.

[14] Xiaoming Zhao, Jing Chen, Xin Lin, and Weidong Huang. Study on microstructure and mechanical properties of laser rapid forming inconel 718. *Materials Science and Engineering: A*, 478(1-2):119–124, 2008.

[15] PA Kobryn, EH Moore, and S Lee Semiatin. The effect of laser power and traverse speed on microstructure, porosity, and build height in laser-deposited ti-6al-4v. *Scripta Materialia*, 43(4):299–305, 2000.

[16] Ozer Aydin and Rahmi Unal. Experimental and numerical modeling of the gas atomization nozzle for gas flow behavior. *Computers & Fluids*, 42(1):37–43, 2011.

[17] Carpenter. Resources for additive manufacturing and metal powders. Accessed October 16, 2023.

[18] IE Anderson, RS Figliola, and H Morton. Flow mechanisms in high pressure gas atomization. *Materials Science and Engineering: A*, 148(1):101–114, 1991.

[19] Randall M German. Powder metallurgy and particulate materials processing: the processes, materials, products, properties, and applications. *(No Title)*, 2005.

[20] Ernesto Urionabarrenetxea, Alejo Avello, Alejandro Rivas, and José Manuel Martín. Experimental study of the influence of operational and geometric variables on the powders produced by close-coupled gas atomisation. *Materials & Design*, 199:109441, 2021.

[21] Chao Cai and Kun Zhou. *Digital Manufacturing: The Industrialization of "Art to Par" 3D Additive Printing*. Elsevier, 2022.

[22] Luis E Criales, Yiğit M Arısoy, Brandon Lane, Shawn Moylan, Alkan Donmez, and Tuğrul Özel. Laser powder bed fusion of nickel alloy 625: Experimental investigations of effects of process parameters on melt pool size and shape with spatter analysis. *International Journal of Machine Tools and Manufacture*, 121:22–36, 2017.

[23] Haniyeh Fayazfar, Mehrnaz Salarian, Allan Rogalsky, Dyuti Sarker, Paola Russo, Vlad Paserin, and Ehsan Toyserkani. A critical review of powder-based additive manufacturing of ferrous alloys: Process parameters, microstructure and mechanical properties. *Materials & Design*, 144:98–128, 2018.

[24] Prince Valentine Cobbinah, Rivel Armil Nzeukou, Omoyemi Temitope Onawale,

and Wallace Rwisayi Matizamhuka. Laser powder bed fusion of potential superalloys: a review. *Metals*, 11(1):58, 2020.

[25] David J Bettinardi and Peter Tkac. Dissolution of additively manufactured mo disks and structures for accelerator based production of mo-99. Technical report, Argonne National Lab.(ANL), Argonne, IL (United States), 2020.

[26] Xinhua Wu. A review of laser fabrication of metallic engineering components and of materials. *Materials Science and Technology*, 23(6):631–640, 2007.

[27] Xin-hua Wu and J Mei. Near net shape manufacturing of components using direct laser fabrication technology. *Journal of Materials Processing Technology*, 135(2-3):266–270, 2003.

[28] William M Steen and Jyotirmoy Mazumder. *Laser material processing*. springer science & business media, 2010.

[29] Marleen Rombouts, Jean-Pierre Kruth, Ludo Froyen, and Peter Mercelis. Fundamentals of selective laser melting of alloyed steel powders. *CIRP annals*, 55(1):187–192, 2006.

[30] AV Gusarov, I Yadroitsev, Ph Bertrand, and I Smurov. Heat transfer modelling and stability analysis of selective laser melting. *Applied Surface Science*, 254(4):975–979, 2007.

[31] CY Kong, RJ Scudamore, and J Allen. High-rate laser metal deposition of inconel 718 component using low heat-input approach. *Physics Procedia*, 5:379–386, 2010.

[32] Andrew J Pinkerton, Richard Moat, Lin Li, Michael Preuss, and Philip Withers. Diode laser metal deposition: The effect of pulsed beam parameters on superalloy microstructure and deposit morphology. In *International Congress on Applications of Lasers & Electro-Optics*, volume 2006, page 302. Laser Institute of America, 2006.

[33] Thomas Schopphoven, Norbert Pirch, Stefan Mann, Reinhart Poprawe, Constantin Leon Häfner, and Johannes Henrich Schleifenbaum. Statistical/numerical model of the powder-gas jet for extreme high-speed laser material deposition. *Coatings*, 10(4):416, 2020.

[34] E Fearon and KG Watkins. Optimisation of layer height control in direct laser deposition. In *International Congress on Applications of Lasers & Electro-Optics*, volume 2004, page 1708. Laser Institute of America, 2004.

[35] Andreas Segerstark. *Laser metal deposition using alloy 718 powder: influence of process parameters on material characteristics*. PhD thesis, University West, 2017.

[36] Gangxian Zhu, Dichen Li, Anfeng Zhang, Gang Pi, and Yiping Tang. The influence of laser and powder defocusing characteristics on the surface quality

in laser direct metal deposition. *Optics & Laser Technology*, 44(2):349–356, 2012.

[37] Lino Costa and Rui Vilar. Laser powder deposition. *Rapid prototyping journal*, 15(4):264–279, 2009.

[38] Xipeng Tan, Yihong Kok, Yu Jun Tan, Marion Descoins, Dominique Mangelinck, Shu Beng Tor, Kah Fai Leong, and Chee Kai Chua. Graded microstructure and mechanical properties of additive manufactured ti–6al–4v via electron beam melting. *Acta Materialia*, 97:1–16, 2015.

[39] Lore Thijs, Frederik Verhaeghe, Tom Craeghs, Jan Van Humbeeck, and Jean-Pierre Kruth. A study of the microstructural evolution during selective laser melting of ti–6al–4v. *Acta materialia*, 58(9):3303–3312, 2010.

[40] Nima Shamsaei, Aref Yadollahi, Linkan Bian, and Scott M Thompson. An overview of direct laser deposition for additive manufacturing; part ii: Mechanical behavior, process parameter optimization and control. *Additive Manufacturing*, 8:12–35, 2015.

[41] James D Hunt. Steady state columnar and equiaxed growth of dendrites and eutectic. *Materials science and engineering*, 65(1):75–83, 1984.

[42] Kai Zhang, Shijie Wang, Weijun Liu, and Xiaofeng Shang. Characterization of stainless steel parts by laser metal deposition shaping. *Materials & Design*, 55:104–119, 2014.

[43] C Selcuk. Laser metal deposition for powder metallurgy parts. *Powder Metallurgy*, 54(2):94–99, 2011.

[44] I Yadroitsev, I Yadroitsava, and I Smurov. Strategy of fabrication of complex shape parts based on the stability of single laser melted track. In *Laser-based Micro-and Nanopackaging and Assembly V*, volume 7921, pages 78–90. SPIE, 2011.

[45] Mark Ensz, Michelle Griffith, William Hofmeister, Joel A Philliber, John Smugeresky, and Melissa Wert. Investigation of solidification in the laser engineered net shaping (lens) process. Technical report, Sandia National Laboratories (SNL), Albuquerque, NM, and Livermore, CA ..., 1999.

[46] Dirk Herzog, Vanessa Seyda, Eric Wycisk, and Claus Emmelmann. Additive manufacturing of metals. *Acta Materialia*, 117:371–392, 2016.

[47] Lore Thijs, Karolien Kempen, Jean-Pierre Kruth, and Jan Van Humbeeck. Fine-structured aluminium products with controllable texture by selective laser melting of pre-alloyed alsi10mg powder. *Acta Materialia*, 61(5):1809–1819, 2013.

[48] Di Wang, Changhui Song, Yongqiang Yang, and Yuchao Bai. Investigation of crystal growth mechanism during selective laser melting and mechanical property characterization of 316l stainless steel parts. *Materials & Design*, 100:291–299, 2016.

[49] Nima Haghdadi, Majid Laleh, Maxwell Moyle, and Sophie Primig. Additive manufacturing of steels: a review of achievements and challenges. *Journal of Materials Science*, 56:64–107, 2021.

[50] Thomas Niendorf, Stefan Leuders, Andre Riemer, Hans Albert Richard, Thomas Tröster, and Dieter Schwarze. Highly anisotropic steel processed by selective laser melting. *Metallurgical and materials transactions B*, 44:794–796, 2013.

[51] Jian Liu and Albert C To. Quantitative texture prediction of epitaxial columnar grains in additive manufacturing using selective laser melting. *Additive Manufacturing*, 16:58–64, 2017.

[52] Tobias Ronneberg, Catrin M Davies, and Paul A Hooper. Revealing relationships between porosity, microstructure and mechanical properties of laser powder bed fusion 316l stainless steel through heat treatment. *Materials & Design*, 189:108481, 2020.

[53] Hahn Choo, Logan P White, Xianghui Xiao, Clifton C Sluss, Derek Morin, and Elena Garlea. Deformation and fracture behavior of a laser powder bed fusion processed stainless steel: In situ synchrotron x-ray computed microtomography study. *Additive Manufacturing*, 40:101914, 2021.

[54] Ross Cunningham, Cang Zhao, Niranjan Parab, Christopher Kantzos, Joseph Pauza, Kamel Fezzaa, Tao Sun, and Anthony D Rollett. Keyhole threshold and

morphology in laser melting revealed by ultrahigh-speed x-ray imaging. *Science*, 363(6429):849–852, 2019.

[55] Ruidi Li, Jinhui Liu, Yusheng Shi, Li Wang, and Wei Jiang. Balling behavior of stainless steel and nickel powder during selective laser melting process. *The International Journal of Advanced Manufacturing Technology*, 59:1025–1035, 2012.

[56] Stéphane Gorsse, Christopher Hutchinson, Mohamed Gouné, and Rajarshi Banerjee. Additive manufacturing of metals: a brief review of the characteristic microstructures and properties of steels, ti-6al-4v and high-entropy alloys. *Science and Technology of advanced MaTerialS*, 18(1):584–610, 2017.

[57] Matjaž Godec, Stefan Zaefferer, Bojan Podgornik, Mario Šinko, and Elena Tchernychova. Quantitative multiscale correlative microstructure analysis of additive manufacturing of stainless steel 316l processed by selective laser melting. *Materials Characterization*, 160:110074, 2020.

[58] Shoujin Sun, Milan Brandt, and MJLAM Easton. Powder bed fusion processes: An overview. *Laser additive manufacturing*, pages 55–77, 2017.

[59] Itziar Tolosa, Fermín Garciandía, Fidel Zubiri, Fidel Zapirain, and Aritz Esnaola. Study of mechanical properties of aisi 316 stainless steel processed by "selective laser melting", following different manufacturing strategies. *The International Journal of Advanced Manufacturing Technology*, 51:639–647, 2010.

[60] Chor Yen Yap, Chee Kai Chua, Zhi Li Dong, Zhong Hong Liu, Dan Qing Zhang, Loong Ee Loh, and Swee Leong Sing. Review of selective laser melting: Materials and applications. *Applied physics reviews*, 2(4):041101, 2015.

[61] Zhongji Sun, Xipeng Tan, Shu Beng Tor, and Wai Yee Yeong. Selective laser melting of stainless steel 316l with low porosity and high build rates. *Materials & Design*, 104:197–204, 2016.

[62] Michał Zietala, Tomasz Durejko, Marek Polański, Izabela Kunce, Tomasz Płociński, Witold Zieliński, Magdalena Łazińska, Wojciech Stepniowski, Tomasz Czujko, Krzysztof J Kurzydłowski, et al. The microstructure, mechanical properties and corrosion resistance of 316 l stainless steel fabricated using laser engineered net shaping. *Materials Science and Engineering: A*, 677:1–10, 2016.

[63] Aref Yadollahi, Nima Shamsaei, Scott M Thompson, and Denver W Seely. Effects of process time interval and heat treatment on the mechanical and microstructural properties of direct laser deposited 316l stainless steel. *Materials Science and Engineering: A*, 644:171–183, 2015.

[64] Hanchen Yu, Jingjing Yang, Jie Yin, Zemin Wang, and Xiaoyan Zeng. Comparison on mechanical anisotropies of selective laser melted ti-6al-4v alloy and 304 stainless steel. *materials science and engineering: a*, 695:92–100, 2017.

[65] Jyoti Suryawanshi, KG Prashanth, and U Ramamurty. Mechanical behavior of

selective laser melted 316l stainless steel. *Materials Science and Engineering: A*, 696:113–121, 2017.

[66] Yuan Zhong, Leifeng Liu, Stefan Wikman, Daqing Cui, and Zhijian Shen. Intragranular cellular segregation network structure strengthening 316l stainless steel prepared by selective laser melting. *Journal of Nuclear Materials*, 470:170–178, 2016.

[67] Bastian Blinn, Marcus Klein, Christopher Gläßner, Marek Smaga, Jan C Aurich, and Tilmann Beck. An investigation of the microstructure and fatigue behavior of additively manufactured aisi 316l stainless steel with regard to the influence of heat treatment. *Metals*, 8(4):220, 2018.

[68] Andre Riemer, S Leuders, M Thöne, HA Richard, T Tröster, and T Niendorf. On the fatigue crack growth behavior in 316l stainless steel manufactured by selective laser melting. *Engineering Fracture Mechanics*, 120:15–25, 2014.

[69] Zhongji Sun, Xipeng Tan, Shu Beng Tor, and Chee Kai Chua. Simultaneously enhanced strength and ductility for 3d-printed stainless steel 316l by selective laser melting. *NPG Asia Materials*, 10(4):127–136, 2018.

[70] Y Morris Wang, Thomas Voisin, Joseph T McKeown, Jianchao Ye, Nicholas P Calta, Zan Li, Zhi Zeng, Yin Zhang, Wen Chen, Tien Tran Roehling, et al. Additively manufactured hierarchical stainless steels with high strength and ductility. *Nature materials*, 17(1):63–71, 2018.

[71] J-O Nilsson. Super duplex stainless steels. *Materials science and technology*, 8(8):685–700, 1992.

[72] Robert Gunn. *Duplex stainless steels: microstructure, properties and applications*. Woodhead publishing, 1997.

[73] Alleima and Narva. *Alleima Annual Report*. Alleima at a glance, 2022.

[74] Priyanshu Bajaj, Avinash Hariharan, Anoop Kini, Philipp Kürnsteiner, Dierk Raabe, and Eric Aimé Jägle. Steels in additive manufacturing: A review of their microstructure and properties. *Materials Science and Engineering: A*, 772:138633, 2020.

[75] Kamran Saeidi, Lenka Kevetkova, Frantisk Lofaj, and Zhijian Shen. Novel ferritic stainless steel formed by laser melting from duplex stainless steel powder with advanced mechanical properties and high ductility. *Materials Science and Engineering: A*, 665:59–65, 2016.

[76] AD Iams, JS Keist, and TA Palmer. Formation of austenite in additively manufactured and post-processed duplex stainless steel alloys. *Metallurgical and Materials Transactions A*, 51:982–999, 2020.

[77] Technical data sheet for 2205 alloy. Metalcor, 2023.

[78] Technical data sheet for 2507 alloy. Metalcor, 2023.

[79] Di Zhang, Aobo Liu, Bangzhao Yin, and Peng Wen. Additive manufacturing of duplex stainless steels-a critical review. *Journal of Manufacturing Processes*, 73:496–517, 2022.

[80] Mohammad K Alam, Jill Urbanic, Syed Mohammad Saqib, and Afsaneh Edrisy. Effect of process parameters on the microstructural evolutions of laser cladded 420 martensitic stainless steel. In *Materials science and technology conference proceedings (MS&T15), October*, pages 4–8, 2015.

[81] Mohammad K Alam, Afsaneh Edrisy, Jill Urbanic, and James Pineault. Microhardness and stress analysis of laser-cladded aisi 420 martensitic stainless steel. *Journal of Materials Engineering and Performance*, 26:1076–1084, 2017.

[82] Xiao Zhao, Qingsong Wei, Bo Song, Ying Liu, Xiwang Luo, Shifeng Wen, and Yusheng Shi. Fabrication and characterization of aisi 420 stainless steel using selective laser melting. *Materials and Manufacturing Processes*, 30(11):1283–1289, 2015.

[83] Pavel Krakhmalev, I Yadroitsava, G Fredriksson, and Igor Yadroitsev. In situ heat treatment in selective laser melted martensitic aisi 420 stainless steels. *Materials & Design*, 87:380–385, 2015.

[84] Kamran Saeidi, Daniel Leon Zapata, Frantisek Lofaj, Lenka Kvetkova, Jon Olsen, Zhijian Shen, and Farid Akhtar. Ultra-high strength martensitic 420 stainless steel with high ductility. *Additive Manufacturing*, 29:100803, 2019.

[85] Subrata Deb Nath, Emma Clinning, Gautam Gupta, Vincent Wuelfrath-Poirier, Gilles L'Espérance, Ozkan Gulsoy, Martin Kearns, and Sundar V Atre. Effects of nb and mo on the microstructure and properties of 420 stainless steel processed by laser-powder bed fusion. *Additive Manufacturing*, 28:682–691, 2019.

[86] J Hunt, F Derguti, and I Todd. Selection of steels suitable for additive layer manufacturing. *Ironmaking & Steelmaking*, 41(4):254–256, 2014.

[87] CN Hsiao, CS Chiou, and JR Yang. Aging reactions in a 17-4 ph stainless steel. *Materials Chemistry and Physics*, 74(2):134–142, 2002.

[88] Luca Facchini, Nerio Vicente Jr, Ivan Lonardelli, Emanuele Magalini, Pierfrancesco Robotti, and Alberto Molinari. Metastable austenite in 17–4 precipitation-hardening stainless steel produced by selective laser melting. *Advanced Engineering Materials*, 12(3):184–188, 2010.

[89] Li Wang, Chaofang Dong, Cheng Man, Decheng Kong, Kui Xiao, and Xiaogang Li. Enhancing the corrosion resistance of selective laser melted 15-5ph martensite stainless steel via heat treatment. *Corrosion Science*, 166:108427, 2020.

[90] Sudha Cheruvathur, Eric A Lass, and Carelyn E Campbell. Additive manufacturing of 17-4 ph stainless steel: post-processing heat treatment to achieve uniform reproducible microstructure. *Jom*, 68:930–942, 2016.

[91] Lawrence E Murr, Edwin Martinez, SM Gaytan, DA Ramirez, BI Machado, PW Shindo, JL Martinez, F Medina, J Wooten, D Ciscel, et al. Microstructural architecture, microstructures, and mechanical properties for a nickel-base superalloy fabricated by electron beam melting. *Metallurgical and Materials Transactions A*, 42:3491–3508, 2011.

[92] Lawrence E Murr, Edwin Martinez, Jennifer Hernandez, Shane Collins, Krista N Amato, Sara M Gaytan, and Patrick W Shindo. Microstructures and properties of 17-4 ph stainless steel fabricated by selective laser melting. *Journal of Materials Research and Technology*, 1(3):167–177, 2012.

[93] H Khalid Rafi, Deepankar Pal, Nachiket Patil, Thomas L Starr, and Brent E Stucker. Microstructure and mechanical behavior of 17-4 precipitation hardenable steel processed by selective laser melting. *Journal of materials engineering and performance*, 23:4421–4428, 2014.

[94] Somayeh Pasebani, Milad Ghayoor, Sunil Badwe, Harish Irrinki, and Sundar V Atre. Effects of atomizing media and post processing on mechanical properties of 17-4 ph stainless steel manufactured via selective laser melting. *Additive Manufacturing*, 22:127–137, 2018.

[95] Armando Caballero, Jialuo Ding, Supriyo Ganguly, and Stewart Williams. Wire+ arc additive manufacture of 17-4 ph stainless steel: Effect of different

processing conditions on microstructure, hardness, and tensile strength. *Journal of Materials Processing Technology*, 268:54–62, 2019.

[96] Tyler LeBrun, Takayuki Nakamoto, Keitaro Horikawa, and Hidetoshi Kobayashi. Effect of retained austenite on subsequent thermal processing and resultant mechanical properties of selective laser melted 17–4 ph stainless steel. *Materials & Design*, 81:44–53, 2015.

[97] Yu Sun, Rainer J Hebert, and Mark Aindow. Effect of heat treatments on microstructural evolution of additively manufactured and wrought 17-4ph stainless steel. *Materials & Design*, 156:429–440, 2018.

[98] SD Meredith, JS Zuback, JS Keist, and TA Palmer. Impact of composition on the heat treatment response of additively manufactured 17–4 ph grade stainless steel. *Materials Science and Engineering: A*, 738:44–56, 2018.

[99] Eric A Lass, Mark R Stoudt, and Maureen E Williams. Additively manufactured nitrogen-atomized 17-4 ph stainless steel with mechanical properties comparable to wrought. *Metallurgical and Materials Transactions A*, 50:1619–1624, 2019.

[100] S Sabooni, A Chabok, SC Feng, H Blaauw, TC Pijper, HJ Yang, and YT Pei. Laser powder bed fusion of 17–4 ph stainless steel: A comparative study on the effect of heat treatment on the microstructure evolution and mechanical properties. *Additive Manufacturing*, 46:102176, 2021.

[101] Chaolin Tan, Kesong Zhou, Min Kuang, Wenyou Ma, and Tongchun Kuang. Microstructural characterization and properties of selective laser melted maraging steel with different build directions. *Science and technology of advanced materials*, 19(1):746–758, 2018.

[102] David Bourell, Jean Pierre Kruth, Ming Leu, Gideon Levy, David Rosen, Allison M Beese, and Adam Clare. Materials for additive manufacturing. *CIRP annals*, 66(2):659–681, 2017.

[103] Chaolin Tan, Kesong Zhou, Wenyou Ma, Panpan Zhang, Min Liu, and Tongchun Kuang. Microstructural evolution, nanoprecipitation behavior and mechanical properties of selective laser melted high-performance grade 300 maraging steel. *Materials & Design*, 134:23–34, 2017.

[104] Riccardo Casati, JANNIS NICOLAS Lemke, Maurizio Vedani, et al. Microstructural and mechanical properties of as built, solution treated and aged 18ni (300 grade) maraging steel produced by selective laser melting. *La Metallurgia Italiana*, 1:11–20, 2017.

[105] Yuchao Bai, Yongqiang Yang, Di Wang, and Mingkang Zhang. Influence mechanism of parameters process and mechanical properties evolution mechanism of maraging steel 300 by selective laser melting. *Materials Science and Engineering: A*, 703:116–123, 2017.

[106] Thorsten Hermann Becker and Dimitri Dimitrov. The achievable mechanical properties of slm produced maraging steel 300 components. *Rapid Prototyping Journal*, 22(3):487–494, 2016.

[107] G Casalino, SL Campanelli, N Contuzzi, and AD Ludovico. Experimental investigation and statistical optimisation of the selective laser melting process of a maraging steel. *Optics & Laser Technology*, 65:151–158, 2015.

[108] Eric A Jägle, Zhendong Sheng, Philipp Kürnsteiner, Sörn Ocylok, Andreas Weisheit, and Dierk Raabe. Comparison of maraging steel micro-and nanostructure produced conventionally and by laser additive manufacturing. *Materials*, 10(1):8, 2016.

[109] Sabina Luisa Campanelli, Andrea Angelastro, Carmine Gabriele Signorile, and Giuseppe Casalino. Investigation on direct laser powder deposition of 18 ni (300) marage steel using mathematical model and experimental characterisation. *The International Journal of Advanced Manufacturing Technology*, 89:885–895, 2017.

[110] Philipp Kürnsteiner, Markus B Wilms, Andreas Weisheit, Pere Barriobero-Vila, Eric A Jägle, and Dierk Raabe. Massive nanoprecipitation in an fe-19ni-xal maraging steel triggered by the intrinsic heat treatment during laser metal deposition. *Acta Materialia*, 129:52–60, 2017.

[111] Eric A Jägle, Pyuck-Pa Choi, Jan Van Humbeeck, and Dierk Raabe. Precipitation and austenite reversion behavior of a maraging steel produced by selective laser melting. *Journal of Materials Research*, 29(17):2072–2079, 2014.

[112] Naoki Takata, Ryoya Nishida, Asuka Suzuki, Makoto Kobashi, and Masaki Kato. Crystallographic features of microstructure in maraging steel fabricated by selective laser melting. *Metals*, 8(6):440, 2018.

[113] Riccardo Casati, Jannis N Lemke, Ausonio Tuissi, and Maurizio Vedani. Aging behaviour and mechanical performance of 18-ni 300 steel processed by selective laser melting. *Metals*, 6(9):218, 2016.

[114] Karolien Kempen, Evren Yasa, Lore Thijs, J-P Kruth, and Jan Van Humbeeck. Microstructure and mechanical properties of selective laser melted 18ni-300 steel. *Physics Procedia*, 12:255–263, 2011.

[115] George Adam Roberts, Richard Kennedy, and George Krauss. *Tool steels*. ASM international, 1998.

[116] Karolien Kempen, Bey Vrancken, Sam Buls, Lore Thijs, Jan Van Humbeeck, and Jean-Pierre Kruth. Selective laser melting of crack-free high density m2 high speed steel parts by baseplate preheating. *Journal of Manufacturing Science and Engineering*, 136(6), 2014.

[117] J Mazumder, J Choi, K Nagarathnam, J Koch, and D Hetzner. The direct metal deposition of h13 tool steel for 3-d components. *Jom*, 49(5):55–60, 1997.

[118] J Choi and Y Hua. Dimensional and material characteristics of direct deposited tool steel by co2 laser. In *International Congress on Applications of Lasers & Electro-Optics*. AIP Publishing, 2002.

[119] J Choi and Y Chang. Characteristics of laser aided direct metal/material deposition process for tool steel. *International Journal of Machine Tools and Manufacture*, 45(4-5):597–607, 2005.

[120] Martin Joachim Holzweissig, Alexander Taube, Florian Brenne, Mirko Schaper, and Thomas Niendorf. Microstructural characterization and mechanical performance of hot work tool steel processed by selective laser melting. *Metallurgical and Materials Transactions B*, 46:545–549, 2015.

[121] Raya Mertens, Bey Vrancken, Niels Holmstock, Yannis Kinds, J-P Kruth, and Jan Van Humbeeck. Influence of powder bed preheating on microstructure and mechanical properties of h13 tool steel slm parts. *Physics Procedia*, 83:882–890, 2016.

[122] R Dörfert, J Zhang, B Clausen, H Freiße, J Schumacher, and F Vollertsen. Comparison of the fatigue strength between additively and conventionally fabricated tool steel 1.2344. *Additive Manufacturing*, 27:217–223, 2019.

[123] Julian Krell, Arne Röttger, Karina Geenen, and Werner Theisen. General investigations on processing tool steel x40crmov5-1 with selective laser melting. *Journal of Materials Processing Technology*, 255:679–688, 2018.

[124] Bo Ren, Dehong Lu, Rong Zhou, Zhenhua Li, and Jieren Guan. Preparation and mechanical properties of selective laser melted h13 steel. *Journal of Materials Research*, 34(8):1415–1425, 2019.

[125] JJ Yan, DL Zheng, HX Li, Xiangcai Jia, JF Sun, YL Li, Ma Qian, and Ming Yan. Selective laser melting of h13: microstructure and residual stress. *Journal of Materials Science*, 52:12476–12485, 2017.

[126] Jun Seok Park, Joo Hyun Park, Min-Gyu Lee, Ji Hyun Sung, Kyoung Je Cha, and Da Hye Kim. Effect of energy input on the characteristic of aisi h13 and d2 tool steels deposited by a directed energy deposition process. *Metallurgical and Materials Transactions A*, 47:2529–2535, 2016.

[127] A Bohlen, H Freiße, M Hunkel, and F Vollertsen. Additive manufacturing of tool steel by laser metal deposition. *Procedia Cirp*, 74:192–195, 2018.

[128] L Xue, J Chen, and S-H Wang. Freeform laser consolidated h13 and cpm 9v tool steels. *Metallography, Microstructure, and Analysis*, 2:67–78, 2013.

[129] Dalong Cong, Hong Zhou, Miaoqiang Yang, Zhihui Zhang, Peng Zhang, Chao Meng, and Chuanwei Wang. The mechanical properties of h13 die steel repaired by a biomimetic laser technique. *Optics & Laser Technology*, 53:1–8, 2013.

[130] Min Zhang, Changjun Chen, Lanlan Qin, Kai Yan, Guangping Cheng, Hemin Jing, and Tao Zou. Laser additive manufacturing of m2 high-speed steel. *Materials Science and Technology*, 34(1):69–78, 2018.

[131] J Šafka, M Ackermann, and L Voleskỳ. Structural properties of h13 tool steel parts produced with use of selective laser melting technology. In *Journal of physics: conference series*, volume 709, page 012004. IOP Publishing, 2016.

[132] Maciej Mazur, Paul Brincat, Martin Leary, and Milan Brandt. Numerical and experimental evaluation of a conformally cooled h13 steel injection mould manufactured with selective laser melting. *The International Journal of Advanced Manufacturing Technology*, 93:881–900, 2017.

[133] Robert Abbott Hadfield. *Manganese-steel: I. Manganese in its application to metallurgy: II. Some newly-discovered properties of iron and manganese.* Institution, 1888.

[134] David Havel. Austenitic manganese steel: A complete overview. *Columbia Steel Casting Co., Inc*, 2017.

[135] Motomichi Koyama, Eiji Akiyama, Young-Kook Lee, Dierk Raabe, and Kaneaki Tsuzaki. Overview of hydrogen embrittlement in high-mn steels. *international journal of hydrogen energy*, 42(17):12706–12723, 2017.

[136] Michelia Alba. *Experimental Investigation on Inclusions in Medium Manganese Steels and High Manganese Steels.* PhD thesis, 2021.

[137] Young Feng Gong and Bruno Charles De Cooman. Selective oxidation and subsurface phase transformation of twip steel during continuous annealing. *steel research international*, 82(11):1310–1318, 2011.

[138] Maryam Soleimani, Alireza Kalhor, and Hamed Mirzadeh. Transformation-induced plasticity (trip) in advanced steels: a review. *Materials Science and Engineering: A*, 795:140023, 2020.

[139] Shangping Chen, Radhakanta Rana, Arunansu Haldar, and Ranjit Kumar Ray. Current state of fe-mn-al-c low density steels. *Progress in Materials Science*, 89:345–391, 2017.

[140] Donald T Pierce, Jose Antonio Jiménez, James Bentley, Dierk Raabe, and James E Wittig. The influence of stacking fault energy on the microstructural and strain-hardening evolution of fe–mn–al–si steels during tensile deformation. *Acta Materialia*, 100:178–190, 2015.

[141] Chunyu Liu, Shucheng Shen, Pan Xie, and Cuilan Wu. Deformation behaviors of a fe-20mn-3al-3si trip steel under quasi-static compression and dynamic impact. *Materials Characterization*, 191:112095, 2022.

[142] Bruno C De Cooman, Yuri Estrin, and Sung Kyu Kim. Twinning-induced plasticity (twip) steels. *Acta Materialia*, 142:283–362, 2018.

[143] Peter Evans. *Twinning-induced plasticity in metastable beta titanium alloys*. PhD thesis, Imperial College London, 2017.

[144] RW Neu. Performance and characterization of twip steels for automotive applications. 2013.

[145] VM Blinov, IO Bannykh, EI Lukin, OA Bannykh, EV Blinov, OP Chernogorova, and MA Samoilova. Effect of substitutional alloying elements on the stacking fault energy in austenitic steels. *Russian Metallurgy (Metally)*, 2021:1325–1332, 2021.

[146] Hamza Essoussi, Said Ettaqi, and Elhachmi Essadiqi. The effect of alloying elements on the stacking fault energy of a twip steel. *Procedia Manufacturing*, 22:129–134, 2018.

[147] Hansoo Kim, Dong-Woo Suh, and Nack J Kim. Fe–al–mn–c lightweight structural alloys: a review on the microstructures and mechanical properties. *Science and technology of advanced materials*, 2013.

[148] I Zuazo, B Hallstedt, Bonnie Lindahl, Malin Selleby, M Soler, A Etienne, A Perlade, D Hasenpouth, Véronique Massardier-Jourdan, Sophie Cazottes, et al. Low-density steels: complex metallurgy for automotive applications. *Jom*, 66(9):1747–1758, 2014.

[149] Georg Frommeyer and Udo Brüx. Microstructures and mechanical properties of high-strength fe-mn-al-c light-weight triplex steels. *Steel research international*, 77(9-10):627–633, 2016.

[150] KT Luo, P-W Kao, and D Gan. Low temperature mechanical properties of fe 28mn 5al 1c alloy. *Materials Science and Engineering: A*, 151(1):L15–L18, 1992.

[151] Oscar Acselrad, LC Pereira, J Dille, and J L Delplancke. Room-temperature cleavage fracture of femnalc steels. *Metallurgical and Materials Transactions A*, 35:3863–3866, 2004.

[152] MT Jahn, SC Chang, and YH Hsiao. Transverse tensile and fatigue properties of fe-mn-al-c alloys. *Journal of materials science letters*, 8:723–724, 1989.

[153] IS Kalashnikov, O Acselrad, LC Pereira, T Kalichak, and MS Khadyyev. Behavior of fe-mn-al-c steels during cyclic tests. *Journal of materials engineering and performance*, 9:334–337, 2000.

[154] PRS Jackson and GR Wallwork. High temperature oxidation of iron-manganese-aluminum based alloys. *Oxidation of metals*, 21:135–170, 1984.

[155] Laura Bartlett and David Van Aken. High manganese and aluminum steels for the military and transportation industry. *Jom*, 66:1770–1784, 2014.

[156] H Springer and D Raabe. Rapid alloy prototyping: Compositional and thermo-mechanical high throughput bulk combinatorial design of structural materials based on the example of 30mn–1.2 c–xal triplex steels. *Acta Materialia*, 60(12):4950–4959, 2012.

[157] Zhihui Cai, Hua Ding, Zhengyan Ying, and RDK Misra. Microstructural evolution and deformation behavior of a hot-rolled and heat treated fe-8mn-4al-0.2 c steel. *Journal of materials engineering and performance*, 23:1131–1137, 2014.

[158] Wei-Chun Cheng, Chih-Yao Cheng, Chia-Wei Hsu, and David E Laughlin. Phase transformation of the l12 phase to kappa-carbide after spinodal decomposition and ordering in an fe–c–mn–al austenitic steel. *Materials Science and Engineering: A*, 642:128–135, 2015.

[159] Sang-Heon Kim, Hansoo Kim, and Nack J Kim. Brittle intermetallic compound makes ultrastrong low-density steel with large ductility. *Nature*, 518(7537):77–79, 2015.

[160] MX Yang, FP Yuan, QG Xie, YD Wang, E Ma, and XL Wu. Strain hardening in fe–16mn–10al–0.86 c–5ni high specific strength steel. *Acta Materialia*, 109:213–222, 2016.

[161] Martin Palm and Gerhard Inden. Experimental determination of phase equilibria in the fe al c system. *Intermetallics*, 3(6):443–454, 1995.

[162] Yoshisato Kimura, Kazuyuki Handa, Kunio Hayashi, and Yoshinao Mishima. Microstructure control and ductility improvement of the two-phase γ-fe/κ-(fe, mn) 3alc alloys in the fe–mn–al–c quaternary system. *Intermetallics*, 12(6):607–617, 2004.

[163] Kwan H Han, Jong C Yoon, and Woong K Choo. Tem evidence of modulated structure in fe mn al c austenitic alloys. *Scripta metallurgica*, 20(1):33–36, 1986.

[164] Kazunori Sato, Kazuhiro Tagawa, and Yasunobu Inoue. Age hardening of

an fe-30mn-9al-0.9 c alloy by spinodal decomposition. *Scripta metallurgica*, 22(6):899–902, 1988.

[165] Yi Hsuan Tuan, Chih Lung Lin, Chuen Guang Chao, and Tzeng Feng Liu. Grain boundary precipitation in fe-30mn-9al-5cr-0.7 c alloy. *Materials transactions*, 49(7):1589–1593, 2008.

[166] CY Chao, CN Hwang, and TF Liu. Grain boundary precipitation in an fe-7.8 al-31.7 mn-0.54 c alloy. *Scripta metallurgica et materialia*, 28(1):109–114, 1993.

[167] CY Chao, CN Hwang, and TF Liu. Grain boundary precipitation behaviors in an fe-9.8 al-28.6 mn-0.8 si-1.0 c alloy. *Scripta materialia*, 34(1), 1996.

[168] Laura N Bartlett, David C Van Aken, Julia Medvedeva, Dieter Isheim, Nadezhda I Medvedeva, and Kai Song. An atom probe study of kappa carbide precipitation and the effect of silicon addition. *Metallurgical and Materials Transactions A*, 45:2421–2435, 2014.

[169] Kazunori Sato, Kazuhiro Tagawa, and Yasunobu Inoue. Spinodal decomposition and mechanical properties of an austenitic fe-30wt.% mn-9wt.% al-0.9 wt.% c alloy. *Materials Science and Engineering: A*, 111:45–50, 1989.

[170] Wei-Chun Cheng, Yuan-Sheng Song, Yu-Shan Lin, Kuan-Fu Chen, and Petrus C Pistorius. On the eutectoid reaction in a quaternary fe-c-mn-al alloy: Austenite→ ferrite+ kappa-carbide+ m 23 c 6 carbide. *Metallurgical and Materials Transactions A*, 45:1199–1216, 2014.

[171] Wei-Chun Cheng. Phase transformations of an fe-0.85 c-17.9 mn-7.1 al austenitic steel after quenching and annealing. *Jom*, 66:1809–1820, 2014.

[172] I Kalashnikov, A Shalkevich, O Acselrad, and LC Pereira. Chemical composition optimization for austenitic steels of the fe-mn-al-c system. *Journal of materials engineering and performance*, 9:597–602, 2000.

[173] Radhakanta Rana. Low-density steels. *Jom*, 66(9):1730–1733, 2014.

[174] H Huang, D Gan, and PW Kao. Effect of alloying additions on the [kappa] phase precipitation in austenitic fe-mn-al-c alloys. *Scripta Metallurgica et Materialia;(United States)*, 30(4), 1994.

[175] Auriane Etienne, Véronique Massardier-Jourdan, Sophie Cazottes, Xavier Garat, Michel Soler, Ian Zuazo, and Xavier Kleber. Ferrite effects in fe-mn-al-c triplex steels. *Metallurgical and Materials Transactions A*, 45:324–334, 2014.

[176] CJ Altstetter, AP Bentley, JW Fourie, and AN Kirkbride. Processing and properties of fe mn al alloys. *Materials Science and Engineering*, 82:13–25, 1986.

[177] European Commission, Directorate-General for Research, Innovation, M Bausch, L Samek, H Hofmann, M Didier, G Frommeyer, M Soler, and E Balichev. *Ultra high-strength and ductile FeMnAlC light-weight steels (MnAl-steel)*. Publications Office, 2013.

[178] Kyung-Tae Park, Kwang Geun Jin, Sang Ho Han, Si Woo Hwang, Kayoung Choi, and Chong Soo Lee. Stacking fault energy and plastic deformation of fully austenitic high manganese steels: Effect of al addition. *Materials Science and Engineering: A*, 527(16-17):3651–3661, 2010.

[179] Christian Haase, Christoffer Zehnder, Tobias Ingendahl, André Bikar, Florian Tang, Bengt Hallstedt, Weiping Hu, Wolfgang Bleck, and Dmitri A Molodov. On the deformation behavior of κ-carbide-free and κ-carbide-containing high-mn light-weight steel. *Acta Materialia*, 122:332–343, 2017.

[180] E Welsch, Dirk Ponge, SM Hafez Haghighat, Stefanie Sandlöbes, P Choi, Michael Herbig, Stefan Zaefferer, and Dierk Raabe. Strain hardening by dynamic slip band refinement in a high-mn lightweight steel. *Acta Materialia*, 116:188–199, 2016.

[181] G Frommeyer, EJ Drewes, and B Engl. Physical and mechanical properties of iron-aluminium-(mn, si) lightweight steels. *Metallurgical Research & Technology*, 97(10):1245–1253, 2000.

[182] GR Lehnhoff, KO Findley, and BC De Cooman. The influence of silicon and aluminum alloying on the lattice parameter and stacking fault energy of austenitic steel. *Scripta Materialia*, 92:19–22, 2014.

[183] Ulrich Bohnenkamp and Rolf Sandström. Evaluation of the elastic modulus of steels. *Steel Research*, 71(3):94–99, 2000.

[184] RK You, Po-We Kao, and D Gan. Mechanical properties of fe 30mn 10al 1c 1si alloy. *Materials Science and Engineering: A*, 117:141–148, 1989.

[185] Dierk Raabe, Hauke Springer, Ivan Gutiérrez-Urrutia, Franz Roters, Michael Bausch, J B Seol, Motomichi Koyama, P P Choi, and Kaneaki Tsuzaki. Alloy design, combinatorial synthesis, and microstructure–property relations for low-density fe-mn-al-c austenitic steels. *Jom*, 66:1845–1856, 2014.

[186] Georg Frommeyer, Udo Brüx, and Peter Neumann. Supra-ductile and high-strength manganese-trip/twip steels for high energy absorption purposes. *ISIJ international*, 43(3):438–446, 2003.

[187] Vikas Kumar Saxena, MS Gopala Krishna, PS Chhaunker, and VM Radhakrishnan. Fatigue and fracture behavior of a nickel-chromium free austenitic steel. *International journal of pressure vessels and piping*, 60(2):151–157, 1994.

[188] AS Hamada, LP Karjalainen, and J Puustinen. Fatigue behavior of high-mn twip steels. *Materials Science and Engineering: A*, 517(1-2):68–77, 2009.

[189] Jing-Bang Duh, Wen-Ta Tsai, and Ju-Teng Lee. Fatigue crack growth in fealmn alloys. *Scripta Metallurgica*, 21(2):95–98, 1987.

[190] SC Tjong, SM Zhu, NJ Ho, and JS Ku. Solidification microstructure and creep rupture behaviour of electron beam welded austenitic fe-28m-6al-1c alloy. *Materials science and technology*, 13(3):251–256, 1997.

[191] Jim Son Ku, New Jin Ho, and Sie Chin Tjong. Properties of electron-beam-welded and laser-welded austenitic fe-28mn-5al-1c alloy. *Journal of materials science*, 28:2808–2814, 1993.

[192] Laís Mújica Roncery, Sebastian Weber, and Werner Theisen. Welding of twinning-induced plasticity steels. *Scripta Materialia*, 66(12):997–1001, 2012.

[193] Daniel Keil, Manuela Zinke, and Helge Pries. Weldability of novel fe-mn high-strength steels for automotive applications. *Welding in the World*, 55:21–30, 2011.

[194] Chang-Pin Chou and Chien-Hsun Lee. Weld metal characteristics of duplex fe-30wt.% mn-10wt.% al-xc alloys. *Materials Science and Engineering: A*, 118:137–146, 1989.

[195] JC Garcia, N Rosas, and RJ Rioja. Development of oxidation resistant fe–mn–al alloys. *Met. Prog.*, 122(3):47–50, 1982.

[196] CH Kao and CM Wan. Effect of temperature on the oxidation of fe-7.5 a1-o. 65c alloy. *Journal of materials science*, 23:1943–1947, 1988.

[197] JP Sauer, RA Rapp, and JP Hirth. Oxidation of iron-manganese-aluminum alloys at 850 and 1000 c. *Oxidation of Metals*, 18:285–294, 1982.

[198] SC Tjong. High temperature oxidation of the austenitic fe–9al–30mn–1.0 c and

duplex fe–10al–29mn–0.4 c alloys. *Transactions of the Japan institute of metals*, 28(8):671–678, 1987.

[199] SC Tjong and CS Wu. The microstructure and stress corrosion cracking behaviour of precipitation-hardened fe 8.7 al 29.7 mn 1.04 c alloy in 20% nacl solution. *Materials Science and Engineering*, 80(2):203–211, 1986.

[200] YJ Gau. The influence of alloying elements on the corrosion behavior of fe-mn-al alloys. *Corrosion prevention & control*, 44(2):56–60, 1997.

[201] YH Tuan, CS Wang, CY Tsai, CG Chao, and TF Liu. Corrosion behaviors of austenitic fe–30mn–7al–xcr–1c alloys in 3.5% nacl solution. *Materials Chemistry and Physics*, 114(2-3):595–598, 2009.

[202] Cheng Shun Wang, Cheng Yao Tsai, Chuen Guang Chao, and Tzeng Feng Liu. Effect of chromium content on corrosion behaviors of fe-9al-30mn-(3, 5, 6.5, 8) cr-1c alloys. *Materials transactions*, 48(11):2973–2977, 2007.

[203] Radhakanta Rana, Jenny Loiseaux, and Chris Lahaije. Microstructure, mechanical properties and formability of a duplex steel. In *Materials Science Forum*, volume 706, pages 2271–2277. Trans Tech Publ, 2012.

[204] Kwang-Geun Chin, Chung-Yun Kang, Sang Yong Shin, Seokmin Hong, Sunghak Lee, Hyoung Seop Kim, Kyung-hun Kim, and Nack J Kim. Effects of al addition on deformation and fracture mechanisms in two high manganese twip steels. *Materials Science and Engineering: A*, 528(6):2922–2928, 2011.

[205] A Mohamadizadeh, A Zarei-Hanzaki, HR Abedi, S Mehtonen, and D Porter. Hot deformation characterization of duplex low-density steel through 3d processing map development. *Materials Characterization*, 107:293–301, 2015.

[206] Eva Mazancová, Ivan Ružiak, and Ivo Schindler. Influence of rolling conditions and aging process on mechanical properties of high manganese steels. *Archives of Civil and Mechanical Engineering*, 12(2):142–147, 2012.

[207] JC Benz and HW Leavenworth. An assessment of fe-mn-al alloys as substitutes for stainless steels. *Jom*, 37:36–39, 1985.

[208] VV Satya Prasad, Shivkumar Khaple, and RG Baligidad. Melting, processing, and properties of disordered fe-al and fe-al-c based alloys. *JOM*, 66:1785–1793, 2014.

[209] Fabian Kies, Patrick Köhnen, Markus B Wilms, Frederike Brasche, Konda G Pradeep, Alexander Schwedt, Silvia Richter, Andreas Weisheit, Johannes H Schleifenbaum, and Christian Haase. Design of high-manganese steels for additive manufacturing applications with energy-absorption functionality. *Materials & Design*, 160:1250–1264, 2018.

[210] Fabian Kies, Markus B Wilms, Norbert Pirch, Konda G Pradeep, Johannes H Schleifenbaum, and Christian Haase. Defect formation and prevention in directed energy deposition of high-manganese steels and the effect on mechanical properties. *Materials Science and Engineering: A*, 772:138688, 2020.

[211] Christian Haase, Jan Bültmann, Jan Hof, Stephan Ziegler, Sebastian Bremen, Christian Hinke, Alexander Schwedt, Ulrich Prahl, and Wolfgang Bleck. Exploiting process-related advantages of selective laser melting for the production of high-manganese steel. *Materials*, 10(1):56, 2017.

[212] S Ewald, M Schaukellis, P Koehnen, and JH Schleifenbaum. Laser powder bed fusion of advanced high-strength steels—modification of deformation mechanisms by increasing stacking fault energy. *BHM Berg*, 10(2), 2019.

[213] T Niendorf and Florian Brenne. Steel showing twinning-induced plasticity processed by selective laser melting—an additively manufactured high performance material. *Materials Characterization*, 85:57–63, 2013.

[214] S Amir H Motaman and Christian Haase. The microstructural effects on the mechanical response of polycrystals: A comparative experimental-numerical study on conventionally and additively manufactured metallic materials. *International Journal of Plasticity*, 140:102941, 2021.

[215] Patrick Köhnen, Simon Ewald, Johannes Henrich Schleifenbaum, Andrey Belyakov, and Christian Haase. Controlling microstructure and mechanical properties of additively manufactured high-strength steels by tailored solidification. *Additive Manufacturing*, 35:101389, 2020.

[216] Wei Li, Jikang Li, Xianyin Duan, Chuanyue He, Qingsong Wei, and Yusheng Shi. Dislocation-induced ultra-high strength in a novel steel fabricated using

laser powder-bed-fusion. *Materials Science and Engineering: A*, 832:142502, 2022.

[217] Raiyan Seede, Austin Whitt, Jiahui Ye, Sean Gibbons, Philip Flater, Bernard Gaskey, Alaa Elwany, Raymundo Arroyave, and Ibrahim Karaman. A lightweight fe–mn–al–c austenitic steel with ultra-high strength and ductility fabricated via laser powder bed fusion. *Materials Science and Engineering: A*, 874:145007, 2023.

[218] Lakshmi Lavanya Parimi. *Additive manufacturing of nickel based superalloys for aerospace applications*. PhD thesis, University of Birmingham, 2014.

[219] Sindo Kou. *Welding metallurgy*. John Wiley & Sons, 2020.

[220] Gautam Agarwal. Study of solidification cracking during laser welding in advanced high strength steels. a combined experimental and numerical approach. *Delft University of Technology*, 2019.

[221] Abdullah Alhuzaim. *Microstructural and mechanical properties control during additive manufacturing*. PhD thesis, University of Birmingham, 2021.

[222] EO Hall. The deformation and ageing of mild steel: Iii discussion of results. *Proceedings of the Physical Society. Section B*, 64(9):747, 1951.

[223] NJ Petch. The cleavage strength of polycrystals. *J. Iron Steel Inst.*, 174:25–28, 1953.

[224] Tarasankar DebRoy, HL Wei, JS Zuback, Tuhin Mukherjee, JW Elmer, JO Milewski, Allison Michelle Beese, A de Wilson-Heid, Amitava De, and Wei Zhang. Additive manufacturing of metallic components–process, structure and properties. *Progress in Materials Science*, 92:112–224, 2018.

[225] Kun V Yang, Yunjia Shi, Frank Palm, Xinhua Wu, and Paul Rometsch. Columnar to equiaxed transition in al-mg (-sc)-zr alloys produced by selective laser melting. *Scripta Materialia*, 145:113–117, 2018.

[226] Q Zhang, J Chen, X Lin, H Tan, and WD Huang. Grain morphology control and texture characterization of laser solid formed ti6al2sn2zr3mo1. 5cr2nb titanium alloy. *Journal of Materials Processing Technology*, 238:202–211, 2016.

[227] Shiwen Liu, Haihong Zhu, Gangyong Peng, Jie Yin, and Xiaoyan Zeng. Microstructure prediction of selective laser melting alsi10mg using finite element analysis. *Materials & Design*, 142:319–328, 2018.

[228] Ryan R Dehoff, MM Kirka, WJ Sames, H Bilheux, AS Tremsin, LE Lowe, and SS Babu. Site specific control of crystallographic grain orientation through electron beam additive manufacturing. *Materials Science and Technology*, 31(8):931–938, 2015.

[229] Tien T Roehling, Rongpei Shi, Saad A Khairallah, John D Roehling, Gabe M

Guss, Joseph T McKeown, and Manyalibo J Matthews. Controlling grain nucleation and morphology by laser beam shaping in metal additive manufacturing. *Materials & Design*, 195:109071, 2020.

[230] Rongpei Shi, Saad A Khairallah, Tien T Roehling, Tae Wook Heo, Joseph T McKeown, and Manyalibo J Matthews. Microstructural control in metal laser powder bed fusion additive manufacturing using laser beam shaping strategy. *Acta Materialia*, 184:284–305, 2020.

[231] Tait D McLouth, Glenn E Bean, David B Witkin, Scott D Sitzman, Paul M Adams, Dhruv N Patel, Woonsup Park, Jenn-Ming Yang, and Rafael J Zaldivar. The effect of laser focus shift on microstructural variation of inconel 718 produced by selective laser melting. *Materials & Design*, 149:205–213, 2018.

[232] H Y Wan, Z J Zhou, C P Li, GF Chen, and GP Zhang. Effect of scanning strategy on grain structure and crystallographic texture of inconel 718 processed by selective laser melting. *Journal of materials science & technology*, 34(10):1799–1804, 2018.

[233] Wei Xiong, Liang Hao, Yan Li, Danna Tang, Qian Cui, Zuying Feng, and Chunze Yan. Effect of selective laser melting parameters on morphology, microstructure, densification and mechanical properties of supersaturated silver alloy. *Materials & Design*, 170:107697, 2019.

[234] Duyao Zhang, Dong Qiu, Suming Zhu, Matthew Dargusch, David StJohn, and Mark Easton. Grain refinement in laser remelted mg-3nd-1gd-0.5 zr alloy. *Scripta Materialia*, 183:12–16, 2020.

[235] Duyao Zhang, Dong Qiu, Mark A Gibson, Yufeng Zheng, Hamish L Fraser, Arvind Prasad, David H StJohn, and Mark A Easton. Refining prior-β grains of ti–6al–4v alloy through yttrium addition. *Journal of Alloys and Compounds*, 841:155733, 2020.

[236] Arvind Prasad, Lang Yuan, Peter Lee, Mitesh Patel, Dong Qiu, Mark Easton, and David StJohn. Towards understanding grain nucleation under additive manufacturing solidification conditions. *Acta Materialia*, 195:392–403, 2020.

[237] JC Villafuerte and HW Kerr. Grain structures in gas tungsten-arc welds of austenitic stainless steels with ferrite primary phase. *Metallurgical Transactions A*, 21:979–986, 1990.

[238] A Durga, Niklas Holländer Pettersson, Sri Bala Aditya Malladi, Zhuoer Chen, Sheng Guo, Lars Nyborg, and Greta Lindwall. Grain refinement in additively manufactured ferritic stainless steel by in situ inoculation using pre-alloyed powder. *Scripta Materialia*, 194:113690, 2021.

[239] PC Collins, DA Brice, P Samimi, I Ghamarian, and HL Fraser. Microstructural control of additively manufactured metallic materials. *Annual Review of Materials Research*, 46:63–91, 2016.

[240] Yali Li and Dongdong Gu. Thermal behavior during selective laser melting of commercially pure titanium powder: Numerical simulation and experimental study. *Additive Manufacturing*, 1:99–109, 2014.

[241] PJ Spencer. A brief history of calphad. *Calphad*, 32(1):1–8, 2008.

[242] Zi-Kui Liu. Ocean of data: integrating first-principles calculations and calphad modeling with machine learning. *Journal of Phase Equilibria and Diffusion*, 39:635–649, 2018.

[243] Jan-Olof Andersson, Thomas Helander, Lars Höglund, Pingfang Shi, and Bo Sundman. Thermo-calc & dictra, computational tools for materials science. *Calphad*, 26(2):273–312, 2002.

[244] GH Gulliver. The quantitative effect of rapid cooling upon the constitution of binary alloys. *J. Inst. Met*, 9(1):120–157, 1913.

[245] Erich Scheil. Bemerkungen zur schichtkristallbildung. *International Journal of Materials Research*, 34(3):70–72, 1942.

[246] Trevor Keller, Greta Lindwall, Supriyo Ghosh, Li Ma, Brandon M Lane, Fan Zhang, Ursula R Kattner, Eric A Lass, Jarred C Heigel, Yaakov Idell, et al. Application of finite element, phase-field, and calphad-based methods to additive manufacturing of ni-based superalloys. *Acta materialia*, 139:244–253, 2017.

[247] TW Clyne, M Wolf, and W Kurz. The effect of melt composition on solidification cracking of steel, with particular reference to continuous casting. *Metallurgical transactions B*, 13:259–266, 1982.

[248] Alexandre F Ferreira, Ever G de Melo, and L de Olivé Ferreira. Prediction of secondary-dendrite arm spacing for binary alloys by means of a phase-field model. *steel research international*, 86(1):58–64, 2015.

[249] Peng Peng. On morphology-dependent growth of secondary dendrite arms: Analysis in peritectic systems. *Journal of Alloys and Compounds*, 798:210–219, 2019.

[250] Jianghai Cao, Zihang Zeng, Fuli Zhang, Dongwei Guo, and Zibing Hou. Effect of cooling rates on the local—overall morphology characteristics of solidification structure at different stages for high carbon steel. *Metals*, 11(8):1291, 2021.

[251] Chongliang Zhong, Norbert Pirch, Andres Gasser, Reinhart Poprawe, and Johannes Henrich Schleifenbaum. The influence of the powder stream on high-deposition-rate laser metal deposition with inconel 718. *Metals*, 7(10):443, 2017.

[252] Robert D Field and Hamish L Fraser. Microstructural observations of metal powders using analytical electron microscopy. *Metallurgical Transactions A*, 9:131–134, 1978.

[253] RJ Hill and CJ Howard. Quantitative phase analysis from neutron powder

diffraction data using the rietveld method. *Journal of Applied Crystallography*, 20(6):467–474, 1987.

[254] Seoung-Ho Lim, KenHee Ryou, Kyuseon Jang, Won Seok Choi, Hyuck Mo Lee, and Pyuck-Pa Choi. Hot cracking behavior of additively manufactured d2 steel. *Materials Characterization*, 178:111217, 2021.

[255] Tianxu Li, Zhijiang Wang, Shengsun Hu, Zhenwen Yang, and Ying Wang. Hot cracking during the fabrication of inconel 625/stainless steel 308 l functionally graded material by dual-wire arc additive manufacturing. *Journal of Manufacturing Processes*, 82:461–473, 2022.

[256] Liang Wu, Suvajeet Das, Witalij Gridin, Stefan Leuders, Moritz Kahlert, Malte Vollmer, and Thomas Niendorf. Hot work tool steel processed by laser powder bed fusion: A review on most relevant influencing factors. *Advanced Engineering Materials*, 23(7):2100049, 2021.

[257] Zhongji Sun, Yan Ma, Dirk Ponge, Stefan Zaefferer, Eric A Jägle, Baptiste Gault, Anthony D Rollett, and Dierk Raabe. Thermodynamics-guided alloy and process design for additive manufacturing. *Nature Communications*, 13(1):4361, 2022.

[258] The Welding Institute (TWI) Global. What is hot cracking (solidification cracking)? `https://www.twi-global.com/technical-knowledge/faqs/`

faq-what-is-hot-cracking-solidification-cracking. Accessed on January 11, 2023.

[259] The Welding Institute (TWI) Global. Liquation cracking. https://www.twi-global.com/technical-knowledge/knowledge-summaries/liquation-cracking. Accessed on January 11, 2023.

[260] Dimosthenis Manitsas and Joel Andersson. Hot cracking mechanisms in welding metallurgy: a review of theoretical approaches. In *MATEC web of conferences*, volume 188, page 03018. EDP Sciences, 2018.

[261] JC Borland. Generalized theory of super-solidus cracking in welds. *Br. Weld. J.*, 7:508–512, 1960.

[262] EJ Morgan-Warrena and MF Jordan. A quantitative study of the effect of composition on vveld solidification cracking in lovv-alloy steels. *Metals Technology*, 1(1):271–278, 1974.

[263] JG Garland and N Bailey. Solidification cracking during the submerged arc welding of carbon-manganese steels-detailed assessment of the effect of parent plate compositions. 1978.

[264] The Welding Institute (TWI) Global. Defects - solidification cracking. https://www.twi-global.com/technical-knowledge/job-knowledge/defects-solidification-cracking-044. Accessed on January 11, 2023.

[265] V Kujanpaa, N Suutala, T Takalo, and T Moisio. Correlation between solidification cracking and microstructure in austenitic and austenitic-ferritic stainless steel welds. *Weld. Res. Int.;(United Kingdom)*, 9(2), 1979.

[266] Fuyao Yan, Jiayi Yan, and David Linder. Understanding hot cracking of steels during rapid solidification: an icme approach. *Materials Proceedings*, 3(1):30, 2021.

[267] Siyuan Qin, Yutao Bo, Simone Herzog, Bengt Hallstedt, Anke Kaletsch, and Christoph Broeckmann. influence of process parameters on porosity and hot cracking of aisi h13 fabricated by laser powder bed fusion. *Powders*, 1(3):184–193, 2022.

[268] TW Clyne and DAVIES GJ. The influence of composition on solidification cracking susceptibility in binary alloy systems. 1981.

[269] Xinyan Yan and Jen C Lin. Prediction of hot tearing tendency for multicomponent aluminum alloys. *Metallurgical and Materials Transactions B*, 37:913–918, 2006.

[270] J Li and Q-Y Shi. Minimizing buckling distortion in welding by weld cooling. In *Minimization of Welding Distortion and Buckling*, pages 214–240. Elsevier, 2011.

[271] Benjamin James Sutton. *Solidification behavior and hot cracking susceptibility*

of high manganese steel weld metals. PhD thesis, The Ohio State University, 2013.

[272] MF Gittos, SMI Birch, and RJ Pargeter. Solidification cracking susceptibility in c-mn steel co 2 laser welds. *Hot Cracking Phenomena in Welds III*, pages 225–262, 2011.

[273] TW Clyne and W Kurz. Solute redistribution during solidification with rapid solid state diffusion. *Metallurgical Transactions A*, 12:965–971, 1981.

[274] VP Kujanpää, SA David, and CL White. Formation of hot cracks in austenitic stainless steel welds-solidification cracking. *Welding Journal*, 65(8):203s–212s, 1986.

[275] CD Lundin, CH Lee, R Menon, and V Osorio. Weldability evaluations of modified 316 and 347 austenitic stainless steels: Part i–preliminary results. *Welding Journal*, 67(2):35s–46s, 1988.

[276] T Ogawa and E Tsunetomi. Hot cracking susceptibility of austenitic stainless steels. *WELDING J.*, 61(3):82, 1982.

[277] The Welding Institute (TWI) Global. Welding of austenitic stainless steel. `https://www.twi-global.com/technical-knowledge/job-knowledge/welding-of-austenitic-stainless-steel-103`. Accessed on January 9, 2023.

[278] VAB De Nelson III and JC Lippold. An investigation of weld hot cracking in duplex stainless steels. *Weld. Res. Suppl*, 1985.

[279] Olena Volkova, Hans-Peter Heller, and Dieter Janke. Microstructure and cleanliness of rapidly solidified steels. *ISIJ international*, 43(11):1724–1732, 2003.

[280] Morteza Narvan, Kassim S Al-Rubaie, and Mohamed Elbestawi. Process-structure-property relationships of aisi h13 tool steel processed with selective laser melting. *Materials*, 12(14):2284, 2019.

[281] Fang Pengjun, Xu Yi, Li Xinggang, and Chen Ya. Influence of atomizing gas and cooling rate on solidification characterization of nickel-based superalloy powders. *Rare Metal Materials and Engineering*, 47(2):423–430, 2018.

[282] Stan A David and JM Vitek. *International Trends in Welding Science and Technology: Proceedings of the 3rd International Conference on Trends in Welding Research, Gatlinburg, Tennessee, USA, June 1-5, 1992*. ASM International, 1993.

[283] Gaoyuan Ouyang, Brandt Jensen, Chad R Macziewski, Tao Ma, Fangqiang Meng, Qishen Lin, Lin Zhou, Matt Kramer, and Jun Cui. Characterization of ordering in fe-6.5% si alloy using x-ray, tem, and magnetic tga methods. *Materials Characterization*, 158:109973, 2019.

[284] JH Yu, JS Shin, JS Bae, Z-H Lee, Taek Dong Lee, HyuckMo Lee, and EJ Lavernia. The effect of heat treatments and si contents on b2 ordering reaction

in high-silicon steels. *Materials Science and Engineering: A*, 307(1-2):29–34, 2001.

[285] Max Müller, Dorothea Czempas, David Bailly, and Gerhard Hirt. Twin roll casting and secondary cooling of 6.0 wt.% silicon steel. *Metals*, 11(10):1508, 2021.

[286] Woong Kil Choo, JH Kim, and JC Yoon. Microstructural change in austenitic fe-30.0 wt% mn-7.8 wt% al-1.3 wt% c initiated by spinodal decomposition and its influence on mechanical properties. *Acta Materialia*, 45(12):4877–4885, 1997.

[287] Peng Chen, Xiaowu Li, and Hongliang Yi. The κ-carbides in low-density fe-mn-al-c steels: A review on their structure, precipitation and deformation mechanism. *Metals*, 10(8):1021, 2020.

[288] Lingshan Li, Hao Chen, Zhirong Liao, Yue Yang, and Dragos Axinte. Investigation of the grain deformation to orthogonal cutting process of the textured alloy 718 fabricated by laser powder bed fusion. *International Journal of Machine Tools and Manufacture*, page 104050, 2023.

[289] Wen Shifeng, Li Shuai, Wei Qingsong, Chunze Yan, Zhang Sheng, and Shi Yusheng. Effect of molten pool boundaries on the mechanical properties of selective laser melting parts. *Journal of Materials Processing Technology*, 214(11):2660–2667, 2014.

[290] Hideaki Ikehata and Eric Jägle. Evaluation of microstructure and tensile properties of grain-refined, ti-alloyed ferritic stainless steel fabricated by laser powder bed fusion. *Materials Science and Engineering: A*, 818:141365, 2021.

[291] Bo Song, Shujuan Dong, Pierre Coddet, Hanlin Liao, and Christian Coddet. Fabrication of nicr alloy parts by selective laser melting: columnar microstructure and anisotropic mechanical behavior. *Materials & Design*, 53:1–7, 2014.

[292] Fuyao Yan, Wei Xiong, and Eric J Faierson. Grain structure control of additively manufactured metallic materials. *Materials*, 10(11):1260, 2017.

[293] Neil J Harrison, Iain Todd, and Kamran Mumtaz. Reduction of micro-cracking in nickel superalloys processed by selective laser melting: A fundamental alloy design approach. *Acta Materialia*, 94:59–68, 2015.

[294] John H Martin, Brennan D Yahata, Jacob M Hundley, Justin A Mayer, Tobias A Schaedler, and Tresa M Pollock. 3d printing of high-strength aluminium alloys. *Nature*, 549(7672):365–369, 2017.

[295] Maria L Montero-Sistiaga, Raya Mertens, Bey Vrancken, Xiebin Wang, Brecht Van Hooreweder, Jean-Pierre Kruth, and Jan Van Humbeeck. Changing the alloy composition of al7075 for better processability by selective laser melting. *Journal of Materials Processing Technology*, 238:437–445, 2016.

[296] Thomas Boegelein, Sebastien N Dryepondt, Amit Pandey, Karl Dawson, and

Gordon J Tatlock. Mechanical response and deformation mechanisms of ferritic oxide dispersion strengthened steel structures produced by selective laser melting. *Acta Materialia*, 87:201–215, 2015.

[297] Takahiro Kimura and Takayuki Nakamoto. Microstructures and mechanical properties of a356 (alsi7mg0. 3) aluminum alloy fabricated by selective laser melting. *Materials & design*, 89:1294–1301, 2016.

[298] Dennis Karlsson, Chia-Ying Chou, Niklas Holländer Pettersson, Thomas Helander, Peter Harlin, Martin Sahlberg, Greta Lindwall, Joakim Odqvist, and Ulf Jansson. Additive manufacturing of the ferritic stainless steel ss441. *Additive Manufacturing*, 36:101580, 2020.

[299] Hideaki Ikehata, David Mayweg, and Eric Jaegle. Grain refinement of fe–ti alloys fabricated by laser powder bed fusion. *Materials & Design*, 204:109665, 2021.

[300] Xiao Peng Li, Gang Ji, Z Chen, Ahmed Addad, Y Wu, HW Wang, Jef Vleugels, Jan Van Humbeeck, and Jean-Pierre Kruth. Selective laser melting of nano-tib2 decorated alsi10mg alloy with high fracture strength and ductility. *Acta Materialia*, 129:183–193, 2017.

[301] Adriaan B Spierings, Karl Dawson, Thorsten Heeling, Peter J Uggowitzer, Robin Schäublin, Frank Palm, and Konrad Wegener. Microstructural features

of sc-and zr-modified al-mg alloys processed by selective laser melting. *Materials & Design*, 115:52–63, 2017.

[302] Bandar AlMangour, Dariusz Grzesiak, Tushar Borkar, and Jenn-Ming Yang. Densification behavior, microstructural evolution, and mechanical properties of tic/316l stainless steel nanocomposites fabricated by selective laser melting. *Materials & Design*, 138:119–128, 2018.

[303] Keiji Nakajima, Hajime Hasegawa, Sakhob Khumkoa, and Shozo Mizoguchi. Effect of a catalyst on heterogeneous nucleation in pure and fe-ni alloys. *Metallurgical and Materials Transactions B*, 34:539–547, 2003.

[304] Bandar AlMangour, Dariusz Grzesiak, and Jenn-Ming Yang. Scanning strategies for texture and anisotropy tailoring during selective laser melting of tic/316l stainless steel nanocomposites. *Journal of Alloys and Compounds*, 728:424–435, 2017.

[305] Dimitrios Siafakas, Taishi Matsushita, Åsa Lauenstein, Johan Ekengård, and Anders EW Jarfors. The influence of deoxidation practice on the as-cast grain size of austenitic manganese steels. *Metals*, 7(6):186, 2017.

[306] WJ Poole, A Mitchell, and F Weinberg. Inoculating stainless steel with titanium nitride. *High Temperature Materials and Processes*, 16(3):173–182, 1997.

[307] GN Heintze and R McPherson. Solidification control of submerged arc welds in steels by inoculation with ti. *Welding Journal*, 65(3):71s–82s, 1986.

[308] RR Preston. The solid solution hardening of steel by silicon. In *Strength of Metals and Alloys*, pages 1025–1030. Elsevier, 1979.

[309] Je Doo Yoo and Kyung-Tae Park. Microband-induced plasticity in a high mn–al–c light steel. *Materials Science and Engineering: A*, 496(1-2):417–424, 2008.

[310] Uzair Ahmed Dar, Haris Hameed Mian, Muhammad Abid, Muhammad Bilal Nutkani, Abuzar Jamil, and Muhammad Zakir Sheikh. Quasi-static compression and deformation behavior of additively manufactured flexible polymeric lattice structure. *Journal of Materials Engineering and Performance*, 31(4):3107–3119, 2022.

[311] J Bernal Ostos, RG Rinaldi, C m Hammetter, GD Stucky, FW Zok, and AJ Jacobsen. Deformation stabilization of lattice structures via foam addition. *Acta Materialia*, 60(19):6476–6485, 2012.

[312] Waiel A Elmadih, Wahyudin P Syam, Ian Maskery, and Richard Leach. Additively manufactured lattice structures for precision engineering applications. 2017.

[313] Zahra Nasiri, Sajad Ghaemifar, Meysam Naghizadeh, and Hamed Mirzadeh. Thermal mechanisms of grain refinement in steels: a review. *Metals and Materials International*, 27:2078–2094, 2021.

[314] Johannes Günther, Florian Brenne, Matthias Droste, Marco Wendler, Olena Volkova, Horst Biermann, and Thomas Niendorf. Design of novel materials

for additive manufacturing-isotropic microstructure and high defect tolerance. *Scientific reports*, 8(1):1298, 2018.

[315] D Dev Singh, T Mahender, and Avala Raji Reddy. Powder bed fusion process: A brief review. *Materials Today: Proceedings*, 46:350–355, 2021.

[316] Bandar Al-Mangour. *Powder metallurgy of stainless steel: State-of-the art, challenges, and development*, pages 37–80. 01 2015.

[317] Morgan Letenneur, Vladimir Brailovski, Alena Kreitcberg, Vladimir Paserin, and Ian Bailon-Poujol. Laser powder bed fusion of water-atomized iron-based powders: process optimization. *Journal of Manufacturing and Materials Processing*, 1(2):23, 2017.

[318] Gayan Adikari Appuhamillage. *New 3D Printable Polymeric Materials for Fused Filament Fabrication (FFF)*. PhD thesis, 2018.

Appendix A

Laser-Powder Bed Fusion printing parameters

The printing parameters of the DoE used to develop the L-PBF process window in high Mn Fe-Mn-Al-C low density steels are listed in Table A.1, where the layer thickness was not included in the table as it was kept constant in 20 microns.

Table A.1
Printing parameters used in L-PBF to define the process window in high Mn Fe-Mn-Al-C low density steels, where v stands for laser speed, and h for hatch spacing between adjacent laser tracks

Cube	Power, W	v, mm/s	LED, J/mm	h, mm	VED, J/mm^3
1	150	300	500	0.11	227
2	150	300	500	0.09	278
3	150	500	300	0.11	136
4	150	500	300	0.09	167
5	150	700	214	0.09	119
6	150	700	214	0.07	153
7	175	300	583	0.11	265
8	175	300	583	0.09	324
9	175	500	350	0.11	159
10	175	500	350	0.09	194
11	175	700	250	0.09	139
12	175	700	250	0.07	179
13	175	900	194	0.09	108
14	175	900	194	0.07	139
15	200	500	400	0.11	182
16	200	500	400	0.09	222
17	200	700	286	0.11	130
18	200	700	286	0.09	159
19	200	900	222	0.09	123
20	200	900	222	0.07	159
21	200	1100	182	0.09	101
22	200	1100	182	0.07	130